Bjørn Thorud

Dynamic Modelling and Characterisation of a Solid Oxide Fuel Cell Integrated in a Gas Turbine Cycle

Doctoral thesis
for the degree of doktor ingeniør

Trondheim, October 2005

Norwegian University of
Science and Technology
Faculty of Engineering Science and Technology
Department of Energy and Process Engineering

NTNU
Innovation and Creativity

NTNU
Norwegian University of
Science and Technology

Doctoral thesis
for the degree of doktor ingeniør

Faculty of Engineering Science and Technology
Department of Energy and Process Engineering

ISBN 82-471-7242-9 (printed ver.)
ISBN 82-471-7241-0 (electronic ver.)
ISSN 1503-8181

Doctoral Theses at NTNU, 2005:176

Printed by Tapir Uttrykk

Preface

This thesis is submitted in partial fulfilment of the requirements for the degree “Doktor Ingeniør” at the Norwegian University of Science and Technology (NTNU).

The work was carried out at the Department of Energy and Process Engineering at the Faculty of Engineering Science and Technology, with Professor Olav Bolland as supervisor and Rolf Jarle Aaberg as co-supervisor.

The research was funded by The Norwegian Research Council, Statkraft and Shell Technology Norway.

Acknowledgements

Sincere gratitude goes to my supervisor, Professor Olav Bolland, who has guided me throughout the work of this thesis. His encourage, support and capability to pose adequate questions is greatly acknowledged as a main contributor to the progress of the work. Håvard Karoliussen is greatly acknowledged for guiding me safely into the world of electrochemistry. His knowledge within the field of SOFC technology and his modelling skills has undoubtedly been invaluable for the project. Numerous discussions with my SOFC-research fellows Christoph Stiller and Arnstein Norheim have further contributed to the quality assurance of the project. Jan Van Herle and his research group at the École Polytechnique Fédérale de Lausanne (EPFL) receive gratitude for inviting me for a short scientific stay. I would especially like to thank Diego Larrain for valuable discussions regarding modelling and for showing me the EPFL SOFC-research facilities.

I would also like to thank the students who have participated in this project. Their continuous questions and curiosity have served as inspiration to go deeper into the subject of SOFC technology.

Gratitude goes to Norges Forskningsråd, Statkraft and Shell Technology Norway for financing the project, and Rolf Jarle Aaberg from Statkraft receives appreciation for giving valuable inputs to the project.

Last but not least, I would like to thank my fiancée, Karen, for her love and support and for making me keep my head up through periods of adversity. Our son Eirik receives thanks for letting his father use part of his fathers leave to continue the work on the thesis. My family is acknowledged for their support and inspiration.

Abstract

This thesis focuses on three main areas within the field of SOFC/GT-technology:

- Development of a dynamic SOFC/GT model
- Model calibration and sensitivity study
- Assessment of the dynamic properties of a SOFC/GT power plant

The SOFC/GT model developed in this thesis describes a pressurised tubular Siemens Westinghouse-type SOFC, which is integrated in a gas turbine cycle. The process further includes a plate-fin recuperator for stack air preheating, a prereformer, an anode exhaust gas recycling loop for steam/carbon-ratio control, an afterburner and a shell-tube heat exchanger for air preheating. The fuel cell tube, the recuperator and the shell-tube heat exchanger are spatially distributed models. The SOFC model is further thermally integrated with the prereformer. The compressor and turbine models are based on performance maps as a general representation of the characteristics. In addition, a shaft model which incorporates moment of inertia is included to account for gas turbine transients.

The SOFC model is calibrated against experimentally obtained data from a single-cell experiment performed on a Siemens Westinghouse tubular SOFC. The agreement between the model and the experimental results is good. The sensitivity study revealed that the degree of prereforming is of great importance with respect to the axial temperature distribution of the fuel cell.

Types of malfunctions are discussed prior to the dynamic behaviour study. The dynamic study of the SOFC/GT process is performed by simulating small and large load changes according to three different strategies;

- Load change at constant mean fuel cell temperature
- Load change at constant turbine inlet temperature
- Load change at constant shaft speed

Of these three strategies, the constant mean fuel cell temperature strategy appears to be the most rapid load change method. Furthermore, this strategy implies the lowest degree of thermal cycling, the smoothest fuel cell temperature distribution and the lowest current density at part-load. Thus, this strategy represents the overall lowest risk with respect to system malfunctions and degradation. In addition, the constant mean fuel cell temperature strategy facilitates high efficiency part-load operation. The constant turbine inlet temperature strategy proved to lead to unstable operation at low load, and thus it is considered to be the least adequate method for load change. For both the constant mean fuel cell temperature strategy and the constant TIT strategy, surge might be a problem for very large load reductions. The slowest response to load changes was found for the constant shaft speed strategy. Furthermore, this strategy leads to very low fuel cell temperatures at low loads. This in combination with a possible higher degradation rate makes the constant shaft speed strategy unsuited for large load variations. Nevertheless, operation at constant shaft speed may be facilitated by air bypass, VIGV or compressor blow off.

Table of Contents

Nomenclature

c_p	Heat capacity, [J/kgK]
D	Diffusion constant, [m^2/s]
$\bar{e}$	Electron
F	Faraday constant, 96 485 C/mol
FU	Fuel Utilisation, [%]
G	Gibbs free energy, [J/mol]
H	Enthalpy, [J/mol]
h	Heat transfer coefficient, [W/m^2K] / enthalpy [J/kg]
I	Current, [A] / Moment of inertia, [kgm^2]
i	Current density, [A/m^2]
j	Flux, [mol/m^2s] / Colburn factor
k	Thermal conductivity, [W/mK]
k_B	Boltzmann's constant, $1.38065 \cdot 10^{-23}$, [J/K]
l	Plate spacing [m]
M	Molecular weight, [kg/mol]
$\dot{m}$	Mass flow, [kg/s]
N	Shaft speed, [rpm] / Total molar flow rate [mol/s]
$\dot{n}$	Molar flow, [mol/s]
p	Partial pressure, [Pa]
P	Total pressure, [Pa] / Power, [W]
Pr	Prandtl number
q	Heat flux, [W/m^2]
R	Universal gas constant, 8.314 J/Kmol / Electric resistance [Ω]
r	Radius, [m]
Re	Reynolds number
RW	Ohmic resistance times length, [Ω m]
St	Stanton number
T	Temperature, [K]
t	Time, [s] / thickness, [m]
t_f	Fin thickness, [m] (heat exchanger)
V	Voltage, [V]

v	Velocity, [m/s] / Specific volume [m^3/kg]
$\bar{v}$	Average molecular speed, [m/s]
y	Mole fraction

Greek Symbols

α	Ratio between heat transfer area and volume between the plates (heat exchanger)
β	Factor used in the off-design maps
γ	Polytropic exponent
Δ	Arithmetic difference
δ	Plate thickness (heat exchanger), [m]
ε	Porosity / ratio between fin area and the heat transfer area (heat exchanger)
η	Efficiency / Voltage, [V]
μ	Viscosity, [Ns/m^2]
ν	Atomic diffusion volume
π	Pressure ratio
ρ	Density [kg/m^3]
σ	Stefan Boltzmann constant, $5.67051 \cdot 10^{-8}$ [W/m^2K^4]
τ	Tortuosity
ω	Angular velocity, [rad/s]

Subscripts

a	Anode
Alt	Alternator
AST	Air Supply Tube
c	Cathode
comp	Compressor
diff	Diffusion
Dim	dimensionless
DP	Design Point
eff	Effective
Exp	Expander
f	fluid

i	Inner radius / specie *i*
is	Isentropic
K	Knudsen
o	Outer radius
pol	Polarisation
por	Pore (refering to porous media)
red	Reduced
Rev	Reversible
SP	Setpoint
w	Wall

Abbreviations

APU	Auxiliary Power Unit
AC	Alternating Current
B	Bulk
BMT	Bench Mark Test
CPO	Catalytic Partial Oxidation
CGO	Gadolinia-doped ceria oxide
DC	Direct Current
DIR	Direct Internal Reforming
EVD	Electrochemical Vapour Deposition
GT	Gas Turbine
HAT	Humid Air Turbine
HDS	Hydro Desulphurization
HRSG	Heat Recovery Steam Generator
ICGT	Intercooled Compression Gas Turbine
IIR	Indirect Internal Reforming
IP-SOFC	Integrated Planar Solid Oxide Fuel Cell
IR-SOFC	Internal Reforming Solid Oxide Fuel Cell
MEA	Membrane Electrode Assembly
LHV	Lower Heating Value
OCV	Open Circuit Voltage
POX	Partial Oxidation

PF	Plate-fin (heat exchanger)
PS	Primary surface (heat exchanger)
rpm	Rotations per minute (usually applied to gas turbine shaft speed)
SOFC	Solid Oxide Fuel Cell
ST	Steam Turbine
STIG	Steam Injected Gas Turbine
SW	Siemens Westinghouse
TIT	Turbine Inlet Temperature
UHC	Unreacted Hydro Carbons
VIGV	Variable Inlet Guide Vains
YSZ	Yttria Stabilized Zirconia
3PB	Three-Phase Boundary

Definitions

Current density is the ratio between the current production and the active surface of a fuel cell.

Degree of prereforming is the ratio between converted and supplied fuel to the prereformer. A mathematical description based on methane is given in Equation 4–1.

Fuel utilisation is the ratio between utilised and supplied fuel to the fuel cell. Mathematical definitions are given in Equation 4–19 and Equation 4–20.

Gross efficiency is the efficiency calculated from the gross power and the lower heating value of the fuel.

Gross power is the overall power produced by the plant, i.e. electrical power output from fuel cell prior to the power converter, pluss the shaft power.

Knudsen diffusion is diffusion in a channel with smaller radius than the average distance between the molecule collisions. (Equation 4–45, Equation 4–46, Equation 4–65, Equation 4–66)

Net efficiency is the ratio between the net power (electrical) output and the fuel energy based on the lower heating value of the fuel.

Net power is the power supplied to the grid, i.e. gross power, less parasitic power consumption and power convertion losses.

Ordinary diffusion is the unobstructed diffusion in a solute.

Power density is the ratio between the net power and the volume of the plant, including balance of plant equipment.

Relaxation time is the time it takes from initiation of a load change till the deviation from the target load is 2% (relative to the load change magnitude) . A mathematical description is given in Equation 7–1.

Surface diffusion is a mechanism where molecules are adsorbed at the surface of a solid and diffuse along the surface. The mobility of the molecules depend on the adsorption energy.

Time to steady state is the time neccessary for the system to recover fully from a disturbance.

1 Introduction

"A model is neither true nor false - it is more or less useful"

(Stafford Beer, 1985)

Energy is the backbone of the modern society as we know it, and the global energy demand is steadily increasing. Society's dependence on electricity has clearly been demonstrated by the major black-outs in the US, Copenhagen and Italy which occurred in 2003. Increasing oil prices have further boosted the awareness of society's dependence on fossil fuels. In addition, the consequences of the fossil fuel economy have become steadily more apparent by the reduced state of health among city inhabitants and the threat of global climate change. Thus, facing the dilemma of increased energy demand at reduced emission levels, focus has been put on more efficient and environmentally friendly energy technologies. One of the many technologies concurrent to this perspective is the fuel cell.

1.1 Fuel Cell History

The invention of the fuel cell is often credited to the welsh lawyer William Robert Grove, which was the first to build a working fuel cell (1839). However, the Swiss scientist Christian Friedrich Schönbein discovered the fuel cell principle already in 1838, and published his discovery in January 1839. Several scientists contributed to further research on the subject, and in the beginning of the 18^{th} century it was reported that the technology was only a few steps away from being implemented for marine propulsion. As we know, that happened several decades later, but a milestone was reached in 1893 when Friedrich Wilhelm Ostwald was able to provide an explanation of the working principle of the fuel cell. A further milestone was reached as Francis Thomas Bacon successfully constructed a 5 kW alkali fuel cell in 1959. This type of fuel cell was the first to be used in practical applications as it was implemented in the Apollo space program in the 1960s.

The first breakthrough for the solid oxide fuel cell (SOFC) was in the late 1890s when Walther Hermann Nernst discovered various types of conductivity in doped zirconium oxide. He also discovered that the material emitted a white light when hot, and this led into a patented light bulb. The patent was later sold to George Westinghouse who produced light bulbs until tungsten filament based lamps took over. However, it was first in the 1930s that the SOFC was demonstrated, and in the late 1950s Westinghouse started experimenting with stabilised zirconia in fuel cells. The research has been continued until today, and Siemens Westinghouse Power Corporation (former Westinghouse) is today considered to be the world leader in SOFC technology. Siemens Westinghouse is also the first company to demonstrate a SOFC/GT power cycle, but a growing interest steadily increases the competition.

1.2 SOFC Activities in Norway

In Norway, SOFC research was first initiated by the late Professor Per Kofstad, a professor of inorganic chemistry at the University of Oslo. In the late 1980s he managed to gather a group consisting of SI (now SINTEF), NTNF[1] (now NFR[2]), Norsk Hydro and Saga (taken over by Hydro in 1999), Statoil and Statkraft. The research project was called NorCell, and they started off by using 4 textbooks and carefully reading SOFC patents from Westinghouse. The budget was 25 millions NOK and the first phase was finished in 1991. By then Statoil left the group to continue work by themselves, while Elkem with its subsidiary Ceramatec (USA) joined the second phase of the project. NorCell II had a budget of 50 millions NOK, and the main achievement was the "Oslo Demo" which was a 1.4 kW planar SOFC stack. Due to the disproportion between commercial expectations and experimental results, NorCell II was closed down in 1994, one year before schedule. Most of the technology was patented by Ceramatec, which Elkem later sold back to its management. Ceramatec then established the subsidiary SOFCo in partnership with Babcock and Wilcox (USA) to continue the SOFC research.

The termination of NorCell II caused several researches to go into Statoil's project, which was called Mjøllner. This project had developed in parallel to the NorCell project and Statoil had managed to include both NTNU/SINTEF and Prototech into the research group. The project had a budget of 150 millions NOK and it employed 25 engineers and scientists, many of them PhD students at NTNU. When the project was finished, Statoil and partners had been able to demonstrate a 10kW SOFC for 200 hours. Despite the successful demonstration, the research was terminated in 1998 as Statoil was unable to find industrial partners to finance the further development. Prototech has continued research on SOFCs until today, and they are still the only Norwegian company involved in SOFC development.

Early in 2000 NTNU and SINTEF took initiative to launch a research project on hydrogen as energy carrier, based upon a feasibility study recently performed for NFR [Kvamsdal, 2000]. The central recommendations of the study were that Norway should intensify its research within the fields of hydrogen production and storage and PEM fuel cells. This was also the focus of the original NTNU/SINTEF project proposal, but Professor Olav Bolland took initiative to include the subject of SOFG/GT modelling as part of the project. At the time of the project proposal he had already received prospects of financing from Shell, as they were in an early stage of planning a SOFC-plant at Kollsnes. In January 2001 NTNU/SINTEF received financing from NFR and industrial partner to cover four PhD-projects:

System analysis
- Control and optimization of fuel cells
- Integration of pressurized high-temperature fuel cells and gas turbine cycles (SOFC/GT)

1. Norges Teknisk Naturvitenskapelige Forskningsråd
2. Norges Forskningsråd, (The Research Council of Norway)

Process and materials technology
- Materials for PEM-technologies
- Fuel cells for cogeneration of hydrochloric acid and electric power

The budget of the total project was 10.3 millions NOK, of which 2.6 mill came from the industrial partners Hydro, Statkraft and Shell. The project was led by SINTEF Materials and Chemistry. This thesis represents the SOFC/GT-part of the main research project.

1.3 Background and Motivation

Fuel cells have the potential for high efficiency energy conversion, and they are very well suited to operate on hydrogen. Consequently, this technology appears to be very suitable for a post-fossil-fuel based energy economy. However, the transition from a fossil fuel based energy system to a hydrogen based system is complicated and will take time. The SOFC suits well into this perspective, as it is the most applicable fuel cell type for both fossil fuels and hydrogen. Furthermore, the high operating temperature of SOFCs facilitates the combination with gas- and steam turbines to reach electrical efficiencies beyond the limitations of conventional technologies. Fuel cells in general are able to achieve high efficiencies even for small units, and this makes them very suitable for distributed generation. As several cities already incorporate natural gas grids, SOFCs can readily be integrated into both the electrical and the natural gas grid to supply heat and power.

SOFC/GT power plants have been suggested for several applications such as stand-alone power plants, distributed generation, large scale power production and marine propulsion. However, requirements for the different types of applications vary substantially. Power production of distributed or large power plants, may remain almost steady for days, while large and fast load changes may be experienced when used in isolated grids and for marine propulsion. Due to its novelty, little is known about dynamic behaviour of SOFC/GT systems and experimental investigation of system limitations may prove to be vastly expensive. In this respect mathematical system modelling is an inexpensive tool which may be used to increase understanding of system dynamic behaviour. It may further be used in system development by establishing a basis for decision making, but findings from dynamic studies may also be used to assess the applicability of SOFC/GT systems for various market segments.

The work of this thesis aims at establishing a dynamic SOFC/GT model adequate for both basic system analysis as well as control system design. In Chapter 2 a technological background of SOFC/GT systems are given, while Chapter 3 gives a review of models described in the open literature. A description of the developed model is given in Chapter 4, while the reliability and sensitivity of the model is discussed in Chapter 5. In order to establish a basis for the evaluation of the dynamic study described in Chapter 7, possible system- and component malfunctions are discussed in Chapter 6. Concluding remarks and suggestions for further work are given in Chapter 8.

The work presented in this thesis is a result of a close cooperation between the author and PhD-student Christoph Stiller, which also is employed at the Department of Energy and

Process Engineering at NTNU. The author has focused his work on SOFC/GT model development and basic dynamic behaviour characterisation of such a system, while Christoph Stiller has focused on part-load characterisation and control system development. The same SOFC/GT model has been used in both projects and the close project integration is further reflected in the common papers which are shortly described in the next chapter.

1.4 Papers Included in the Thesis

During the work with the thesis, a total of 6 papers have been published. The paper references are listed below, followed by a short paper description.

Paper I: Christoph Stiller, Bjørn Thorud, Steinar Seljebø, Øistein Mathiesen, Håvard Karoliussen, Olav Bolland, *Finite-volume modelling and hybrid-cycle performance of planar and tubular solid oxide fuels,* Journal of Power Sources, 141 (2005) 227-240.

Paper II Thorud, B., Stiller, C., Weydahl, T., Bolland, O., Karoliussen, H., *Part-load and load change simulation of tubular SOFC systems*, Proceedings of the 6th European Solid Oxide Fuel Cell Forum, Vol 2.

Paper III Christoph Stiller, Bjørn Thorud, Olav Bolland, *Safe Dynamic Operation of a simple SOFC/GT Hybrid Cycle*, ASME TURBO EXPO 2005, GT2005-68481.

Paper IV Rambabu Kandepu, Lars Imsland, Bjarne A. Foss, Christoph Stiller, Bjørn Thorud, Olav Bolland, *Control-Relevant SOFC Modeling and Model Evaluation*, Proceedings of ECOS 2005, the 18th Conference on Efficiency, Cost, Optimization, Simulation and Environmental Impact of Energy Systems, Trondheim, Norway, June 20-22, 2005. Vol 3, p 1139-1146.

Paper V Miriam Kemm, Christoph Stiller, Azra Selimovic, Bjørn Thorud, Tord Torisson, Olav Bolland, *Planar and Tubular Solid Oxide Fuel Cells - Comparison of Transient Process Behaviours*, Solid Oxide Fuel Cells IX, May 15-20 2005, Québec City, Canada.

Paper VI Christoph Stiller, Bjørn Thorud, Olav Bolland, Rambabu Kandepu, Lars Imsland, *Control Strategy for a Solid Oxide Fuel Cell and Gas Turbine Hybrid System.* Submitted to the Journal of Power Sources.

Paper I describes two 2D steady-state models for solid oxide fuel cells with planar and tubular geometries fuelled by methane. The full paper is reproduced in Appendix A. The fuel cell models have been written in FORTRAN and implemented into PRO/II for hybrid system simulation. The influence of the different fuel cell geometries upon system behaviour is compared by a parametric study where pressure ratio, air inlet temperature, air flow rate and anode exhaust gas recycling are altered. The main finding of the paper is that the internal air preheating of the tubular design facilitates high efficiency operation at higher pressure ratios than for the planar design. It is further discovered that the enhanced ohmic loss in tubular fuel cells is somewhat compensated by the ability to

operate at lower air excess ratios. An electrical efficiency of more than 65% is achievable for both fuel cell designs.

The author's contribution to this paper is the supervision of the two MSc.-students Steinar Seljebø and Øistein Mathiesen who developed the two models. The author was further involved in the result analysis and the writing of the paper.

Paper II, which is reproduced in Appendix B, describes a quasi-2D dynamic SOFC-system model, including anode exhaust gas recycling, prereformer and afterburner. The model is written in gPROMS and it is suitable for both steady-state and dynamic modelling. The system is further modelled with boundary conditions corresponding to a pressurised SOFC/GT system. The paper presents steady-state performance maps in addition to a dynamic behaviour analysis. The main achievements of this paper are the dynamic model presentation, the novel presentation of part-load performance maps and the presentation of dynamic results originating from different load change strategies. A load change strategy which maintains a constant mean fuel cell temperature is further identified as a promising approach to load change.

In this paper the author contributed with the dynamic model development, result compilation as well as writing the paper.

Paper III is an investigation of part-load performance and dynamic behaviour of a SOFC/GT plant. The model used in this study comprise of map-based compressor and expander models, non-dimensional prereformer and afterburner models, a quasi-2D tube-shell heat exchanger, a quasi-2D plate-fin recuperator, an ejector model and a quasi-2D tubular SOFC model. The SOFC model used in this paper is basically the same as used in Paper II, except that gas transport limitations have been included. The full paper is reproduced in Appendix C. The main achievement of this paper is the presentation of full-cycle part-load performance maps, which also identifies areas of non-feasible operation. Based on the performance maps a simplified load change strategy emphasizing high efficiency, safe operation and minimum SOFC temperature cycling is proposed and tested. Finally, improvements of the presented load change strategy are suggested resulting from the dynamic result analysis.

The main contribution of the author to this paper is the development of the SOFC model and assisting the main author in the result interpretation and paper writing.

Paper IV gives a description of a dynamic lumped SOFC model, which is developed for control relevant modelling. The full paper is reproduced in Appendix D. Two different approaches to the lumped model are compared with the detailed SOFC model presented in Paper II and III. The first approach implies simply one lumped volume, while the second approach implies using two instances of the lumped model in order to represent 1/3 and 2/3 of the fuel cell, respectively. The main findings of this paper are that the lumped model shows similar dynamic behaviour to the detailed model, and that the discrepancy between the spatially distributed model and the lumped model can be reduced by using two instances of the lumped model.

The main contribution of the author to this paper is the development of the spatially distributed SOFC model.

Paper V gives a brief description of two quasi-2D dynamic SOFC models, representing planar and tubular design. A dynamic load change comparison is performed by step-wise changing the operational voltage of both models, starting from the respective design points. Start-up and shut-down analysis is also included in the examination. The main findings in this paper are that the planar geometry adapts quicker to new operating conditions, but that the tubular geometry implies lower thermal gradients than the planar design. It is further found that start-up and shut-down relaxation time is similar for both designs.

The main contribution of the author to this paper is the development of the tubular SOFC model, as well as supporting the main authors in result interpretation and paper writing.

Paper VI presents a detailed dynamic SOFC/GT system model and an adequate multi-loop control system strategy. The SOFC model used in this study includes the Butler-Volmer approach to activation polarisation calculation and it has been calibrated against experimental data. Compared to paper paper II and III, the presented system model includes spatially distributed ejector and indirect internal reformer (IIR). The paper presents full-cycle performance maps which serve as a basis for the establishment of a multi-loop feedback control strategy. The control system is further assessed according to incidents of load change, load-curve following, changes in ambient conditions and subcomponent malfunctions. The main achievement of this paper is the demonstration of full-system dynamic model capabilities as well as the presentation an appropriate control system.

The contribution of the author to this paper is the development and extension of the tubular SOFC model as well as the model calibration. Furthermore, the author assisted the main author of the paper in writing the paper.

2 Technology of SOFC/GT systems

It is the intention of this chapter to give a description of the essential components that comprise a SOFC/GT system. Special emphasis is put on the novel technology components, but in order to establish a basis for understanding the mathematical model described in Chapter 4, technology of well known components are explained as well.

2.1 The Solid Oxide Fuel Cell

The basic technology of SOFCs has been known since Nernst first described zirconia (ZrO_2) as an oxygen ion conductor in the late 1890s. Today, a century later, zirconia is still the most common electrolyte material in SOFCs. However, production methods and design have been improved to give higher reliability, efficiency and power density.

The main feature of solid oxide fuel cells (SOFC) is the all solid state and its high operating temperature. This promotes a variety of cell designs and they are specially suited for co-generation of heat and power. In addition, waste-heat can be further utilized in a bottoming cycle and a fuel lower heating value (LHV) to electricity conversion efficiency of more than 65% is achievable [Pålsson, 2002]. With an operating temperature around $1000\,^{\circ}\mathrm{C}$, emissions of pollutants such as NO_x are likely to be very small. Furthermore, sulphur compounds must be removed from the fuel before it can be utilized in the fuel cell, and hence SO_x-emissions are negligible.

2.1.1 Principle

Basically, a SOFC consists of two porous electrodes, separated by a solid electrolyte (Figure 2-1). In the 3-phase region between the cathode, electrolyte and gaseous oxygen, oxygen accepts electrons from the cathode (Equation 2–1) and the oxygen ions migrate through the electrolyte. In the 3-phase region on the anode, the oxygen ions react with CO and H_2 to form H_2O and CO_2. Fuel is supplied over the anode surface as partly reformed methane, which is fully reformed to CO and H_2 on the anode surface. CO and H_2 diffuse through the porous anode to the electrolyte surface where it reacts with the oxygen ions according to Equation 2–2 and Equation 2–3. The electrons are conducted through an external circuit from the anode to the cathode and thereby creating an electric current. In the water-gas shift reaction CO might react with steam to form CO_2 and H_2 according to Equation 2–4.

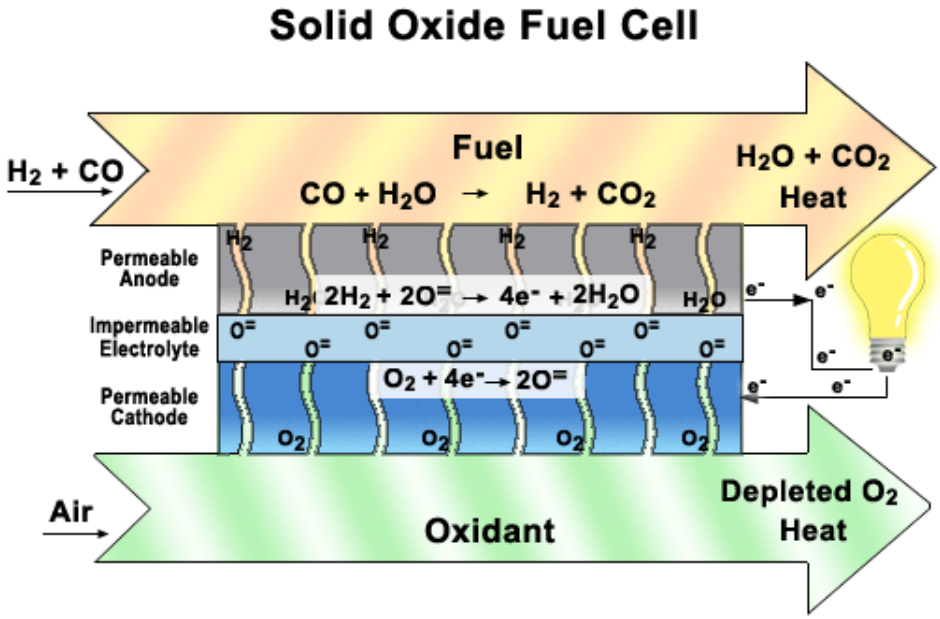

Figure 2-1. Basic principle of a Solid Oxide Fuel Cell [NASA, 2005].

$$O_2 + 4e^- \rightarrow 2O^{2-} \qquad \text{Cathode reaction} \qquad (2\text{–}1)$$

$$H_2 + O^{2-} \rightarrow H_2O + 2e^- \qquad \text{Anode reaction for hydrogen} \qquad (2\text{–}2)$$

$$CO + O^{2-} \rightarrow CO_2 + 2e^- \qquad \text{Anode reaction for carbon monoxide} \qquad (2\text{–}3)$$

$$CO + H_2O \leftrightarrow CO_2 + H_2 \qquad \text{Shift reaction} \qquad (2\text{–}4)$$

$$E_{emf} = \frac{-\Delta G^0}{nF} + \frac{RT}{nF}\ln\left(\frac{p_{H_2} \cdot p_{O_2}^{1/2}}{p_{H_2O}}\right) \cdot P_{ref}^{1/2} \qquad \text{Nernst Equation} \qquad (2\text{–}5)$$

The Nernst equation, which is given in Equation 2–5, relates the operating voltage of a fuel cell to the thermodynamics of the electrochemical reactions. The operating voltage is often also called electromotoric force (emf). In the Nernst equation, n represents the number of electrons transferred in the reaction, R is the universal gas constant, T is the temperature in K, F the Faraday constant, p the partial pressure and P_{ref} is the total pressure at standard conditions (1 atm). All pressures are given in Pa. The theoretical maximum voltage produced by a fuel cell can be measured if no current is produced and is hence often termed “Open Circuit Voltage” (OCV). It can also be calculated from the Nernst equation. From the Nernst equation it can be seen that if any of the reacting species are fully consumed, the voltage will drop to zero or even below zero if a voltage is put on

the cell. In order to assure an adequate operating voltage, surplus of air is often supplied to the cathode, while the fuel utilisation is normally kept at approximately 85%.

Current production is associated with three main types of losses; polarisation-, ohmic- and diffusion losses. As can be seen from Figure 2-2, each type of loss dominates at different operating ranges of the fuel cell. Polarisation losses are caused by slowness of the reactions taking place at the electrode surface and may be considered as a reaction resistance. Consequently, polarisation losses are related to the whole operating range, but they dominate for small current densities. Ohmic losses are caused by ohmic resistance in the cell materials, and they are linearly dependant on current and current path. Ohmic losses in SOFCs are highly temperature dependant, especially for the electrolyte, which is responsible for a major fraction of the ohmic losses.

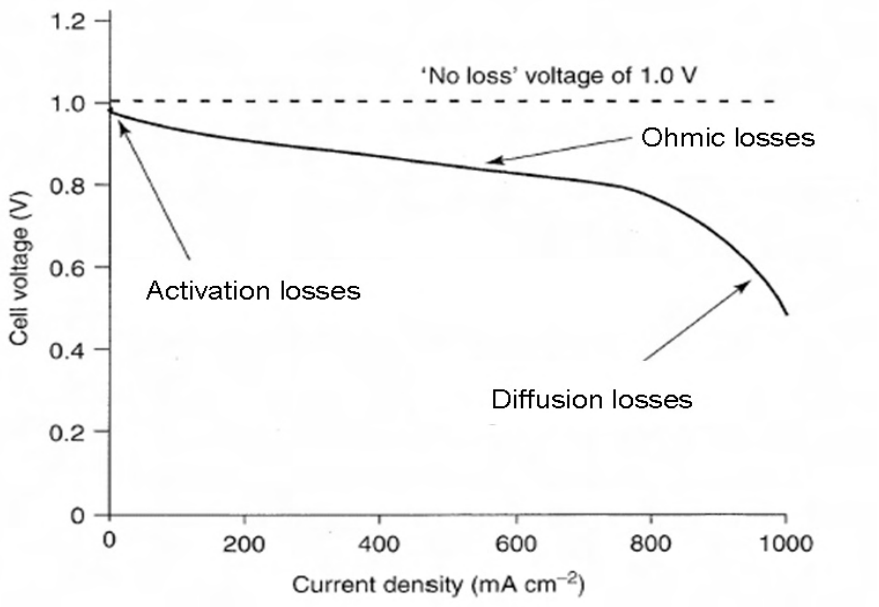

Figure 2-2. Current-Voltage characteristics of a fuel cell operating at 1073K [Larminie, 2000].

The reacting species in the fuel cell must be transported from the usually laminar gas flow through the porous electrode to the reaction site. Hence the main transport mechanism is diffusion. Diffusion is rather slow, and at high current density, this might be the limiting factor for the electrochemical conversion (Figure 2-2). Additionally, the products of the electrochemical reactions are formed at the anode, and this leads to dilution of the fuel and increased diffusion resistance. Hence the Nernst voltage, given by Equation 2–5, will decrease from the fuel inlet to the outlet. If the operating cell voltage exceeds the Nernst voltage, the backward reaction will occur and the cell will operate as an electrolyser. This can be fatal for the cell, as it might lead to oxidation of the nickel in the anode, which is further associated with volume change and the possibility of material cracking.

Normally, the cell will operate in the range where ohmic resistance is the dominating loss mechanism and it will produce a voltage of 0.6-0.7 V [Larminie, 2000]. This is a rather low voltage for practical power supply, and thus several cells are coupled in series in a stack to increase the voltage. As the current and voltage will change due to the operating conditions, a DC/AC-converter has to be implemented to be able to supply the grid with an appropriate power quality.

An ideal (reversible) fuel cell will be able to convert the total Gibbs free energy into electricity. Hence the theoretical efficiency limit can be calculated from the Gibbs free energy and the reaction enthalpy:

$$\eta_{max} = \frac{\Delta \bar{g}_f}{\Delta \bar{h}_f} \tag{2–6}$$

It is important to notice that this efficiency definition is with reference to a thermal system. Theoretically, $\Delta \bar{s}_f$ can be less than zero, and in this case the efficiency limit in Equation 2–6 would be larger than 1. However, this is rarely the case and Equation 2–6 is generally applied to fuel cells.

Since the Gibbs free energy decreases with increasing temperature, the maximum efficiency will decrease with increasing temperature. This means that the efficiency limit of a high temperature fuel cell is lower than for a low temperature fuel cell.

The efficiency of an actual fuel cell is most often calculated as the power divided by the lower heating value of the fuel;

$$\eta_{cell} = \frac{P}{\dot{n}_{fuel} \cdot \Delta h_{LHV}} \tag{2–7}$$

In this equation $\dot{n}_{fuel}$ denotes the molar fuel flow, while Δh_{LHV} is the molar reaction heat at standard conditions, which are 298 K and 1 atm (Lower heating value). The definition given in Equation 2–7 is used in efficiency calculations in the presented work.

A further key parameter often used to merit fuel cell systems is the power density, which is defined by Equation 2–8. The volume which is to be used in the power density calculation is the total volume of the power plant, including the balance of plant equipment. The balance of plant equipment is further described in Chapter 2.3.

$$\text{Power Density} = \frac{\text{Power}}{\text{Volume}} \tag{2–8}$$

2.1.2 Materials

Besides being good conductors (electronic, ionic or both), the materials used in solid oxide fuel cells must possess adequate properties to remain stable, both chemically and mechanically within reducing and/or oxidizing environments. It is also important that they remain stable during the considerable higher temperatures they are exposed to during

fabrication. In addition, they should have similar coefficients of thermal expansion in order to avoid delamination and crack formation during fabrication and operation. The interconnect and electrolyte must be dense to prevent gas mixing and the electrodes must be porous to allow the gas transport to the reaction areas. Other desirable properties are high strength, ease of manufacture and low cost.

Only a limited number of materials exhibit these properties and the most common ones will be described briefly in this chapter.

Electrolyte

In addition to the properties mentioned above it is important that the electrolyte has a high ionic conductivity and low or no electronic conductivity. It is also important that it is dense in order to prevent fuel cross-over. There are two main types of electrolytes that can be considered for SOFC-applications; oxygen-ion conductors and proton conductors. Both types are made of oxides, but the latter is currently in an early development phase and will not be considered here.

Most oxides considered for SOFC applications are mixed conductors. The mechanisms of conduction are n-type (electrons), p-type (electron holes) and ionic. The conduction mechanisms vary with oxygen partial pressure and the lattice structure. The lattice structure also varies with the temperature. Generally the electronic conductivity dominates for very low (n-type) and very high (p-type) oxygen partial pressures. However, for typical SOFC oxygen partial pressures the electronic conductivity is negligible compared to the ionic conductivity.

Pure zirconia (ZrO_2) exhibits 3 different lattice structures from room temperature to 2370 °C, where it becomes ionic conductive. The alteration of lattice structure is also associated with about 3-5% change in volume. In order to retain the ionic conductive structure even at room temperature, about 8-10% yttria is added as a dopant. The dopant blocks the ionic conductive structure from transition to another lattice structure and also introduces defects which increase the ionic conductivity. Other dopants that could be used are CaO, MgO and Sc_2O_3. The ionic conductivity increases with temperature and usually SOFCs with YSZ electrolytes operate at approximately 950 °C. By reducing the electrolyte thickness, however, one can operate SOFCs with YSZ electrolytes at reduced temperatures. By doing so, the magnitude of the resistance can be maintained, although the specific resistance increases. In order to maintain an appropriate mechanical strength these thin electrolyte cells must be supported either by the anode, cathode or a porous substrate.

In SOFCs the YSZ electrolyte is generally fabricated as a polycrystalline dense film or layer. This is either done by the particulate approach or the deposition approach. For both methods the ideal powder should be a homogenous mixture of zirconia and dopant evenly distributed on an atomic scale. The particulate approach involves compaction of the powder into desired shape and densification at elevated temperature (tape casting and tape calendering). The deposition approach involves the formation of a thin layer by a

chemical or physical process. This could either be done by electrochemical vapour deposition (EVD) or plasma spraying [Kordesch, 1996].

Generally YSZ exhibits little or no chemical interaction with the other fuel cell materials. But at high operating temperatures (>1200° C) ZrO_2 reacts with $LaMnO_3$ (cathode) to form insulating phases at the interface. These insulating layers cause the cell performance to degrade significantly.

Anode

Apart from being electronically conductive, the main function of the anode is to reform hydrocarbons and provide reaction sites for the electrochemical oxidation of the fuel. The reaction sites are at the three-phase boundary (TPB) between fuel gas, anode and electrolyte. The larger the TPB, the larger is the activity of the electrochemical reactions, which again influences the power density of the fuel cell. As already mentioned in Chapter 2.1.1, the reacting species must diffuse through the anode to the reaction sites. In order to achieve a high diffusion rate the anode must therefore be porous. Tortuosity and average pore radius play important roles with respect to diffusion, and these parameters are to a certain extent controlled by the production process. Furthermore, the anode must be tolerant towards certain levels of contaminants present in the fuel gas such as sulphur.

The most common anode material is a porous cermet consisting of nickel and YSZ. Here nickel serves both as electronic conductor and reforming catalyst. YSZ is used as support in order to assure a relatively equal thermal expansion coefficient between the anode and the electrode. As the anode has to contain at least 30 vol.% Ni to have a sufficient conductivity, there is a mismatch between the thermal expansion coefficients. Despite this mismatch Ni-YSZ has proven to be suitable for use in SOFCs. One way to reduce the effect of the differences in thermal expansion coefficients is to reduce the thickness of the anode.

Ni - YSZ anodes are generally known to be chemically stable for SOFC applications. However, Ni-particles have a high surface area, and there will always be a thermodynamically driving force to decrease the free energy, i.e. minimize the surface area by sintering. Thus this type of anodes may exhibit degradation over time, but it can be partly reduced by optimum Ni-particle distribution [Tu, 2005].

In most cases, the SOFC anode is made with NiO and YSZ. The NiO is then reduced “in situ” to nickel metal exposed to the fuel in the fuel cell. The TPB area can be controlled partly by controlling the powder size and Ni to YSZ-ratio. The fabrication technique also influences the structure.

Cathode

The main objective for the cathode is to provide reaction sites for the electrochemical reduction of the oxidant. Material properties such as porosity, tortuosity and average pore radius are as important for the cathode as for the anode. The most commonly used cathode material today is doped Lanthanum Manganite ($LaMnO_3$). To increase electric

conductivity and avoid phase transitions, $LaMnO_3$ is usually doped with Strontium (Sr) or Calcium (Ca).

The preparation of the cathode is usually decided by the stack design. For tubular cells the cathode layers are deposited on a porous support by slurry coating or simply extruded. For segmented cells in series, the cathode is prepared by flame spraying of the ceramic powders onto the surface of the electrolyte. Tape casting, printing, spraying and depositing can be used in planar cell production. Each method gives a different cathode structure, but all methods use fine powders as starting materials.

As already mentioned, $LaMnO_3$ might react with YSZ to form insulating phases at elevated temperatures. This effect has been observed at temperatures above 1200° C, where the cathode reacts with the YSZ electrolyte to form $La_2Zr_2O_7$ and other insulating phases at the interphase. These phases can also create thermal stresses at the interphase. Thus $LaMnO_3$ is sintered at temperatures between 1250° C and 1400° C, and during operation it is crucial that the temperature never exceeds 1200° C for a long period.

Interconnect

The interconnect has to maintain a high electric conductivity even in the high temperature dual atmosphere (planar). It is also required that no chemical interactions with the other components occur. So far, Sr doped $LaCrO_3$ has proven to be a quite sufficient material. This is a perovskite material with an ABO_3 structure where A is a divalent cation and B is a tetravalent cation. The melting point of Sr doped $LaCrO_3$ is as high as 2510° C. The dopant is introduced to avoid phase transitions and thus a change in properties accompanied by changes in temperature. Ten percent strontium on a molar basis is usually sufficient to stabilize the material.

$LaCrO_3$ shows a p-type electric conduction, which varies with the atmosphere. In a hydrogen atmosphere the oxygen loss reduces the charge carrier and thereby decreases the conductivity of the material. In planar cells, the interconnect often separates the anode and cathode chamber. For the case of $LaCrO_3$, this means that it is exposed to a dual atmosphere and there will be a conductivity gradient across the material.

$LaCrO_3$ does not interact with other cell materials at the cell operating conditions, but above 1300° C mixtures of $LaCrO_3$ and $LaMnO_3$ (cathode) form a solid solution. Thus co-firing with the other cell components is avoided. In the planar design, $LaCrO_3$ might interact with the glass sealants that are used.

Material Development

A large effort is put into finding new materials which facilitates SOFC operation at lower temperature with reduced losses [Singhal, 2003], [Jiang, 2004]. At reduced temperatures metallic interconnectors may be employed and this might reduce production cost of the SOFC. Metallic interconnectors are also better thermal conductors, and implementation of such interconnectors will drastically reduce the thermal stresses of the materials

[Rechenauer, 1992]. Reduced operating temperature is also believed to increase lifetime of the cell.

2.1.3 Cell and Stack Design

There are three main approaches for cell design; tubular cells, planar cells and monolithic cells. The three of them differ in the extent of dissipative losses, sealing methods, stack design and power density. The highest power density has been reached by the monolithic design, which looks like a corrugated cardboard box in cross section. However, there are some difficulties with sealing and thermally induced tensions, which again cause delamination and breakage of the cells. Therefore most cells produced today are either planar, tubular or a combination of the two.

Planar Cells

The planar design is currently produced by a number of companies, like Sulzer Hexis (CH), Prototech (N), HTCeramix (CH) and Haldor Topsoe A/S (DK). The cells are quadratic, rectangular or circular and they normally have an active surface of approximately 100-120 cm^2. The cells are put together in electrical series in a stack assembly consisting of anode, electrolyte, cathode and interconnector, where the interconnector connects the anode of one cell to the cathode in the next (Figure 2-3). A disadvantage of connecting the cells in series like this is that if one cell fails, the whole stack falls out. Hence, planar stacks are usually made of a small number of cells.

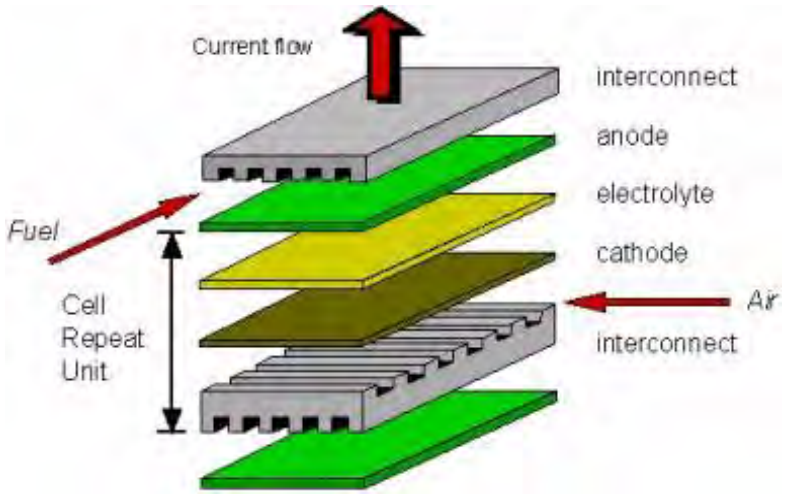

Figure 2-3. Basics of a flat plate cross-flow SOFC. (Courtesy Craig Fisher)

Different gas flow regimes exist for the planar design. An investigation of characteristics of cross-flow, co-flow and counter-flow has shown that co-flow is affiliated with the lowest degree of thermal stress for the fuel cell [Rechenauer, 1992]. Actually, cross-flow configuration has proven to be the least favourable design with respect to thermal

gradients. Nevertheless, cross-flow is the most used flow configuration for planar SOFCs, and this is mainly due to a less complicated manifolding system and reduced constraints for the sealants.

The planar design offers advantages such as relatively cheap production methods, simple design and high power density. The challenges are connected to finding a sealing material which does not interact with the other cell materials and at the same time avoids fuel- and oxidant cross-over at the high operating temperature.

Tubular Cells

Siemens Westinghouse Power Corporation has developed a “seal-less” tubular SOFC (Figure 2-4). In this design, thin layers of electrolyte and anode are deposited on a cathode tube. The tube is produced by extrusion and sintering. In a strip along the tube is a gas-tight layer of interconnector. The tube is closed in one end and air is supplied to the closed end by an inner tube. The fuel is provided to the outside of the tube, and air and fuel flow co-currently.

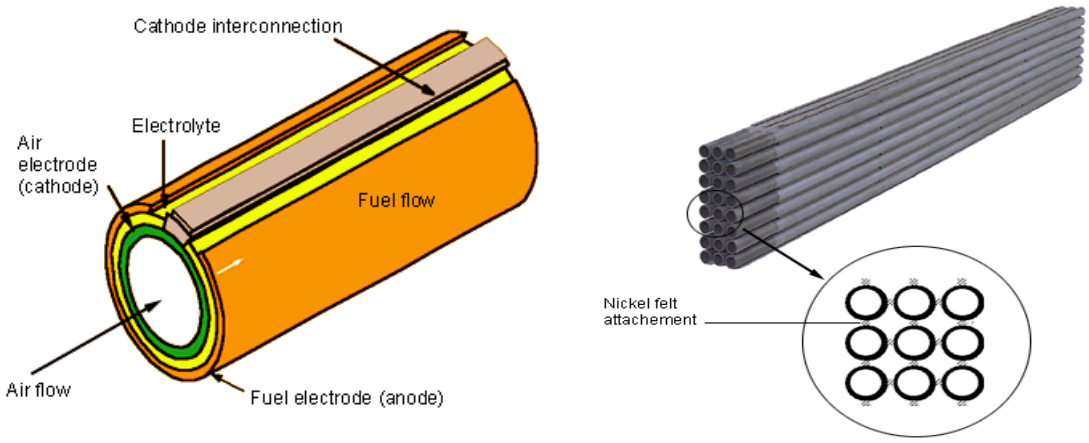

Figure 2-4. A slice of the tubular SOFC developed by Siemens Westinghouse (left), and the stacking of the cells (right). (Courtesy Siemens Westinghouse)

Tubular cells of this design can be fixed in one end, and thus there are fewer problems with thermally induced tensions. By placing the afterburner close to the manifolding system, it is also possible to omit the use of sealants.

In the Siemens Westinghouse design a stack is formed by several bundles, where each bundle consists of 3 x 8 tubes connected in series (right, Figure 2-4). Between each tube, Nickel felt is introduced to assure a temperature flexible electrical conductor.

The disadvantage of tubular SOFCs is cost, complexity and the relative low power density. Siemens Westinghouse is now developing a flattened tube, which is shown in Figure 2-5 [Lu, 2005]

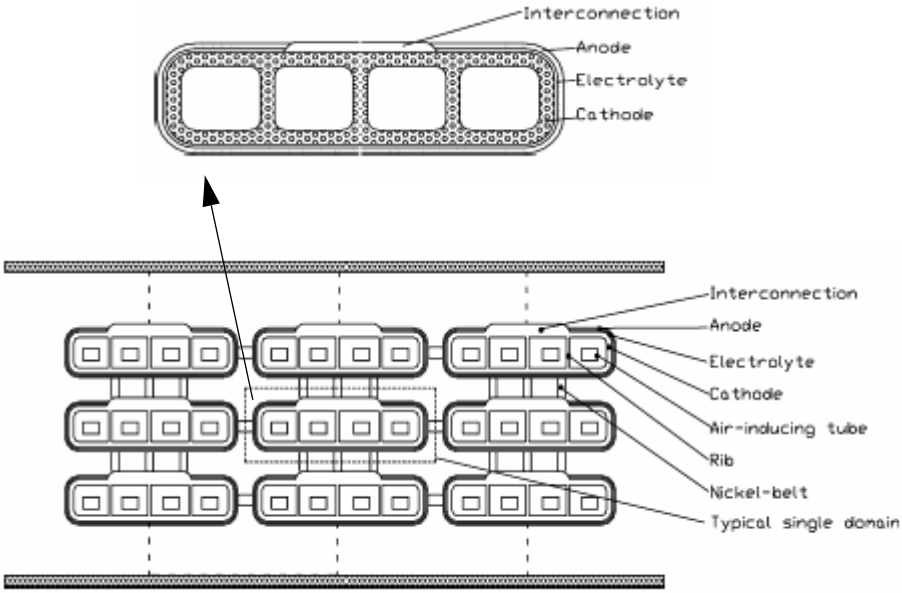

Figure 2-5. The flattened SOFC tube developed by Siemens Westinghouse. The single tube is shown on the top, while the stacking is shown below.

The flattened tube is an approximation to obtain the high power density that can be achieved from planar cells, but with the benefits of seal-less design and reduced thermal stress that can be obtained from the tubular design. In the flattened tube design, the cathode supports the structure and it contains four almost quadratic chambers (Figure 2-5, top). The electrolyte and anode are deposited on the cathode as thin layers. Ohmic losses are reduced by the "bridges" between the chambers of the cathode. They serve as short-cuts for the electric current, minimising the current path and hence the ohmic loss.

Segmented-cell-in series

Segmented-cell-in-series can either be tubular, flat or a combination of both. The main difference between the segmented-cell-in-series and the planar design are that the stacks are formed by a number of smaller cells connected in series with respect to electrical current and gas flows. (Figure 2-6)

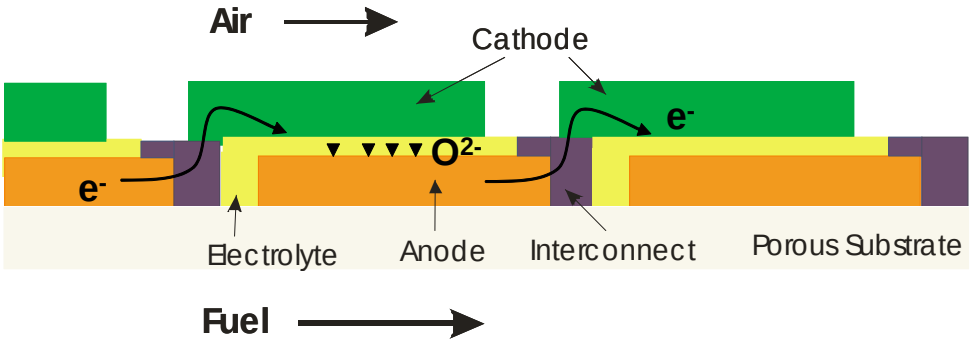

Figure 2-6. In segmented-cells-in-series a stack is formed by several small cells connected together in series. The interconnect is placed between each cell and connects the anode of one cell to the cathode of the next cell. The cells are supported by a porous substrate.

Segmented cells in series offer a high fuel utilization and efficiency, but they are more expensive than the flat plate design. Mitsubishi Heavy Industries and Rolls-Royce are companies that pursue this design. Mitsubishi Heavy Industries has developed a tubular stack with some similarities to the Siemens Westinghouse design (Figure 2-7, left). With this design one tube can be considered as a stack. Rolls-Royce has a stack which is a mixture between flat plate and tubular design. Their integrated planar solid oxide fuel cell stack (IP-SOFC) consists of up to 29 flat cells which are connected in series (Figure 2-7, right). The “tubes” are thin and rectangular and as for the Siemens Westinghouse type, they are fixed only at one point.

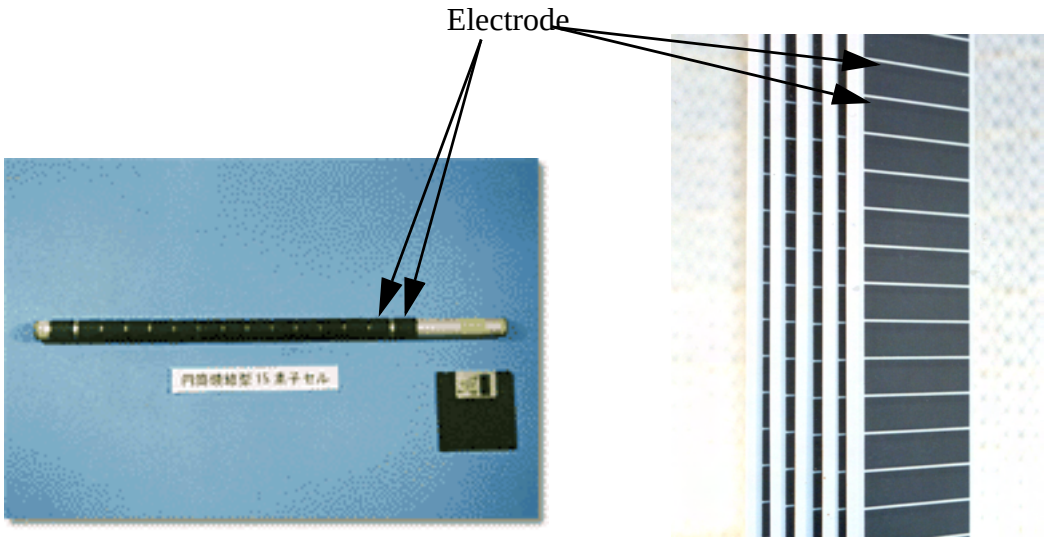

Figure 2-7. The tubular segmented-cell-in series developed by Mitsubishi Heavy Industries (left), and the integrated planar Solid oxide fuel cell stack developed by Rolls-Royce (right).

2.2 Bottoming Cycle

As mentioned in Chapter 2.1.1, the maximum efficiency of a fuel cell is related to the Gibbs free energy, which decreases with increasing temperature. In a heat engine, work is produced through heat exchange between a hot and a cold source. The Carnot efficiency gives the maximum theoretical efficiency of a heat engine, and it behaves exactly opposite to the fuel cell with respect to efficiency. (Equation 2–9)

$$\eta_{carnot} = \frac{T_{hot} - T_{cold}}{T_{hot}} \qquad (2–9)$$

When plotted in the same efficiency chart, it can be seen that a combination of high temperature fuel cells and a heat engine can achieve very high efficiencies (Figure 2-8). This is the motivation for the combination of high temperature fuel cells and heat engines.

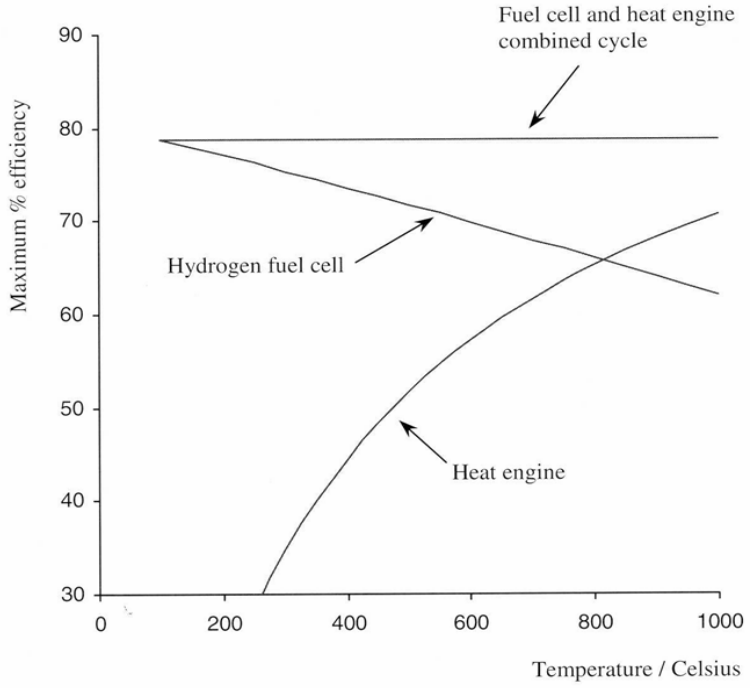

Figure 2-8. Maximum heat engine efficiency and the maximum hydrogen fuel cell efficiency plotted together with the maximum hybrid cycle efficiency. [Larminie, 2000]

Additionally, fuel cell power density is increased at elevated pressure. From the Nernst equation (Equation 2–5), it can be shown that increasing the operating pressure of a fuel cell leads to increased voltage. The relationship between pressure and voltage change is shown in Equation 2–10.

$$\Delta V = \frac{RT}{nF}\ln\left(\frac{P_2}{P_1}\right) \qquad (2\text{–}10)$$

In Equation 2–10, ΔV denotes voltage change, R is the universal gas constant, T the temperature in Kelvin, F Faradays constant and P_1 and P_2 are initial and final pressure.

2.2.1 Gas Turbine

A gas turbine cycle is based on the theoretical Brayton Cycle in which a gas is compressed, heated and expanded, but in contrast to a reciprocating engine (Otto/Diesel cycle), the compression, heating and expansion takes place in different components (Figure 2-9). These components can be designed and produced separately, tested and put together to form a variety of cycles. The number of components is not limited to the three described above, but a cycle may consist of several compressors and expanders, facilitating compressor intercooling and reheat expansion. Heat exchangers may also be included in order to use the exhaust heat to preheat the compressed gas before it enters the combustion chamber.

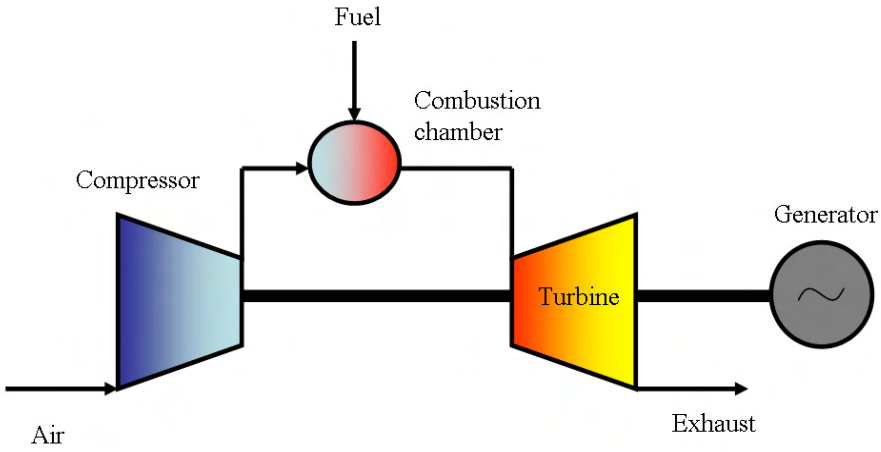

Figure 2-9. A simple gas turbine process.

Gas turbines are largely used within power production and the power range goes from 70 kW to 330 MW. Electrical efficiency depends on the component design as well as the cycle layout and size of the plant. Usually, electrical efficiency is between 30 and 40%, but it can be further improved by adding a bottoming cycle, such as a steam turbine. Electrical efficiency for a large power plant combining gas- and steam turbines is nearly 60%.

A gas turbine can either be indirectly or directly integrated with the high temperature fuel cell process. In indirect integration, the combustion chamber of the gas turbine process is exchanged with a heat exchanger where exhaust from the fuel cell stack is used to heat air coming from the compressor. In this concept, the fuel cell can operate under atmospheric

pressure. Although this reduces the requirements for sealants in the SOFC stack, a great challenge remains on finding an appropriate heat exchanger. Due to a very high operating temperature and pressure difference between the hot and cold side, the heat exchanger must be made of special alloys, and it might be very expensive. An indirect integration is also likely to have a low efficiency compared to the direct integration, due to heat transfer and pressure losses in the heat exchanger.

When the gas turbine is directly integrated with the fuel cell stack, the stack "replaces" the combustion chamber in the conventional GT process (Figure 2-10). Pressurization of the stack increases power output further, according to Equation 2–10, but there are also some extra challenges regarding design and control of the process. For instance, large pressure gradients between anode and cathode must be avoided due to the natural brittleness of the cell materials. Pressurised operation also requires reliable sealants or complete control of leakages. Further challenges are associated with dynamic and part-load system operation.

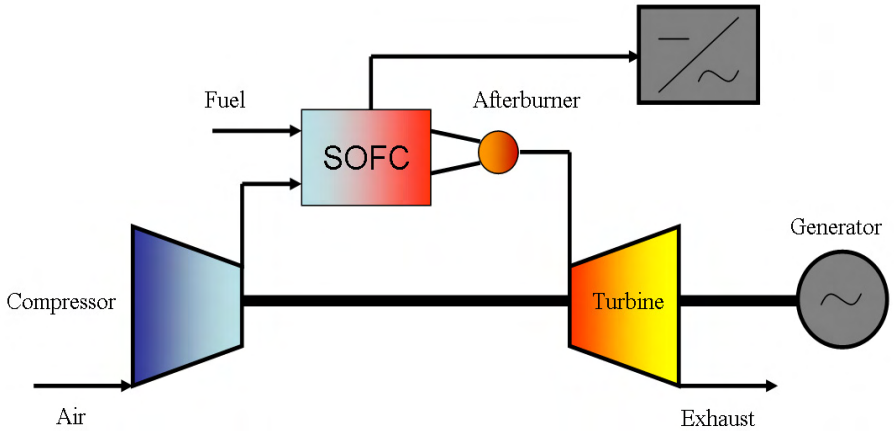

Figure 2-10. A SOFC/GT cycle layout for direct integration of the SOFC.

Today no turbine especially designed for hybrid operation exists. Calculations show that such a turbine is likely to have an optimum pressure ratio of 4-6 with a turbine inlet temperature (TIT) of 800-900°C [Pålsson, 2002]. Conventional turbines are usually designed for higher pressures and TITs. The benefits of a tailored designed turbine for SOFC applications would be a total power increase of 20-50%, a fuel efficiency increase of 20-30% and a total cost reduction of up to 40% [Ali, 2001]. Commercial turbines are likely to be used in the first generation SOFC/GT applications in order to reduce cost. That means that the stack must be designed to fit the gas turbine with respect to gas flows and temperature. A rebuild of the gas turbine combustion chamber and piping system is further unavoidable.

2.2.2 Steam Turbine

The steam turbine (ST) cycle is based on the theoretical Rankine cycle, in which a liquid is compressed, evaporated, expanded and condensed. Each step in the cycle takes place in a different component, and as for the gas turbine, a variety of cycles may be constructed from these basic components. In large power plants, expansion of the fluid is usually divided into high pressure-, medium pressure- and low pressure turbines. This facilitates reheating of the fluid, and thereby electrical efficiency may be improved. It is also possible to extract steam for use in industrial processes. Steam turbines are usually employed only for larger power plants due to the economy of scale, and the largest power plants have a capacity of up to 1000 MW.

A steam turbine cycle can utilise almost any type of fuel, and steam turbines are known to operate on biomass, household waste, nuclear fuel, coal and geothermal heat. In large natural gas powered power plants, steam turbines are often used in combination with gas turbines. In this combined cycle, the hot turbine exhaust gases are used in a heat recovery steam generator (HSRG) to generate steam to a steam turbine.

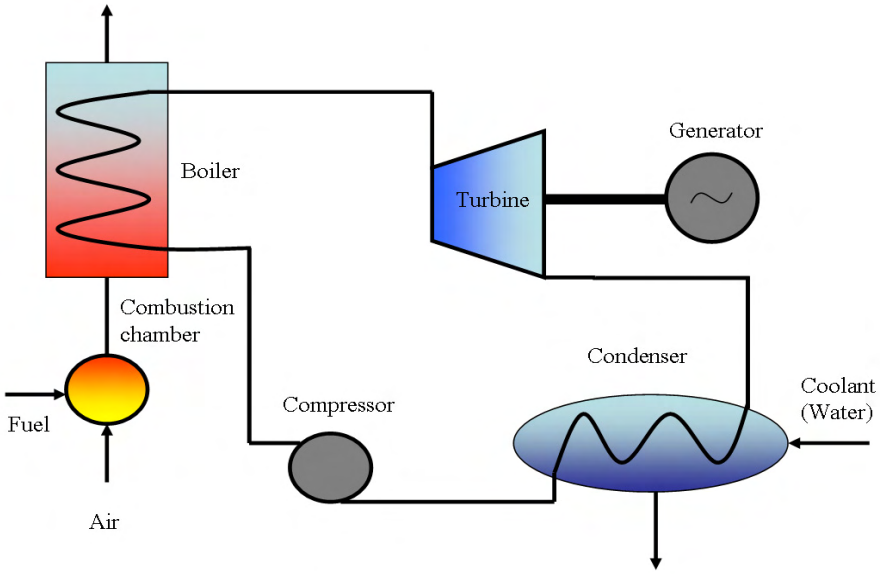

Figure 2-11. A basic steam turbine cycle

A SOFC/GT cycle may utilise the hot gas turbine exhaust in the same way as a combined cycle. Such a SOFC/GT-ST cycle represents a very efficient process, by which more than 80% electrical efficiency could be reached for units larger than 10 MW [Winkler, 2000], [Winkler 2002]. However, this process is likely to be more expensive than the SOFC/GT-cycle, and so far it has not been demonstrated.

The SOFC could also be integrated with a steam cycle only. This represents a far less complicated system than the SOFC/GT-ST system, as the SOFC may operate at

atmospheric conditions. A SOFC-ST plant could reach 10% higher efficiency than a stand-alone SOFC process. This cycle is also likely to be more expensive than the SOFC/GT-cycle. Another reason for not building a SOFC-ST plant is that the SOFC/GT cycle reaches a higher power output than the SOFC-ST cycle [Pålsson, 2002].

2.3 Balance of Plant Equipment

Reliable operation of solid oxide fuel cells requires fuel supply of the right quality, adequate heat integration and effective system control. These requirements are fulfilled by a basic set of equipment that is involved in any SOFC process.

2.3.1 Fuels and Fuel Processing

Solid oxide fuel cells are not only able to operate on hydrogen, but also fuels containing carbon. This makes SOFCs highly fuel flexible and SOFCs have been reported operating on heating oil, fermentation gas [Jenne, 2002], natural gas [George, 2000], methanol, formic acid [Saunders, 2002] and gasoline [Khandkar, 1999]. Gasified coal and gasified biomass have also been proposed as fuels for SOFCs.

Desulphurisation

Sulphur is known to reduce effectiveness of certain catalysts by creating a strong bonding to the catalyst, and thereby occupying the active surface. Nickel, which is used in the SOFC anode and some prereformers, is one of the catalysts which are intolerant towards even small amounts of sulphur. Usually, there has to be less than 0.1 ppm sulphur containing compounds in the fuel for the catalyst not to be poisoned [Larminie, 2000].

Natural gas may contain small amounts of sulphur in the form of H_2S, either naturally or added as an odorant for safety reasons. Removal of H_2S is usually straight-forward, and it may be absorbed either in a bed of zinc oxide (Equation 2–11) or an activated carbon filter. This reaction is nearly adiabatic and the pressure drop is fairly small.

$$H_2S + ZnO \rightarrow ZnS + H_2O \qquad (2–11)$$

Organic sulphur compounds are not absorbed as easily in zinc oxide or active coal, and must be converted into H_2S in order to be removed. This conversion may occur in a hydrodesulphurisation (HDS) reactor, which only can be utilised if a hydrogen rich gas is present. In SOFC applications, some of the prereformed fuel may be recirculated for hydrogen supply of the HDS reactor. The reactor uses nickel-molybdenum oxide or cobalt-molybdenum oxide as catalyst, and it converts organic sulphur containing compounds into a hydrocarbon and H_2S. An example of the reaction is shown in Equation 2–12.

$$(C_2H_5)_2S + 2H_2 \rightarrow 2C_2H_6 + H_2S \qquad (2–12)$$

The hydrogenolysis reaction is promoted at higher temperatures (300-400 °C) and under excess hydrogen. This means that for fuels with a large carbon content, other methods than HDS must be used.

Prereformer

Any fuel that is to be used in a SOFC has to be decomposed into hydrogen and carbon monoxide in order to participate in the electrochemical reactions. Methane can be reformed directly on the anode surface if steam is present, but reforming of higher hydrocarbons is difficult to achieve without the formation of solid carbon. Since carbon deposition might damage the cell, most SOFC applications have a prereformer prior to the cell. The prereformer converts the fuel into a hydrogen rich mixture of methane, carbon monoxide and carbon dioxide (Equation 2–13). The methane can be reformed according to Equation 2–14, while most of the carbon monoxide reacts to form hydrogen (Equation 2–15). The steam is often supplied to the prereformer by recirculating part of the anode exhaust gases.

$$C_nH_m + nH_2O \rightarrow nCO + \left(\frac{m}{2} + n\right)H_2 \qquad (2–13)$$

$$CH_4 + H_2O \rightarrow CO + 3H_2 \qquad (2–14)$$

$$CO + H_2O \leftrightarrow CO_2 + H_2 \qquad (2–15)$$

Internal reforming of methane is facilitated by the presence of nickel in the anode. This method offers a high degree of thermal integration and utilization of steam produced by the electrochemical reaction. Owing to the reforming taking place directly on the anode, this method is often referred to as “direct internal reforming” (DIR).

Steam reforming is highly endothermic and hence the prereformer is often integrated thermally with the fuel cell stack in what is called “indirect internal reforming” (IIR). A prereformer may also receive heat supply from an external source.

Steam reforming depends on a reliable supply of steam to the process. This could either be supplied by recirculation of parts of the anode exhaust gases, or from an external steam generator that utilises excess heat. Thermodynamically, recirculation of exhaust gases is clearly the most effective, but this method also adds more complexity to the system.

In absence of steam sources, partial oxidation (POX) represents a good alternative for fuel reforming. This method is an understoichiometric combustion of the fuel, and thus yields a fuel with lower energy content than that of steam reforming. Almost half of the fuel reacts fully with oxygen to produce carbon dioxide, steam and heat. The steam reacts with the remaining methane according to the steam reforming reaction given in Equation 2–14, utilizing the heat produced by the oxidation. The reaction given in Equation 2–16 therefore represents the sum of these two reactions.

$$CH_4 + \frac{1}{2}O_2 \rightarrow CO + 2H_2 \qquad (2\text{–}16)$$

Partial oxidation has no need for catalysts when operating at high temperatures (1200-1500 °C). In this case, it has the advantage that no sulphur sensitive catalysts are used, but the sulphur still has to be removed before the fuel enters the cell. Another advantage with partial oxidation is that it is able to handle heavier petroleum fractions than a catalytic process. It is therefore suitable for processing fuels such as diesel, petrol and residual fractions. Although partial oxidation is a well known process and is used in large scale commercial plants, there are some challenges linked to down-scaling the process and to reaction control.

If the temperature is reduced and a catalyst employed, the process described by Equation 2–16 is called a catalytic partial oxidation (CPO). Platinum-metal and nickel based materials are catalysts that support CPO.

As the POX reaction produces the heat needed for the reactions itself, it can not utilize the excessive heat from the fuel cell. Another disadvantage with POX is that if air is used as the oxidant source, hydrogen is diluted by the presence of nitrogen. This results in lowering the Nernst potential, which again lowers the system efficiency. However, the great advantage of partial oxidation is its system simplicity, as there is no need for recirculation of fuel or external steam generation.

Autothermal reforming is another method of fuel processing, which is a combination of steam reforming and partial oxidation. Fuel, oxygen (or air) and steam is fed to a catalytic reformer, where the above mentioned reactions take place. The advantage of autothermal reforming is that less steam is needed than for the steam reforming and that all the heat needed can be supplied by the partial oxidation of the fuel. This method requires no complex heat management, which results in a less complicated system. Autothermal reforming is particularly of interest for mobile applications.

Reformers for hydrocarbons are generally available on the market, but in case of IIR the prereformer may have to be redesigned for in order to achieve an optimum heat transfer between the stack and prereformer.

2.3.2 Ejector

Ejectors provide compression without any moving parts. Ejectors can be produced in almost any type of material and they are often used to handle complicated gases, such as hot-, corrosive-, explosive- or dusty gases. Other benefits of ejectors are that no sealants or maintenance is needed, and in the industry they are often used in fume removal, venting or as an emergency vacuum source. The fuel cell industry has also become increasingly interested in ejectors.

The ejector consists of a nozzle, a suction zone, a mixing chamber, a diffuser throat and an outlet (Figure 2-12). A high pressure fluid (actuating fluid) is expanded in the nozzle and thereby its velocity is increased. The high velocity stream enters the mixing chamber where it decelerates while the low pressure fluid (induced fluid) is accelerated and at the

same time the gases are being mixed. This results in a suction of the induced fluid. Velocity of the gas mixture is reduced in the diffuser and this causes pressure to rise.

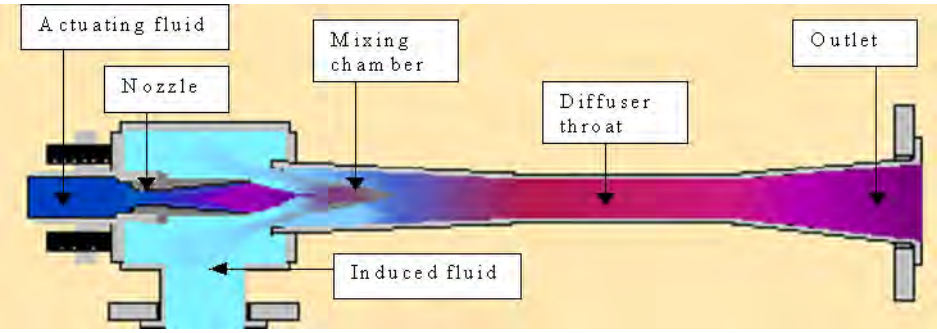

Figure 2-12. An ejector uses a motive (inducive) gas with a high pressure to rise the pressure of a second (induced) gas. (Courtesy: Fox Valve Development Corp.)

The flow rate of the induced gas depends on the pressure ratio of the activating fluid, and whether the ejector is super- or subsonic. In any case, ejectors have a rather narrow operating range with respect to flow rate. Therefore, several ejectors of different sizes are often installed in applications designed for large variations in flow rate. By implementing a battery of ejectors with an adequate control system for switching and combining the different ejectors, their operational range may be expanded.

Due to the working principle and the simple design, ejectors are advantageous to employ for recirculation of the hot and corrosive exhaust gases in SOFC applications. If placed prior to the prereformer, it may use fresh fuel as the actuating fluid and anode exhaust gas as the induced fluid. With this configuration a fully mixed gas may be delivered to the prereformer at an adequate temperature.

2.3.3 Afterburner

Fuel in a SOFC is continuously diluted by the products from the electrochemical reactions. This fuel dilution causes a drop in Nernst voltage (Equation 2–5), which makes SOFCs unsuitable for 100% fuel conversion. Usually, SOFCs are designed to convert only 85% of the fuel. The remaining fuel is combusted either directly at the fuel cell exit by mixing anode- and cathode exhaust gases or in a separate afterburner. Careful design is needed in case of the first approach, as radiation from the hot flames may cause large thermal gradients in the cell materials. In that respect, it may seem more convenient to include a separate afterburner. A separate afterburner may also promote supplementary firing for the gas turbine in a SOFC/GT cycle.

Off-gases from a SOFC have a very low calorific value and diluting air is not readily available at an adequate temperature, unless a separate air blower or a stack bypass is implemented. This means that SOFC off-gases can not be combusted in a commercial

combustor. However, calculations have shown that specially designed SOFC afterburners may operate over a large range and at the same time achieve very low emissions [Hermann, 2002].

2.3.4 Heat Exchanger

Heat exchangers are extensively used in industrial processes and they exist in a variety of designs. Common for all heat exchangers is that the effectiveness depends on heat transfer area, fluid properties and flow configuration. Primary surface (PS) or plate-fin (PF) heat exchangers represent designs with a high heat transfer area with respect to volume, and they are highly efficient for heat transfer between gases. Compactness of both PS and PF is accomplished by folding of the plates for the heat transfer area, and this makes the cross-section look similar to a corrugated cardboard structure. Other designs are tube-shell configurations or designs where one or both streams have multiple passes. Counter-flow is generally the most efficient flow pattern, but cross-flow configurations are mostly used due to a simpler manifolding system and lower cost. A PF cross-flow- and a PF counter flow heat exchanger are shown in Figure 2-13. The design principle of a PS counter-flow heat exchanger is shown in Figure 2-14.

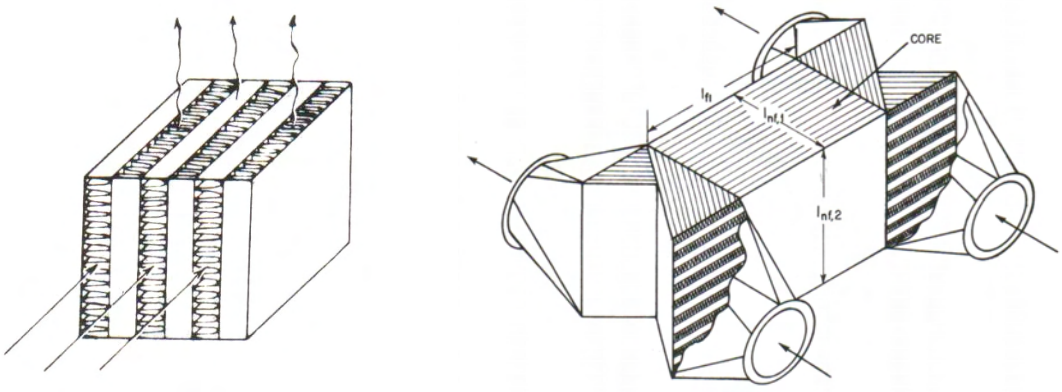

Figure 2-13. A cross flow plate-fin heat exchanger (left) and a counter flow plate-fin heat exchanger (right) [Kays, 1984].

For the SOFC system, it is important that the entering gases are supplied at a high temperature. This may be achieved by preheating the entering gases in a heat exchanger, using hot exhaust gas as heating fluid. The heat exchanger also influences the overall system by increasing the thermal efficiency and reducing the optimum operation pressure. The latter is important for small turbines where high pressure ratios are more difficult to achieve.

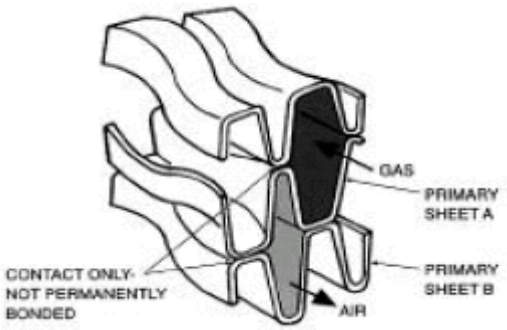

Figure 2-14. Design principle for a primary surface cross flow heat exchanger [Kays, 1984].

2.3.5 Power Electronics

A fuel cell produces direct current (DC), and if connected to the electrical grid, the current must be transformed into alternating current (AC). This may be done in a DC/AC-converter, which usually has an almost constant conversion efficiency of 95%. The converter must be designed for synchronisation with the grid, and it is advantageous if it facilitates fuel cell voltage control.

Mechanical work produced by a gas turbine is usually transformed into electrical current by an electrical generator. If the shaft speed is constant and runs with the same frequency as the grid, the generator may be directly connected to the grid. If the turbine shaft speed corresponds to half the grid frequency, a double spool alternator may be used. If not, either a gear box or an AC/AC-transformer must be included. Most generators have an energy efficiency of approximately 95%.

A SOFC/GT-cycle will produce both alternating and direct current. The two of them may either be independently connected to the grid by suitable power electronics, or the current may be connected to the same bus in order to make the system appear as a single power source to the grid. The latter may be achieved if a rectifier (AC/DC) is applied to convert AC from the gas turbine generator into DC with the same voltage as the SOFC. Such a system would facilitate a common DC bus for the SOFC and GT and only one DC/AC converter is needed. However, there are many ways of assembling a power electronics system for a SOFC/GT cycle, and the preferred system would also depend on system configuration, size and operation mode of the plant.

2.3.6 Other Components

Nitrogen Supply System

The SOFC stack requires an inert or reducing environment on the anode when exposed to temperatures higher than 600 ° C. If exposed to an oxidising atmosphere, the anode might be damaged or degraded. A sufficient reducing environment is sustained during normal operation, by reforming of the natural gas and the presence of steam. At low temperatures, which usually occur during start up and shut down, a non-flammable inert gas, such as nitrogen must be supplied. Accordingly, a nitrogen supply system must be added to the system. This system can either be a tank storage system, supplied by an external source, or a nitrogen production and storage system on the plant site. The nitrogen supply system has a connection to the fuel supply system and is used under three conditions:

- Emergency or safety stop
- Start up
- Shut down

When activated, the nitrogen flows from the storage system into the fuel supply and dilutes the fuel in the whole system until a non-flammable gas remains. During start up, the nitrogen is used to heat the fuel cell until operation temperature is reached, and fuel can be introduced.

Steam Generator/Boiler

In case of steam reforming a boiler for steam generation is required. Owing to the sensitivity of the cell this boiler has to operate on demineralised water. For processes with no internal steam generation, such as exhaust gas recirculation, the boiler is likely to operate on natural gas during start up and exhaust gas heat during operation. If exhaust gas recirculation is implemented, the boiler will only be used for a short time during start up.

Hydrogen Supply System

If the fuel contains aromatic compounds of sulphur, there is a need for an external hydrogen supply for the hydrogenolysis. Hydrogen can be produced on site by an electrolyser, utilizing DC from the fuel cells. The electrolyser must be sized to be able to continuously produce the amount of hydrogen needed during normal operation.

Water Treatment and Storage

The steam boiler and the hydrogen supply system require demineralised water. Such a system generally operates on municipal water, and contains a filter, deioniser and storage tank. The system must be sized to be able to deliver enough water for start up, where both the boiler and the hydro supply system are used.

Auxiliary Air Compressor

Excess air is needed during emergency shut downs or regular shut downs. The purpose of the auxiliary air compressor is to protect the air side of the fuel cell. For safety reasons compressed air is supplied to a storage tank, which facilitates immediate supply of compressed air in case of an emergency shut down. The auxiliary air compressor can be an off-shelf regular dual fuel internal combustion engine driven compressor.

3 Literature Review on Modelling

Modelling of solid oxide fuel cells has been performed since the late 80's. The first models were mere lumped models, and many parameters were unknown due to lack of experimental data. During the 90's increasing interest led to a number of experiments to determine mathematical relations for phenomena such as steam reforming and polarisation. Together with increasing calculation capacity, it was possible to produce more detailed models, and in the late 1990s a number of projects for system modelling were initiated. Today modelling research is pursued both on detailed single cell modelling (micro-scale) as well as systems modelling with fairly detailed stack models.

This chapter aims at establishing a basis for the development of the dynamic model presented in Chapter 4. A large number of models have been developed for steady-state calculations both for design and off-design. Extensive studies on different systems have also been performed, but so far little has been published on dynamic modelling. Most of the inspiration for the dynamic model development has come from steady-state models, and hence the comprehensive review on steady-state models.

3.1 Modelling Approaches

There are large differences in the level of details in the models presented in the open literature. Lumped models based on overall thermodynamic equations have been largely used for studies of different cycle configurations [Winkler, 2000], [Rao, 2001] and to some extent for part-load studies [Campanari, 2000], [Costamagna, 2001], [Chan, 2002]. The great benefit of using lumped models is simplicity of the model development and short calculation time. A large amount of experimental data and mathematical relations exists for components such as compressors, expanders and heat exchangers, so these components can be modelled fairly accurately despite the lumped approach. The lumped approach in SOFC models also facilitates uncomplicated changes between different geometries, as this only involves changes in geometry specific parameters. Accordingly, lumped models are also easier to adjust to experimental data. The disadvantage of lumped SOFC models is that they can only account for mean values of the parameters and it follows that more detailed investigation of the cell is needed to check for undesirable effects such as thermal cracking, coking or exceeding temperature limits locally [Magistri, 2002]. This problem may be partly avoided by using a lumped model for system calculations, and a detailed model to test the validity of the results.

Obviously, implementing a detailed SOFC model in the system model gives the most accurate results and this approach has been followed in [Pålsson, 2000]. In this publication a two-dimensional SOFC model written in FORTRAN has been implemented as a user added routine in the modelling tool ASPEN Plus. This method represents the most advanced technique presented in the open literature so far.

3.2 SOFC/GT Cycle Configurations

The most typical hybrid configuration suggested in the literature is a recuperated gas turbine process with a SOFC as the core unit of the system. An example of such a process is depicted in Figure 3-1. Most simulations of this system aim at optimizing the steady state operational parameters such as operating pressure, cell voltage and turbine inlet temperature (TIT). This type of system has been investigated in [Pålsson, 2002], [Campanari, 2000] and [Costamagna, 2001]. Electrical efficiency predictions for the system are in the range of 58-65% for sub MW-class units.

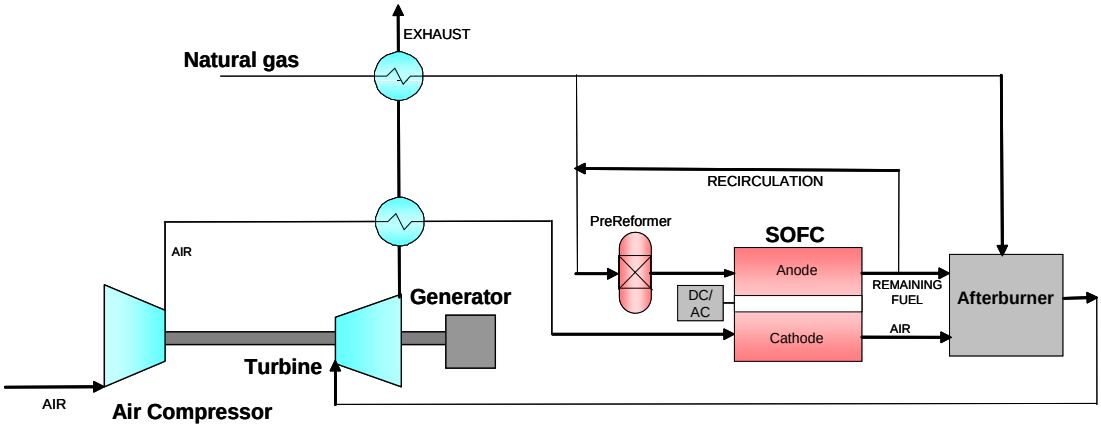

Figure 3-1. A typical SOFC/GT process layout.

In [Selimovic, 2002] an improvement of the reference system in Figure 3-1 is suggested. The improved system consists of two SOFC stacks connected in series with respect to gas flow. Due to the higher efficiency of the fuel cells compared to the gas turbine this would increase the total electric efficiency from 60.5% to 65.2%. A similar suggestion for improvement is proposed in [Winkler, 2000]. This system consists of three SOFC modules connected in series with respect to gas flows, but with intermediate expansion between the stacks to cool the cathode gases. Pressure ratio of this process is suggested to be around 15-20 and the system efficiency is predicted to be above 80%. Even higher pressure ratios are suggested in [Yi, 2004]. In this paper a pressure ratio of 50 for a process with an intercooled compressor and a two-stage expansion is suggested. It is further proposed that the fuel should be humidified in order to supply steam for the reforming reaction and to increase efficiency by increased mass flow. Electrical efficiency of the 600 MW plant is predicted to be more than 75%. In [Rao, 2001] a Humid Air Turbine hybrid system (SOFC-HAT) is suggested. In this cycle steam is supplied to the compressed air before it enters the stack. The system also incorporates a two-stage intercooled compression and two-stage expansion. Two versions of the cycle is proposed; Single-SOFC-HAT (Figure 3-2) and Dual SOFC-HAT. The main difference between the two cycles is that the Dual SOFC-HAT includes two stacks connected in series with respect to gas flow, but with intermediate expansion. Cycle electrical efficiency is estimated to 69% and 76% for the single and dual cycles, respectively.

Further suggestions for cycle improvements include adding a steam turbine after the gas turbine (SOFC/GT-ST) or injecting steam directly into the afterburner (Steam Injected Turbine, STIG). In a comparison performed in [Kuchonthara, 2003] the SOFC/GT-ST and SOFC/GT-STIG are compared with the SOFC/GT-HAT cycle proposed in [Rao, 2001]. The HAT cycle proved to have the best efficiency of these three cycles.

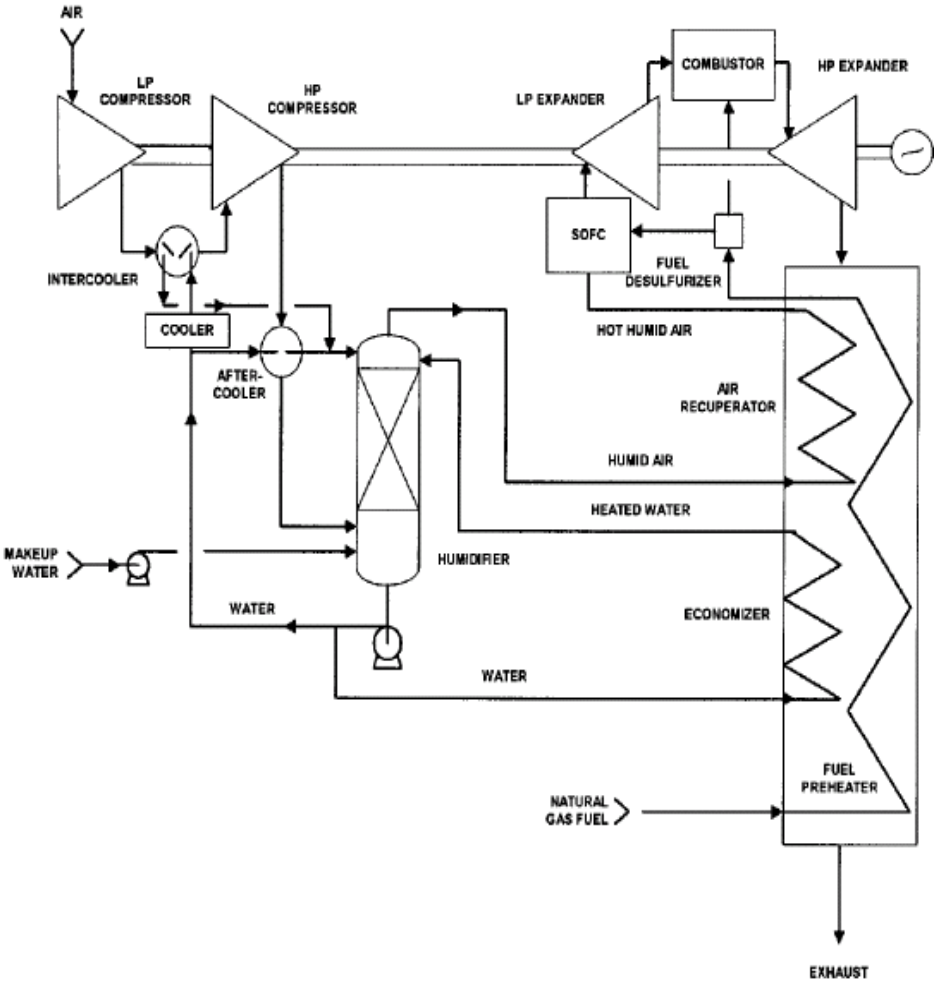

Figure 3-2. The single SOFC-HAT cycle proposed in [Rao, 2001]

An interesting feature of SOFCs is that the exhaust gases mainly consist of steam, CO_2 and unreacted hydrocarbons (UHC). If able to combust the UHC with pure oxygen, CO_2 may end up highly concentrated by condensing the steam. This cycle represents a major simplification compared to conventional CO_2-capture and it has been suggested in [Riensche, 2000] and [Inui, 2003]. The electrical efficiency of the 100 kW-plant described in [Riensche, 2000] is estimated to be between 55 and 60%, while the electrical efficiency for the 600 MW plant presented in [Inui, 2003] is estimated to be as high as 64%.

An outline of the presented models is given in Table 3.1. From the right most column it can be seen that electrical efficiency estimations of the various models and cycles vary

between 61.1% and 76%. There are also differences among the electrical efficiency calculations for the basic SOFC/GT-cycle. From the same table it can be seen that most of the models feature a lumped approach to the SOFC-model, and results from this type of approach depends to a large extent upon the assumptions which are taken during the model construction. The diversity of the electrical efficiency predictions thus suggests that the lumped model approach is mainly suitable for rough cycle estimations.

Table 3.1: Overview of SOFC/GT models from the literature.

Author	SOFC model	Plant size	Type	η_{El}
Campanari, 2000	Lumped - tubular	250 kW	SOFC-GT	65%
Chan, 2000	Lumped - tubular	2.1 MW	IRSOFC-GT	62.2%
Costamagna, 2001	Lumped - tubular	~300 kW	SOFC-GT	61.1%
Inui, 2003	Lumped	600 MW	SOFC-GT-CO_2-Free	64%
Pålsson, 2000	2D-flat plate	500 kW	SOFC-GT	65%
Rao, 2001	Lumped?[a] - tubular	-	SOFC-HAT Dual SOFC-HAT	69% 76%
Kuchonthara, 2003	Lumped	-	SOFC-GT/ST SOFC-STIG SOFC-HAT	60-63% 48-63% 60-68%
Yi, 2004	Lumped?[a] - tubular	630 MW	SOFC-ICGT	75%

a. The model description in the paper is unclear, but it seems likely that the approach is lumped.

3.3 Steady State Models for Design Point and Part-Load Calculations

As shown in chapter 3.2, a large number of publications have been produced concerning layout and performance estimations of different hybrid cycles. It has also been proven that these types of cycles have a potential for high efficiency (Table 3.1). However, a power

plant may operate at design-point[1] only part of the time, therefore investigation of part-load performance is of interest for practical applications.

In [Costamagna, 2001] a part-load study on a similar system to the one which is depicted in Figure 3-1 is performed. For fixed shaft speed it was assumed that power could only be controlled by the fuel flow and this led to air utilisation (AU) oscillations and loss of efficiency. At variable shaft speed AU and fuel utilisation (FU) as well as stack inlet temperatures could remain fairly constant with only a small penalty on efficiency. Similar results was found in [Campanari, 2000], although this paper suggests a different strategy for load reduction. In this paper it was suggested that load should be decreased by a reduction of AU and current density. Following this part-load strategy a reduction in turbine inlet temperature (TIT) could also be achieved and thus power could be reduced in the gas turbine as well as the stack. For part-load operation with variable shaft speed it was suggested that AU was kept constant while reducing current density. Provided that the stack inlet temperature was kept constant, this approach would maintain a constant TIT. In [Chan, 2003b] it is proposed that power should be reduced by shifting load from the stack to the gas turbine. This part-load strategy implies that a stack by-pass for both fuel and air exists. Furthermore, it would lead to relatively constant fuel consumption and a massive loss in efficiency. The authors claim that the main intent of establishing this strategy is to keep the components matched while operating at part-load, and still maintain a relatively high stack temperature. However, this strategy leads to a high loss of efficiency and they suggested that the strategy should be followed only for short intervals of power reduction.

Lumped models are used in [Costamagna, 2001], [Campanari, 2000] and [Chan, 2003b]. As already mentioned in Chapter 3.1, feasibility of operational points calculated by these types of models needs to be checked. Such an examination on the lumped model presented in [Costamagna, 2001] is performed in [Magistri, 2003], and it was found that even a small increase of ambient temperature would lead to the maximum cell temperature exceeding the limit. To overcome this problem stack power should be reduced, and this led to increased electric efficiency. A study on part-load behaviour for fixed and variable gas turbine shaft speed was also performed in [Magistri, 2003]. In the paper it is suggested that FU should be kept constant while varying AU for constant shaft speed. For variable shaft speed it is suggested that AU and current density should be reduced. The findings in [Magistri, 2003] are the same as in [Campanari, 2000], [Costamagna, 2001] and [Chan, 2003b] i.e. that variable shaft speed is superior with respect to maintaining a high efficiency at part load. Another result from the calculations is that the surge margin could be the limiting factor for part-load operation with variable shaft speed.

In [Pålsson, 2001] part-load studies are conducted by using a 2D-flat plate SOFC stack model. In this system a gas heater/cooler is included prior to the SOFC stack in order to control the gas inlet temperatures. For part-load operation it is proposed that the TIT should be held constant while varying the shaft speed. This leads to increased power fraction[2] from the SOFC stack due to increased stack FU and reduced gas turbine

1. The operational point for which a cycle is designed to operate.
2. The power contribution from the SOFC with respect to the overall power production.

efficiency. Due to problems in matching the SOFC and the GT it is suggested that the operating range of a hybrid power plant should be set to 55-100% load, corresponding to a gas turbine load range of 20-100%.

Table 3.2: Part-load operation strategies for SOFC/GT power plants

Author	Design load	Load range	Part-load strategy
Campanari, 2000	250 kW	100 - 10%	Red. AU and curr. density
Costamagna, 2001	390 kW	100 - 23%	Fixed rpm[a]: Red. fuel flow Var. rpm: Const AU and FU.
Pålsson, 2001	500 kW	100 - 55%	Var. rpm: Var. TIT, gas heater/cooler prior to stack to control stack inlet temperature
Kimijima, 2002	300 kW	100 - 40%	Fixed rpm: Red. SOFC power and AU. Extra fuel to combustor to maintain TIT. Var. rpm: Red AU. Const FU
Chan, 2003b	1.7 MW	100 - 55%	Const. fuel flow, load shift from SOFC to GT, low PL efficiency
Magistri, 2003	2.0 MW	Fixed rpm: 100-60% Free rpm: 90-58%	Fixed rpm: Red. fuel flow at const FU, variable AU Var. rpm: Red. stack temp, AU and curr. density.
Thorud, 2004[b]	136 W	140-40%	Constant mean fuel cell temperature or constant TIT.

a. rpm - Rotations per minute, referring to the gas turbine shaft speed.
b. This paper includes both steady-state part-load and dynamic investigations and it is discussed in Chapter 3.4.2. It is reproduced in Appendix B.

3.4 Dynamic Models

Once size, configuration and design point has been decided, one can start to look into the dynamics of the SOFC/GT power plant. Dynamic system behaviour is relevant in several aspects. It may for instance decide whether SOFC/GT power plants are suitable for peak-shaving market applications or base-load power production. Knowledge about the system dynamic behaviour is also important for the control system design, as it is important to operate the plant with minimum degradation and maximum economical profit. So far only one single hybrid power plant has been built, and no relevant information from operational experiences or experimental data has been published so far. The only manner to increase comprehension of dynamic behaviour is through dynamic models, and until experimental results are revealed these models cannot be fully verified.

3.4.1 Single Cell Models

Achenbach was probably one of the first authors to publish results from a dynamic SOFC model [Achenbach, 1995]. He studied the cell response from a step-wise change in current density and voltage with a flat-plate adiabatic single cell model. He also studied the differences in dynamic behaviour for different cell designs and bipolar plates (i.e. metallic and ceramic plates). An important boundary condition for these studies is that the fuel and air supply is at a sufficiently high level for the target power, prior to the initiation of the load change. His findings were that a reduction in current density resulted in a step-wise undershooting of the voltage with respect to the final steady-state value. As criteria for comparing time response of different load changes he defined a parameter called relaxation time. The relaxation time was the time period necessary to recover 90% of the dynamic voltage drop resulting from the difference $U(t \to \infty) - U(t = +0)$. For all his calculations he found that the relaxation time was within 100-300 seconds. The same phenomenon was observed with opposite sign for a current density increase. He also found that magnitude of the undershooting was relative to the step change, but the relaxation time was independent of the initial step size. From parameter studies he found that relaxation time was dependant on heat capacity and thermal conductivity of the cell materials, indicating the temperature dependency of the power production. Finally, Achenbach presented a correlation for prediction of relaxation time from two characteristic numbers such as Fourier number and a “Source” number. The latter number was a correlation representing cell material and geometry specific data.

A dynamic quasi-1D tubular Siemens Westinghouse SOFC model is presented in [Haynes, 2002]. The model includes a lumped thermal capacitance approach to the solid temperature calculation, while fuel concentrations are calculated according to both time and geometrical position in the tube. The model is developed to model unslaved response to load changes, i.e. the response of the fuel cell isolated from transient effects caused by balance of plant equipment. A boundary condition for the simulations is thus that the fuel and air supply remains unchanged during the transients. The load change is performed by a step-wise reduction in operational fuel cell voltage, and it is found that the fuel cell is exposed to two main transient mechanisms; electrochemical and thermal transients. The electrochemical response is very fast and within the range of seconds, while the thermal response is orders of magnitude slower. It is further found that lowering the voltage may both reduce and increase load, depending on the initial operating point. The fuel utilisation is an additional parameter which influence load increase capabilities, as a high initial fuel utilisation limit the magnitude of the maximum load that can be supplied. To increase the capability for rapid power enhancement it is therefore suggested that SOFCs should operate at low fuel utilisation and high voltage.

In [Ota, 2003] a quasi 2D-tubular[1] SOFC model is used to compare steady-state and dynamic properties for a SWPC-type cell (Ø=2.2cm) and a micro-tubular SOFC (Ø=2.4mm). The calculations showed that the micro-tubular cell had much faster response with respect to a voltage drop. In fact, the SWPC-type cell needed 180s to reach steady-state with respect to power, while the micro-tube used only 15s.

1. 2D-calculation of solid temperatures and 1D-calculation of gas flows.

In [Magistri, 2004a] a lumped model is compared with a detailed model (1D), with the intention to verify the dynamic behaviour of the lumped model. This paper is an extension of the more basic steady-state comparison which is performed in [Magistri, 2002]. The investigation of the dynamic behaviour of the two models presented in [Magistri, 2004a] is performed by examining the dynamic response resulting from a step-wise change in either voltage or fuel flow. The results are mainly given graphically, and they show that relaxation time is predominantly independent of step size. This confirms the findings from [Achenbach, 1995].

An overview of the dynamic single cell models is given in Table 3.3, and it can be seen that different dynamic scenarios have been modelled by the different authors. The response times given in the table are therefore not directly comparable. However, they are given in order to establish a general impression of dynamic behaviour for SOFCs.

Table 3.3: Dynamic single cell models from the literature

Author	SOFC model	Field of interest	Response time
Achenbach, 1995	Flat plate, quasi 2D	Current denst. change	~100-200s[a]
Haynes, 2002	Tubular-SW, quasi - 1D	Power increase by voltage reduction, unslaved response	Dimensionless time-scale
Ota, 2003	Tubular - Ø = 2.2cm/2.4mm, quasi-2D	Start-up, voltage drop	Volt. drop:15s / 180s[b]
Magistri, 2004a	Tubular-SW, 1D[c]/lumped	Volt. & Fuel Flow variations / Verification of lumped model	Only graphical results given in this paper.

a. 90% dynamic voltage recovery
b. Time to steady-state with respect to power
c. Dimension not given explicitly in the paper but the paper refers to the model presented in [Magistri, 2002].

3.4.2 Dynamic SOFC System Models

A dynamic SOFC model developed for electrical power systems simulation is presented in [Padullés, 2000]. The main intention of this model was to investigate the SOFC-plant dynamics with respect to active and reactive power production. In that respect it was not intended to be a helpful tool for the plant designer, but rather to increase knowledge on how this type of system would be able to fit into the electrical grid. The model was based on Siemens Westinghouse's 100kW atmospheric plant, which at that time was located in the Netherlands. The model was implemented in Matlab SIMULINK, and it had main focus on the power electronics of the system. The fuel cell was modelled based on a

lumped approach. The authors found that the power electronics might loose synchronisation with the net, if stack level dropped below a certain value. From their dynamic studies they found that the stack would respond immediately to a current change, although this might seriously destroy or degrade the stack. Hence, they found it difficult to predict the system dynamics without any knowledge of what safety restrictions that might be implemented into a control system.

A quasi-2D tubular SOFC system model, consisting of a prereformer unit, a splitter unit, an afterburner unit and a SWPC-like SOFC tube unit is presented in [Thorud, 2004]. The model was implemented in gPROMS and the boundary conditions were set as if the system was implemented into a hybrid system. The authors investigated both steady-state part-load performance as well as dynamic behaviour. As a result of the part-load study they presented part-load performance maps for the stack. From the performance maps they extracted two strategies for dynamic operation. In the first strategy they suggested that the start and end point of the load change should have the same turbine inlet temperature. In the second strategy they suggested that mean solid temperature of the stack should have the same value for the new operational point as before the load change. They found that maintaining a constant mean solid temperature of the stack had the quickest response with respect to time.

Table 3.4: Published dynamic SOFC system models

Author	SOFC model	Field of interest	Time to steady state
Padullés, 2000	Tubular - Lumped	Atmospheric SOFC Grid integration / Power electronics, current reduction	Voltage: ~380s
Thorud, 2004[a]	Tubular - quasi-2D	SOFC/GT Part-load / Dynamics - operation strategy	Power: ~100s / 10 000s
Magistri, 2004b	Tubular - Lumped	SOFC/GT. Fuel reduction at const. shaft speed	Power: ~1000s

a. Appendix B

One of the most advanced dynamic hybrid system models presented so far is presented in [Magistri, 2004b]. This model incorporates ejector, heat exchangers, fuel reforming, compressor and expander and it is implemented using the TRANSEO code in the MATLAB-Simulink environment. Every component of the system is modelled using a “lumped-model” approach for off-design and a constant area pipe to account for gas residence times of the respective component. Magistri et al. simulated a reduction by 10% of the ejector nozzle pressure while maintaining constant shaft speed and fuel utilisation. They showed that three time-scale phenomena are present at the anode side of the fuel cell. These phenomena are the almost negligible residence time of the gases, the

depressurization time and the long-term thermal effect. For this simulation depressurization time was approximately 100s and the time for thermal stabilisation was approximately 300s. Power output of the hybrid system was stabilized after nearly 1000s. They also showed that the pressure difference between anode and cathode remained within secure limits and although a reduction in steam to carbon ratio was observed this parameter also stabilised at a safe value. Due to reduced average stack temperature, an increase in air flow rate accompanied by a reduction in pressure ratio was observed. This means that the compressor moves away from the surge line during the transient.

3.5 Conclusion

This chapter has shown some of the great effort which has been put into modelling of SOFC systems. Most of the work has been on steady-state design case modelling for system layout, and several advanced cycle configurations have been investigated. Common for all the suggested cycle configurations is that they all have very high efficiencies, even for small units. Furthermore, part-load investigations have shown that these hybrid systems are able to maintain a high efficiency for a large area of operation. The diversity of suggested part-load strategies also shows that this is a field that requires more research. Apart from real operational experience, SOFC/GT system dynamics seems to be the field with the least knowledge at the present time.

A lumped approach to the cell stack may seem tempting, especially for dynamic models which may have a long calculation time. From the review of different models presented in this chapter, it is clear that SOFCs properties can be modelled fairly accurate with the lumped approach, but that has only been proven for steady-state models. As knowledge about dynamic properties is scarce, we do not really know if the lumped approach is sufficiently accurate for these types of studies. A lumped approach to a dynamic model might leave out some of the interesting effects present in such systems. Hence, the detailed approach to the model described in Chapter 4.

4 Dynamic SOFC/GT Model

Most of the different cycle layouts presented in Chapter 3.2 have emerged from a basic SOFC/GT system which is presented in Figure 3-1. The system consists mainly of a gas turbine, heat exchangers and a fuel cell stack with fuel processing. The mathematical model which will be presented here is based on this system. Each unit-operation component is modelled in a single model and this makes it easier to rearrange the models to simulate other system layouts. Hence, most presented cycles in Chapter 3.2 can be modelled from the set of components presented here. The layout of the presented system model is shown in Figure 4-1.

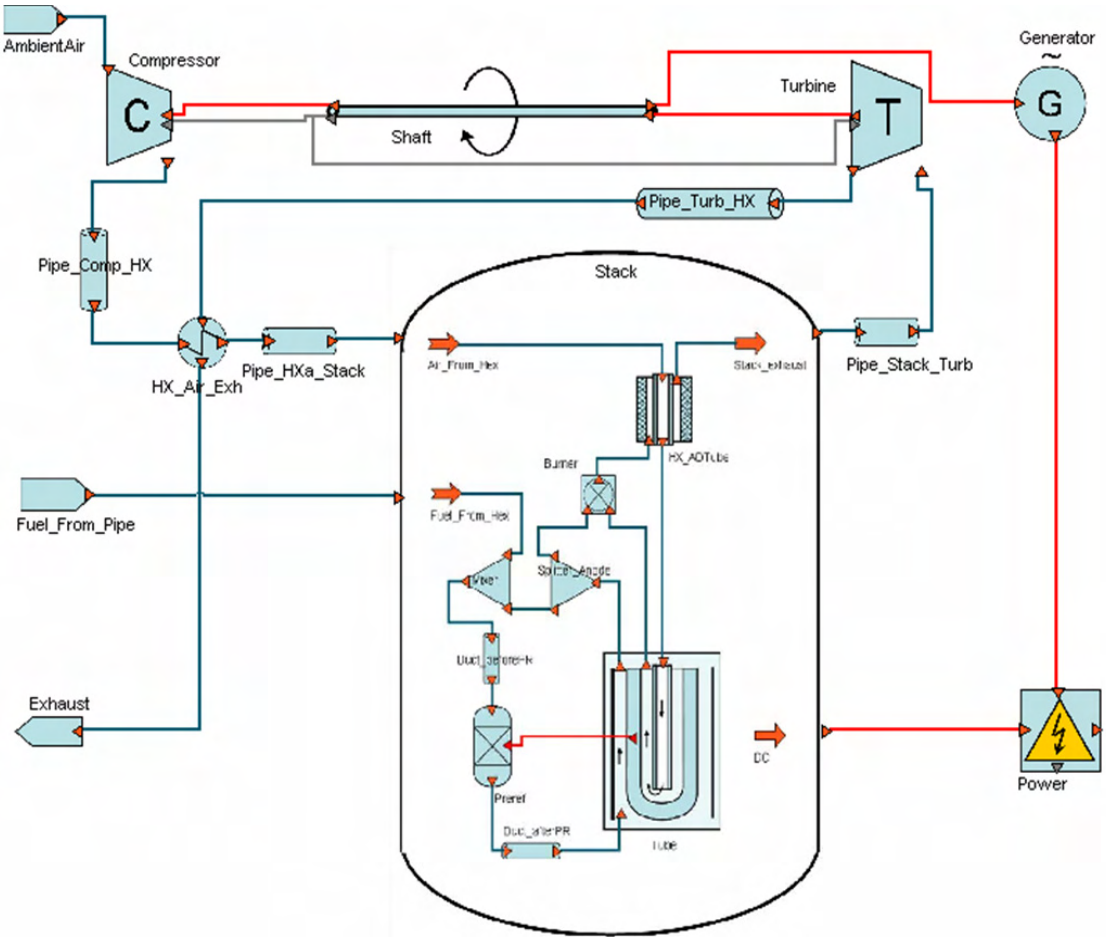

Figure 4-1. The SOFC/GT system model layout. Blue lines represent gas flows, the red triangles show the direction of the flow, the red lines represent energy flows and the black line represents the shaft speed. The stack is placed within a pressurised tank.

It is the intention of this chapter to give a thorough description of the mathematical model. However, since most technological uncertainties and modelling challenges are related to the SOFC system, the treatment of this sub-system is emphasised.

4.1 The Fuel Cell System

The fuel cell system model is built as a stand-alone fuel cell stack model with additional models for heat exchangers and power electronics. It comprises an air heat exchanger, a fuel prereformer, an anode exhaust gas recycle loop, a tubular SWPC-like fuel cell and an afterburner (Figure 4-2). The system is designed to fit the fuel and air flow of a single tube, and hence the output of the system must be multiplied by the number of tubes to represent a whole stack. This means that the heat transfer between the fuel cell tube and the prereformer is sufficient to reform just enough fuel for one single tube. In a real system one prereformer might serve several tubes, and hence temperature losses to the prereformer will be unevenly distributed between the tubes. Despite this simplification, this model represents the most detailed model when compared to other models presented in the literature (Chapter 3) and it also makes it possible to solve the equations within a reasonable computation time.

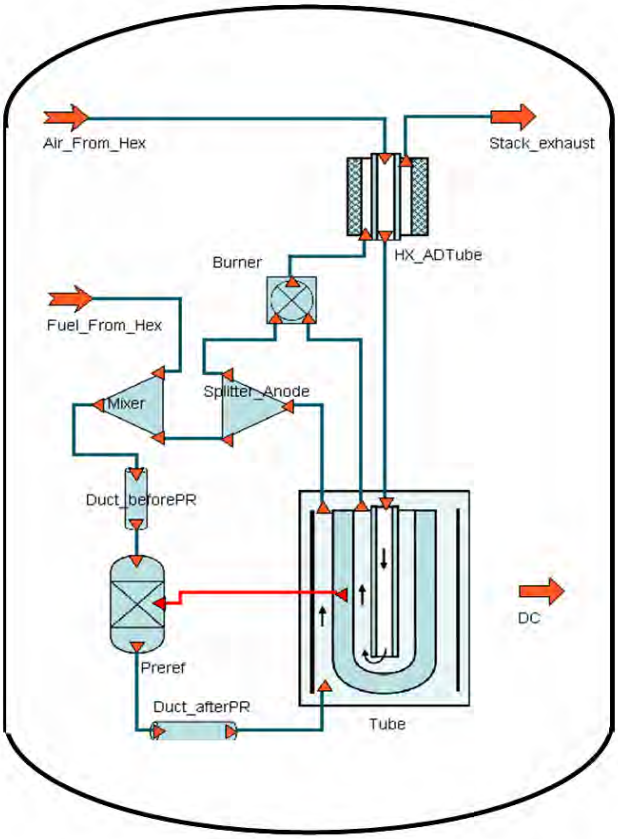

Figure 4-2. Flow sheet for the fuel cell stack. The stack is placed within a pressurised tank. Blue lines denote gas flows and the red line denotes energy transfer.

In the fuel cell system model, fresh fuel enters the ejector where it is mixed with the anode exhaust gas. The ejector is further described in Chapter 4.1.1. The mixed fuel from the ejector is further fed into the prereformer which is modelled as a continuously stirred Gibbs reactor. The prereformer calculates a new fuel composition, based on supplied heat from the fuel cell, internal energy of the gas and fuel composition. Pipe models are introduced prior to and after the prereformer to account for gas residence time of the prereformer. The pipe model is further described in Chapter 4.5.1. One of the important parameters of the prereformer model is the degree of prereforming, which is calculated as the molar flow ratio between the exiting and entering fuel (methane). The formula is given in Equation 4–1. The partially reformed fuel is supplied to the fuel cell, which is fully described in Chapter 4.2.

$$\eta_{preref} = \left(1 - \frac{\dot{n}_{out}}{\dot{n}_{in}}\right)_{CH_4} \tag{4–1}$$

The anode exhaust gas is split into two streams, where one of the streams is fed to the Afterburner. In the afterburner the excess fuel is fully combusted together with the cathode air, and an exit composition and temperature is calculated.

4.1.1 Ejector

The part of the anode exhaust, which is not fed into the afterburner, is recirculated in order to supply steam to the reforming process. As described in Chapter 2.3.2, the induced fluid (anode exhaust gas) is sucked into an ejector by the activating fluid (fresh fuel). The split ratio between the two streams is decided by the pressure ratio in the ejector and the inlet pressure in the afterburner. For simplicity reasons it was chosen to model the ejector as a mixer and a splitter. The mixer calculates a new temperature and composition of the two gases, based on internal energy, composition and flow rates. It also sets the pressures to be equal to the fresh fuel pressure. The splitter splits the anode exhaust gas stream into two streams with equal properties in a ratio that assures a steam to carbon ratio of 2 for the reference case.

This approach imposes two possible error sources to the system. The first error is that the energy used to raise the pressure level of the recycled gas, is not accounted for. However, when considering the amount of energy needed to raise the pressure of the recycled gas compared to the total energy production, this error is likely to be very small. The second possible error is connected to the dynamic and off-design behaviour of the ejector with respect to mass flow of the recycled gas. But as described in Chapter 2.3.2, it is possible to control mass flow of the recycled gas by implementing several ejectors, and hence it is believed that the flow rates calculated by the presented model are achievable in a real system.

4.2 Fuel Cell

Creating a detailed SOFC model for dynamic system modelling purposes is a mixed experience. On one hand, the model has to be detailed enough to represent dynamics of a

fuel cell used in a SOFC/GT process, and it should be possible to use to locate invalid operational points. On the other hand, calculation time should be kept within practical limits. This conflict of interest resulted in an iterative process where different approaches to the problem were tested. The result of this process is a quasi-2-dimensional fuel cell model, with the main assumptions listed below:

- Geometry is uniform in the tangential direction
- The gas flows are fully developed and laminar
- The gases can be treated as ideal with temperature dependent specific heat
- Radiative effects are negligible for the gases
- Axial heat conduction of the gases is neglected
- Thermal radiation between the cathode surface and the outer surface of the air supply tube occurs only in the radial direction. (Radial radiation accounts for app 90% of the total radiation due to the short distance between the tubes.)
- Radiation from the anode is equally distributed in the tangential direction
- Voltage is uniform along the fuel cell length
- No electrical current flows in the axial direction
- On the anode, only hydrogen is consumed electrochemically
- The water gas shift equation is always in equilibrium

4.2.1 Geometry and Material Properties

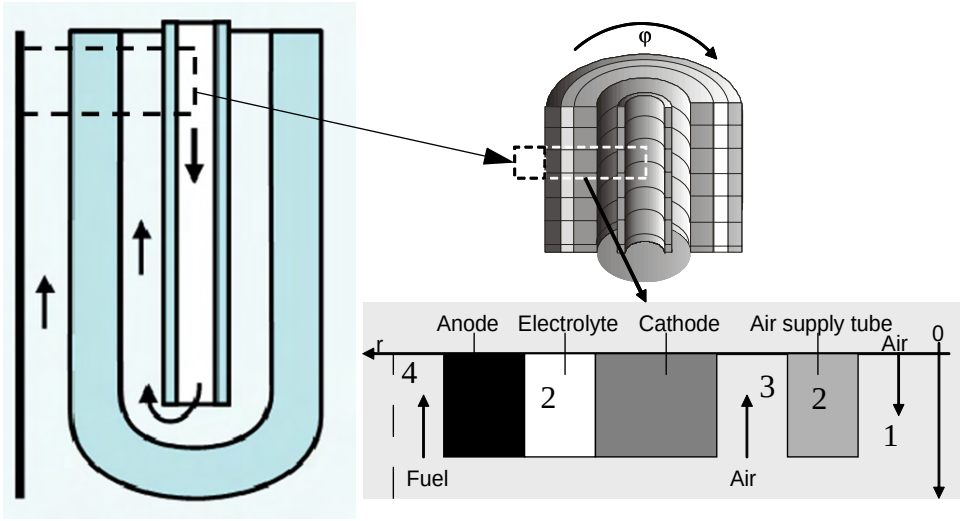

Figure 4-3. Discretization scheme of the tubular fuel cell tube. The axis centre is placed at the cold air inlet, which is on top of the tube. The numbers in the figure refer to Equation 4–2 - Equation 4–6.

The fuel cell is a 1.5 m long tube with an outer radius of 1.1 cm and it is closed at one end (Figure 4-3). Within the fuel cell tube is another tube with an outer radius of 0.4 cm for supply and preheating of air. At the bottom of the air supply tube, the air turns and flows co-currently with the fuel between the cathode and the air supply tube. Fuel is supplied on

the outside of the outer tube in the fuel plenum. The dimensions of the fuel cell tube are given in Table 4.1 and the material properties are given in Table 4.2.

Table 4.1: Fuel cell tube dimensions

Parameter	Inner radius [mm]	Outer radius [mm]	Thickness [mm]
Air Supply tube	2.5	4.0	1.50
Cathode	8.66	10.86	2.20
Electrolyte	10.86	10.90	0.040
Anode	10.90	11.00	0.10

Table 4.2: Properties of the fuel cell materials

Parameter	Air supply tube	Cathode	Electrolyte	Anode
Material	Al_2O_3	Sr-$LaMnO_3$	YSZ	Ni-YSZ
Thermal conductivity [W/mK]	11.8[a]	9.6[b]	2.7[b]	6.23[b]
Heat capacity [J/kgK]	1167[a]	300[c]	500[c]	400[c]
Density [kg/m^3]	3970[a]	5300[d]	6000[d]	7740[d]
Porosity [%]	-	30[c]	-	40[c]
Tortuosity	-	4	-	4
Average pore radius [m]	-	10^{-6}	-	10^{-6}

a. [Mills, 1995]
b. [Gemmen, 2000]
c. [Bossel, 1992]
d. [Tanaka, 2000]

4.2.2 Heat Balance

The heat balance of the solid materials are calculated in a two dimensional central finite difference discretization scheme, while the gas flows are calculated by a one dimensional up-wind finite difference method. The break-down of the cell geometry is shown in Figure 4-3.

In order to account for radial heat transfer between the air in the air supply tube (AST) and the wall of the AST (number 1 in Figure 4-3), Newton's law of cooling was employed. The contribution of axial heat conduction in the gas is minor when compared to the convective heat transfer. Hence only the gas transport term is considered for heat transport in the axial direction. The relation is given in Equation 4–2.

$$\frac{dT_{air}}{dt} + v_{air}\frac{dT_{air}}{dz} = \frac{2h}{c_{p,\,air}\rho_{air}r_{AST,\,i}}(T_{AST} - T_{air}) \tag{4–2}$$

In Equation 4–2, v_{air} denotes the mean velocity of the air, $c_{p,air}$ air heat capacity, ρ_{air} air density, $r_{AST,i}$ is the inner radius of the air supply tube and h is the convective heat transfer coefficient. The Nusselt number for constant heat flux and laminar flow (Nu = 4.364) and temperature dependant thermal conductivity are used to calculate the convective heat transfer coefficient.

Heat transfer in radial and axial direction in the solid (number 2 in Figure 4-3) is calculated by Equation 4–3. Here c denotes heat capacity, ρ density and k_r and k_z denote thermal conductivity in the radial and axial directions, respectively. For the air supply tube the thermal conductivity is equal in both directions.

$$c\rho\frac{dT}{dt} = \frac{k_r}{r}\frac{d}{dr}\left(r\frac{dT}{dr}\right) + k_z\frac{d^2T}{dz^2} \tag{4–3}$$

The anode, cathode and electrolyte are treated as one single material and thus thermal conductivity is different for the two directions. In the radial direction k_r is calculated from an equivalent thermal resistance for three resistances in a series. The heat capacity, density and thermal conductivity in axial direction are calculated with respect to the volume fraction of the different materials.

In the closed end of the tube, air from the inner tube turns and flows in the opposite direction between the cathode and the outer surface of the AST (number 3 in Figure 4-3). Heat is transferred between these two surfaces radially. As for the air inside the AST, it is accounted for by Newton's law of cooling, but the convective heat transfer coefficients are different for the two walls. Convective heat transport in the axial direction is also accounted for. The relation is given in Equation 4–4, where c_p expresses thermal capacity, ρ density, v_{air} is the gas flow velocity, h convective heat transfer coefficient and r is the radius. The subscript "*AST*" stands for Air Supply Tube, "*o*" means outer radius, "*i*" means inner radius and "*c*" means cathode.

$$c_{p,\,air}\rho_{air}\frac{dT_{air}}{dt} + v_{air}c_{p,\,air}\rho_{air}\frac{dT_{air}}{dz} =$$

$$\frac{2r_{AST,\,o}h_{AST,\,o}}{r_{c,\,i}^2 - r_{AST,\,o}^2}(T_{AST,\,o} - T_{air}) + \frac{2r_{c,\,i}h_{c,\,i}}{r_{c,\,i}^2 - r_{AST,\,o}^2}(T_{c,\,i} - T_{air}) \tag{4–4}$$

The convective heat transfer terms are calculated from tabulated Nusselt values for flow between two tubes found in [Rohsenow, 1998]. These values have also been verified by calculations described in [Campanari, 2004].

Due to the high operating temperature, heat is transferred by radiation between the cathode surface and the outer surface of the AST. The radiative heat transfer is put as a boundary condition to the two surfaces in the form given in Equation 4–5.

$$\dot{Q}_{rad} = \varepsilon\sigma F_{c-AST}(T_c^4 - T_{AST}^4) \tag{4–5}$$

In this equation $\dot{Q}_{rad}$ denotes the total transferred heat, ε is the emittance of the surface, σ is the Boltzmann constant and $F_{c\text{-}AST}$ is the shape factor between the cathode surface and the AST surface.

The fuel flows in a plenum between the fuel cell tubes and hence temperature and composition are influenced also by the closest tubes in the stack (number 4 in Figure 4-3). But since this model only comprises one single tube, it is assumed that the fuel temperature only is affected by this tube. Furthermore, an equivalent radius for the outer border of the gas flow is calculated from the fuel flow cross-sectional area. With this equivalent geometry, calculation of the fuel temperature can utilize the same procedure as for the gas flows within the tube. The relation is given in Equation 4–6, where the difference between equivalent radius of the fuel flow outer border and the radius of the tube is denoted Δr.

$$c_{p,fuel}\rho_{fuel}\frac{dT_{fuel}}{dt} + c_{p,fuel}\rho_{fuel}v_{fuel}\frac{dT_{fuel}}{dz} =$$

$$\frac{2h_{fuel}r_{a,o}}{((r_{a,o}+\Delta r)^2 - r_{a,o}^2)}(T_{a,o} - T_{fuel}) \tag{4–6}$$

In Equation 4–6 the subscript "*a,o*" denotes the outer radius of the anode. The heat transfer coefficient, h_{fuel}, is calculated from tabulated Nusselt numbers for laminar flow along tubes found in [Rohsenow, 1998].

The heat balance of the fuel cell is closely connected to the kinetics of the chemical reactions. The amount of heat related to the reaction can be calculated from the reaction rate ($\dot{r}$) and the reaction enthalpy (ΔH), according to Equation 4–7.

$$\dot{q} = \dot{r} \cdot \Delta H \tag{4–7}$$

Correct allocation of the different reactions is important in order to model a realistic temperature distribution. Steam reforming is an endothermic process which is catalysed by nickel in the anode. It is assumed to take place at the anode surface. The shift reaction is not dependant on the presence of nickel and can appear in the gas phase as well as on the surface. However, the concentration of CO is likely to be highest where the reforming

reaction takes place and thus the source term from the shift reaction is placed to the anode surface together with the source term for the steam reforming. The electrochemical reaction usually takes place at the three-phase boundary between anode, electrolyte and fuel gas, but for simplicity the source term of this reaction is placed on the anode surface as well. The anode is very thin compared to the cathode and implementing this source term at the surface should not have a big influence on the temperature gradient in the solid. Hence, all the source terms from the chemical reactions are implemented as heat fluxes in the boundary condition for heat transfer between the fuel cell solid and fuel. The relation is given in Equation 4–8.

$$k_r \left.\frac{dT}{dr}\right|_{a,\,o} = h_{fuel}(T_{fuel} - T_{a,\,o}) - q_{preref} - q_{intref} + q_{shift} + q_{elchem} \qquad (4\text{–}8)$$

In Equation 4–8 q_{intref} denotes the heat flux from the internal reformation of methane, q_{shift} expresses the heat flux that follows the shift reaction and q_{elchem} represents the heat flux from the electrochemical reaction. Calculation of the reaction rates used in the chemical source terms are discussed in the next chapter. The last term, q_{preref}, represents the radiative heat flux between the fuel cell tube and the prereformer and it calculated from Equation 4–9.

$$\dot{Q}_{preref} = \varepsilon_a \sigma \frac{F_{preref}}{L_{tube}} \int_0^{L_{tube}} (T_a^4 - T_{preref}^4) dz \qquad (4\text{–}9)$$

As mentioned in Chapter 4.1, the prereformer is modelled as a continuously stirred Gibbs reactor (CSTR), without any spatial discretization. Hence the integral has been introduced in Equation 4–9, in order to calculate the overall radiation between each node in the anode surface and the bulk temperature of the prereformer. The shape factor (F_{preref}) is not based on geometrical considerations, since the prereformer geometry is unknown. However, based upon a heat transfer analysis, it is assigned a value which enables the degree of prereforming (Equation 4–1) to reach 80% for the reference case.

4.2.3 Mass Balance

The prereformed fuel entering the anode is a mixture of CH_4, CO_2, CO, H_2 and H_2O. Methane and steam react at the anode surface according to Equation 4–10, where nickel in the anode serves as a catalyst.

$$CH_4 + H_2O \rightarrow CO + 3H_2 \qquad (4\text{–}10)$$

Several authors have described the kinetics of this reaction by empirical correlations. In [Ødegård, 1995] a relation between nickel content of the anode, partial pressure of the methane and the temperature is described. (Equation 4–11)

$$\dot{r}_{CH_4} = k \cdot \exp\left(\frac{-\Delta H_{Act}}{RT}\right) \cdot p_{CH_4}^{1.2} \qquad (4\text{–}11)$$

The parameter, *k*, was found to be 6300 mol/(hour $\cdot g_{Ni} \cdot atm^{1.2}$) with an activation energy ΔH_{Act} of 58 kJ/mol_{CH_4}. The reaction rate, $\dot{r}_{CH_4}$, is given in moles CH_4/(hour $\cdot g_{Ni}$). In [Achenbach, 1994] a similar expression for the steam reforming of methane is proposed, but with a different dependence on methane partial pressure. This paper also relates the kinetics to the anode surface rather than the nickel content of the anode (Equation 4–12)

$$\dot{r}_{CH_4} = k \cdot \exp\left(\frac{-\Delta H_{Act}}{RT}\right) \cdot p_{CH_4} \tag{4–12}$$

The pre-exponential factor, *k*, given by Achenbach is 4274 (mol $\cdot m^2 \cdot$ bar $\cdot$ s) and ΔH_{Act} is 82 kJ/mol. The two models show similar behaviour and the numerical results are within the same range. Without knowing the exact composition of the anode i.e. the nickel content, it is more convenient to use Achenbach's model for the steam reforming and therefore Achenbach's approach is chosen for this model.

Carbon monoxide produced by steam reforming may react electrochemically according to Equation 2–3, or it can react further with steam to produce hydrogen in the shift reaction, which is described in Equation 4–13.

$$CO + H_2O \leftrightarrow CO_2 + H_2 \tag{4–13}$$

Diffusion of CO in the anode is approximately half to that of hydrogen and kinetics of the shift reaction is very fast under the SOFC operating conditions. It is therefore reasonable to assume that the CO concentration at the three phase boundary is very small compared to hydrogen, and for simplicity it is assumed that only hydrogen is reacting electrochemically. Consequently, only the shift reaction is considered in order to calculate the mole balance of CO and CO_2.

Due to the rapid kinetics of the shift reaction, it can be assumed that it will remain close to equilibrium. Thus, using the equilibrium constant (Equation 4–14) and an appropriate parameter, an expression for the reaction rate of the shift reaction is Equation 4–15.

$$K_{Shift} = \exp\frac{-\Delta G^0_{Shift}}{R \cdot T} \tag{4–14}$$

$$\dot{r}_{CO} = k\left(y_{CO} \cdot y_{H_2O} - \frac{y_{CO_2} \cdot y_{H_2}}{K_{shift}}\right) \tag{4–15}$$

The shift constant, K_{shift}, is calculated from Gibbs free energy for the reaction (ΔG^0_{Shift}). The reaction rate constant, *k*, accounts for both the forward and backward reaction and it is assigned a high enough value to ensure that equilibrium always is fulfilled. This is not a physical parameter, but this method has been used by other authors such as in [Yakabe, 2001].

The reaction rates of hydrogen and oxygen are directly connected to the current, *I*, and the relation between reaction rate and the current is given by Faraday's law, which is given in Equation 4–16 and Equation 4–17.

$$\dot{r}_{H_2} = \frac{I}{2F} \tag{4–16}$$

$$\dot{r}_{O_2} = \frac{I}{4F} \tag{4–17}$$

Knowing the main chemical reactions in the tube, a molar balance based on concentrations for each component can be set up (Equation 4–18).

$$\frac{dc_i}{dt} + v \cdot \frac{dc_i}{dz} = \frac{1}{V} \cdot \sum_{j=1}^{rx} \dot{r}_{i,j} \tag{4–18}$$

The first term in Equation 4–18 accounts for hold-up of the species while the second term accounts for the transport. c_i denotes concentration of specie *i* in mol/m^3, *v* is the mean velocity of the fluid, *V* is the volume of the control volume, $\dot{r}_{i,j}$ is reaction rate of reaction *j* involving the component *i* and *rx* is the total number of reactions that involves the component.

As mentioned in Chapter 2.1.1, SOFCs are usually designed to use approximately 85% of the fuel. Fuel utilisation (FU) is an important parameter for adequate SOFC operation and it is sensitive with respect to the operating conditions. It is defined as the amount of utilised fuel divided by the supplied fuel, Equation 4–19.

$$FU = \left(\frac{\dot{n}_{fuel,\,in} - \dot{n}_{fuel,\,out}}{\dot{n}_{fuel,\,in}} \right) \cdot 100\% \tag{4–19}$$

Measurements of the fuel composition of the exiting fuel in SOFC applications are usually not feasible due to the high temperature. Nevertheless, we know from Equation 4–16 that the consumed fuel is equivalent to the current. So by rewriting Equation 4–19 using Equation 4–16, we can express the fuel utilisation as a function of the total current (*I*) and the entering fuel ($\dot{n}_{fuel,\,in}$);

$$FU = \left(\frac{I}{2F\dot{n}_{fuel,\,in}} \right) \cdot 100\% \tag{4–20}$$

Measurements of current and entering fuel are straight-forward and hence the expression in Equation 4–20 can be used to monitor fuel utilisations in practical SOFC applications. In the presented model, both equations are implemented for comparison. However, when fuel utilisation is referred to in the following chapters, it is calculated by Equation 4–20, if not otherwise is explained.

4.2.4 Coking

Decomposition of natural gas takes place at temperatures above 650°C in absence of steam and oxygen (Equation 4–21). Large hydrocarbons decompose easier than small molecules. Another mechanism of coke formation is the Boudouard coking given in Equation 4–22. Coke formation is a critical issue for fuel cells as the coke might occupy active sites on the catalyst of the prereformer or at the SOFC anode and block further reactions. Coking can be very fast and block the fuel channels of a solid oxide fuel cell if the steam supply is shut down. If this happens, the stack has to be dismantled and the carbon removed mechanically.

$$CH_4 \rightarrow C(s) + 2H_2 \quad \text{Pyrolysis of methane} \tag{4–21}$$

$$2CO \leftrightarrow C(s) + CO_2 \quad \text{Boudouard coking} \tag{4–22}$$

$$C(s) + H_2O \leftrightarrow CO + H_2 \tag{4–23}$$

As long as the fuel is allowed to flow through the channel, coke can be removed if the reaction given in Equation 4–22 reacts in the opposite direction or according to Equation 4–23. To prevent coking in the first place, one has to be sure that there is enough steam available throughout the cell. This is usually achieved by a steam to carbon ratio of 2-3.

The presented model does not calculate agglomeration of coke as an effect from the two first equations given above, nor does it calculate the carbon consumption according to Equation 4–23. However, a carbon formation check, based on Gibbs free energy, is implemented in order to examine the possibility of carbon formation. Since Gibbs free energy is the driving force for all spontaneous reactions, it is assumed to be an adequate measure of the possibility of carbon formation. In this analysis it is also important to consider all the reactions involving solid carbon, as well as the direction of the reactions. Say, if solid carbon is likely to be produced by the Boudouard reaction, however immediately consumed according to Equation 4–23, solid carbon formation is unlikely in an overall perspective.

In order to calculate the general possibility of solid carbon formation, Gibbs free energy can be calculated for the overall reaction given in Equation 4–24, which is the sum of Equation 4–21 and Equation 4–22.

$$CH_4 + 2CO \leftrightarrow 2C(s) + 2H_2 + CO_2 \tag{4–24}$$

The consumption of solid carbon is further indirectly accounted for in the model by the water gas shift reaction given in Equation 4–13, since Equation 4–23 is the sum of the Boudouard reaction and the backwards water-gas shift reaction. Having established the

overall reaction for carbon formation, the Gibbs free energy for the formation of solid carbon may now be calculated from Equation 4–25.

$$\Delta G_{CarbDep} = \Delta G_{rx}^{0} + RT\ln\left(\frac{p_{CO_2} \cdot p_{H_2}^2}{p_{CH_4} \cdot p_{CO}^2}\right) \qquad (4\text{–}25)$$

According to the second law of thermodynamics, a negative value of $\Delta G_{CarbDep}$ means that the reaction given in Equation 4–24 is spontaneous towards the right, and hence carbon deposition is likely to occur.

4.2.5 Losses

Recalling Chapter 2.1.1, the maximum theoretical voltage that can be generated by the cell can be calculated from the Nernst equation (Equation 2–5). The actual cell voltage is therefore the reversible potential, E_{emf}, less the losses associated with ohmic resistance, activation polarisation and diffusion (Equation 4–26)

$$U_{cell} = E_{Rev} - IR - \eta_{act} - \eta_{diff} \qquad (4\text{–}26)$$

In Equation 4–26 U_{cell} denotes the cell voltage, I express the current, R is the ohmic resistance, η_{act} denotes the activation polarisation voltage for both cathode and anode and η_{diff} is the voltage loss due to diffusion resistance of the reacting species.

Ohmic Losses

The materials used in SOFC applications have poor electrical, respective ionic conductivity at ambient temperatures, but at elevated temperatures their conductivity improves. Specific electric conductivity as a function of temperature can be found in [Bossel, 1992]. The temperature dependency is given in Equation 4–27 to Equation 4–29.

$$\sigma_a = \frac{95 \times 10^6}{T_a}\exp\left(\frac{-1150}{T_a}\right) \qquad \text{Anode, } [\Omega^{-1}\text{m}^{-1}] \qquad (4\text{–}27)$$

$$\sigma_c = \frac{42 \times 10^6}{T_c}\exp\left(\frac{-1200}{T_c}\right) \qquad \text{Cathode, } [\Omega^{-1}\text{m}^{-1}] \qquad (4\text{–}28)$$

$$\sigma_e = 3.34 \times 10^4 \exp\left(\frac{-10300}{T_e}\right) \qquad \text{Electrolyte, } [\Omega^{-1}\text{m}^{-1}] \qquad (4\text{–}29)$$

Specific electric conductivity of the anode and specific ionic conductivity of the electrolyte are plotted in against temperature in Figure 4-4. The figure shows that specific electric conductivity of the anode is quite good even at low temperature, but that the electrolyte requires a high temperature to become ionic conductive. The cathode displays a similar behaviour with respect to temperature as the anode, although the magnitude is approximately half that of the anode.

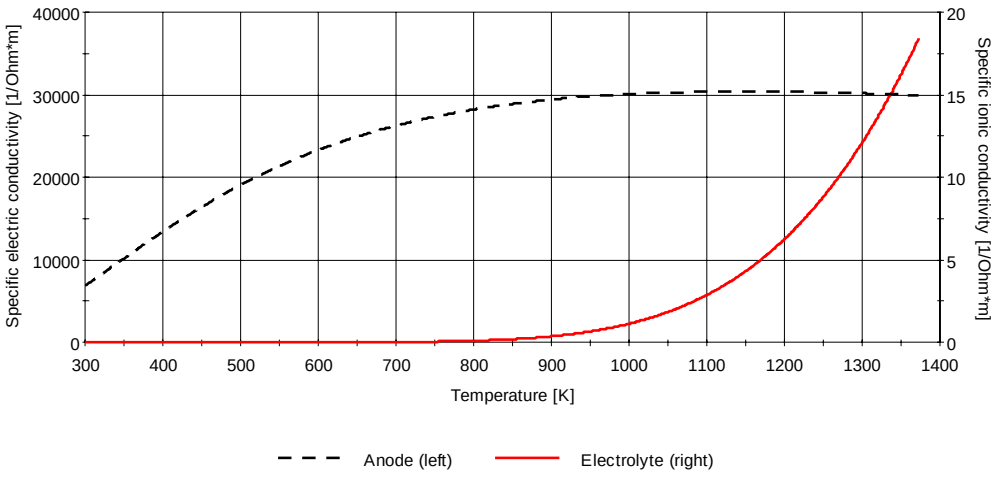

Figure 4-4. Specific electric conductivity of the anode (left hand axis) and specific ionic conductivity of the electrolyte (right hand axis) as a function of solid temperature.

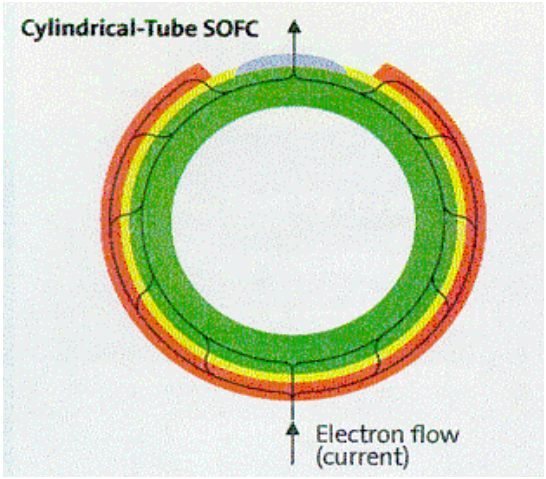

Figure 4-5. Flow path of electrons and ions in a cross-section of a tubular SOFC tube.

Geometry of the fuel cell is of great importance with respect to ohmic resistance, because of the linear relationship between specific resistance and current path. Figure 4-5 shows that current in a tubular SOFC mostly moves in the tangential and radial direction. The presented model is not discretized in the tangential direction, but tangential effects are accounted for by an analytical relation given in [Nisancioglu, 1989]. The relation is given in Equation 4–30 to Equation 4–32 and it is based on specific electric conductivities, σ, for the different materials as well as geometry. The geometry is represented by the thickness of the materials, δ, length of the electrolyte in circumferential direction, L_e, and length of the interconnect, L_{icm}. The outcome of this equation is *RW*, which is given in

ohmic resistance per meter of the tube, Ωm. Thereby this equation facilitates calculation of ohmic resistance for a slice of the tube.

$$RW = \frac{\{(\sigma_a\delta_a)^{-2} + (\sigma_c\delta_c)^{-2}\}\cosh Je + (\sigma_a\sigma_c\delta_a\delta_c)^{-1}(2 + Je\sinh Je)}{2\left(\frac{\sigma_e}{\delta_e}\right)^{1/2}\{(\sigma_a\delta_a)^{-1} + (\sigma_c\delta_c)^{-1}\}^{3/2}\sinh Je}$$

$$+ \frac{\sqrt{\frac{\delta_{icm}}{\sigma_{icm}}(\sigma_a\delta_a)^{-1}}}{2\tanh J_{icm}} \qquad (4\text{–}30)$$

$$Je = \frac{L_e}{2}\sqrt{\frac{\sigma_e}{\delta_e}\{(\sigma_a\delta_a)^{-1} + (\sigma_c\delta_c)^{-1}\}} \qquad (4\text{–}31)$$

$$J_{icm} = \frac{L_{icm}}{2}\sqrt{\frac{\sigma_{icm}}{\sigma_a\delta_a\delta_{icm}}} \qquad (4\text{–}32)$$

Diffusion Losses

The electrochemical reactions occur close to or at the three-phase boundary between electrode, electrolyte and gas. Hence the reacting species have to be transported from the gas bulk to the electrode surface and further through the porous electrode to the reaction site. Owing to mostly laminar flows in fuel cells, diffusion is the main mechanism for this transport. Under normal operating conditions voltage drop due to diffusion resistance is very small, but as described in Chapter 2.1.1, it becomes a limiting factor at high current densities. The importance of diffusion during transients is not known, but it may play a role if the current density relative to the fuel flow is high. Hence diffusion has been implemented to study this effect.

There are several possible approaches to model diffusion. One way to describe it is to estimate the species concentration at the three phase boundary and then use this concentration in the Nernst equation (Equation 2–5) instead of using the bulk concentration. The disadvantage of using this method is that information of the diffusion resistance magnitude is “hidden” within the Nernst equation. If the Nernst equation is based on bulk concentrations and the diffusion resistance is represented as a voltage, one can easily compare the influence of each type of loss within the cell.

Diffusion losses are due to a concentration gradient of the species from the bulk phase to the three-phase boundary. This gradient is only present if current is withdrawn from the fuel cell. Hence, one can assume that the cell potential when no current is extracted is given by Equation 4–33, where *“B”* denotes bulk properties.

$$E_{i=0} = \frac{-\Delta G^0}{nF} + \frac{RT}{nF}\ln\left(\frac{p_{H_2,B}\cdot p_{O_2,B}^{1/2}}{p_{H_2O,B}}\right) \qquad (4\text{–}33)$$

When a small current is extracted from the cell, the concentrations at the three-phase boundary (*TPB*) change and the cell potential can be described from Equation 4–34.

$$E_{i\neq 0} = \frac{-\Delta G^0}{nF} + \frac{RT}{nF}\ln\left(\frac{p_{H_2,\,TPB}\cdot p_{O_2,\,TPB}^{1/2}}{p_{H_2O,\,TPB}}\right) \tag{4–34}$$

The voltage loss due to diffusion resistance can now be established as the difference between Equation 4–33 and Equation 4–34. Rearranging and separating the anode and cathode potentials gives Equation 4–35.

$$\eta_{diff} = \frac{RT_a}{nF}\ln\left(\frac{p_{H_2,\,TPB}\cdot p_{H_2O,\,B}}{p_{H_2,\,B}\cdot p_{H_2O,\,TPB}}\right) + \frac{RT_c}{2nF}\ln\left(\frac{p_{O_2,\,TPB}}{p_{O_2,\,B}}\right) \tag{4–35}$$

$$\frac{dc}{dt} = D\frac{d^2c}{dz^2} \tag{4–36}$$

Concentration as a function of time and position can be calculated by Fick's 2. law, given in Equation 4–36. For tubular SOFCs, however, diffusion is relatively fast due to the high temperature and the short distance for the molecules to diffuse (Table 4.1). Solving Equation 4–36 numerically with typical numbers for SOFC operating conditions, gives a time to steady-state of less than 0.01 s for diffusion in the anode and less than 2 s for the cathode for a change of concentration by 100%. With respect to time to steady state for voltage, which is in the range of 120 - 300 s [Achenbach, 1995], the diffusion response time is very short and hence time dependency of diffusion is neglected in the presented model. Assuming steady state for diffusion reduces the equation given in Equation 4–36, to Fick's first law which is given in Equation 4–37. This simplifies the system considerably, and computing time of the model can be kept low.

$$j = -D\frac{dc}{dz} \tag{4–37}$$

On the cathode, only oxygen participates in the electrochemical reaction and consequently net molar flow of nitrogen through the cathode will be zero. For oxygen, there will be a net molar flow through the cathode and into the electrolyte corresponding to the current. Assuming that mass transport through the cathode can be expressed by summing diffusion and convection, a mole balance for nitrogen and oxygen can be put up:

$$N_{N_2} = 2\pi rL\left(-\frac{D_{eff,\,N_2}P_c}{RT_c}\cdot\frac{dy_{N_2}}{dr}\right) + y_{N_2}\times N_{tot} = 0 \tag{4–38}$$

$$N_{O_2} = 2\pi rL\left(-\frac{D_{eff,\,O_2}P_c}{RT_c}\cdot\frac{dy_{O_2}}{dr}\right) + y_{O_2}\times N_{tot} = 2\pi rL\frac{i}{nF} \tag{4–39}$$

In Equation 4–38 and Equation 4–39 the first term on the right-hand side is the diffusive contribution to the mass transport, while the convective term is given as the mole fraction, *y*, times the total molar flow N_{tot}. The term, $2\pi rL$, represents the surface through which the mass transport occurs. Diffusion is accounted for by the term in parenthesis and it is

calculated by using the ideal gas law employed for Fick's first law (Equation 4–37). D_{eff} represents the effective diffusion coefficient and will be defined later. P_c is the cathode pressure and y is the molar fraction. The total transport of oxygen molecules through the cathode can be calculated by Faraday's law, which is given in Equation 4–17, can be rewritten in terms of current density, i, times the perpendicular surface, $2\pi rL$, to give the total molar flow of oxygen. This is the right most term in Equation 4–39.

$$y_{N_2} = 1 - y_{O_2} \tag{4–40}$$

By considering the relation between nitrogen and oxygen mole fractions, given in Equation 4–40, and by assuming that the pressure at the three phase boundary equals the bulk pressure, there are only two unknown variables (N_{tot}, y_{O_2}) in Equation 4–38 and Equation 4–39. The expressions in Equation 4–40 and Equation 4–38 can be further simplified by employing Equation 4–40 in Equation 4–38, rearranging and adding Equation 4–38 to Equation 4–39:

$$N_{N_2} + N_{O_2} = 2\pi rL\left(\frac{D_{eff,N_2}P_c}{RT_c} - \frac{D_{eff,O_2}P_c}{RT_c}\right)\cdot\frac{dy_{O_2}}{dr} + N_{tot} \tag{4–41}$$

In Equation 4–41 the sum of nitrogen and oxygen molar flow (right hand) equals the total molar flow, and hence the term in parenthesis must be zero for the equation to be fulfilled. Thereby it has been proven that the effective diffusion coefficients for nitrogen and oxygen are equal.

From Equation 4–40 and the findings of Equation 4–41, an equation for the total transport of moles can now be derived:

$$N_{tot} = -\frac{2\pi rLD_{eff,O_2}P_c}{(1-y_{O_2})RT_c}\cdot\frac{dy_{O_2}}{dr} \tag{4–42}$$

From the assumption of uniform pressure distribution from the bulk to the three phase boundary, it is clear that the molar transport of oxygen due to convection is likely to be small. This is because the driving force for convection now only can be diffusion, a mechanism which is often called diffusion induced convection.

Using the relation given in Equation 4–42 in Equation 4–39, the surface term, $2\pi rL$, can be cancelled, and the following relation can be derived:

$$\frac{D_{eff,O_2}}{y_{O_2}-1}\cdot dy_{O_2} = \frac{iRT_c}{nFP_c}\cdot dr \tag{4–43}$$

An expression for the molar fraction of oxygen at the three phase boundary as a function of the bulk mole fraction can be obtained by integrating Equation 4–43 from the bulk to the three phase boundary. However, prior to performing the integral, a further investigation of the diffusion mechanism in the porous cathode is necessary.

Porous media, such as the electrodes, usually comprise an irregular pattern of bent channels. Some of these channels are dead-ended, while some of them lead through the material along a curved path. If the porous media is impermeable, molecules can only be transported through the media by following the channels, and this influences the overall diffusion. Overall diffusion is further influenced by the number of channels, which depends on the porosity of the material. Taking these two effects into account, the overall effective diffusion coefficient in a porous media, D_{eff}, may be calculated from the porosity, ε, and the tortuosity, τ. The tortuosity can be looked upon as the average elongation of the diffusion path compared to diffusion in a pure solute [Cussler, 1997].

$$D_{eff} = D \cdot \frac{\varepsilon}{\tau} \tag{4–44}$$

Depending on the size of the channels in the porous media, different diffusion mechanisms may dominate. Ordinary diffusion, according to the gas kinetic theory, usually dominates for large sized channels, but for smaller channels the influence from the walls becomes dominant. There are at least three ways that molecules can be transported through the channels, and they depend on the interaction between the solute, the solvent and the walls. One mechanism is the Knudsen diffusion where molecules collide more often with the walls than with other molecules. It follows that the distance between molecular collisions must be larger than the channel diameter for this type of diffusion to dominate. The ratio between the distance between molecular collisions l and the channel diameter d is defined as a dimensionless group, called the Knudsen number, Kn;

$$Kn = \frac{l}{d} \tag{4–45}$$

The parameter l can further be estimated from Equation 4–46, where k_B is the Boltzmann's constant, T is the temperature, σ_{ii} is the collision diameter and p is the pressure.

$$l = \frac{k_B T}{\sqrt{2}\pi\sigma_{ii}^2 p} \tag{4–46}$$

The Knudsen number can be used to estimate the diffusion mechanism that dominates the mass transport in the porous media. High values indicate dominance of Knudsen diffusion, while small numbers indicate that diffusion can be estimated from Equation 4–44, using the diffusion coefficient from the gas kinetic theory [Cussler, 1997].

For hydrogen diffusing through a porous SOFC anode at 1000 ° C and 1 atm, the Knudsen number will be in the range of 0.25. The Knudsen numbers for steam and oxygen at the same conditions will be in the range of 0.28 and 0.16, respectively. These numbers suggest that the diffusion in the cathode as well as the anode is in a transition regime where both ordinary and Knudsen diffusion are likely to occur [Cheremisinoff, 1986]. A third mechanism, in which adsorbed species on the electrode surface is transported along the surface, may also occur in parallel to ordinary and Knudsen diffusion. However, this

surface diffusion is likely to be small compared to the two other mechanisms [Mills, 1995] and it is omitted for simplicity of the model. In the transition regime, the effective diffusion coefficient of a non-dilute component in a two-component gas mixture depends on the mole fraction, the relation between the molecular masses, α, as well as the Knudsen- and the ordinary diffusion coefficients [Cheremisinoff, 1986]:

$$D_{eff,\,O_2} = \frac{D_{O_2} D_{K,\,O_2}}{D_{K,\,O_2}(1 - \alpha y_{O_2}) + D_{O_2}} \tag{4–47}$$

$$\alpha = 1 - \left(\frac{M_{O_2}}{M_{N_2}}\right)^{1/2} \tag{4–48}$$

A further discussion of the ordinary and the Knudsen diffusion coefficients will be given later in this chapter. Considering the different diffusion mechanisms in the bulk and the porous media, it is convenient to divide the integral over Equation 4–43 into two; one for diffusion in the bulk phase and one for diffusion in the cathode. In the bulk phase, the diffusion coefficient can be assumed to be constant with respect to the oxygen mole fraction. Hence taking the integral over Equation 4–43 from the bulk radius of the cathode air to the cathode surface (*CS*) yields the following explicit equation for the mole fraction of oxygen at the cathode surface:

$$y_{O_2,\,CS} = 1 + (y_{O_2,\,B} - 1)\exp\left(\frac{iRT_c}{D_{O_2} nFP_c}\right) \cdot (r_{c,\,i} - r_B) \tag{4–49}$$

For diffusion in the cathode, the expression becomes a bit more complicated when Equation 4–47 is implemented in Equation 4–43 together with Equation 4–44:

$$\frac{D_{O_2} D_{K,\,O_2}}{D_{K,\,O_2}(1 - \alpha y_{O_2}) + D_{O_2}} \cdot \frac{1}{y_{O_2} - 1} \cdot dy_{O_2} = \frac{\tau_c iRT_c}{\varepsilon_c nFP_c} \cdot dr \tag{4–50}$$

Performing the integral over the cathode from the cathode surface to the three phase boundary and rearranging gives the following implicit relation for the oxygen mole fraction at the TPB:

$$\frac{[D_{K,\,O_2}(\alpha y_{O_2,\,CS} - 1) - D_{O_2}](y_{O_2,\,TPB} - 1)}{[D_{K,\,O_2}(\alpha y_{O_2,\,TPB} - 1) - D_{O_2}](y_{O_2,\,CS} - 1)} =$$

$$\exp\left(\frac{\tau_c iRT_c (r_{c,\,o} - r_{c,\,i})[D_{O_2} - D_{K,\,O_2}(\alpha - 1)]}{\varepsilon_c nFD_{O_2} D_{K,\,O_2}}\right) \tag{4–51}$$

For the anode it is assumed that only hydrogen participates in the electrochemical reactions, and there will be an equimolar counter-current flow of hydrogen and steam between the bulk and the three phase boundary. Hydrogen will diffuse towards the three-

phase boundary where it reacts with oxygen and the product (steam) will diffuse away from the reaction site towards the bulk flow. By assuming that the bulk pressure equals the pressure at the three phase boundary of the anode, there will be no convective transport of molecules through the anode due to a pressure difference. Furthermore, diffusion induced convection will be negligible due to the equimolar counter-current flow of hydrogen and steam. These considerations result in the following mole balance for the anode:

$$N_{tot} = N_{H_2} + N_{H_2O} = N_{H_2} - N_{H_2} = 0 \tag{4–52}$$

Using Fick's first law in combination with the ideal gas law, the mole transport of hydrogen may be described as a function of the surface, $2\pi rL$, perpendicular to the molar flux, which is calculated from the effective diffusion coefficient of hydrogen in the gas mixture, $D_{eff,H2}$, the anode pressure, P_a, the universal gas constant, R, the anode temperature, T_a, and the hydrogen mole fraction, y_{H2}. (Equation 4–53)

$$N_{H_2} = -2\pi rL\frac{D_{eff,H_2}P_a}{RT_a}\cdot\frac{dy_{H_2}}{dr} \tag{4–53}$$

The hydrogen molar flow can also be calculated from the surface and current density, i, by Faraday's law (Equation 4–16).

$$N_{H_2} = 2\pi rL\frac{i}{2F} \tag{4–54}$$

Combining Fick's first law and Faraday's law, the surface term can be cancelled, and the differential equation for the hydrogen mole fraction can be established;

$$dy_{H_2} = -\frac{iRT_a dr}{2FD_{eff,H_2}P_a} \tag{4–55}$$

As for the cathode, it is simpler to integrate Equation 4–55 in two steps; from the bulk to the anode surface (*AS*) and from the anode surface to the three phase boundary. Taking the first integral yields the following expression for the hydrogen mole fraction at the anode surface:

$$y_{H_2,AS} = y_{H_2,B} - \frac{iRT_a(r_B - r_{a,o})}{2FD_{H_2}P_a} \tag{4–56}$$

As shown previously, diffusion in the anode is in the transition area between ordinary diffusion and Knudsen diffusion, and hence Equation 4–47 and Equation 4–48 should be employed in Equation 4–55. However, for equimolar counter-current diffusion, Equation 4–47 is reduced to what is known as the Bosanquet formula [Cheremisinoff, 1986]:

$$\frac{1}{D_{eff,i}} = \frac{1}{D_{j,i}} + \frac{1}{D_{K,i}} \tag{4–57}$$

Using Equation 4–57 in Equation 4–44 and rearranging, an expression for the effective diffusion coefficient in the anode can be established:

$$D_{eff,\,i} = \frac{D_{i,\,j} D_{K,\,i} \times \varepsilon_a}{(D_{i,\,j} + D_{K,\,i})\tau_a} \tag{4–58}$$

The relation in Equation 4–58 can be used to estimate the effective diffusion coefficients for both hydrogen and steam. Being independent on the molar fraction of the specie, the effective diffusion coefficient in Equation 4–55 can be considered to be independent on the integration. Performing the integral over the anode thickness, t_a, and using the anode surface mole fraction as boundary condition, an expression for the mole fraction of hydrogen at the three-phase boundary can be found;

$$y_{H_2,\,TPB} = y_{H_2,\,AS} - \frac{iRT_a t_a}{2FD_{eff,\,H_2} P_a} \tag{4–59}$$

The same procedure applied to steam yields the following relations;

$$y_{H_2O,\,AS} = y_{H_2,\,B} + \frac{iRT_a (r_B - r_{a,\,o})}{2FD_{H_2O} P_a} \tag{4–60}$$

$$y_{H_2O,\,TPB} = y_{H_2O,\,AS} + \frac{iRT_a t_a}{2FD_{eff,\,H_2O} P_a} \tag{4–61}$$

Ordinary diffusion coefficients for gases are generally in the order of 10^{-6} m^2/s, but may vary considerably with temperature, pressure and gas composition. To estimate the ordinary diffusion coefficient, the Fuller equation found in [Reid, 1987] can be used (Equation 4–63). The expression is only valid for binary gas mixtures, and may only be directly used for the air on the cathode side. Nevertheless, utilising a mixing rule also multi-component diffusion coefficients for the fuel mixture can be estimated [Mills, 1995]. This relation is given in Equation 4–62.

$$D_{j,\,m} = \frac{(1 - y_j)}{\sum_i \frac{y_i}{D_{j,\,i}}} \tag{4–62}$$

The Fuller equation is based on a number of experiments and the value "V"in Equation 4–63 is an experimental value called "Atomic Diffusion Volume". It can be found in literature, e.g. in [Reid, 1987]. The factor $M_{j,i}$ states the relation between the molecular weights of the two components and it is described in Equation 4–64.

$$D_{j,\,i} = \frac{0.00143\mathrm{T}^{1.75}}{P \cdot M_{j,\,i}^{1/2} [V_j^{1/3} + V_i^{1/3}]^2} \tag{4–63}$$

$$M_{j,i} = 2\left[\frac{1}{M_j} + \frac{1}{M_i}\right]^{-1} \quad (4\text{–}64)$$

In [Selimovic, 2002] a similar approach to calculate the potential loss due to diffusion, as described above is utilised (Equation 4–35 and Equation 4–55 - Equation 4–62). For calculation of the diffusion constants, the Chapman-Enskog theory which gives an estimated overall error of 8% is used. The Fuller equation has an approximated error of 4% and hence this presumably more accurate relation was used in the presented work.

$$D_{K,i} = \frac{2}{3} r_{por} \bar{v}_i \quad (4\text{–}65)$$

In the Knudsen diffusion equation, which is given in Equation 4–65, $D_{K,i}$ is the Knudsen diffusion coefficient for component *i*, r_{por} is the effective pore radius and $\bar{v}_i$ is the average molecular speed of species *i* and it can be described by Equation 4–66;

$$\bar{v}_i = \left(\frac{8RT}{\pi M_i}\right)^{1/2} \quad (4\text{–}66)$$

Activation Polarisation Losses

Activation polarisation losses are often also denoted polarisation overvoltage or polarisation overpotential. This type of loss is related to the reaction mechanisms that occur on the electrode in an electrochemical device. The physics of activation polarisation are not yet fully understood, although a large effort has been put into investigating the mechanisms behind the phenomena [Singhal, 2003]. However, it is believed that the electrode reactions are related to reaction steps involving surface adsorption, dissociation (oxygen), surface diffusion to a three phase boundary between the electrode, gas phase and electrolyte and the electrochemical reaction. From numerous experiments it is clear that the activation polarisation depends on length of the three phase boundary, partial pressure of oxygen in the atmosphere, oxygen vacancy in the electrolyte, oxygen vacancy mobility in the electrolyte, electron concentration in the electrode and temperature [Singhal, 2003]. The activation polarisation may further depend on the amount of impurities present in the material and the production method [Mogensen, 2002]. Thus cells produced at different facilities and different batches must be treated individually. Since activation polarisation occurs on a micro-level, investigation of this phenomenon is very difficult, and part of the uncertainty is related to the decision of the rate determining step.

A convenient and often used way of modelling activation polarisation is to assume that the electrode reactions follow in an adsorption- and charge transfer step [Kordesch, 1996], [Singhal, 2003]. Assuming that the charge transfer step determines the kinetics, the Butler-Volmer equation may be used to estimate the activation polarisation for one electrode (Equation 4–67).

$$i = i_0\left\{\exp\left(\frac{\beta n F \eta_{act}}{RT}\right) - \exp\left[-\frac{(1-\beta) n F \eta_{act}}{RT}\right]\right\} \quad (4\text{–}67)$$

Here i_0 denotes the exchange current density, which depends on catalytic activity of the electrode, and β is the transfer coefficient which normally has a value of approximately 0.5. The two exponential terms of Equation 4–67 represent reduction and oxidation and they are often called anodic and cathodic terms, respectively. The first term of the equation dominates for large positive overvoltage, while the second term dominates for large negative overvoltage.

In SOFC models where Equation 4–26 is applied, it is often necessary to have an explicit expression for the activation overvoltage. This is often achieved by simplifying Equation 4–67 for three different instances of the activation polarisation. In the first approach, it assumed that the activation polarisation is very small and hence the relation given in Equation 4–68 can be employed in Equation 4–67.

$$\exp\left(\frac{\beta nF\eta_{act}}{RT}\right) \approx 1 + \frac{\beta nF\eta_{act}}{RT} \tag{4–68}$$

$$i = i_0\left\{1 + \left(\frac{\beta nF\eta_{act}}{RT}\right) - 1 - \left(\frac{-nF\eta_{act}}{RT}\right) - \left(\frac{\beta nF\eta_{act}}{RT}\right)\right\} \tag{4–69}$$

This procedure yields Equation 4–69, which can be further simplified to give Equation 4–70:

$$\eta_{act,\,low} = \frac{RT}{nFi_0} \cdot i \tag{4–70}$$

For high activation overvoltage, the Butler-Volmer equation can be simplified for either high positive (anodic) or high negative (cathodic) activation overvoltage. For a high positive overvoltage the cathodic (second) term in the Butler-Volmer equation becomes negligably small and the equation can be simplified to give Equation 4–71.

$$i = i_0\left\{\exp\left(\frac{\beta nF}{RT} \cdot \eta_{act,\,c}\right)\right\} \tag{4–71}$$

Taking the logarithm on both sides of the equation and rearranging, an explicit expression for the cathodic activation polarisation can be established:

$$\eta_{act,\,c} = \frac{RT}{\beta nF} \cdot \ln\left(\frac{i}{i_0}\right) \tag{4–72}$$

$$\ln(x) = \ln(10) \cdot \log(x) \tag{4–73}$$

By introducing the logarithm to the base of 10, Equation 4–72 can also be written as the following relation:

$$\eta_{act,\,c} = \frac{RT\ln(10)}{\beta nF} \cdot \log\left(\frac{i}{i_0}\right) \tag{4–74}$$

For high negative values of the activation polarisation, the same procedure can be applied to achieve a similar expression:

$$\eta_{act,\,a} = -\frac{RT\ln(10)}{(1-\beta)nF}\cdot\log\left(\frac{|i|}{i_0}\right) \tag{4–75}$$

In Equation 4–74 and Equation 4–75, the first terms after the equation sign can be considered as constants. Equation 4–74 is often called Tafel's equation for cathodic activation overvoltage while Equation 4–75 is called Tafel's equation for anodic activation overvoltage. For simplicity, Tafel's equation and Equation 4–70 are often used in SOFC modelling [Selimovic, 2002], [Campanari, 2004], [Singhal, 2003]. Due to their simplification, it is however important to check the validity of the equations for each operational point. A study of the relative error between the simplified expressions and the full Butler-Volmer equation is performed in [Chan, 2001]. This study shows that using the simplified approach may introduce a relative error as high as 15% for intermediate values of the activation polarisation voltage.

An expression for the exchange current density, which is an important parameter in all the presented equations for activation polarisation, can be deduced from the Nernst equation (Equation 2–5), Faraday's law (Equation 4–16) and reaction kinetics theory. This results in Equation 4–76, where k is a constant, E_a is the activation energy, β is the transfer coefficient, which is also used in the Butler-Volmer equation, and $[O]$ and $[R]$ are the concentrations of the oxidizing and the reducing species respectively.

$$i_0 = nFk\cdot\exp\left(\frac{-E_a}{RT}\right)\cdot[O]^{\beta}\cdot[R]^{1-\beta} \tag{4–76}$$

Similar expressions to Equation 4–76 have also been found experimentally. In [Costamagna, 1998] a study on mathematical relations for estimation of the exchange current density was performed. In this study, it was found that the exchange current density of the anode can be described by Equation 4–77, while the exchange current density of the cathode can be described by Equation 4–78.

$$i_{0,\,a} = \gamma_a\cdot\left(\frac{p_{H_2}}{p_{ref}}\right)\left(\frac{p_{H_2O}}{p_{ref}}\right)^{m}\exp\left(\frac{-E_{act,\,a}}{RT_a}\right) \tag{4–77}$$

$$i_{0,\,c} = \gamma_c\cdot\left(\frac{p_{O_2}}{p_{ref}}\right)^{0.25}\exp\left(\frac{-E_{act,\,c}}{RT_c}\right) \tag{4–78}$$

The difference between the theoretically deduced and the experimentally obtained equations for exchange current density indicates that the charge transfer step probably is not the limiting factor for the activation polarisation. This is also indicated in [Divisek, 1994] and [Larrain, 2003], where other equations than the Butler-Volmer equation proved to fit better to the experimental results.

In this chapter a variety of methods for modelling activation polarisation has been shown, and a literature study would reveal further methods. For the presented model it was

therefore decided to implement the most acknowledged method, which is the Butler-Volmer equation (Equation 4–67). Equation 4–76 was chosen for the calculation of the exchange current density for the anode as well as for the cathode. The constants used in the equation were estimated from experimental data found in [Singhal, 2003], and the resulting relations are given in Equation 4–79 and Equation 4–80. The equation constants γ_a and γ_c represents the term *nFk* in Equation 4–76 for the anode and cathode, respectively. A description of the parameter estimation is given in Chapter 5.1. It is important to notice that Equation 4–79 incorporates the partial pressure of carbon monoxide, although it is not considered in the electrochemical reactions. However, one can assume that the presence of carbon monoxide and carbon dioxide will influence the activation polarisation and hence it is accounted for in this model [Mogensen, 1993], [Onuma, 2000], [Singhal, 2003].

$$i_{0,a} = \gamma_a \cdot \left(\frac{p_{H_2}}{p_{ref}} + \frac{p_{CO}}{p_{ref}}\right)^{0.5} \left(\frac{p_{H_2O}}{p_{ref}} + \frac{p_{CO_2}}{p_{ref}}\right)^{0.5} \exp\left(\frac{-E_{act,a}}{RT_a}\right) \tag{4–79}$$

$$i_{0,c} = \gamma_c \cdot \left(\frac{p_{O_2}}{p_{ref}}\right)^{0.5} \exp\left(\frac{-E_{act,c}}{RT_c}\right) \tag{4–80}$$

Equation 4–77 and Equation 4–78 were also tested, but the relations in Equation 4–79 and Equation 4–80 proved to fit better to the experimental results given in [Singhal, 2003].

Table 4.3: Estimated coefficients for Equation 4–79 and Equation 4–80.

γ_a [A/m^2]	γ_c [A/m^2]	$E_{act,a}$ [J/mol]	$E_{act,c}$ [J/mol]
$1.956 \cdot 10^{10}$	$1.026 \cdot 10^{10}$	$140 \cdot 10^3$	$149 \cdot 10^3$

4.3 Gas Turbine

A gas turbine can either be modelled by a direct detailed approach or from overall thermodynamic equations and relations that describe the overall behaviour. In order to create a flexible model with low calculation time, the latter approach has been chosen for this work. The model itself has been developed by Ragnhild Ulfsnes and Christoph Stiller and the contribution of the author is the integration of the gas turbine model with the SOFC system model [Ulfsnes, 2006], [Stiller, 2006].

The gas turbine model is divided into 5 sub-models, i.e. compressor, compressor map, shaft, expander and expander map. Both the map-models are further submodels of the expander and the compressor, respectively. Their purpose is to estimate off-design performance of their respective components. The shaft model accounts for any transient effects and it assures that compressor and expander are matched in terms of shaft speed.

4.3.1 Compressor Map Model

Delivery pressure, temperature, isentropic efficiency and flow rate for a given compressor depend on shaft speed, inlet temperature, inlet pressure and thermodynamic properties of the gas. A compressor is usually designed for a basic set of values of these parameters and operation at this condition is often referred to as design point operation. Operation under any other condition is referred to as off-design operation. Experimental results from off-design operation are often summarised in performance maps, in which the number of free variables are reduced by use of non-dimensional numbers for better readability. A dimensional analysis shows that constant reduced speed lines (N_{red}, Equation 4–81) can be plotted in two charts with reduced flow rate ($\dot{m}_{red}$, Equation 4–83) on the x-axis and with isentropic efficiency (η_{is}) or pressure ratio (π, Equation 4–82) on the y-axis [Saravanamuttoo, 2001]. In equation Equation 4–81 to Equation 4–83 the subscripts 01 and 02 relate to the stagnation values at the entry and exit respectively. The performance map for the modelled radial compressor is shown in Figure 4-6.

$$N_{red} = \frac{N}{\sqrt{T_{01}}} \tag{4–81}$$

$$\pi = \frac{p_{02}}{p_{01}} \tag{4–82}$$

$$\dot{m}_{red} = \frac{\dot{m}\sqrt{T_{01}}}{P_{01}} \tag{4–83}$$

The bold line that connects all the constant reduced speed lines in the lower part of Figure 4-6 is the surge line. Operation at any point above this line may result in a compressor surge. Surge in compressors may occur either if the flow rate is insufficient to maintain the down-stream pressure or if there is an aerodynamic stall on the first stages of the compressor. In any case a surge may be fatal for the compressor and it is important that operation is within a safe distance from the surge line.

The benefit of presenting performance in a map becomes evident when off-design of a gas turbine is to be predicted. If two of the four variables are known, they can be used to locate the operating point in the performance map. Once this point is fixed, the remaining parameters can readily be found from the map.

The map shown in Figure 4-6 only presents absolute values for a specific compressor, but it may be generalised if the design point parameters are used to establish dimensionless operational parameters. Equation 4–84 shows an example of how the pressure ratio is made dimensionless. Here is π the actual pressure ratio, π_{Dim} is the dimensionless value while π_{DP} is the pressure ratio of the design point. The other parameters used in the performance map are made dimensionless in the same manner.

$$\pi_{Dim} = \frac{\pi}{\pi_{DP}} \tag{4–84}$$

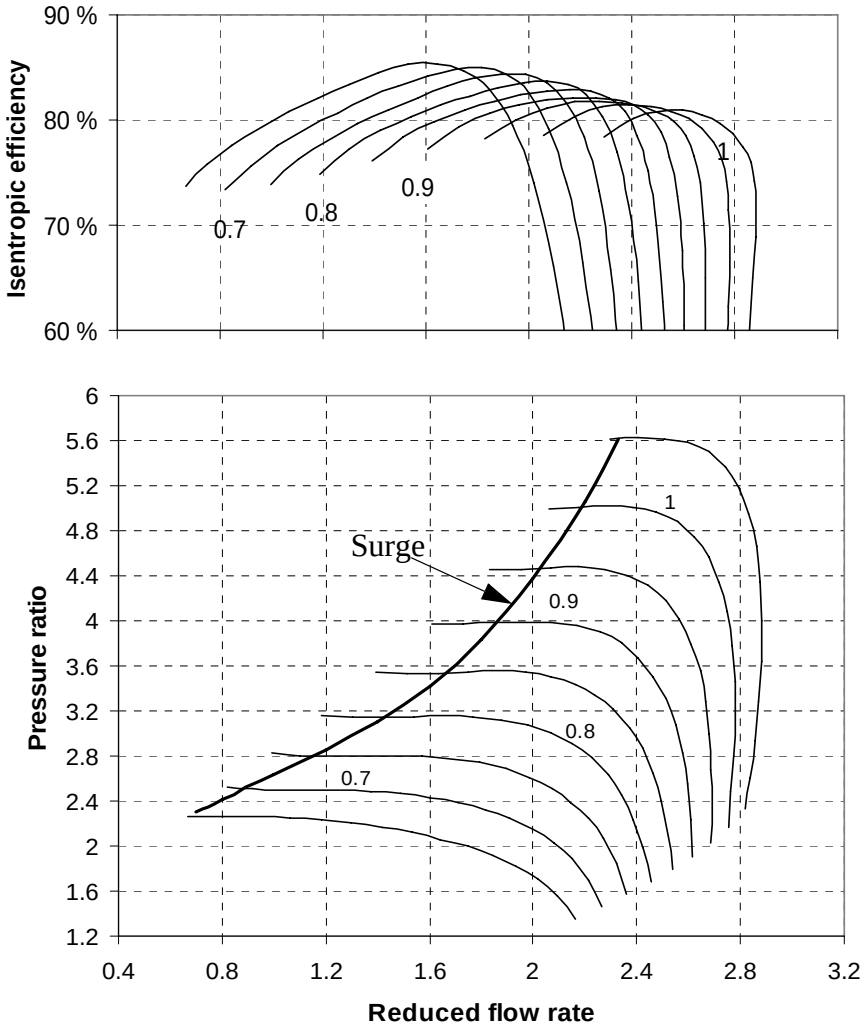

Figure 4-6. The performance map which is used for off-design calculations of the compressor. It is based on a generic map deduced from the DLR radial compressor from [Kurzke, 2004].

A normalised performance map is shown in Figure 4-7. The design point is now found at the cross section where the pressure ratio and the reduced and dimensionless flow rate equal 1.

From Figure 4-7 it can be seen that some of the constant reduced speed lines are almost vertical. This is due to the compressor operating in a choked condition. However, the vertical nature of these lines induces a problem when the map is used electronically, since there are multiple values for the pressure ratio at a given reduced mass flow. From the same map it is also visible that parts of the constant reduced speed lines are horizontal, and hence there are multiple values for the reduced dimensionless flow rate for a given pressure ratio. To cope with this, auxiliary coordinates which intersect the reduced speed lines are introduced. These coordinates are often denoted β-lines and they facilitate

reading of the maps independently of the line shape. Principally, the shape of the β-grid can be selected arbitrarily as long as there are precise interceptions of the reduced speed lines.

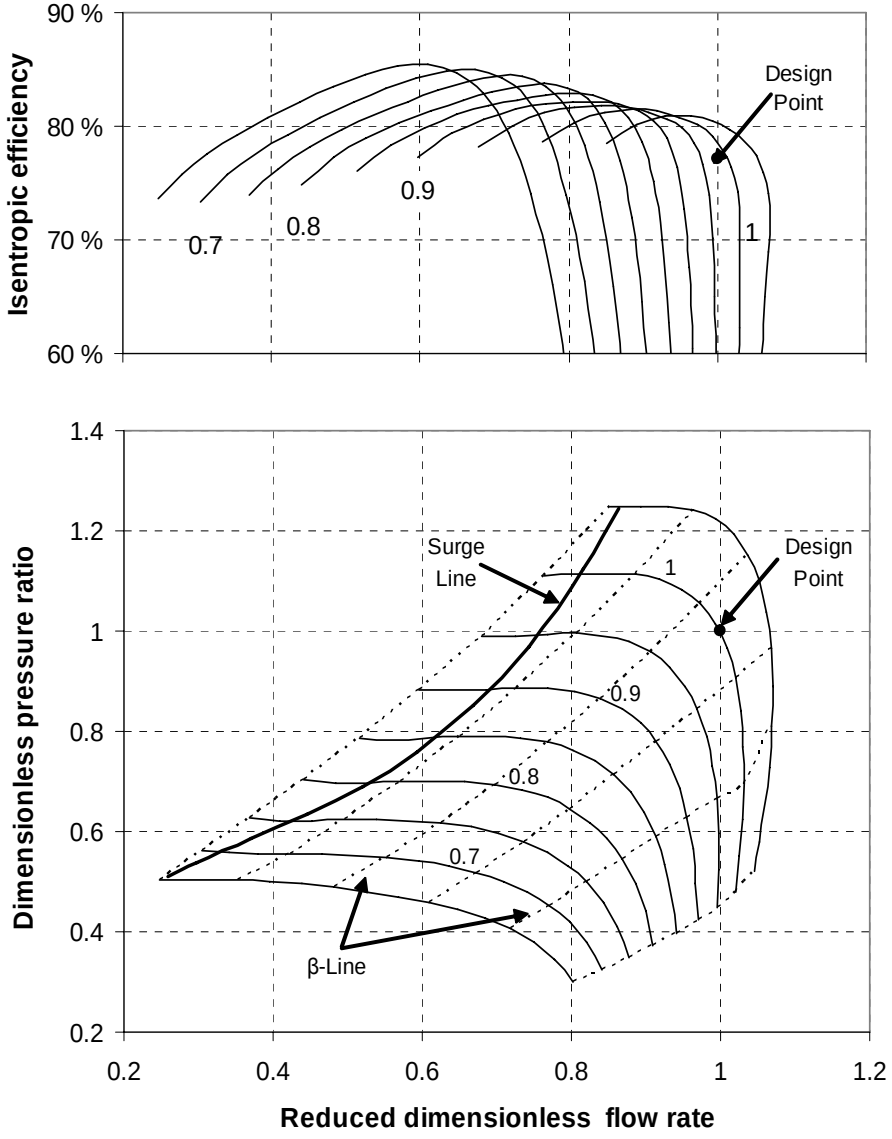

Figure 4-7. Normalised performance map for a compressor.

The foundation for a generic performance map has now been established, and what remains is to find the right type of equation and fit it to the experimental values. To sum up, the following relations must be established;

$$\dot{m}_{dim,\,red} = \frac{f(N_{dim,\,red}, \beta)}{\dot{m}_{red,\,0}} \tag{4–85}$$

$$\eta_{is,\,dim} = f(N_{dim,\,red}, \beta) \tag{4–86}$$

$$\pi_{dim} = \frac{f(N_{dim,\,red}, \beta)}{\pi_0} \tag{4–87}$$

$$\pi_{surge} = f(\dot{m}_{dim,\,red}) \tag{4–88}$$

Polynomials of 4th and 5th degree have been used to fit the relations in Equation 4–85 to Equation 4–88 to experimental data from a radial compressor tested by DLR (Deutschen Zentrum für Luft und Raumfahrt). The data from this compressor have been found in a database assembled by Kurzke [Kurzke, 2004]. Data from the same compressor have also been used in SOFC/GT system studies in [Chan, 2003a/b]. The dimensionless off-design performance map used in this model is depicted in Figure 4-7. It should be noted that this off-design map is only valid for normalised shaft speeds in the range of 0.65 to 1.1 and below the surge line.

In most compressor applications, the risk of surge is avoided by operating a certain distance from the surge line. The distance to surge is often denoted “surge margin”. In this work the surge margin is defined according to Equation 4–89.

$$\text{Surge margin} = \frac{\pi_{surge}}{\pi} \tag{4–89}$$

4.3.2 Compressor Model

The compressor is implemented as a thermodynamic model which calculates the outlet temperature, pressure and mass flow from the properties of the incoming gas and shaft speed. These variables are further used to calculate the compressor work. The following assumptions are made for the compressor:

- Gas residence time is negligible
- Fouling and degradation is not accounted for
- The compressor is adiabatic
- The kinetic energy of the gas is negligible compared to the enthalpy, i.e. $h_{01} = h_{in}$, $T_{01} = T_{in}$, $P_{01} = P_{in}$, etc.

Performance of the compressor may be described by seven parameters;

- Inlet pressure, P_{in}
- Inlet temperature, T_{in}
- Shaft speed, N
- Outlet temperature, T_{out}
- Outlet pressure, P_{out}
- Flow rate, $\dot{m}$

- Isentropic efficiency, η_{is}

The two first parameters are known as they are related to the ambient conditions. For the remaining five variables the equations for reduced values given in Equation 4–81 to Equation 4–83 may be applied. These three equations connect the remaining variables together in the performance map.

When the operational point is located, pressure ratio, isentropic efficiency and flow rate are known. The exit pressure can be found from Equation 4–90, where *P* denotes the pressure and π denotes the pressure ratio.

$$P_{out} = P_{in}\pi \tag{4–90}$$

Using the thermodynamic properties package Multiflash [Multiflash, 2001], the isentropic outlet temperature can be calculated from Equation 4–91. The isentropic enthalpy change is found in Equation 4–92 and divided by the isentropic efficiency to reveal the real enthalpy change in Equation 4–93.

$$s(T_{is,\,out}, P_{out}, y) - s(T_{in}, P_{in}, y) = 0 \tag{4–91}$$

$$\Delta h_{is} = h(T_{is,\,out}, P_{out}, y) - h(T_{in}, P_{in}, y) \tag{4–92}$$

$$\Delta h = \frac{\Delta h_{is}}{\eta_{is}} \tag{4–93}$$

Knowing the mass flow and real enthalpy change, the compressor work may be calculated from Equation 4–94.

$$W_{Comp} = \dot{m}\Delta h \tag{4–94}$$

$$\Delta h = h(T_{out}, P_{out}, y) - h(T_{in}, P_{in}, y) \tag{4–95}$$

The outlet condition of the gas is further calculated from the real enthalpy change in Equation 4–95.

4.3.3 Expander Map Model

An expander operating close to the design point is normally choked. If a constant isentropic efficiency is assumed, the exit properties may be calculated from the choked nozzle relation given in Equation 4–96 [Traupel, 1966]. Here $\dot{m}$ denotes the flow rate and

P is the pressure. The subscript *DP* denotes the design point value, 03 and 04 are the subscripts for the expander inlet and outlet condition stagnation values, respectively.

$$\frac{\dot{m}}{\dot{m}_{DP}} = \frac{P_{03}}{P_{03,\,DP}} \sqrt{\frac{1-\left(\frac{p_{04}}{p_{03}}\right)^2}{1-\left(\frac{p_{04,\,DP}}{p_{03,\,DP}}\right)^2}} \qquad (4\text{–}96)$$

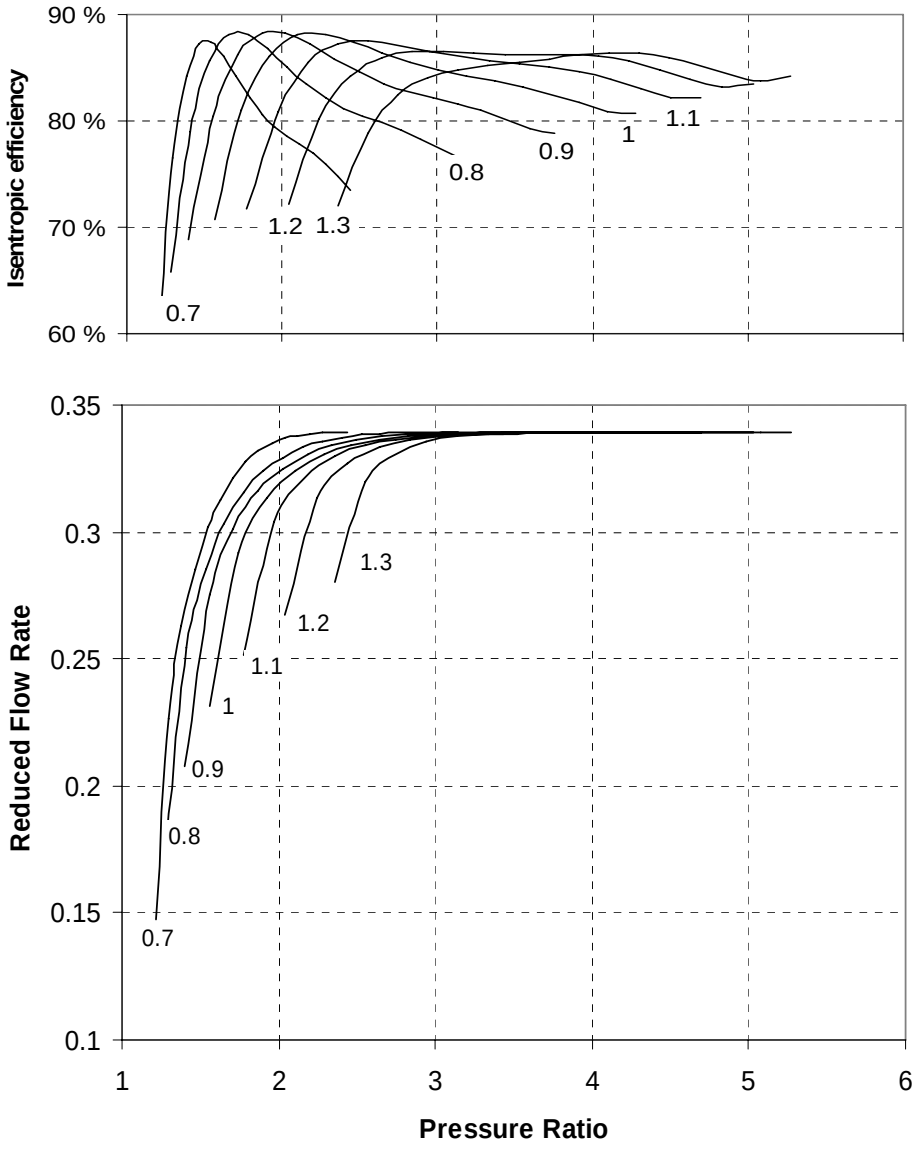

Figure 4-8. The original radial expander performance map used for the expander off-design calculation.

A radial expander, which is modelled here, usually has a very large operation range where it operates in choked condition. This can also be seen from the horizontal nature of part of the constant shaft speed lines in Figure 4-8. The figure also shows that the chocked nozzle assumption is invalid for low pressure ratios (Lower than 3 for this specific expander). As mentioned in Chapter 2.1.1, the optimum pressure ratio of a gas turbine process integrated with a SOFC is likely to be 4-6. This means that low load operation at reduced pressure of the process will be outside of the valid range for the choked nozzle equation. Therefore an expander performance map has been included in the model.

The expander map is established by the same procedure as for the compressor and the same equations are used for calculation of the reduced parameters (Equation 4–81 to Equation 4–83). The use of the same dimensionless variables for description of compressor and expander performance enables easy numerical coupling of the two components. The shaft speed of the two components must be equal (single shaft only) and the expander flow rate can readily be estimated as the sum of compressor and fuel mass flow, less any bleeds. Figure 4-8 shows the performance map of the radial expander used in this model. The experimental data for the expander was taken from a map in Kurzke's map collection, referred to as NASA-CR-174646 [Kurzke, 2004].

As for the compressor, a 5th variable has to be introduced in order to establish a unique solution of pressure ratio when the expander is choked. Again the parameter β is introduced and the same type of relations as given in Equation 4–85 to Equation 4–88 is used. A 5^{th} order polynomial was found adequate for fitting of the isentropic efficiencies for this specific expander. The experimental values for the constant speed lines in the mass flow - pressure ratio diagram were estimated by an elliptic equation. The dimensionless expander performance map is shown in Figure 4-9.

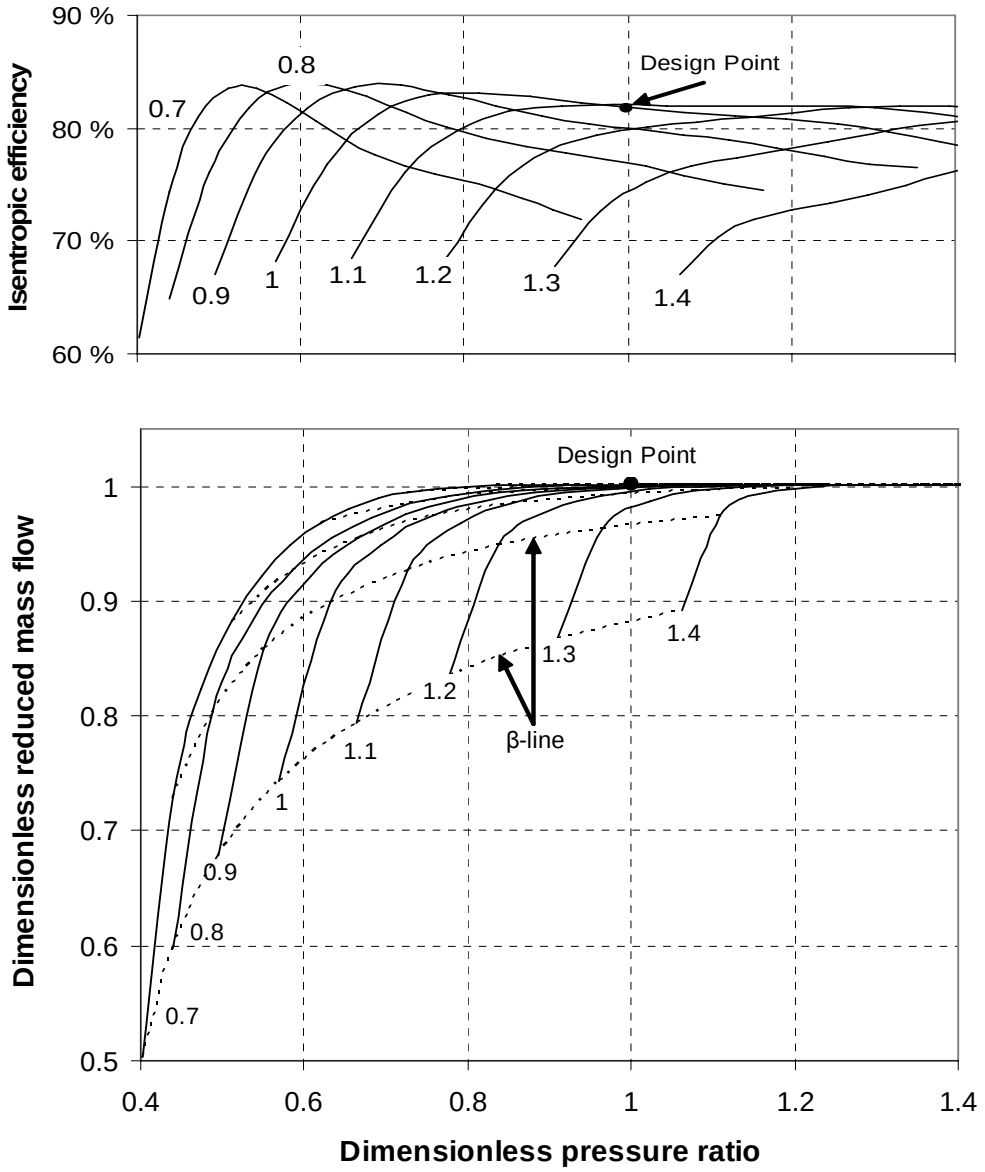

Figure 4-9. The dimensionless expander performance map incorporating the β -lines.

4.3.4 Expander Model

The expander model is constructed in a similar way as the compressor. It uses dimensionless values, and it is based on over-all thermodynamic equations using the expander map model for off-design calculations. Accordingly, the design point parameters must be given. The following assumptions are made for the expander model.

- Gas residence time is negligible

- Fouling is not accounted for
- The expander is adiabatic.
- The kinetic energy of the gas is negligible compared to the enthalpy, i.e. $h_{01} = h_{in}$, $T_{01} = T_{in}$, $P_{01} = P_{in}$, etc.

The operational point of the expander is found in the performance map by the same procedure as for the compressor. Once the operational point has been found in the performance map, the isentropic end point temperature is found from Equation 4–97 by using Multiflash [Multiflash, 2001]. The isentropic enthalpy change is found from Equation 4–98. By using the isentropic efficiency obtained from the performance map, the real enthalpy change can be calculated by Equation 4–99. The real enthalpy is used to find the real exit properties of the gas as in Equation 4–100.

$$s(T_{is,\,out}, P_{out}, y) - s(T_{in}, P_{in}, y) = 0 \tag{4–97}$$

$$\Delta h_{is} = h(T_{is,\,out}, P_{out}, y) - h(T_{in}, P_{in}, y) \tag{4–98}$$

$$\Delta h = \Delta h_{is}\eta_{is} \tag{4–99}$$

$$\Delta h = h(T_{out}, P_{out}, y) - h(T_{in}, P_{in}, y) \tag{4–100}$$

The expander work can now be calculated from the mechanical efficiency (η_m) real enthalpy change and the mass flow. (Equation 4–101).

$$W_{\exp} = \eta_m \cdot \dot{m} \cdot \Delta h \tag{4–101}$$

4.3.5 Shaft Speed Model

When the gas turbine operates at steady-state, there has to be compatibility between compressor power, expander power and load (alternator power) as well as for flow rate of the compressor and the expander. These requirements are summarised in Equation 4–102, where *P* denotes power given in W, and the subscript *Exp*, *Compr* and *Alt* stands for expander, compressor and alternator, respectively.

$$0 = P_{Exp} - P_{Compr} - P_{Alt} \tag{4–102}$$

During steady-state operation, the shaft speed model will make sure that the requirements of Equation 4–102 are fulfilled at the same shaft speed, i.e. keeping the compressor and expander matched.

If the requirements of Equation 4–102 are not fulfilled, there is a surplus of power, which imposes in an excess torque on the shaft (Equation 4–103). The excess torque will result in shaft acceleration if not corrected for by the control system.

$$\Delta P = P_{Exp} - P_{Compr} - P_{Alt} \tag{4–103}$$

It follows that during a transient; only compatibility of flow is required. It is also evident that the surplus of work is the driving force for the shaft acceleration and that the acceleration will last until this imbalance has been adjusted for by the system.

The relation between acceleration of the shaft and the torque τ is given by Newton's second law of motion;

$$\tau = I\dot{\omega} \tag{4–104}$$

where I is the moment of inertia of the shaft and $\dot{\omega}$ is the angular acceleration. Power on a rotating body is defined as torque multiplied with the angular velocity ω;

$$P = \tau\omega \tag{4–105}$$

By using Equation 4–104 in Equation 4–105, rearranging and using the excess power from Equation 4–103, an equation for the angular acceleration due to excess shaft power can be established;

$$\frac{d\omega}{dt} = \frac{\Delta P}{I\omega} \tag{4–106}$$

Moment of inertia I is constant for a given geometry and rotation centre and it may be calculated by the general formula given in Equation 4–107,

$$I = \int_V r^2 \rho dV \tag{4–107}$$

or by assuming that the shaft can be described as a rotating disc with radius r and mass m. The inertia of a rotating disc is calculated from Equation 4–108.

$$I = \frac{1}{2} \cdot m \cdot r^2 \tag{4–108}$$

The angular velocity ω is calculated from the shaft speed N given in rpm by Equation 4–109.

$$\omega = \frac{\pi N}{30} \tag{4–109}$$

The shaft speed may be operated according to two different strategies; constant speed or variable speed. When operating at constant speed, the high frequency converter may be omitted provided that the shaft speed corresponds to the electrical grid frequency. For variable speed operation, power electronics can be employed to control the shaft speed. For this type of operation, a simplified controller has been implemented. The controller algorithm is given in Equation 4–110.

$$\frac{\Delta P}{I\dot{\omega}} = Min(MaxSpCh, Gain \cdot |N_{SP} - N|) \cdot Sign(N_{SP} - N) \cdot \frac{\pi}{30} \qquad (4\text{–}110)$$

Maximum allowable acceleration is *MaxSpCh*, target speed is denoted N_{SP} (setpoint) while actual speed is denoted *N*. *Gain* is a constant value which decides the duration of the speed change relative to the speed change magnitude.

4.4 Heat Exchanger

Compact heat exchangers are often used in recuperated gas turbine cycles. Plate-fin or primary surface heat exchangers are two examples of such compact heat exchangers (Chapter 2.3.4). For this model a single-pass counter-flow plate-fin heat exchanger was chosen.

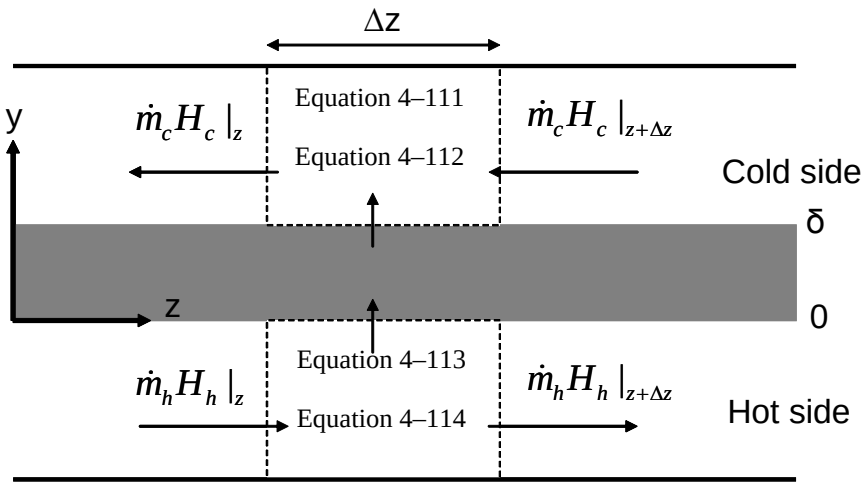

Figure 4-10. Energy balance of one control volume in the heat exchanger model.

$$\rho_c \cdot \frac{du}{dt} \cdot Ac_c \cdot \Delta z \qquad (4\text{–}111)$$

$$U_c \cdot As_c \cdot (T_w|_{y=\delta} - T_{f,c}) \qquad (4\text{–}112)$$

$$U_h \cdot As_h \cdot (T_{f,h} - T_w\big|_{y=0}) \tag{4–113}$$

$$\rho_h \cdot \frac{du}{dt} \cdot Ac_h \cdot \Delta z \tag{4–114}$$

The heat exchanger is modelled as two channels separated by a flat wall (Figure 4-10). The channels are discretized along the flow direction in a one-dimensional discretization scheme, while the wall is discretized in the direction perpendicular to the flow as well as in the flow direction. The following assumptions are made for the heat exchanger model:

- The heat exchanger is adiabatic
- The fluid flow regimes are fully developed
- Heat transfer is due to convection and conduction
- Radiation is neglected
- Properties of the gases are evenly distributed within each control volume, i.e. bulk values are assumed.
- The flat plate shown in Figure 4-10 represents the total mass of the heat transfer area, and hence it accounts for thermal inertia of the whole heat exchanger (including fins and casing).
- The effect of the fins to the heat transfer is be described by geometrical considerations and fin efficiency.
- Fouling is neglected.

Kays and London performed experiments on a number of different heat exchangers with different designs and flow patterns. Geometry of the heat exchangers as well as the experimental results are published in [Kays, 1984]. The surface type referred to as 11.1 in [Kays, 1984] was used in the presented model and the fin geometry data are reproduced in Table 4.4.

Table 4.4: Geometrical data for surface type 11.1 in [Kays, 1984]

Parameter	Value
Plate spacing, l	$6.35 \cdot 10^{-3}$ m
Plate thickness, δ	$0.3 \cdot 10^{-3}$ m
Fin thickness, t_f	$0.152 \cdot 10^{-3}$ m
Hydraulic radius, R_h	$0.771 \cdot 10^{-3}$ m
Heat transfer area/Volume between the plates, α	1204 m^2/m^3
Fin area/total heat transfer area, ε	0.756

A heat balance over a control volume of the fluid with corrections for the fin geometry results in Equation 4–115. The term to the left of the equality sign in the equation accounts for accumulation of thermal energy in the fluid. Here A_c denotes the cross-sectional area perpendicular to the flow, ρ is the density of the fluid, c_p is the heat capacity and T_f is the fluid temperature.

$$A_c \rho c_p \frac{dT_f}{dt} = \alpha A_{surf} \eta_{surf} h(T_f - T_w) - \dot{m} \frac{dh_f}{dz} \tag{4–115}$$

The right most term in Equation 4–115 accounts for the thermal energy that flows in and out of the control volume, where $\dot{m}$ represents the flow rate and h_f the fluid enthalpy. In the first term to the right of the equality sign, heat transfer between the fluid and the heat exchanger wall is accounted for. The first parameter α is the ratio between the heat transfer area (including the fins) and the volume between the plates and it is given in Table 4.4. The next parameter, A_{surf}, represents the total heat transfer area while the next two parameters represent the surface efficiency (η_{surf}) and the convective heat transfer coefficient, h. η_{surf} and h will be discussed thoroughly later, while T_f and T_w denote the fluid and wall temperatures, respectively.

In a heat exchanger utilising fins, there will be a temperature gradient from the tip to the root of the fin, resulting in a lower temperature difference between the fluid and surface on the fin tip. Since temperature difference is the driving force for heat exchange, this leads to a reduced efficiency of the heat transferring surface. If one considers the heat transferred in the ideal heat exchanger to be Q_{ideal} (infinite conductivity) and the heat transferred in the real heat exchanger to be Q_{actual}, efficiency of the heat transfer surface in the real heat exchanger can be estimated according to Equation 4–116.

$$\eta_{surf} = \frac{Q_{actual}}{Q_{ideal}} \tag{4–116}$$

According to [Kays, 1984], the heat transfer surface efficiency can also be calculated from geometrical considerations as in Equation 4–117, where ε is the fin area divided by the total heat transfer area (Table 4.4).

$$\eta_{surf} = 1 - \varepsilon(1 - \eta_{fin}) \tag{4–117}$$

The fin efficiency, η_{fin}, which is used in calculation of the total surface efficiency, is further a function of the thermal conductivity of the wall k_w, the fin thickness t_f, the convective heat transfer coefficient, h, and the plate spacing l. Calculation of the fin efficiency is given in Equation 4–118 to Equation 4–119, where the parameter ψ is used as an intermediate variable.

$$\eta_{fin} = \frac{\tanh\psi}{\psi} \tag{4–118}$$

$$\psi = \left(\frac{2h}{k_w t_f}\right)^{1/2} \cdot \frac{l}{2} \tag{4–119}$$

The convective heat transfer coefficient may be estimated from the experimental data obtained from [Kays, 1984]. In their experiments, Kays and London plotted the Colburn j-factor (Equation 4–120) versus the Reynolds numbers between 500 and 10 000.

$$j = StPr^{-2/3} \tag{4–120}$$

As can be seen from Equation 4–120, the Colburn j-factor is a function of the Stanton number (*St*) and the Prandtl number (*Pr*). The Stanton number is further a function of the mass flux ($\dot{m}_v$, [kg/m^{2}s]), the thermal heat capacity (c_p) and the heat transfer coefficient.

$$St = \frac{h}{\dot{m}_v \cdot c_p} \tag{4–121}$$

The Prandtl number is calculated from the thermal heat capacity (c_p), the viscosity (μ) and the heat conductivity (k) in Equation 4–122.

$$Pr = \frac{c_p \mu}{k} \tag{4–122}$$

$$Re = \frac{4R_h \dot{m}_v}{\mu} \tag{4–123}$$

The Reynolds number (*Re*) is calculated from Equation 4–123, where the hydraulic radius R_h is taken from Table 4.4. The thermodynamic properties used in the calculation of the Stanton, Prandtl and Reynolds numbers can be calculated by using the thermodynamic properties package Multiflash [Multiflash, 2001], while the mass flux is given from the flow rate and the cross-sectional area. By knowing every variable, except the convective heat transfer coefficient, in Equation 4–121 to Equation 4–123, the latter may be calculated from the Colburn j-factor.

The experimentally obtained relation between the Colburn factor and the Reynolds number from [Kays, 1984] is shown in Equation 4–124, with the constants listed in Table 4.5.

$$StPr^{-2/3} = C_1 + C_2Re^{-1} + C_3Re^{-2} + C_4Re^{-3} + C_5Re^{-4} + C_6Re^{-5} \tag{4–124}$$

Table 4.5: Constants from Equation 4–124

C_1	0.002125607696	C_4	31750925.93
C_2	12.68684358	C_5	-1.489539418E+010
C_3	-29070.42711	C_6	2.546890142E+012

The wall which separates the two fluids is discretized in the flow direction (z) and through the cross section (y). Calculation of the heat balance of the wall can readily be performed by applying the same equation as used for the air supply tube in the SOFC model (Equation 4–3), but related to an orthogonal grid. The final equation is given in Equation 4–125, where the subscript *w* denotes the wall.

$$\frac{d^2T_w}{dz^2} + \frac{d^2T_w}{dy^2} = \frac{\rho_w c_w}{k_w} \cdot \frac{dT_w}{dt} \tag{4–125}$$

The frictional pressure loss of a heat exchanger can be estimated using Equation 4–127. The friction factor (*f)* for the specific surface was measured by Kays and London and is given by Equation 4–126

$$f = 0.0080346683711 + \frac{8.670051012}{Re} + \frac{2433.735607}{Re^2} \tag{4–126}$$

Together with the geometric parameters given in Table 4.5, the moody friction factors can be used to calculate the pressure loss in the heat exchanger [Kays, 1984].

$$\frac{\Delta P}{P_{in}} = \frac{\dot{m}_v^2}{2} \cdot \frac{v_{in}}{P_{in}}\left[(K_{in} + 1 - \sigma^2) + 2\left(\frac{v_{in}}{v_{out}} - 1\right) + 2\left(\frac{v_{in}}{v_{out}} - 1\right) + f\alpha\frac{v_m}{v_{in}} - (1 - \sigma^2 - K_{out})\frac{v_{out}}{v_{in}}\right] \tag{4–127}$$

In Equation 4–127, *v* denotes the specific volume of the gas, σ is the ratio between the free flow area and the frontal area while K_{in} and K_{out} represent the entrance and exit loss, respectively. For simplicity, these losses are neglected in the presented model. Further, the subscript *in* denotes inlet condition, *out* is the outlet value and *m* is the average value.

4.5 Balance of Plant

4.5.1 Piping

Piping is necessary for gas distribution within the SOFC/GT system. The piping system will have a small effect on the overall system performance and efficiency through heat and pressure loss. Gas residence time of the piping system will further affect the system overall dynamic response during load change. The described influence of the piping system will to a large extent depend on system design. If for instance most of the piping is placed within the high pressure vessel together with the fuel cell stack, heat loss from the pipes is likely to be very small. Pressure loss depends on pipe length and diameter, but the most important parameter is the number of pipe bends. Residence time within the piping system depends solely on the volume of the pipes when the volumetric flow rates are given.

There are many approaches to design a SOFC/GT system with respect to the piping system, and hence there is an uncertainty connected to the final layout. As a consequence

of this uncertainty, it is difficult to put up an assumption of the extent of losses and dynamic effects the piping system might have on the overall system. Since the model is developed for dynamic modelling, the pipe model used in the presented model only account for gas residence times of the pipes. Heat loss and pressure loss are omitted. Residence time of the tubes is accounted for by modelling the pipe as a tube with constant cross-section area and a given length. With this approach the pipe model may also be used to model residence times of dimensionless components without having any effect on the heat and pressure loss of the specific component. As can be seen from Figure 4-1, several instances of the pipe model is used, and for each instance a different cross-section area and length is applied in order to account for what is assumed to be a proper gas residence time.

4.5.2 Desulphurisation

The modelled system is assumed to operate on natural gas, which basically consists of methane and some small amounts of higher hydrocarbons and a very small quantity of hydrogen sulphide (H_2S). This means that the hydrodesulphurisation (HDS) reactor mentioned in Chapter 2.3.1, may be omitted in the presented model. Accordingly, only hydrogen sulphide must be removed from the fuel, prior to the prereformer. Still with Chapter 2.3.1 in mind, we recall that the adsorption of H_2S is nearly adiabatic and almost without any pressure loss. By assuming that the adsorption of H_2S is without any pressure loss and totally adiabatic, modelling of the desulphurisation unit can be done by a pipe which accounts for the residence time. In the presented model, the pipe between the fuel mixer and prereformer accounts for the residence time of the desulphurisation unit.

4.5.3 Power Electronics

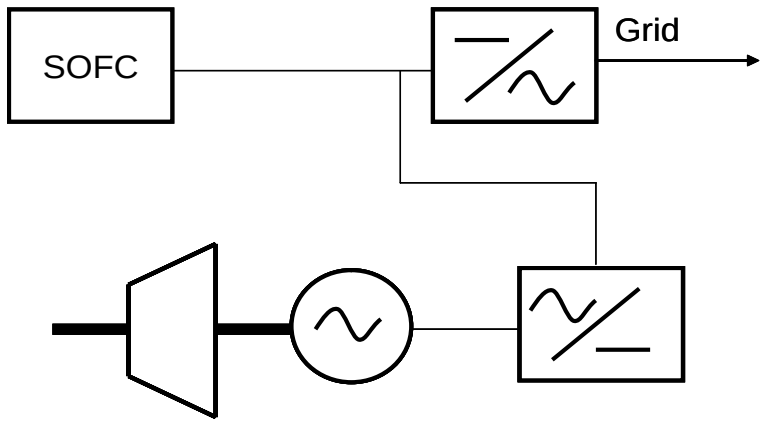

Figure 4-11. Power electronics system for the hybrid cycle

A hybrid SOFC/GT power plant produces both alternating current and direct current. A high speed micro turbine with variable shaft speed will deliver alternating current (AC)

with variable frequency. The SOFC stack will deliver direct current (DC) with a voltage, which varies with the operating conditions. Thus in order to be able to supply the grid with an appropriate electricity quality, power electronics is needed in the interface between the power plant and the grid. The proposed power electronics system layout for this SOFC/GT system is given in Figure 4-11.

Rectification and alteration of the current is performed through several circuits, switches and filters in the power electronics. Losses are low when compared to the rest of the SOFC/GT system and mostly related to the switches. Furthermore, power converters are able to adjust to new operating conditions within less than a second, and this means that dynamics of the power electronics can be neglected in the presented model. Hence a constant efficiency of 95% has been assumed for each of the components seen in Figure 4-11. It is further assumed that the system has a parasitic power consumption of 5 kW, independent of the total power production.

4.5.4 Other Components

Among the components described as balance of plant components, are the water treatment unit, hydrogen storage, nitrogen supply system and steam generator. These are components used under very special conditions and for simplicity they are omitted in the presented model. However, due to the structure of the model, they should be easy to implement, if necessary.

4.6 Thermodynamic Properties of the Gases

The thermodynamic properties package “Multiflash” [Multiflash, 2001], which is included in the gPROMS modelling environment, was used in the presented work. Multiflash is developed by Infochem Computer Sciences Ltd. and is an external thermodynamic properties package with a gPROMS interface. It includes equations of state, activity coefficient and transport property models, flash calculations, component data banks, petroleum fraction correlations and a PVT (pressure-volume-temperature) analysis facility. Multiflash requires a separate input file for specification of the species, data bank and calculation methods. Calls for property calculations can be performed directly from the gPROMS code.

The gas mixtures used in the SOFC/GT process model is basically a gas mixture of methane, syngas, combustion products and air. Throughout the whole model all components remain in their gas phase and hence only single phase behaviour must be calculated. An equation of state model appropriate for this type of calculations is the Soave-Redlich-Kwong model (SRK) with vapour pressure fitting. It is widely used for hydrocarbon mixtures, but it is not recommended for strongly polar or hydrogen mixtures. However, by adding the Van-Der-Waals mixing rule, the SRK model may also be used for polar mixtures. Accuracy is further increased by using binary interaction parameters from the oil and gas data bank implemented in Multiflash.

Vapour thermal conductivity is calculated from the Chung-Lee-Starling model, which is a method that mainly is applicable to components available in oil and gas processing

operations. Accuracy of the model is enhanced by a vapour thermal conductivity mixing rule, which makes use of parameters from a Multiflash data bank.

4.7 Implementation of the code in gPROMS

The model described in this chapter has been fully implemented in the gPROMS modelling environment which is a modelling and simulation language for solving of mixed systems of integral, partial differential and algebraic equations (IPDAEs) [Oh, 1996], [gPROMS, 2004]. The gPROMS system can be used for both dynamic and steady-state calculations and it distinguishes between two fundamental instances of a modelling entity; *models* and *tasks*. A *model* is a set of equations and definitions required to describe a system, while a *task* is a set of external actions and disturbances put on the system. A *process* is an instance of a *task* which drives the model. In a SOFC/GT system each unit operation component can be described by separate sub-*models* which are assembled in one overall *model* to describe the plant configuration. The overall *process* may then be considered as a set of actions taken by the operator of the plant.

gPROMS features a set of discretization methods and mathematical solvers for the user to choose from. This reduces the programming task setting up the mathematical equations and choosing the right discretization method and solver for the problem. This saves time and labour in model development, when compared to for instance FORTRAN or MATLAB which are often employed in SOFC modelling (Chapter 3). gPROMS is an equation oriented solver and is generally very fast compared to sequential solvers, but initialisation of a problem might be a challenge.

In this work each unit operation model has been described in a separate model in order to establish a library of different components. Every model has been assigned the same interface format (gas flow properties and/or energy flow) which makes it easy to assemble a system. Within the gPROMS modelling environment it is also possible to have several instances of the same model. In the presented model, several instances of the heat exchanger, pipe and splitter has been used.

5 Verification and Sensitivity Studies

When modelling, it is important to recognize that a model usually represents a simplification of the real system. Furthermore, computational codes are exposed to programming bugs and numerical errors due to the discretization of the differential equations. In order to justify the model simplifications and diminish the influence of computational errors, it is therefore of great importance that the model is verified either against experimental data or through computational plausibility tests. The intention of this chapter is to investigate the validity of the model by using both methods mentioned above. First a fuel cell model verification is described and this is followed by a sensitivity study of some selected parameters. The compressor and expander models are not investigated, as they are based on experimentally developed performance maps. Finally, a conclusion on the validity of the model is made.

5.1 SOFC Model Calibration and Verification

The presented SOFC model is based on a similar design to the tubular SOFC developed by Siemens Westinghouse. References to this design can be found in [Yi, 2003], [Singhal, 2003], [Singhal, 2002], [George, 2000] and [Veyo 2003]. Unfortunately, sufficient data to produce an exact model of the tubular Siemens Westinghouse SOFC are not published. Therefore, data from a great variety of sources have been used for parameters such as thermal conductivity, electrode porosity, electrode pore radius, electric conductivity etc. The parameters used in the model are already presented in detail in Table 4.1, Table 4.2 and Equation 4–27 to Equation 4–29.

As mentioned in Chapter 4.2.5, activation polarisation can be expected to vary between different cell designs, production methods, production facilities and batches. Calibration of the SOFC model, with respect to activation polarisation, is therefore necessary in order to be able to model the fuel cell behaviour in a proper manner. Unfortunately, the author was unable to acquire any experimental data from activation polarisation measurements of tubular SOFCs operating on methane. Instead, voltage-current density plots from Figure 8.16 in [Singhal, 2003] was used to calibrate the model. The plots show the voltage-current density characteristics of the tubular Siemens Westinghouse SOFC, when operating on a mixture of 89% hydrogen and 11% steam at 1000 °C, 940 °C and 900 °C, respectively. The measurements were made under atmospheric conditions with 85% fuel utilisation and air with a stoichiometric ratio of 4 as oxidant. The plots are reproduced in Figure 5-1.

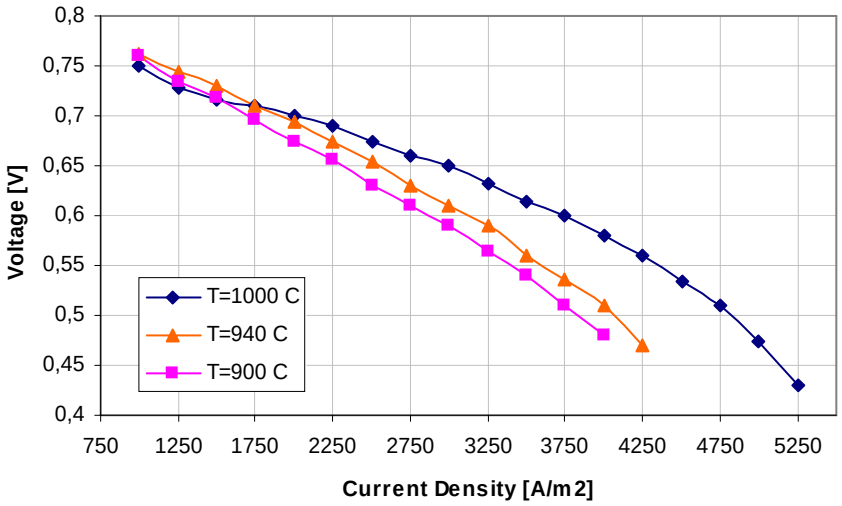

Figure 5-1. Voltage-current density plot of a tubular Siemens Westinghouse SOFC. (Figure 8.16 in [Singhal, 2003]).

A voltage-current density characteristic of a fuel cell represents the overall behaviour of the fuel cell, and it can therefore not be used directly to estimate the activation polarisation properties of the fuel cell. However, by comparing measured current density-voltage characteristics with the calculated characteristics, a relation for the activation polarisation equation can be estimated. Within the gPROMS modelling environment, parameter estimation is a standard routine, which is facilitated by the possibility to import experimental data and a standard mathematical solver for solving estimation problems. This routine was used to calibrate the presented model against the data from [Singhal, 2003].

Prior to the execution of the parameter estimation it is important to consider the validity of the outcome. With the given set of experimental data it is necessary to compute the whole SOFC model in order to perform the parameter estimation. As most of the material property data are collected from different sources and not based on measurements of the actual fuel cell, it is clear that the resulting activation polarisation equation will involve an uncertainty. In fact, the described method implies that every model- and measurement deviation is summed in the estimated activation polarisation equation. Thus, the final equation can not be considered to be a good description of the activation polarisation itself, but as an equation which correlates the model to the experimental results. However, since the main intention of the model is to predict behaviour of a SOFC, and the model equation with the largest uncertainty is used to calibrate the model, this procedure can be justified.

In the model calibration, it is assumed that the voltage-current density experiments referred to in [Singhal, 2003], were performed on a single tubular SOFC placed in a furnace. Accordingly, the boundary condition for the anode radiation has been set to be a surface with a constant temperature, able to maintain a constant mean anode temperature

of 1000 °C, 940 °C and 900 °C, respectively. It is further assumed that the inlet temperatures of the gases are 100 °C below the mean fuel cell temperature.

The objective of the model calibration is to find an expression for the exchange current density which together with the Butler-Volmer equation (Equation 4–67) fits to the data from [Singhal, 2003]. Therefore, both the theoretically deduced expressions in Equation 4–79 and Equation 4–80 as well as the experimentally obtained expressions in Equation 4–77 and Equation 4–78 are investigated. Fitting these equations to the experimental data is a mathematical problem with four degrees of freedom, since there are four constants which are to be determined (γ_a, γ_c, $E_{act,\,c}$, $E_{act,\,c}$). With this many degrees of freedom, several mathematical solutions may exist. In order to investigate the sensitivity of the problem, several estimations were performed with different initial guesses for the constants. However, the system proved to be rather stiff, and every estimation converged towards the same solution. Finally, an adequate fit was found using Equation 4–79 and Equation 4–80, employing the numerical values shown in Table 4.3.

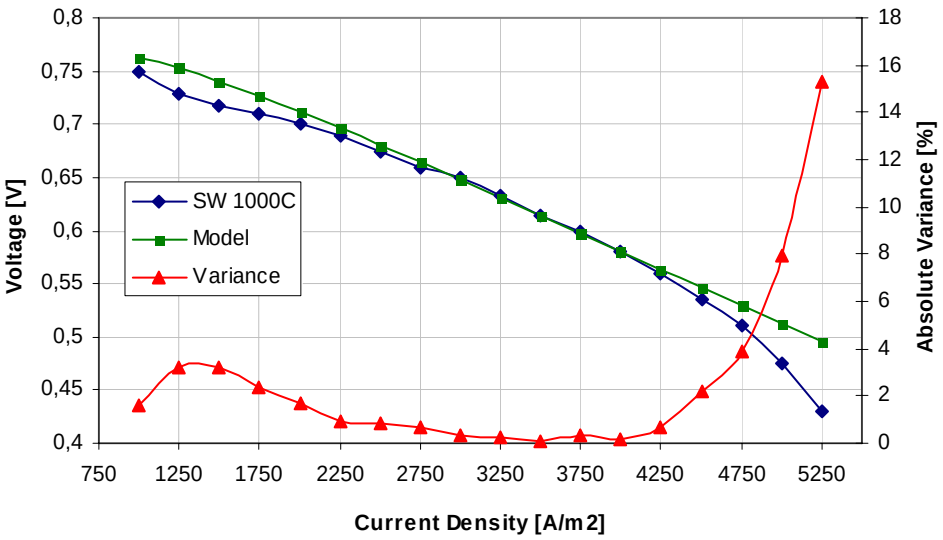

Figure 5-2. Comparison between measured voltage-current density characteristics of a tubular Siemens Westinghouse SOFC and predicted characteristics by the presented model at 1000 °C. The relative variance of the model is shown on the right axis.

Figure 5-2 shows a comparison between model-predicted and measured voltage-current density characteristics at 1000 °C. The relative variance in each point is shown on the right axis. From an analysis of the two plots, it can be seen that the model predicts a higher voltage for low current densities, although the variance is relatively small. Activation polarisation dominates for small current densities (See Figure 2-2 on page 9), and thus the overprediction of voltage may be caused from an underestimation of the activation polarisation loss in the model. In the domain where ohmic resistance dominates the fuel cell behaviour, (See Figure 2-2 on page 9) the model predicted curve lies above the measured curve. From the right axis we can see that the deviation between the two curves

is close to zero. At high current density, where diffusion resistance usually is the dominating loss mechanism, the model overpredicts the voltage by almost 16%. This large deviation may be caused by assuming the wrong material properties for the porous electrodes (Table 4.2). It may also be caused by the simplification of the fuel plenum geometry, which is described in Chapter 4.2. However, the mean relative variance between the model and the experimental results are 2.5% for the case shown in Figure 5-2, and this may be considered to be a good fit.

A comparison between model-predicted and measured voltage-current density characteristics at 900° C is shown in Figure 5-3. This figure indicates that the model overestimates the ohmic resistance, as the gradient of the model predicted curve is somewhat steeper than the measured. Considering the good fit in the ohmic regime in Figure 5-2, this indicates a divergency between actual temperature dependency of the material electric conductivities and the model equations given in Equation 4–27 to Equation 4–29. The deviation may also be caused from using Equation 4–30 to Equation 4–32 in the ohmic resistance calculation. In these equations it is assumed that ohmic resistance can be treated as uniform within a “slice” of the tube whereas electric conduction in the axial direction is neglected. A full 3D-calculation would be needed in order to check the validity of this assumption, and this is considered to be too computing intensive for the presented dynamic model.

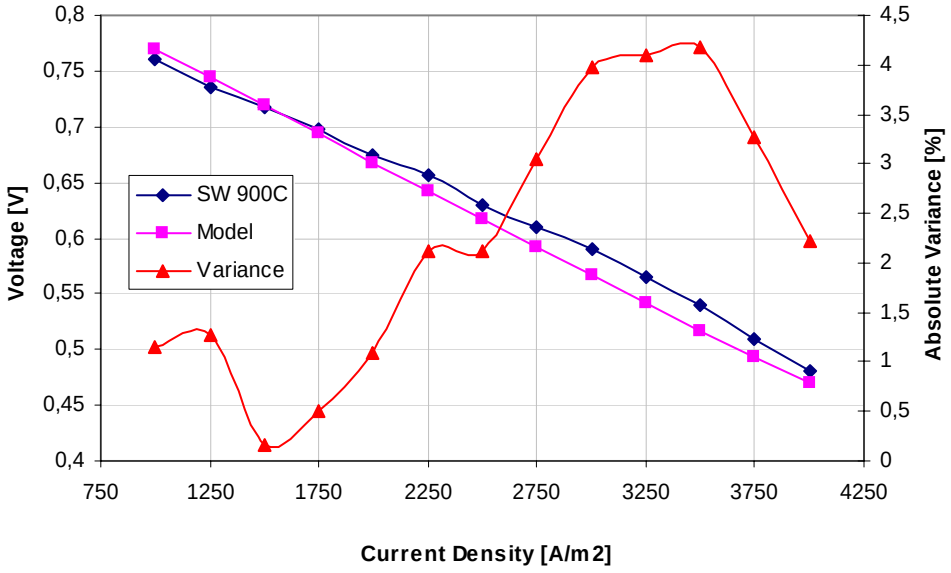

Figure 5-3. Comparison between measured voltage-current density characteristics of a tubular Siemens Westinghouse SOFC and predicted characteristics by the presented model at 900° C. The relative variance of the model is shown on the right axis.

The mean relative variance between the model-predicted voltage-current density and the experimental results are 2.3% at 900° C and 1.4% at 940° C. This gives a mean relative variance of 2.2% between the model and the experimental data between 900° C and

1000° C. Considering the fact that none of the cell parameters come from measurements of the actual fuel cell, a good agreement between the model and the experiment have been achieved.

5.2 Reference Case

The reference case for the dynamic and sensitivity studies is a quasi-optimized operational point of the system shown in Figure 5-4. In this system both the compressor and expander models are scaled to fit the chosen air flow of the fuel cell stack so that they both operate at design conditions at the reference point. The system as such is not optimized, and therefore it is referred to as “quasi-optimized”.

Relevant cycle data of the reference case is shown in Figure 5-4. Most of the values of the key parameters are similar to what can be found in the open literature [Rao, 2001], [Costamagna, 2001], [Kimijima, 2002], [Yi, 2003] and published data from Siemens Westinghouse. The system is based on the pressurised stack from Siemens Westinghouse which consists of 1152 fuel cell tubes. Pure methane is used as fuel and dry air at standard conditions is given as the entry for the compressor. The temperature distribution in the fuel cell is shown in Figure 5-5.

In the reference case it is assumed that the fuel can be sufficiently heated by anode exhaust gas recycling prior to entering the prereformer. The recycling ratio is adjusted to give a steam to carbon ratio of 2. The remaining heat needed to achieve 80% prereforming is supplied by radiation from the fuel cell tube. This rather high degree of prereforming is supported by [Song, 2004], and it will be shown later that this has a large influence of the temperature distribution within the fuel cell (Chapter 5.3.2). Air is preheated due to compression and by two heat exchangers; a recuperator and a tube-shell heat exchanger. In the recuperator, turbine exhaust heat is used to increase the temperature of the air, while the tube-shell heat exchanger uses heat from the combustion products. The fuel cell geometry also comprises internal air preheating. The compression pressure ratio is 3.2 and the speed of the shaft is 70.000 rpm. The turbine inlet temperature is 1162 K and the exhaust exits the system at 498 K. No district heating is considered.

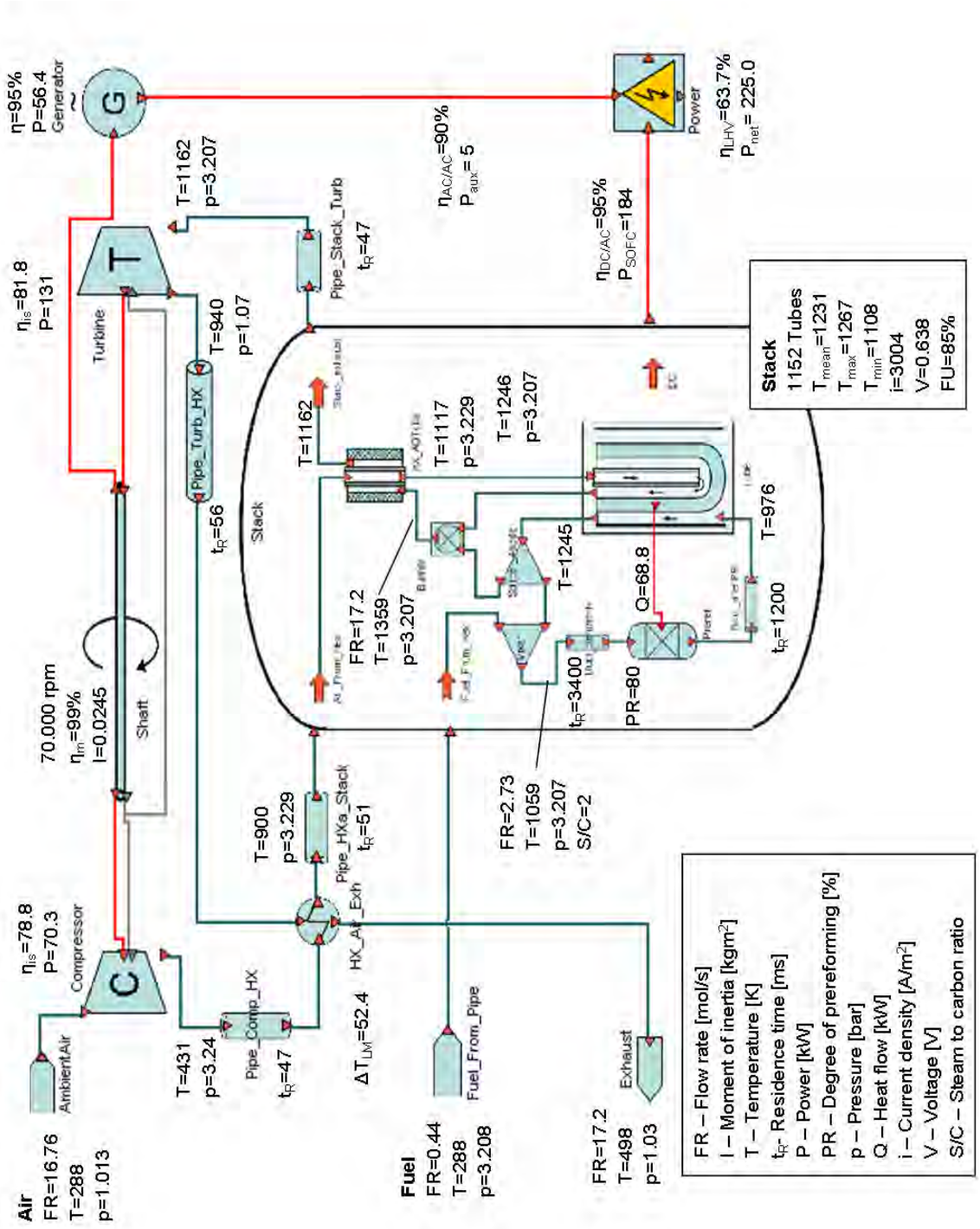

Figure 5-4. The SOFC/GT system used in the dynamic and sensitivity studies. The figure also shows the numerical values of some key operational parameters throughout the process.

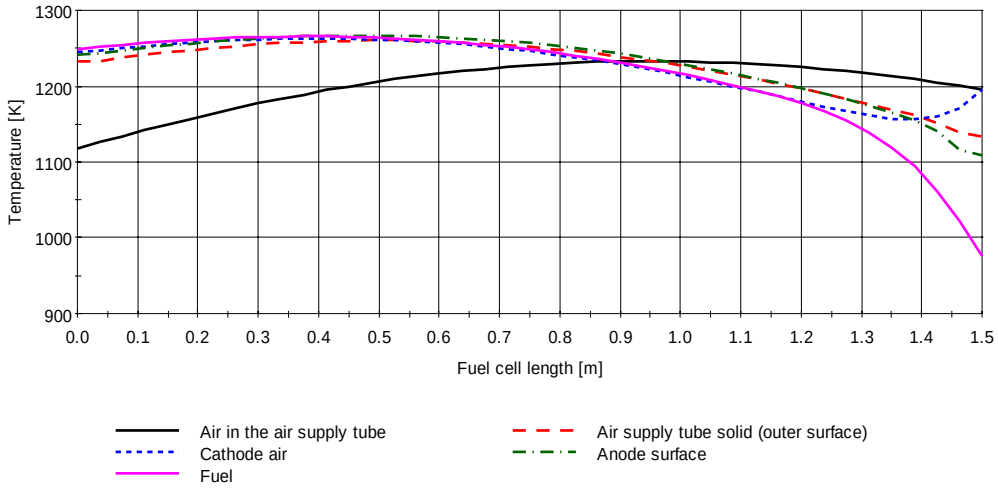

Figure 5-5. The temperature distribution along the fuel cell for the reference case. Cold air enters from the left, while fresh fuel is supplied from the right in the figure.

Power production for the reference case is 225 kW with a net electric efficiency of 63.7% (LHV). Of the total power, 75.6% is produced by the fuel cell stack and the rest by the gas turbine.

5.3 Parametric Study of the SOFC/GT Model

With a sensitivity study it is possible to identify the relative importance of system assumptions and input parameters, but sensitivity studies may also be used to assist hardware development by identifying research areas that yield the largest improvement for the least effort.

In the sensitivity study shown here, only one parameter is changed at the time while the rest are kept constant at their reference case values (Figure 5-4). This applies to both steady-state calculations and dynamic calculations. Load is changed by the same approach for all the dynamic studies, and it is performed simply by reducing the shaft speed of the gas turbine by 10%, while the fuel flow is reduced by 20% of their reference values, respectively. Both the shaft speed and the fuel flow are reduced over a period of 50s.

5.3.1 Sensitivity of Fuel Cell Parameters

Diffusion

Diffusion losses in the fuel cell are rather small for intermediate values of current densities (Chapter 2.1.1), but at high current densities they become increasingly important. Besides temperature and pressure, the magnitude of the diffusion losses depends on material data,

such as tortuosity, porosity and average pore radius. It is the intention of this sensitivity study to investigate the relative importance of the material parameters at normal operating conditions.

Equation 4–44 shows that the effective diffusion coefficient depends on the porosity and tortuosity, whereas the average pore radius influences the diffusion mechanism itself as well as the Knudsen diffusion coefficient (Equation 4–45 and Equation 4–65). A small pore radius leads to Knudsen diffusion controlled mechanism, whereas a large pore radius leads to an ordinary diffusion controlled mechanism. In this sensitivity study, the average pore radius has been varied between $5 \cdot 10^{-8}$ to $1 \cdot 10^{-4}$ m. These values represent the upper and lower limits to the transition regime controlled diffusion mechanism, which is described in Chapter 4.2.5. Above and below these values of the pore radius, the diffusion mechanisms are Knudsen- and ordinary diffusion controlled.

In the study, all operating parameters were kept at their reference case values, and the investigated parameters were varied one by one. Because the largest part of the diffusive losses are related to the anode, the cathode properties were kept constant during the analysis. In [Cussler, 1997] it is stated that the tortuosity of most materials is within the range of 2-6, and therefore this range was chosen for the presented sensitivity study. The porosity of the anode was varied between 20% and 70%.

Figure 5-6 shows the anodic diffusive loss distribution, in volts, for different values of porosity, average pore radius and tortuosity. The variation of the diffusion losses for the middle of the fuel cell (z = 0.75 m) are displayed in Figure 5-7. In this sensitivity study operating fuel cell voltage, mean temperature, temperature gradients and the fuel cell power remained fairly constant. Hence, their behaviour is not shown here.

Figure 5-6 shows that the magnitude of the diffusive losses is rather small compared to the operating voltage of the fuel cell for the given current density. From both Figure 5-6 and Figure 5-7 it can be seen that there is a linear relationship between the tortuosity and the diffusion losses. The figures also show that a 20% reduction in the porosity from the reference case increases the losses by 20%, but a 40% reduction in porosity increases the losses by more than 50%. Considering Figure 5-6, it seems that a larger porosity than 40-50% only leads to a minor reduction in the losses. The same effect can be seen for the average pore radius larger than $1 \cdot 10^{-6}$ m (reference case). However, reducing the pore radius by one order of magnitude from the reference case increases the loss by a factor of almost 5.

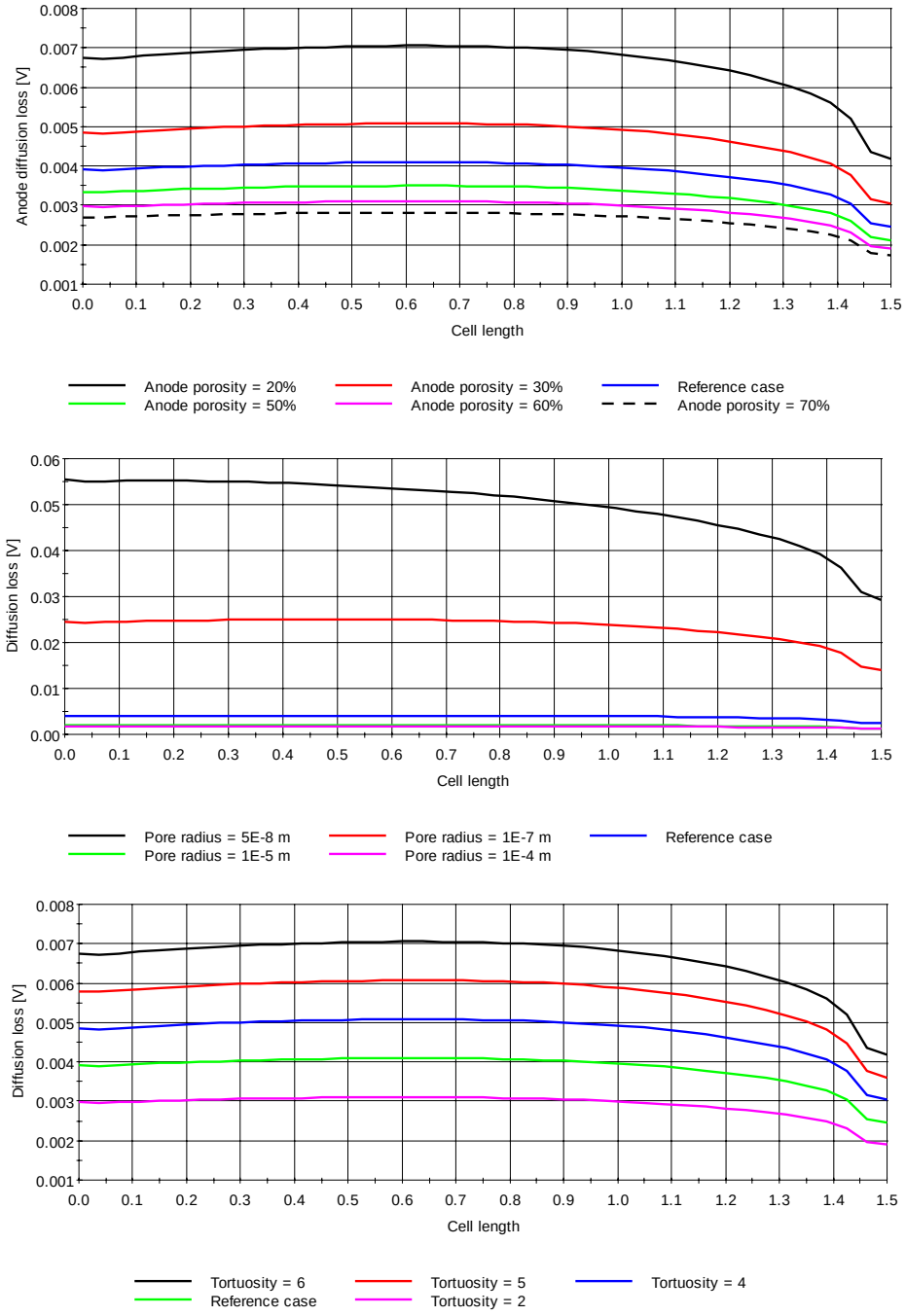

Figure 5-6. Diffusion loss sensitivity. Fuel and air enters from the right.

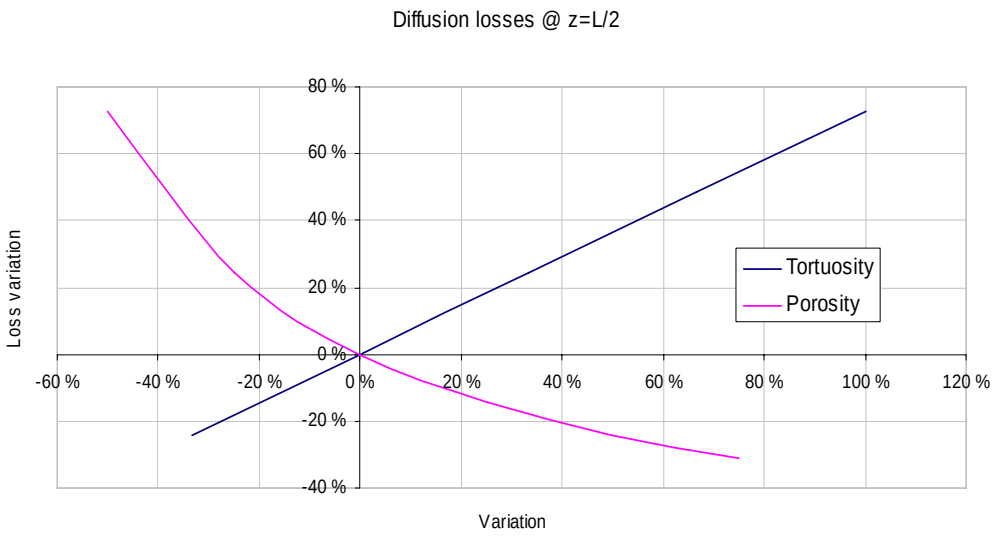

Figure 5-7. Diffusion loss sensitivity at z = L/2 for variations of tortuosity and porosity. Relative variance of tortuosity and porosity is shown on the x-axis, while the corresponding voltage loss variation is shown on the y-axis. (Reference Case: Tortuosity = 3, Porosity = 40%)

In general, the variations of tortuosity, average pore radius and porosity may lead to large relative changes in the diffusion losses, but at normal current densities the magnitude of the losses themselves are too small to affect the cell performance. A dynamic investigation of the diffusive losses will also show that the diffusive losses at the given current density only has a minor effect on the output of the fuel cell.

Activation Polarisation

As shown previously in Chapter 5.1, the values of the constants in the Butler-Volmer equation and the equation for the exchange current density were estimated in order to fit the presented mathematical model to experimental data from Siemens Westinghouse. However, without any detailed measurement of the activation polarisation itself, it is important to investigate the sensitivity of the two equations. Therefore a sensitivity study on the activation polarisation was performed by varying the constants used in Equation 4–69 (Butler-Volmer) and Equation 4–79 (Exchange current density). The reference case values of these constants are shown in Table 4.3.

From the Butler-Volmer equation it can be seen that the constant, β, mainly decides the relative importance of the anodic and cathodic terms. A glance at Equation 4–79 shows that β also decides the relationship between the exchange current density and the reacting species. A further investigation of Equation 4–79 shows that γ_a mainly decides the magnitude of the exchange current density and hence the magnitude of the activation polarisation loss. A large value of γ_a leads to a high exchange current density and thereby reduced loss. The last constant in the equation, which is the activation energy, $E_{act,a}$,

decides the temperature dependency of the exchange current density. A large value of $E_{act,a}$ implies a reduced temperature dependency and vice versa.

Cathodic activation polarisation loss usually dominates the overall activation polarisation losses of a SOFC, but in the presented model the relationship between anodic and cathodic activation polarisation loss can not be expected to represent a real fuel cell. This is a consequence of the activation polarisation parameter estimation being based on voltage current-density plots only. For this reason, and due to an interest in investigating the relationship between the β-parameter and the H_2- and H_2O-mole fractions with respect to activation polarisation, only the anode was considered in this sensitivity study.

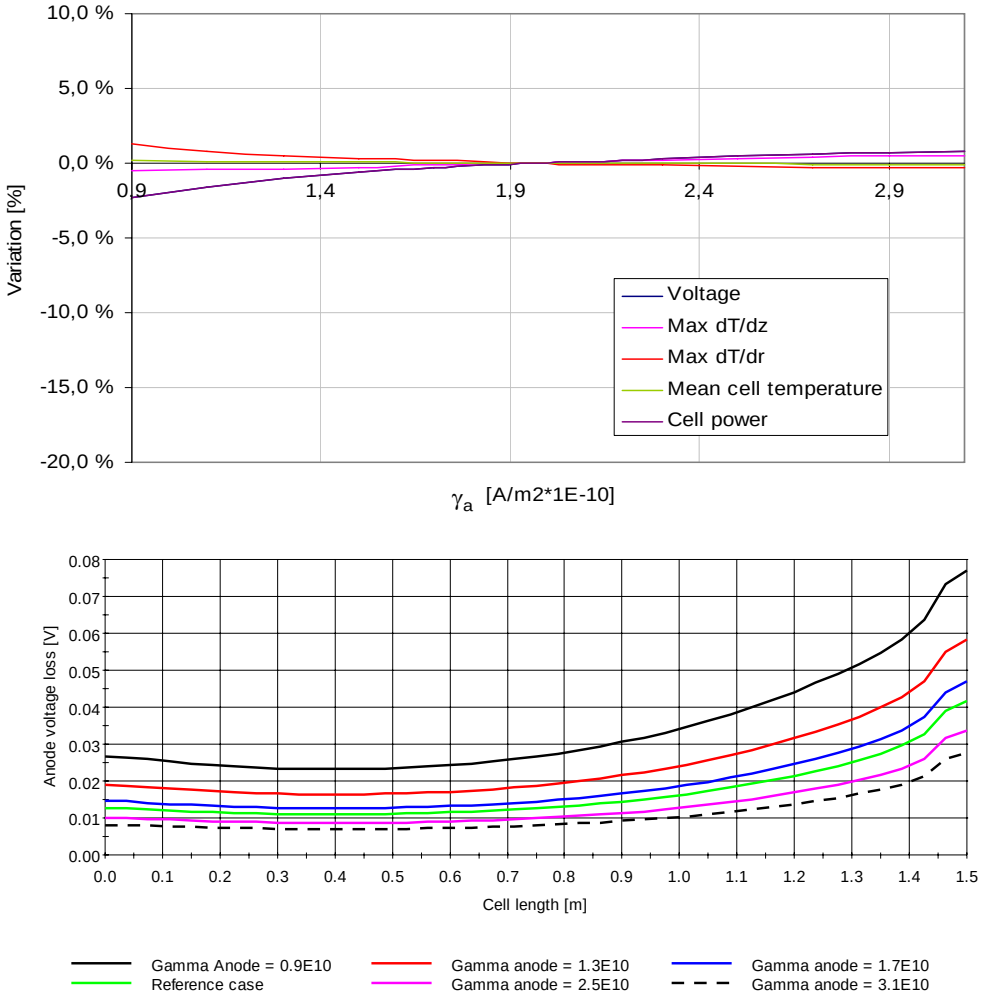

Figure 5-8. Results from the sensitivity study of γ_a. The chart on the top shows the relative variation of operating cell voltage, temperature gradients, mean cell temperature and power for variations of γ_a. (Fuel cell power and voltage lie on top of each other) The lower chart shows the activation polarisation loss distribution over the cell length for the same range of γ_a as in the upper chart.

The sensitivity study was performed under the same conditions as for the diffusion loss investigation. Operating cell voltage, temperature gradients, mean cell temperature, power and activation polarisation loss were considered to be the most important parameters with respect to the investigated equations. Their behaviour are shown in Figure 5-8, Figure 5-9 and Figure 5-11.

Figure 5-8 shows the results from the sensitivity analysis of γ_a. The chart on the top displays the relative variation of the operating cell voltage, temperature gradients, mean cell temperature and power for values of γ_a between $9 \cdot 10^9$ to $3.1 \cdot 10^{10}$. The resulting distribution of the activation polarisation voltage loss over the fuel cell length is shown in the chart below.

The chart in the top of Figure 5-8 shows that a reduction in γ_a by 50% only reduces the fuel cell power and the voltage by approximately 2%. The relative low influence of γ_a in the investigated range, may be explained by a relative low activation polarisation voltage loss when compared to the operating voltage (lower chart). Consequently, γ_a has an even lower impact on mean fuel cell temperature and the temperature gradients within the fuel cell solid. As already explained in Chapter 2.1.1 and Figure 2-2, the relative importance of activation polarisation will increase at lower current densities. Accordingly, the low relative influence of the parameter variations on the system can be said to be expected.

From the lower chart in Figure 5-8 it can also be seen that the relative shape of the activation polarisation curves remain almost unaffected by the variations of γ_a. This confirms the findings from the analysis of the Equation 4–79, which was performed prior to the sensitivity study.

Figure 5-9 shows the results from the sensitivity study of the activation energy, $E_{act,a}$, used in the calculation of the exchange current density. The upper chart shows that reducing the value of $E_{act,a}$ has little impact on the monitored parameters. Increased values of $E_{act,a}$, however, proves to have a large impact on for instance the power production, which is reduced by almost 19% when $E_{act,a}$ is increased by 21%. This can be explained by Equation 4–79, as a large value of $E_{act,a}$, leads to reduced exchange current density. This can also be seen from the lower chart, which displays the activation polarisation voltage loss distribution over the fuel cell length. From this chart it can be seen that the magnitude of the losses increases a lot when $E_{act,a}$ is increased from 140 to 170 kJ/mol.

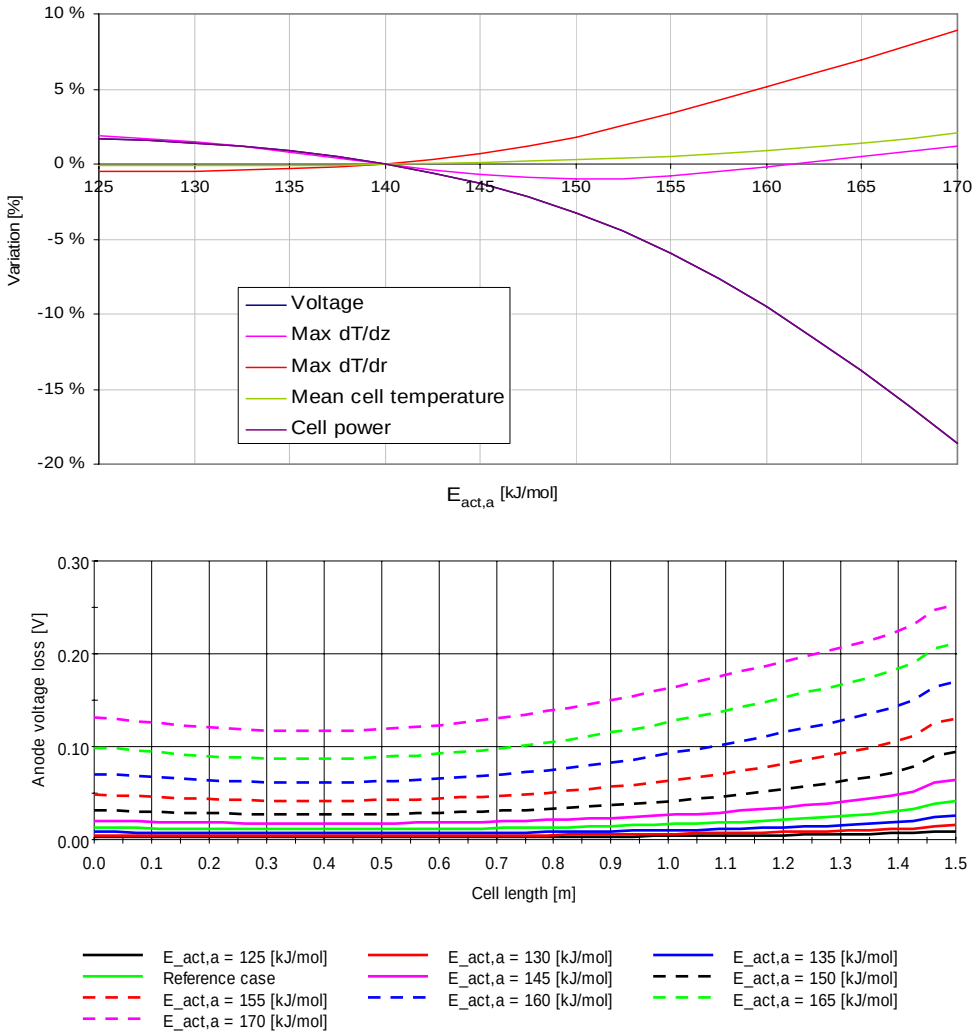

Figure 5-9. Sensitivity of $E_{act,a}$ towards the activation polarisation voltage loss. The upper chart shows the influence on voltage, temperature gradients, mean fuel cell temperature and fuel cell power, while the lower chart shows the influence on activation polarisation distribution. Due to current density being kept constant in the sensitivity study, voltage and power lie on top of each other in the upper chart.

The upper chart in Figure 5-9 also shows that the radial thermal gradient is sensitive towards $E_{act,a}$, especially when the value of this parameter is increased. When $E_{act,a}$ is increased from 140 to 170 kJ/mol, the maximum thermal gradient in the radial direction increases by almost 9%. To some extent, this behaviour can be explained by variations in the current density distribution, which is shown in Figure 5-10. From the figure it can be seen that a large value of $E_{act,a}$ implies a more uneven distribution of the current density. Due to the relationship between the heat production and current density, a more uneven distribution of the current density will lead to larger variations in local heat production. An investigation of the temperature gradient distribution in the fuel cell solid (not shown),

shows that the location of the maximum radial temperature gradient is found at the fuel entry for both small and large values of $E_{act,a}$. Considering the reduced current density at the fuel entry (Figure 5-10) for large values of $E_{act,a}$, and the fact that the strongly endothermic methane reforming reaction takes place at the same location, leads to the following possible explanation for the relationship between maximum radial temperature gradient and $E_{act,a}$; An increased value of $E_{act,a}$ leads to increased losses at the fuel entry of the fuel cell, and therewith reduced current density. This causes a reduction in the local heat production and more heat must be supplied trough the fuel cell solid material, either from downstream (axial direction) the fuel cell or from the hot cathode air (radial direction). Figure 5-9 shows that there is only a slight increase in the temperature gradients in the axial direction, and hence one can assume that most of the heat is supplied from the hot cathode air, i.e. radially through the cell material. This means that there must be an increased temperature gradient through the solid material in order to supply the requested amount of heat.

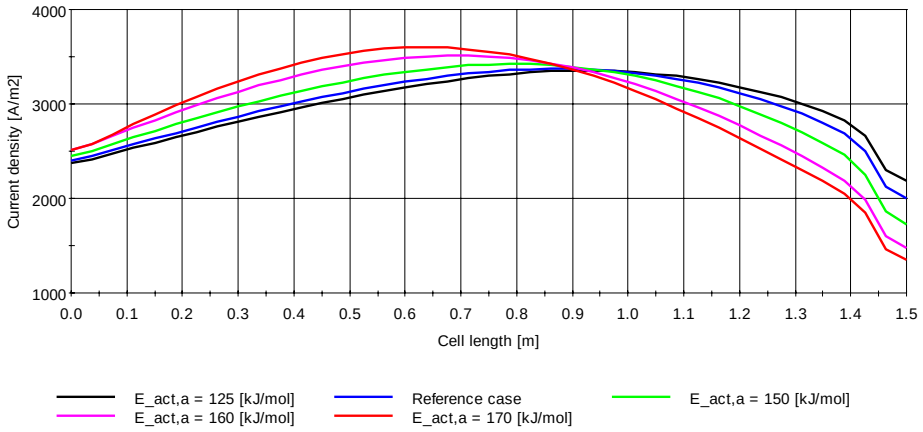

Figure 5-10. Current density distribution sensitivity versus the value of activation energy used in the exchange current density calculation.

As opposed to γ_a, which proved not to influence the activation polarisation distribution profile, the behaviour of $E_{act,a}$ may be explained by a stronger relation between the value of $E_{act,a}$ and the temperature. This connection between temperature and $E_{act,a}$ was predicted in the analysis of Equation 5-2. However, it is difficult to isolate the effect $E_{act,a}$ has on the temperature only through the presented numerical study, since changes in the activation polarisation distribution profile imply changes in current density distribution and hence also the temperature distribution itself.

This sensitivity study has indicated a temperature dependency between $E_{act,a}$ and the activation polarisation voltage loss, just as predicted by the equation analysis. The study has also shown that the magnitude of the activation polarisation voltage is sensitive towards $E_{act,a}$, and this may be explained by the fact that $E_{act,a}$ is used in an exponential term. Therefore a rather small variation in $E_{act,a}$ may lead to a large variation in the exchange current density.

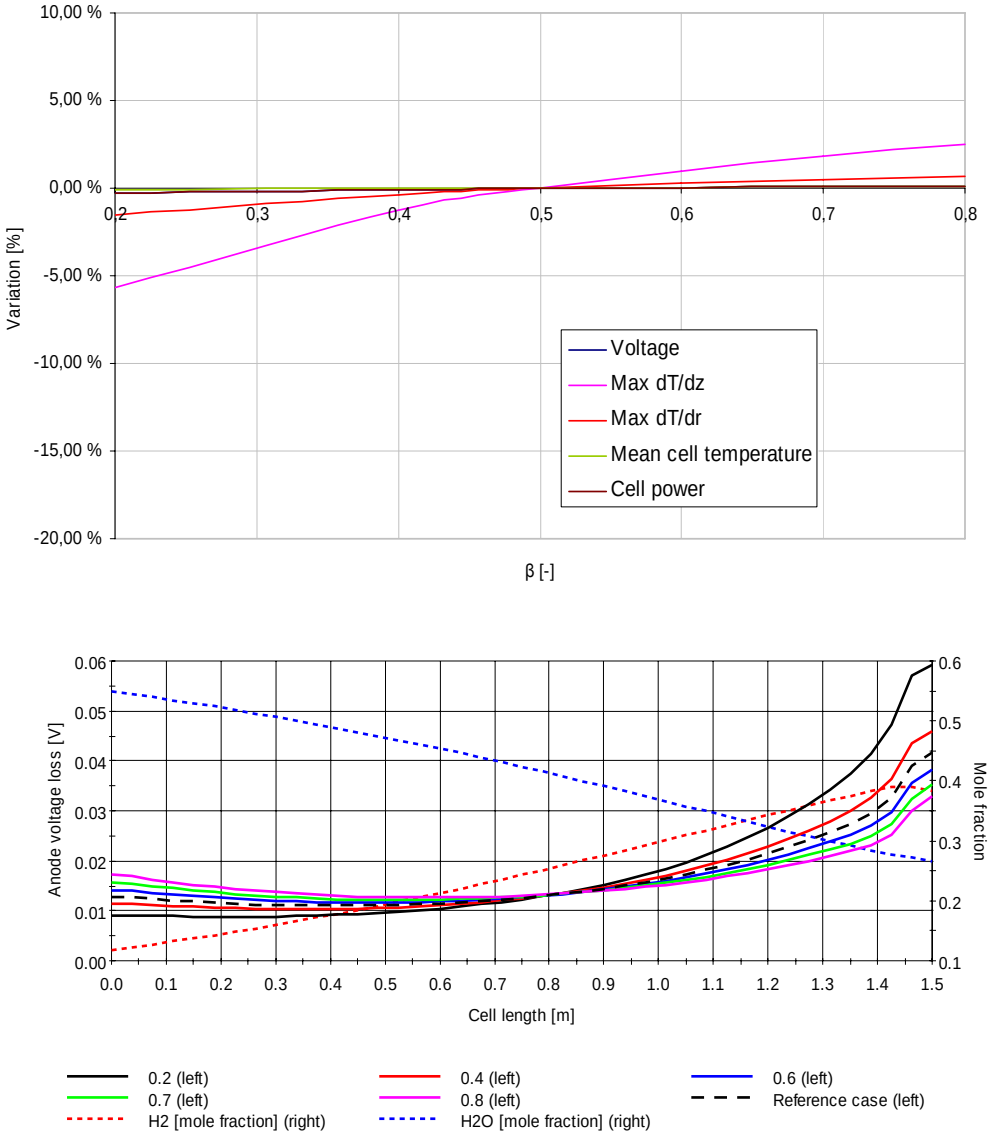

Figure 5-11. Results from the sensitivity study of β. The upper chart shows the relative variation of voltage, temperature gradients, mean fuel cell temperature and power. (Fuel cell power and voltage lie on top of each other). The lower chart shows the activation polarisation voltage loss distribution as well as the molar fraction distribution of H_2 and H_2O for the reference case. (The concentrations vary slightly with β, but for better readability, it is not shown here)

The initially performed equation analysis of the influence of β, with respect to the activation polarisation, predicted that β mainly would have an influence on the relationship between activation polarisation and the reacting species. Figure 5-11 verifies this prediction, as variations in β proves to change the activation polarisation distribution, according to the concentration of the reacting species. However, there seems to be an

inverse relationship between β and the concentration of the species, as a low value of β leads to a high influence of H_2 and vice versa for H_2O.

The upper chart in Figure 5-11 shows that the temperature gradients are influenced by variations of β, while the other parameters remain fairly unaffected. This may be explained by the relationship between β and the activation polarisation distribution. Since β mainly has an effect on the loss *distribution* and not the absolute value of the activation polarisation, mean fuel cell temperature, voltage and power production remain fairly constant despite the variations of β. It may therefore be concluded that β mainly has an influence on the distribution of the activation polarisation and not the magnitude. Hence system sensitivity towards this parameter is near to negligible.

Parameters Used in the Heat Transfer Calculation

In order to investigate the sensitivity of the temperature distribution of the cell, Nusselt numbers, radiative emissivity and heat conductivity have been investigated. The sensitivity study was performed according to the same procedure as described above.

The Nusselt numbers are used in the calculation of the convective heat transfer coefficients used in Equation 4–2, Equation 4–4 and Equation 4–6, and their numerical values have been found in [Rohsenow, 1998]. The sensitivity study showed that the value of the Nusselt numbers had a negligible effect on the power production of the fuel cell, but that they have a small influence on the temperature distribution. This means that a variation in the Nusselt numbers affect the location of the maximum and minimum temperatures, rather than the mean temperature of the fuel cell. The largest effect is seen on the temperature gradients in the axial direction. The dynamic studies showed that variations of the Nusselt numbers are negligible with respect to power relaxation time.

The sensitivity of the emissivities showed similar behaviour as for the Nusselt numbers, and variations of the emissivity lead to changes in the temperature profiles while the mean cell temperature was unaffected. One interesting finding was that very low values of the emissivity lead to increased outlet temperatures of the gases, and this again lead to increased turbine inlet temperatures and a load shift from the fuel cell to the gas turbine. The dynamic effect of variations of the emissivity was negligible.

Variations of the thermal conductivity proved only to have a small effect on the radial temperature profile of the fuel cell tube. Other effects could not be found neither for steady-state nor dynamic operation.

5.3.2 System Components and Operating Parameters

Degree of prereforming

There are two main reasons for investigating the sensitivity of the degree of prereforming on the system model. The first reason is the close thermal integration between the prereformer and the fuel cell, and the other reason is the strongly endothermic nature of the methane reforming reaction itself. A high degree of prereforming will require a larger

amount of heat supply from the fuel cell, and reduce the cooling effect on the first part of the fuel cell tube. A reduction in the degree of prereforming will lead to the opposite behaviour. This effect is clearly seen in Figure 5-12, which shows the anode surface temperature distribution for degrees of prereforming varying from 10% to 95%. It is worth noticing, that current density and steam to carbon ratio was kept constant during the calculations, while the voltage was allowed to vary in order to achieve 85% fuel utilisation.

The effect seen in Figure 5-12 can partly be explained by the voltage variation, as it is known that a higher voltage leads to a more even distribution of the electrochemical reaction and the therewith associated heat production [Rechenauer, 1992]. Recalling Equation 4–9, the heat supply from the fuel cell to the prereformer is modelled as radiation from the anode surface to the equilibrium temperature of the prereforming reactor. In the model, the degree of prereforming is controlled by the non-physical radiation shape factor between the anode surface and the prereformer. Changing the degree of prereforming is thus simply performed by adjusting this factor. A higher value of the shape factor leads to a higher degree of prereforming by increased heat radiation. Since the reactor is modelled as a CSTR Gibbs reactor, every spatial point on the anode surface radiates towards the same temperature. Due to the highly nonlinear nature of radiation, most heat is supplied from the points with the highest temperature. A higher degree of prereforming thus leads to a flatter axial temperature profile.

An interesting property revealed by the sensitivity study, is that the local temperature at 56 cm down the fuel cell tube seems to be unaffected by variations in the degree of prereforming (Figure 5-12). A closer investigation of this phenomenon shows that the temperature at this location varies only by a few Kelvin for different degrees of prereforming while the amount of radiative heat transfer varies heavily. The explanation for this phenomenon may rather be related to mathematics than to real physical behaviour. The prereformer is modelled as a CSTR Gibbs reactor with uniform temperature, and the temperature depends on the amount of heat radiation received from the fuel cell. Hence, a possible explanation for the phenomenon may be that the “turning point” represents a temperature close to the prereformer temperature for all values of prereforming. It may also be explained by a singularity in the SOFC/GT mathematical model, although this is complicated to prove mathematically.

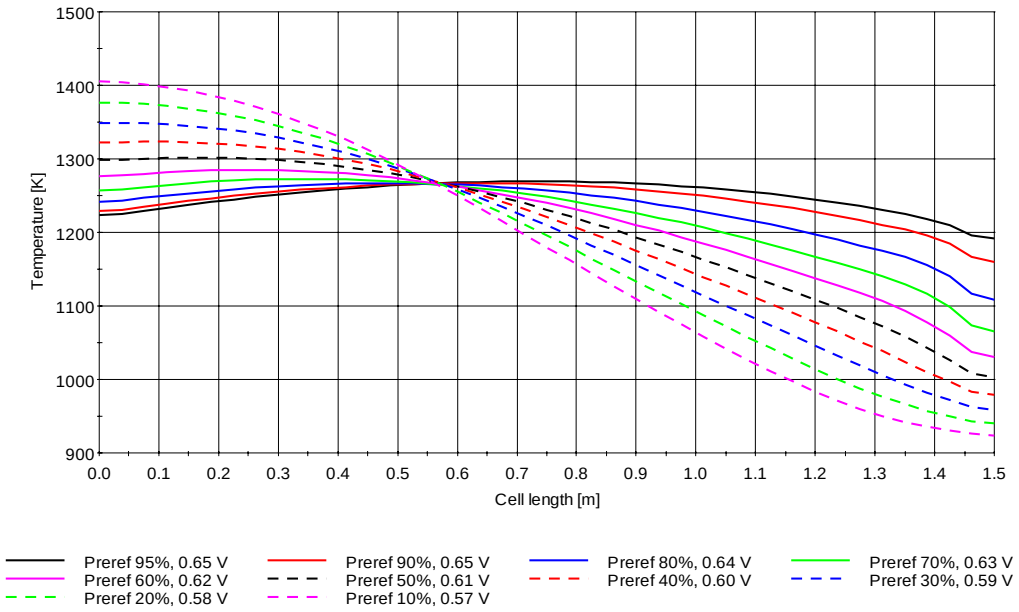

Figure 5-12. Temperature distribution of the anode surface when the degree of prereforming degree is varied between 95% and 10%. Current density is fixed, while voltage is varied during this study.

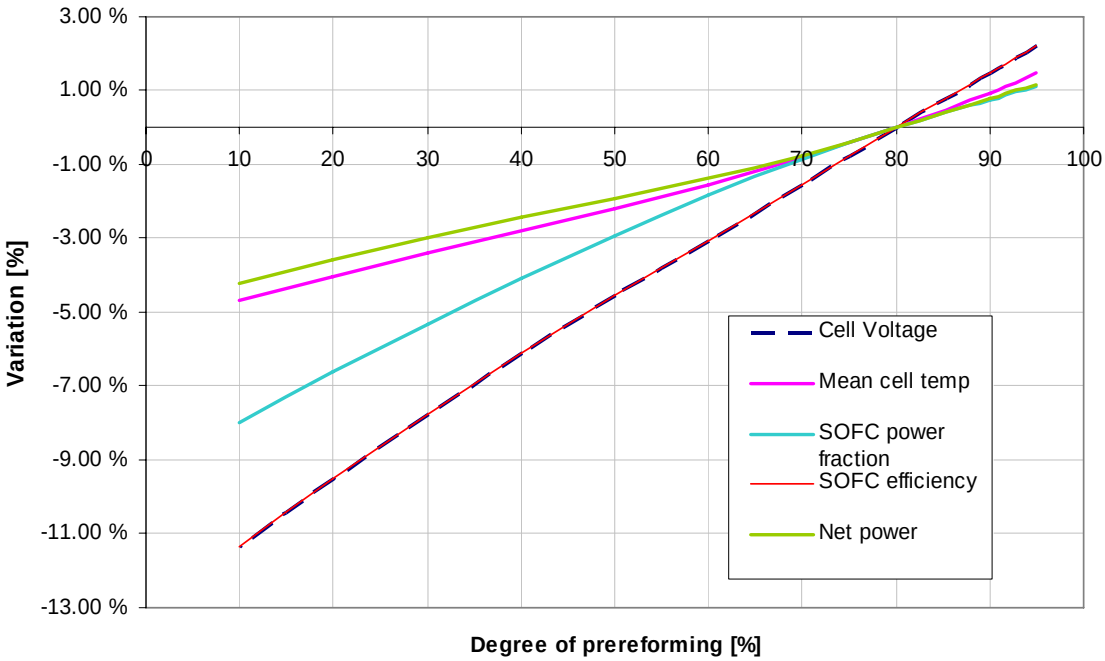

Figure 5-13. Influence of degree of prereforming on some key parameters.

Figure 5-13 shows the sensitivity of the degree of prereforming towards mean fuel cell temperature, cell voltage, cell efficiency, SOFC power fraction and the net power production. The figure shows that fuel cell power and fuel cell efficiency follow each other quite exactly, and this can be explained by the fact that both fuel utilisation and current density are kept constant during the study. It also shows that the mean fuel cell temperature decreases for lower degrees of prereforming. This indicates that the effect of cooling is superior when methane reforming occurs on the anode surface compared to when it occurs within the prereforming reactor. It may also partly be explained by radiation from the prereformer to the anode surface at high levels of prereforming, since this involves a higher prereformer temperature.

It is clear from the sensitivity study that the degree of prereforming has a great influence on the temperature distribution of the anode surface. Considering that the heat exchange between the prereformer and fuel cell mostly occurs due to radiation (which is highly nonlinear) a more detailed model should be developed to investigate this effect further. The development of such a model is not within the scope of this work, but based on the findings of the presented sensitivity analysis, Christoph Stiller has indeed expanded the presented system model by a spatially distributed indirect internal reformer (IIR). This IIR-model has been employed in the paper which is reproduced in Appendix F.

The sensitivity of the degree of prereforming has also been studied dynamically. In this study the shape factor between the fuel cell tube and the prereformer as well as the recycle ratio of the anode exhaust gases were kept constant. The sensitivity study of the dynamics was limited to the investigation of degrees of prereforming corresponding to 95%, 80% and 40% at the starting point. The load change was initiated after 2 seconds.

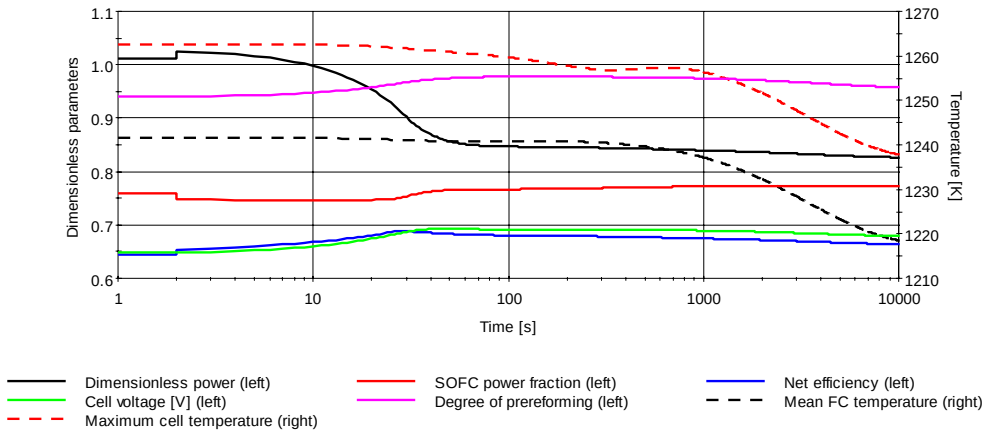

Figure 5-14. Dynamic behaviour for 95% prereforming.

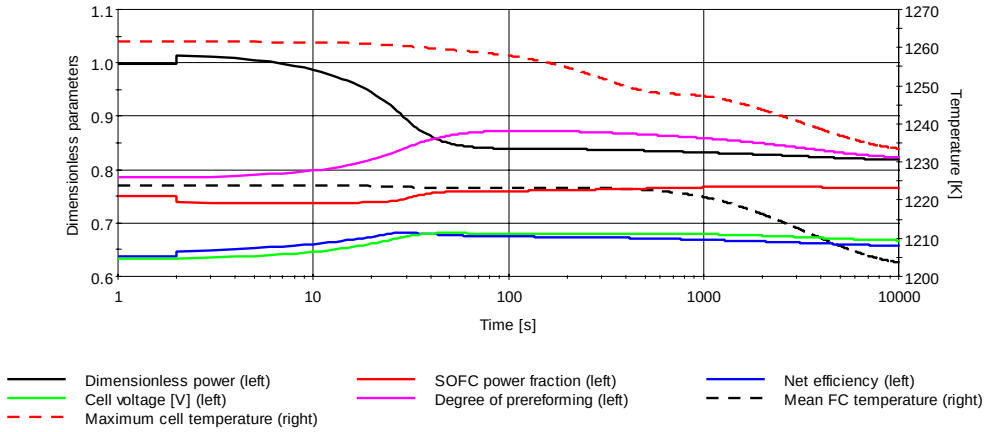

Figure 5-15. Dynamic response for 80% prereforming.

Figure 5-14 to Figure 5-16 shows the dynamic response when the degree of prereforming initially is set to 95%, 80% and 40% respectively. From the figures, it can be seen that power increases immediately after reducing the shaft speed. This can be explained by the fact that the generator is used to slow down the shaft speed. When decelerating, more load has to be put on the alternator, and hence the short increase in power production. The three cases also show the same behaviour with respect to the degree of prereforming, which increases shortly after the initiation of the load change. The largest change in the degree of prereforming can be seen for the case of 80% prereforming, whereas the smallest change is to be seen for the case of 40% prereforming. The figures also show a reduction in both mean and maximum cell temperatures after approximately 100s. This also causes a reduction in the degree of prereforming, as the heat flow from the fuel cell to the prereformer is reduced.

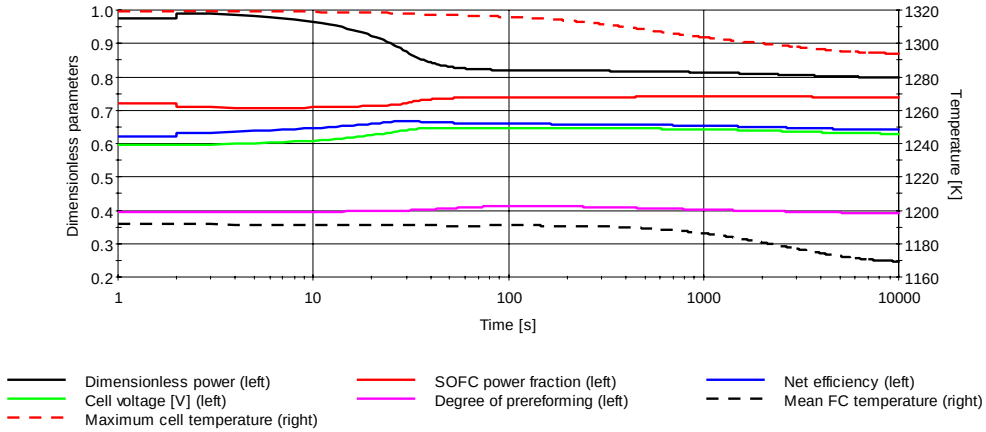

Figure 5-16. Dynamic response for 40% prereforming

A comparison of the three figures shows that the initial degree of prereforming has no influence on the relaxation time of the power production. However, the figures show that the degree of prereforming does have an influence on the variations in mean fuel cell temperature and degree of prereforming. Due to the connection between these two parameters, the largest variations in both parameters are seen for the same case (80% prereforming).

Ambient Temperature

Figure 5-17 shows the sensitivity of some key parameters towards the ambient temperature. In this calculation, all parameters were kept constant, except the ambient temperature. From the figure it can be seen that 15° C is the ambient temperature from the reference case. The percentual variations of the shown variables refer to the numerical values from the reference case (Figure 5-4).

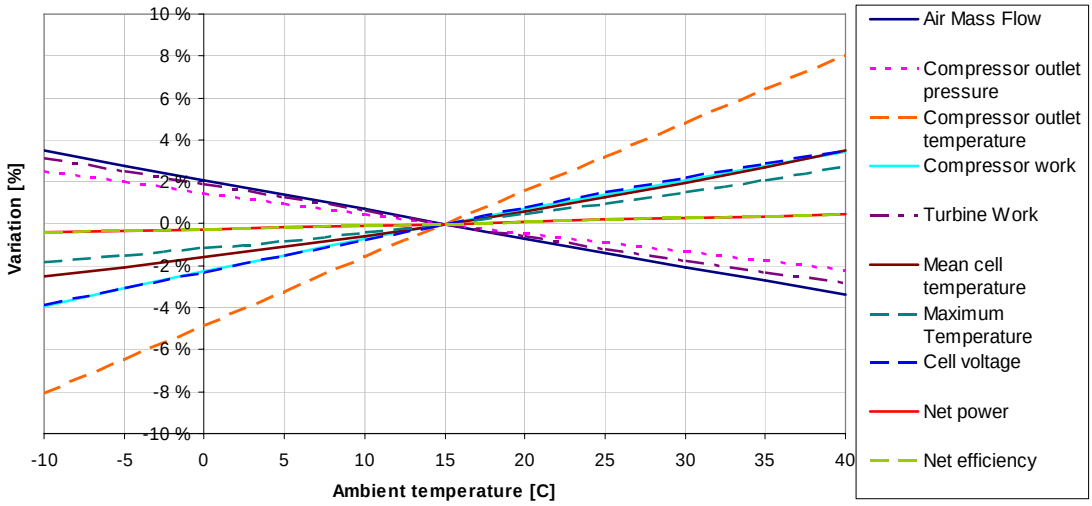

Figure 5-17. Parametric sensitivity towards ambient temperature

Figure 5-17 shows that the ambient temperature only has a minor influence on the net power output and the plant efficiency. The figure also shows that the compressor work decreases and the turbine work increases at lower temperature. This indicates a load shift from the stack to the gas turbine on temperature reductions. The effect is near to linear (on a percentual basis) within the tested area of ambient temperatures, and it can be seen that the opposite happens when the ambient temperature increases. Both the mean cell temperature and the maximum solid temperature is lowered by a few percent at reduced ambient temperatures. The temperatures stay within safe limits for the whole range.

The dynamic behaviour of the system was also tested with respect to the ambient temperature. For simplicity only the upper and lower ambient temperatures were tested (-10° C, 40° C), and they proved to have no effect on the dynamics of the system. It may therefore be concluded that the system is fairly insensitive towards variations in the

ambient temperature, both with respect to net power production and safety aspects related to temperatures and temperature gradients.

Recuperator Size

The size of the recuperator influences the amount of heat that can be transferred from the exhaust gas to the compressed air. A smaller recuperator leads to reduced heat exchange and vice versa. The SOFC/GT system sensitivity towards the size of this component was investigated by varying the heat transfer area of the recuperator from 30% to 200% relative to the reference case. Figure 5-18 shows the relative variation of cell voltage, net efficiency, stack inlet temperature, compressor outlet pressure and possibility of carbon deposition as a function of the relative size of the recuperator (x-axis).

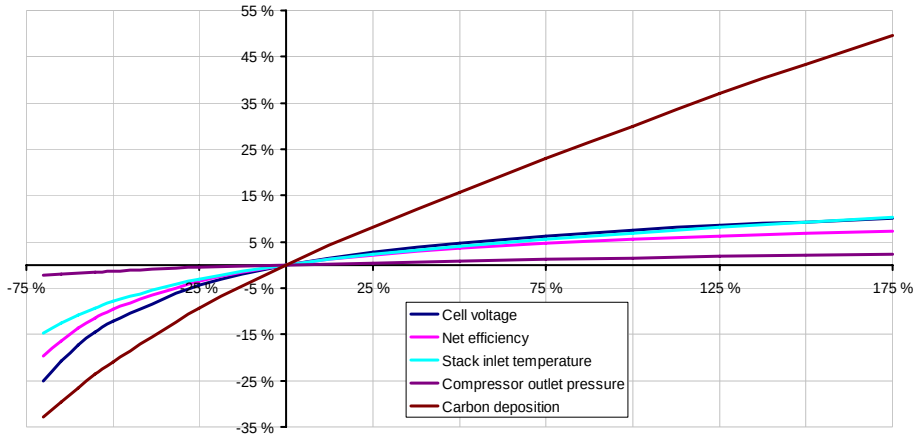

Figure 5-18. System sensitivity towards changes of the recuperator size.

The figure clearly shows that increased recuperator size leads to increased stack inlet temperature, and hence increased fuel cell voltage and efficiency. The figure also indicates that there is a near logarithmic relationship between recuperator size and system efficiency. An explanation for this behaviour may be a system efficiency dependency on recuperator efficiency, as recuperator efficiency is known to have a logarithmic relationship between size and efficiency [Mills, 1995]. However, the relationship is only *near* to logarithmic, due to increased efficiency in the stack and the gas turbine as well. Efficiency of the two latter components are not logarithmic with respect to temperature.

Figure 5-18 also shows that the possibility of carbon deposition varies with recuperator size, but this is most likely to caused by the effect the recuperator has on the gas temperatures. However, when considering the absolute value of the possibility of carbon deposition, it remains within safe limits for the whole range of variations.

The effect of recuperator size was also investigated in a dynamic study, where three cases with recuperator surface sizes of 50%, 100% and 200% with respect to the reference case were investigated. The load was changed by reducing the shaft speed by 20% and the fuel

flow by 40% from the reference case. The load reduction was performed over a period of 100 seconds and it corresponds to a load reduction by approximately 35%. The simulation was run for 15,000 seconds (real time).

The study showed that the time from load change to steady-state depends on the recuperator size. This may be explained by the fact that a smaller recuperator has less mass and thereby lower thermal inertia. Furthermore, reduced recuperator size means reduced gas residence time. Thus increased recuperator size leads to increased relaxation time. It was further found that the largest heat exchanger (200%) did not actually reach steady-state. This was for example seen by the stack inlet temperature, which continued to increase very slowly throughout the whole simulation. This effect may be explained from Figure 1 and Figure 2 in Appendix C, which show performance maps for a SOFC/GT cycle. These performance maps are calculated based on a specific system configuration, and the feasible operational range depends on recuperator size. Increasing the recuperator size might thus lead to either shifting the design point towards the left and closer to the border of unstable operation (no steady-state), or it may also lead to a reduction in the feasible operational range itself. In any case, a load reduction by the procedure described above leads to operation within the operational area where no steady-state exists.

One explanation may be that the recuperator is too large for the system at part load. The oversized recuperator means that the system can not get rid of heat surplus when operating at part load and the stack inlet temperature increases. A glance at the compressor and expander performance maps in Chapter 4.3, shows that enhanced turbine inlet temperature leads to reduced compressor mass flow. With reduced mass flow, residence time in the recuperator increases and hence more heat is transferred from the exhaust to the compressed air. Furthermore, fuel cell cooling is reduced and thereby the fuel cell temperature and hence TIT increase. This closes a reinforcing loop, where the stack inlet temperature continues to increase in an uncontrolled manner. Eventually components may melt and reactions between the different materials in the fuel cell may be initiated, and the system may be ruined.

The sensitivity study of the recuperator has shown that the recuperator size is important with respect to the fuel cell operating temperature and the system efficiency. It is further found that the recuperator size influences the relaxation time of the stack inlet, as increased size leads to increased relaxation time. The most interesting finding of this study is the devastating effect an oversized recuperator may have on part-load operation. If no measures, such as recuperator- or fuel cell bypass are undertaken, the system may be seriously damaged.

5.4 Conclusion

The validation of the SOFC model has shown that there is a good agreement between the experimentally obtained results and the calculations. A close investigation of the model output and the experiments has also shown that the model may overestimate the temperature dependency of ohmic resistance of the fuel cell materials, while diffusion losses are underestimated. However, a better agreement between the model and the

experimental results can be achieved if improved measurement data of the material properties were available.

The sensitivity study of the SOFC parameters has shown that the magnitude of activation polarisation voltage loss and diffusion loss depends strongly on the material properties, but that the relative magnitude of these losses with respect the operating voltage is too low to influence the system during normal operating conditions. The study has also shown that the Nusselt numbers, thermal conductivity and emissivity mainly have an influence on the temperature distribution within the fuel cell, and not the system performance itself.

The sensitivity study of the system parameters proved that the degree of prereforming has a large effect on the temperature distribution of the fuel cell and to some extent the system performance. It is suggested that a more detailed study should be performed with a more detailed prereformer model in order to increase understanding of this effect. The study of the ambient temperature showed an influence on the power production allocation between the fuel cell and the gas turbine, while the performance itself remained somewhat unaffected.

One of the most interesting findings in this study was that the recuperator size not only influences the performance of the system, but that a large recuperator may lead to unstable operation when at part-load. Hence, part-load investigation is of great importance when designing SOFC/GT-systems.

6 A Brief Analysis of Operational Limitations

Investigations of SOFC/GT systems by means of mathematical modelling can be very helpful in performance prediction and system design. However, an analysis is of no value, unless system restrictions or limitations are incorporated either in the mathematical model or discussed in the evaluation of the computational results. The aim of this chapter is therefore to establish a basis for the evaluation of the dynamic performance analysis presented in the next chapter.

6.1 SOFC Operational Limitations

The solid structure is often mentioned as a great advantage when the SOFC is compared to the other types of fuel cells. But although it facilitates an almost unlimited number of fuel cell geometries, the solid structure may also be a drawback with respect to operability. The materials with the foremost electrical and catalytic activity are often very brittle and hence handling and operation may be complicated. Investigations have shown that the performance and durability of the materials depends on the production method as well as the operating conditions [Jiang, 2004], [Yakabe, 2004]. The destructive mechanisms that occur within SOFCs can be divided into 3 groups, where either fuel composition, aging effects or temperature are the main cause of the malfunctions.

6.1.1 Fuel Composition Driven Failure Mechanisms

Within the group of fuel composition driven failure mechanisms, we find anode reoxidation, chemically induced stress, nickel poisoning and carbon deposition. Nickel poisoning may occur when the fuel cleaning system fails to remove sulphur-containing compounds. The consequence is an increased interphasial resistance between the anode and the electrolyte, which most often cause reduced operating voltage. However, the fuel cell may recover when exposed to a sulphur-clean and hydrogen rich gas [Singhal, 2003]. Carbon deposition may block active sites on the anode and also reduce the operating voltage, but it may also block the whole fuel channel and hence cause an emergency shut down. This effect is accounted for in the model and it has been discussed previously in Chapter 4.2.4. Avoidance of sulphur poisoning and carbon deposition may be achieved by a reliable fuel cleaning system and good control of the steam to carbon ratio in the fuel that enters the fuel cell, respectively.

Anode reoxidation may occur when oxygen is present in the anode or at very low H_2-partial pressure combined with high H_2O-partial pressure. The presence of oxygen may be a consequence of fuel supply failure, fuel backflow from the combustor or due to reversed operation of parts of the fuel cell (i.e. operating voltage higher than the local Nernst voltage [Gemmen, 2005]). The combination of low H_2-partial pressure and high H_2O-partial pressure may occur at high fuel utilisation, or it may be a consequence from a leakage. Anode reoxidation can cause serious damage to the fuel cell, as it is accompanied by a volume change which may either weaken the material or initiate material cracks [Jiang, 2004]. A study of the anode reoxidation has shown that the

magnitude of the volume change depends on the material porosity, grain size and impurity level [Waldbillig, 2005]. In the same study, it was also found that the kinetics of the reoxidation depends on the production methods and the temperature. The most obvious method for preventing reoxidation is to have complete control of the fuel composition distribution as well as the operating pressure. Implementing a non return valve between the ejector and the fuel cell may also reduce risk, but like any other component, it might experience malfunctions. (And due to the highly reducing atmosphere, it may be very expensive).

At elevated temperatures, some oxygen ion-conducting materials suffer from chemically induced stresses when exposed to gradients in oxygen activity. The effect can be explained by the formation of extra oxygen vacancies at reducing conditions. The structural change is accompanied by a change in volume and hence stresses are induced. For some materials, such as gadolinia-doped ceria oxide (CGO) electrolytes, chemically induced stresses may exceed the strength of the material [Atkinson, 2000]. It is therefore important to control the operating temperature and atmosphere in order to avoid mechanical failure for this type of electrodes.

6.1.2 Ageing Effects

Ageing effects on SOFCs are most often experienced as a reduction in operation voltage, which can be traced back to increased activation polarisation of the electrodes. For Ni-YSZ cermet anodes, this degradation mechanism is believed to be due to nickel agglomeration. Nickel is a high-surface-area solid and the wettability between Ni and YSZ is poor. Hence, there is a large driving force for the nickel particles to agglomerate, i.e. minimize the degree of free energy [Jiang, 2004]. The agglomeration of Ni-particles leads to changes in the micro structure, and therewith altering of material properties such as thermal expansion factor and catalytic activity. This implies that the agglomeration of Ni can lead to increased thermally induced stress and reduced methane reforming rate. The Ni agglomeration is also accompanied by reductions in both TPB length and electric conductivity, and consequently the activation polarisation voltage increases. The extent of nickel agglomeration can be reduced by tailoring the production method of the anode, and it is known that using mixtures of large and small sized YSZ particles can reduce the ageing effects [Tu, 2005]. It is also belived that loss of volatile nickel, such as nickel hydroxide, can contribute to the degradation of the anode. However, it has been found that the degradation kinetics depends on the operating conditions, as high current density, and high steam mole fraction (high fuel utilisation) can lead to a more rapid agglomeration of the Ni particles [Jiang, 2004].

Degradation of the cathode may appear either by the formation of isolating phases between the cathode and electrolyte or due to formation of pores at or in the vicinity of the TPB. The first mechanism is mostly due to the formation of $La_2Zr_2O_7$ and other insulating phases at the interphase, but it is mostly seen for temperatures exceeding 1200 °C [Minh, 1995]. Normally, SOFCs operate way below these temperatures, but local material temperatures may be close to this limit either during load change or part-load operation. The formation of pores in the cathode is known to mostly be a function of the

load, and hence high current densities may lead to increased rate of degradation [Jørgensen, 2000]. Due to the close connection between temperature and current density, the described mechanisms are most likely to have the largest effect at the location of the maximum temperature. Hence, good control of the temperature- and current density distribution is important in preventing the ageing effects.

6.1.3 Temperature Driven Failure Mechanisms

Temperature driven failure mechanisms are mostly related to thermally induced stress in the composite materials, which is caused by conflicting thermal expansion. Consequently, the relative importance of this type of stress depends on the initial structure and strength of the materials as well as the geometry [Atkinson, 2000]. A production method which requires a high temperature also makes the SOFC susceptible towards lower temperatures [Yakabe, 2004]. The sum of residual stresses from the production and thermally induced stresses may eventually prompt delamination or formation of cracks in the materials, and needless to say, this can be devastating for the SOFC. Despite the perception of the damaging effect from thermally induced stresses within the SOFC community, little effort has been put into investigation of these mechanisms. Considering the large effort invested in the search for new materials with improved electric/ionic- and electrocatalytic performance, it may seem as if material strength research is subordinate. Hence, there is little information to be found with respect to the connection between temperature distribution and thermally induced failure mechanisms. Results from the sparse literature there is to be found on thermal stress analysis, indicates that there is a strong connection between residual stress and thermally induced stress, with respect to the possibility of material failure [Nakajo, 2005], [Lowrie, 2000], [Atkinson, 2000]. Hence, the possibility of crack formation and delamination increases when residual stresses are high and the fuel cell is exposed to thermal cycling and large variations in the temperature distribution. Due to the great variety in SOFC materials, and hence material properties, it is difficult to calculate or predict temperature driven failure mechanisms, but knowledge about the temperature distribution may give indications to the overall likelihood of failure as well as the location at which they may occur. Measuring the temperature distribution is generally not feasible in practical applications, but measurements of the SOFC outlet temperature together with operating voltage and power may aid in estimating the temperature profile.

6.2 System Operation Limitations

6.2.1 BOP and Gas Turbine Limitations

The previous discussion has revealed the fragility of the SOFC with respect to operating conditions, but the surrounding system may also be subject to failure. Some of the components, like the prereformer, sulphur removal system and steam supply system are SOFC-supportive systems, and hence a failure in these components may lead to an even larger damage on the SOFC. However, these types of failure mechanisms are less probable in conventional systems and they will not be accounted for in the following analysis.

Malfunctions in gas turbines are generally connected to either fouling, excessive temperatures or compressor surge. The first failure mechanism depends on ambient conditions (land, sea, air) and power cycling, but in any case, it may be considered to be a slow mechanism and it will not be considered further in this discussion. Excessive temperatures may occur in case of uncontrolled fuel supply, and it is mostly a problem related to uncooled gas turbines. The consequence of high temperature exposure of the gas turbine may be increased creep rate and eventually fatigue failure. When used in combination with SOFCs it is therefore important to control the SOFC fuel utilisation, as it is inversely related to the combustor exit temperature. Compressor surge may occur either due to rotating stall or reduced mass flow, and it is mostly related to part-load operation [Saravanamuttoo, 2001]. This is also indicated by the compressor performance map shown previously in Figure 4-6, which shows that the feasible range of operation gets smaller at reduced mass flow rate. The effect of surge is a violent aerodynamic pulsation, which may be sufficiently strong to deform the compressor blades. The phenomenon can be explained by assuming the compressor operating at some point where a mass flow reduction leads to reduced compressor delivery pressure, but not necessarily sufficiently rapid downstream pressure reduction. Hence, mass will flow in the opposite direction until pressure is equalized between the compressor and the downstream components. Meanwhile, the pressure downstream falls leading the compressor to recover and the cycle will be repeated. Rotating stall may also contribute to surge, but it may also exist at nominally stable conditions. Rotating stall occurs when changes of flow incident angle causes aerodynamic stalling in a channel. The flow velocity within the stalled channel is decreased and hence the flow incident angle of the adjacent channels changes. Eventually, the stall is passed on to the next channel, opposite to the rotational direction, while the first channel is enabled to recover. Apart from surge, rotating stall may lead to aerodynamic vibrations which promote fatigue failure in other parts of the gas turbine. Compressor surge control is generally achieved by identification of the operational point in the performance map, and hence the distance, as pressure ratio, to the surge limit (often referred to as the surge margin). In case of operation close to or above the surge limit, measures such as blow-off (bleed) or reduction of the compressor inlet pressure by means of variable inlet guide vanes (VGV) can be taken in order to prevent surge.

Other parts of the system such as recuperator, piping, generator and power conditioner can be designed for a larger operational range than the fuel cell and the gas turbine. Hence the failure mechanisms of these components will not be considered in this analysis.

6.2.2 Feedback Loops and Possible Influence on System Operability

Designing a SOFC/GT system for maximum power and efficiency results in a high level of integration. One seeks to recover heat in heat exchangers, generate steam with waste heat or anode exhaust gas recycling or use excess heat from the fuel cell in fuel reforming. All these methods of efficiency improvement means implementing feedback loops. Dynamics of each single component may be known in advance, but the very presence of feedback loops may change system dynamics considerably. A feedback loop can be either balancing or reinforcing and the behaviour may change as a function of the operational mode. The first type of feedback loops tends to minimize the effect of an external

disturbance, and such feedback loops may be a great advantage with respect to system controllability. Modern nuclear power plants make use of such balancing feedback loops in order to increase system safety. On the other hand, reinforcing feedback loops may enhance the effect of external disturbances, and eventually lead to system run off. A good example of this phenomenon has already been shown in the sensitivity study of the heat exchanger size. Furthermore, an interesting effect can be seen if a balancing and a reinforcing loop with the same time constants act against each other, as this may cause system oscillations. Due to the destructive effects described above, identification of feedback loops can be of great importance with respect to control system design. In the following, possible feedback loops in the SOFC/GT system will be identified and their relative time constants will be discussed on behalf of a brief system analysis.

In Figure 6-1 six feedback loops are identified, and marked by green dashed circles. They are (1) recuperator, (2) air preheater, (3) air supply tube, (4) anode exhaust gas recycling (ejector), (5) gas turbine shaft and (6) radiation between the fuel cell stack and prereformer.

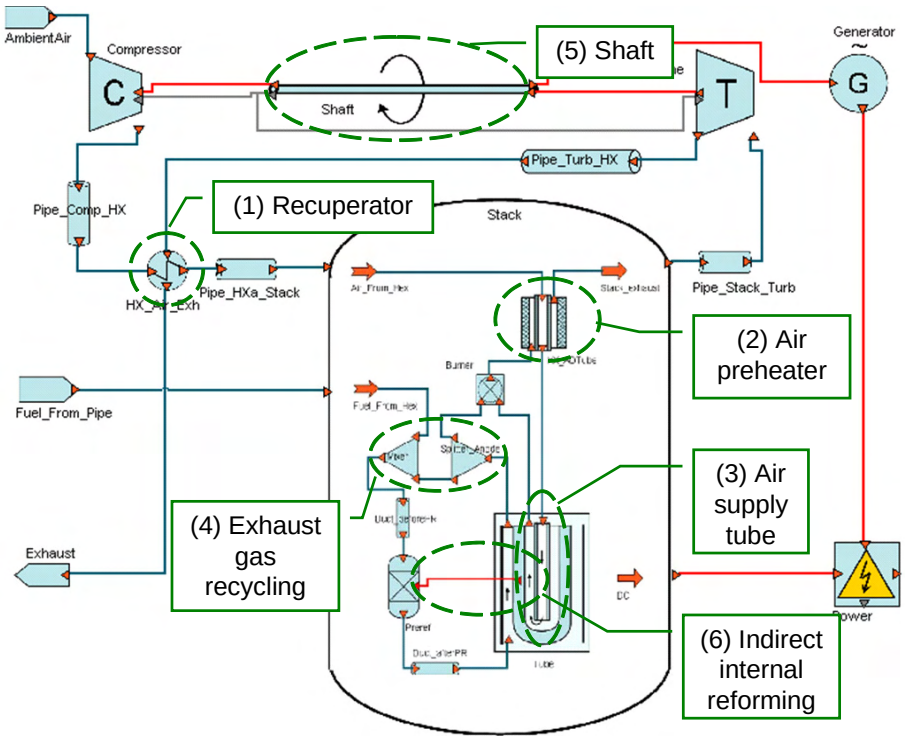

Figure 6-1. Identification of feedback loops in the hybrid system. The feedback loops are identified by dashed green circles.

(1) Recuperator

The purpose of the heat exchangers as well as the air supply tube is to preserve heat within the process in order to achieve a higher efficiency. This means that they connect the

temperature of a hot and cold stream. The effect of the recuperator is that the inlet temperature of the fuel cell stack will be affected by a change in the turbine outlet temperature (TOT) as well as a change in heat capacity (flow rate) of any of the streams. The time delay of this feedback loop is likely to be large as a change put on the cold stream will reach back to the recuperator only after passing through the whole system. Thermal inertia of the heat exchanger material will further delay and perhaps even smoothen temperature fluctuations. However, as shown previously in Chapter 5.3.2, the heat exchangers may form a reinforcing loop in combination with other system components.

(2) Air Preheater

The air preheater connects the hot burner exhaust with the recuperated air, and the effect of this loop is similar to that of the recuperator. It is also believed that this feedback loop can be important with respect to temperature fluctuation smoothening of the TIT. A previous paper (Appendix B) has shown that the burner exit temperature may temporarily increase by as much as 100K due to a load change, but this effect may be reduced by the air preheater. Hence, the effect of the air preheater is expected to mostly be balancing, and with a shorter time constant than that of the recuperator due to shorter residence time.

(3) Air Supply Tube

The air supply tube within the fuel cell facilitates fuel cell internal air preheating, and due to its counter current configuration, it may smoothen the temperature of the fuel cell. It also represents a short-cut with respect to heat transfer, as a temperature disturbance put on the inlet air to some extent may be directly transferred to the exiting cathode air. Hence, the air supply tube represents a balancing feedback loop with a time constant which depends on the air velocity.

(4) Anode Exhaust Gas Recycling

The anode exhaust gas recycling is implemented to ensure steam supply for the steam reforming of methane, which takes place in the prereformer and on the anode surface. This is a feedback loop with respect to fuel composition in addition to temperature and pressure. Compared to the feedback loop related to the heat exchangers, this feedback loop includes transmission of chemical energy in addition to heat. This feedback loop may be especially vulnerable towards fuel composition changes, due to the strongly endothermic nature of the steam reforming. Time delay of this feedback loop is believed to be short due to the low residence time and the direct mixing of fresh fuel and anode exhaust gas.

(5) Gas Turbine Shaft

The shaft connects the compressor and the expander, and thus it represents a feedback loop with respect to temperature and flow rate. However, since the shaft speed is assumed to be controlled by the generator in the presented model, the influence of this feedback loop can be neglected.

(6) Indirect Internal Reforming

The thermal connection between the fuel cell stack and the prereformer is implemented in order to supply the prereformer with an adequate amount of heat for the steam reforming to take place. This feedback loop connects the degree of prereforming and fuel temperature to the fuel cell temperature. Hence a change in composition, flow rate and temperature of the fuel entering the prereformer affects the temperature of the stack. The sensitivity study (Chapter 5.3.1) showed that there is a strong relationship between the degree of prereforming and fuel cell temperature, but thermal inertia of the fuel cell material will cause a relatively high time constant for this feedback loop.

6.3 Conclusion

With respect to SOFC operation limitations diversity in materials employed in SOFC applications and sparse information on the topic, makes it difficult to impose stringent operational limitations on the fuel cell. However, the brief analysis performed in this chapter may serve as a basis for the identification of the most substantial parameters with respect to malfunctions.

Figure 6-2 gives an overview of the malfunction mechanisms described in this chapter. These are displayed in the middle of the figure, while most important parameters with respect to failure are shown to the left. Finally, a set of control parameters are suggested on the right hand side of the figure. The figure shows that pressure monitoring is important with respect to minimize risk of compressor surge and rotating stall. However, this parameter must be combined with either TIT or shaft speed in order to give a reliable analysis of the surge risk. Figure 6-2 also shows that temperature is a very important parameter, due to its implication in most of the destructive mechanisms. Therefore, fuel cell temperature must be measured and/or controlled for any SOFC application. The direct measurement of this parameter is not practically feasible, but the close coupling between temperature distribution and voltage (or current density) may be used together with fuel cell gas outlet temperature or TOT measurements in order to indicate the SOFC internal temperature distribution. Records of temperature cycling data together with operation voltage and power measurements may also assist in estimating the current state of degradation. Fuel flow and fuel utilisation must also be measured and controlled in order to avoid SOFC material damage and excessive TIT. Fuel utilisation is not a direct control parameter, but it may be derived from the fuel flow and current as explained in Equation 4–20. It is further important to monitor pressure during transients in order to reduce the likelihood of backflow from the combustor to the fuel cell anode.

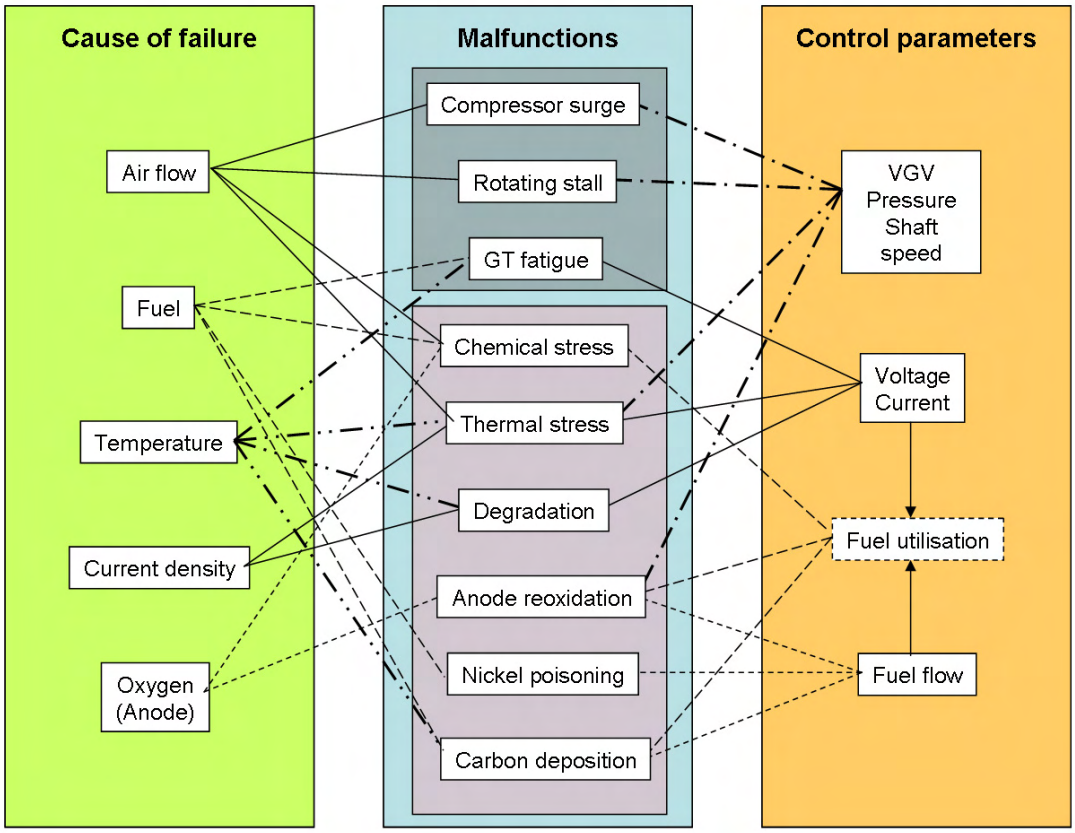

Figure 6-2. The relationship between system malfunctions, their cause and most important control parameters. Malfunctions related to the gas turbine are shown on the top, while the group below shows malfunctions related to the fuel cell.

Six feedback loops have been identified in the presented SOFC/GT system, but only five needs to be considered. The heat exchanger feedback loops (recuperator and air preheater) and prereformer-fuel-cell feedback loops are assumed to be associated with large time constants, while the anode exhaust gas recycling and air supply tube may have small time constants. The air supply tube and the air preheater feedback loops are assumed to mostly have balancing effects on system disturbances.

7 Dynamic Behaviour of a SOFC/GT Power Plant

For a controllable system, like the SOFC/GT-system, the free combination of control parameters represents a multitude of operational modes. Although several paths between operational points may lead to the same target, some of the paths may be more dangerous or quicker than the others. Some of the paths may also possess branches, thus the sequence of decisions taken at each crossing influences the final path. For the SOFC/GT system, this means that the load change strategy (path) as well as the sequential order in which the control parameters are changed is important with respect to safety and response time.

Performance maps for a fuel cell stack have previously been published by the author and his colleagues, and the full paper is reproduced in Appendix B. Performance maps for a SOFC/GT cycle have also been published and they are showed in Appendix C and Appendix F. Such maps may be very helpful in identifying promising load change strategies, but they can not be used to predict any transient effects as a consequence of the load change. Since the main intention of this work is to investigate *dynamic* system response, performance maps for the full cycle have not been developed for the system presented here. However, findings from the paper given in Appendix B have served as inspiration to propose three different load change strategies, which will be investigated in this chapter. The investigation is performed by changing load between 100% and 90% as well as between 100% and 50%. Thereafter, the system response is evaluated with respect to safety and applicability.

7.1 Strategies for Load Change

7.1.1 Three Paths to Load Change

In Chapter 6.1 it was found that the fuel cell operating temperature plays an important role with respect to both degradation and mechanical failure of the SOFC. It is further believed that power production of a SOFC is closely related to its operating temperature, and that the fuel cell materials posses a high thermal inertia. A load change strategy which aims at maintaining a constant mean temperature of the fuel cell membrane electrode assembly (MEA) is therefore suggested as a safe and possibly fast load change strategy. In order to meet this requirement it is necessary to control the air flow in addition to fuel flow and voltage/current. For the presented system, air flow control can be achieved by controlling the GT shaft speed by varying the load of the alternator. Variable shaft speed operation has further been found to be important with respect to part-load efficiency by several authors, i.e. [Campanari, 2000], [Costamagna, 2001], [Magistri, 2003] and [Chan, 2003b]. Other means, such as air blow off (bleed), stack air bypass and variable inlet guide vanes (VIGV) for the compressor may also be used to control the air flow rate. However, they are not considered here as it is not within the scope of this work. Another requirement with respect to safety revealed in Chapter 6.1 is the fuel utilisation, and hence a constant fuel utilisation of 85% (according to Equation 4–20) is assigned to this strategy. In the following discussion, this strategy will be referred to as the “mean fuel cell temperature”

strategy, although it is actually the mean temperature of the fuel cell MEA which is kept constant.

The second strategy which will be investigated is a strategy which aims at maintaining a constant turbine inlet temperature (TIT). In this strategy, fuel utilisation of the fuel cell is kept constant at 85%, while the GT shaft speed is controlled by the generator. In Chapter 6.2 it was found that the TIT has an influence on the GT degradation, and hence it is desired that this temperature remains fairly constant during operation. Operation at constant TIT is further beneficial with respect to GT efficiency, and similar strategies are often used in conventional GT control strategies. This part-load strategy is also proposed in the steady-state part-load investigation described in [Pålsson, 2001].

A further strategy for load change is simply to reduce fuel flow while maintaining a constant fuel utilisation and shaft speed. This strategy is proposed because many gas turbines and generators are designed to operate at a fixed speed which corresponds to the frequency of the electrical grid. This is also a rather simple strategy as it only implies fuel and voltage/current control.

For the two first strategies proposed above, a rather complicated control system is required in order to keep either TIT or mean fuel cell temperature constant at all times during the load change. In order to keep this analysis simple, only start and end point values of TIT and mean fuel cell temperature are identical in the proceeding calculations. Nevertheless, they will be referred to as the “constant TIT”-strategy and the “constant mean fuel cell temperature”-strategy in the following discussion. The strategy which implies fuel flow reduction at constant fuel utilisation and shaft speed will be referred to as the “constant shaft speed”-strategy.

7.1.2 Identification of Load-Lines

In order to change load according to the proposed strategies, it is important to identify so-called load-lines. The purpose of these lines is to connect the control parameters by means of an equation in order to make sure that the requirements of the strategy is fulfilled at any steady-state operational point above and below the reference case operational point. When calculating such load-lines the flexibility of gPROMS becomes apparent. Since it features an equation oriented solver, the only requirement for being able to run a computation is that the equation system is valid. In practice this means that any variable can be assigned a fixed value as long as the model is consistent. Hence, the load-line for constant mean fuel cell temperature strategy can be computed by assigning the reference case values to mean fuel cell temperature (MEA) and fuel utilisation and vary the shaft speed. Thereby the operational voltage, current, power, efficiency, fuel flow, etc. are calculated for any value of the shaft speed. The load-line for constant mean fuel cell temperature can then be estimated by curve-fitting an equation to the numerical results. Calculation of the load-lines for constant TIT and constant shaft speed can be performed according to the same procedure. In order to reduce calculation time, a steady-state version of the dynamic model was used in the load-line calculations for the presented analysis.

The load-line calculations were performed on a Toshiba Tecra M1 laptop with a 1.6 GHz Centrino processor with 1.5 Gb Ram. CPU-time of each calculation was approximately 5 minutes when calculating load-lines ranging from 100% to 30% load.

7.1.3 Evaluating Load Change Strategies

The three load change strategies proposed above will be investigated by four different scenarios, representing small and large load changes. The small load changes are investigated by changing load between the reference case, which represents 100% load and 90%. The large load changes are investigated by changing load between 100% and 50%. Prior to the evaluation and comparison of the different load change strategies, one example of the constant mean fuel cell temperature load change strategy will be presented and discussed with respect to system behaviour. This is then followed by a comparative study, which will be summarized in a discussion at the end of this chapter.

Time to steady-state as a consequence of a load change can be very large for SOFC/GT systems. However, power production can be very close to the target, long time before reaching steady-state. In many cases, being very close to the target suffices and thus a parameter named *power relaxation time* is defined. In this analysis, deviations between target and actual power of 2% have been considered to be a sufficiently good measure for the relaxation time. The mathematical expression for this criterion is given in Equation 7–1.

$$\left| \frac{P_{t = t_{Rel}} - P_{t = 0}}{P_{t = \infty} - P_{t = 0}} \right| \cdot 100\% = 2\% \qquad (7\text{–}1)$$

This definition facilitates comparison of load changes of same size, independent of their direction. This is opposed to if the relaxation time was defined relative to the total power. It also means that load changes of different size are not directly comparable, as the relaxation time criterion results in differences in the actual deviation from the target power. However, the main intention is to compare different load change strategies upon the same magnitude of load change, and for this the relaxation time criteria given in Equation 7–1 is well suited. The load change strategies will also be investigated with respect to safety, where findings from Chapter 6 serve as a basis for the evaluation.

The dynamic calculations were performed on the same computer as described above, and CPU-time of the calculations were 12 minutes or less when the calculations were run for 100000 seconds (~28 hours) with a real-time reporting interval of 5 seconds. Thus, calculation time was less than 1% of the calculated real-time.

7.2 Small Load Reduction at Constant Mean Fuel Cell Temperature

Some key parameters from a 10% load reduction calculation are shown as normalized parameters in Figure 7-1. The reference values for the normalization are the reference case values discussed in Chapter 5.2, and for better readability they are repeated in Table 7.1. The normalization of the parameters is conducted according to Equation 7–2.

$$\text{Normalized parameter} = \frac{\text{Actual value}}{\text{Reference value}} \qquad (7\text{–}2)$$

The load reduction is initiated after 20 seconds of steady-state operation at the reference case. The load shift is performed by changing fuel and shaft speed over a time period of 50 seconds, according to the load-line for constant mean fuel cell temperature for the small load change. The large load change is performed over a period of 85 seconds. It is important to notice that the load change is performed without utilising any type of sophisticated control systems. The load change is thus simply performed by adjusting the control parameters ramp-wise to the new operating condition.

Table 7.1: Reference values for the normalized parameters shown in Figure 7-1

Mean MEA temperature	1230 K
Fuel flow	0.44 mol/s
Shaft speed	70000 rpm
Net power	225 kW
TIT	1162 K
Air flow	16.8 mol/s
Turbine inlet pressure	3.2 bar
Degree of prereforming	80%

From Figure 7-1 it can be seen that the condition of constant mean fuel cell temperature (MEA) is almost fulfilled during the whole load change, as there is only a negligible and temporary temperature increase some time after the load change. From the figure it can also be seen that there is a sudden increase in power at the very moment the load change is started. This is caused by using the generator to reduce shaft speed, and hence the sudden power increase corresponds to the breaking energy absorbed by the generator. For the case shown here, the sudden power increase is 1.3%, and the duration is 10 seconds.

When considering the normalized power curve shown in Figure 7-1, it can be seen that most of the power reduction is achieved within the period of fuel and shaft speed reduction. The power relaxation time according to Equation 7–1 is 430 seconds (7.2 min.), and in the figure it is indicated by a dashed vertical line. A further investigation of the figure shows that there is only a slight reduction in TIT (1.6%), and that the corresponding relaxation time is the same as for the power. It may also be seen that pressure and air flow stabilizes approximately at the same time as power.

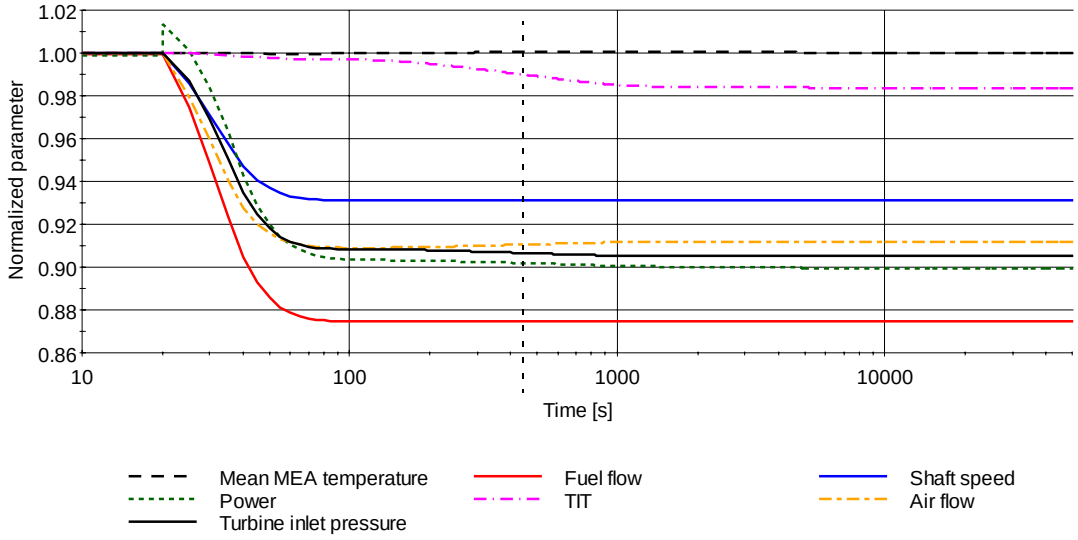

Figure 7-1. Normalized key parameters when changing load from 100% to 90% at constant mean fuel cell temperature.

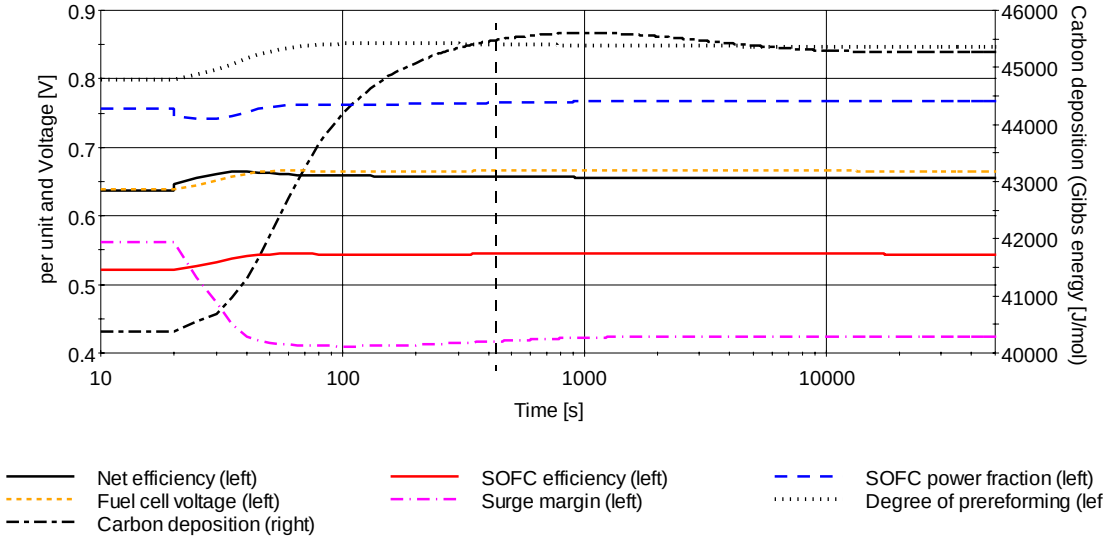

Figure 7-2. Key parameters with respect to efficiency and safety when applying the constant mean fuel cell temperature strategy to a 10% load reduction.

Key parameters, such as net efficiency and SOFC efficiency, SOFC power fraction, fuel cell voltage, degree of prereforming, surge margin and Gibbs free energy for the overall carbon deposition reaction are shown in Figure 7-2. The latter parameter in the plot is the minimum value occurring within the fuel cell, and recalling Chapter 4.2.4, the Gibbs free energy has to be negative for the spontaneous reaction to occur. The SOFC power fraction

parameter is defined as the power contribution of the fuel cell stack to the overall power production.

From Figure 7-2 it can be seen that the net efficiency is slightly higher at the new steady state (1.8 percentage points). With respect to transient effects of efficiency one should keep in mind that efficiency is calculated on behalf of an input-output analysis, which disregards any transient effects. Hence moment of inertia of the shaft speed, thermal inertia and gas residence time represent errors with respect to the efficiency calculation. Nevertheless, investigations of the transient effects on efficiency may be useful in the interpretation of the other parameters. In the example shown here, moment of inertia of the gas turbine shaft may be the reason for the short drop in the SOFC power fraction seen in Figure 7-2. This finding is supported by a comparison of the system and SOFC efficiencies, which shows that there is a peak in the system efficiency, but not the SOFC efficiency during the same time period.

The degree of prereforming (Figure 7-2) increases from 80% to 85% from the reference case to the new steady-state. It can also be seen that the largest part of the change occurs at the same time as the fuel reduction, i.e. the first 50 seconds after the load change. There is also a transient maximum around 1000s. Considering the fact that the mean fuel cell temperature is kept constant, the most likely explanation for the increase seen here is the fuel reduction. Thereby less heat is needed in order to achieve the same degree of prereforming, but since the fuel cell temperature remains constant the degree of prereforming increases. The transient maximum of the degree of prereforming may be explained by the slightly enhanced mean fuel cell temperature during the transient, which is seen in Figure 7-1.

Operation safety is represented in Figure 7-2 by Gibbs free energy for carbon deposition and the surge margin. The curve representing the first parameter shows that the probability of carbon deposition is reduced both during and after the load change, but the probability of surge increases. Starting from 56%, the surge margin is steadily reduced to 41% during the shaft speed reduction. Thereafter it increases slowly to its steady-state value which is 42%. However, the distance to surge is still large, and the probability of surge can be considered to be negligible. From a comparison of Figure 7-1 and Figure 7-2, it can be seen that time to steady-state for the surge margin corresponds very well with TIT, turbine inlet pressure and air mass flow. The reason for the very long time to steady-state seen here may be found in the upper chart in Figure 7-3 which shows snapshots of the anode surface temperature prior to, during and after the load change. The figure shows a temperature reduction at the fuel exit and that this part of the fuel cell cools down very slowly. The fuel exit temperature of the fuel cell influences the TIT, and thus also the turbine power. Hence, a large relaxation time of the fuel cell exhaust implies a large relaxation time for the power.

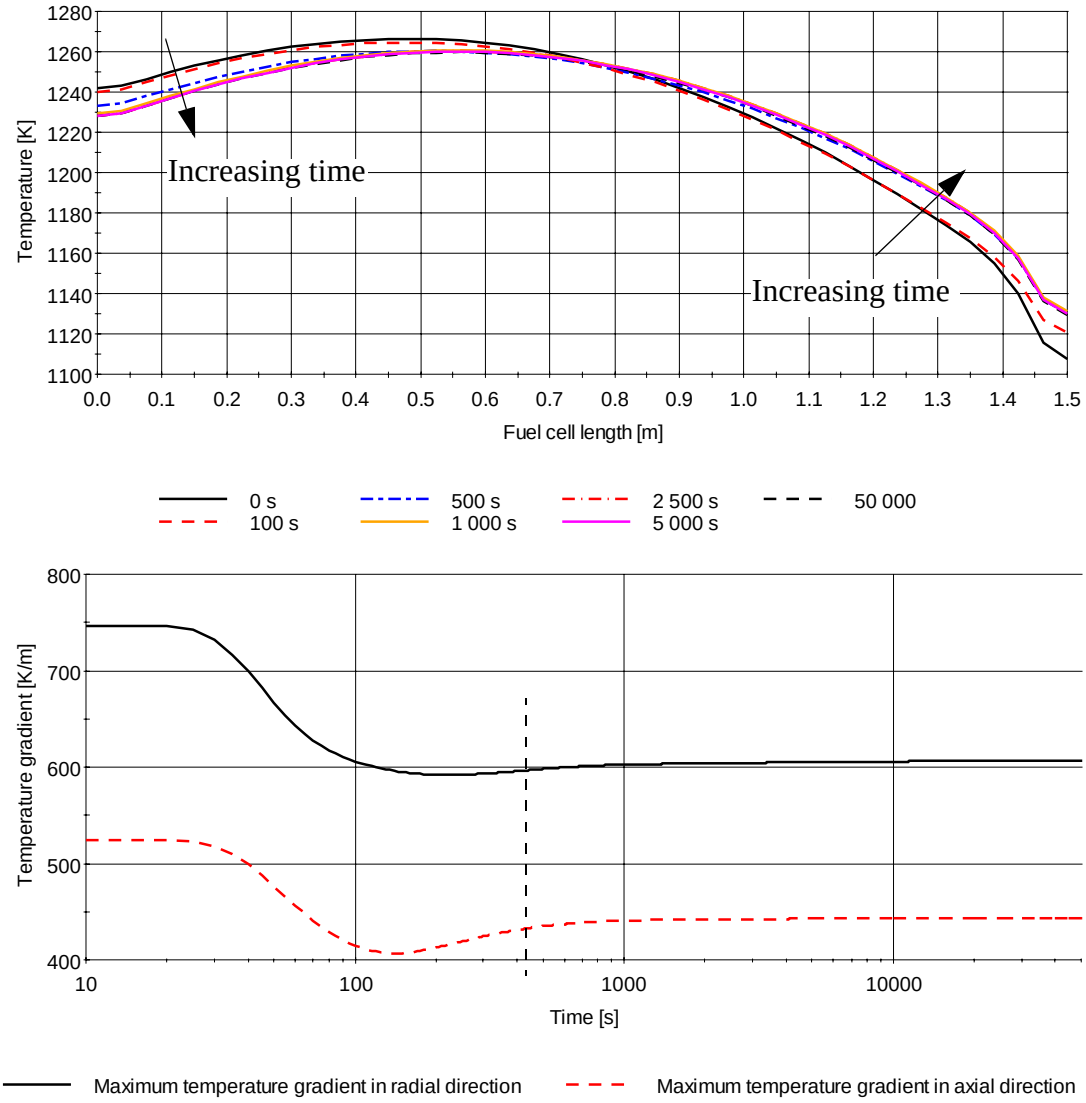

Figure 7-3. Snapshots of the anode temperature profile (top) and maximum temperature gradients (bottom). The times referred to in the upper chart legend indicate the time of the snapshot relative to the x-axis in the lower chart. The fuel inlet is at the bottom of the tube.

The upper chart in Figure 7-3 shows that the part-load temperature profile is flatter than for the reference case, and that most of the change occurs within the first 480 seconds after the load change. This corresponds very well with the power relaxation time seen in Figure 7-1. The flattening of the temperature profile indicates reduced thermal gradients and hence reduced thermal stress. This is also confirmed by the lower chart of the figure, which shows the maximum temperature gradients occurring within the MEA. In fact, the maximum radial temperature gradient is reduced by almost 150 K/m. The reduction in the maximum axial temperature gradient is somewhat lower, but the initial value of this gradient is far less than for the radial direction. The lower chart also shows that both the

radial and axial temperature gradients reach a temporarily minimum in the first period after the load change. In this case, it may be caused by the rapid increase in degree of prereforming, which is caused by the fuel flow reduction. This causes the temperature at the inlet to rise quicker than for the rest of the tube, and hence there is a temporary minimum in the maximal temperature gradients. This type of behaviour can be expected in any device where a hot and cold fluid flows through. If the inlet temperature or mass flow of any of the streams is changed, there will be a temperature front moving in the flow direction until a new steady state condition has been reached. However, a general consideration of Figure 7-3 indicates that despite the relatively quick load change, there is little risk with respect to thermally induced cracking or delamination for the case shown here.

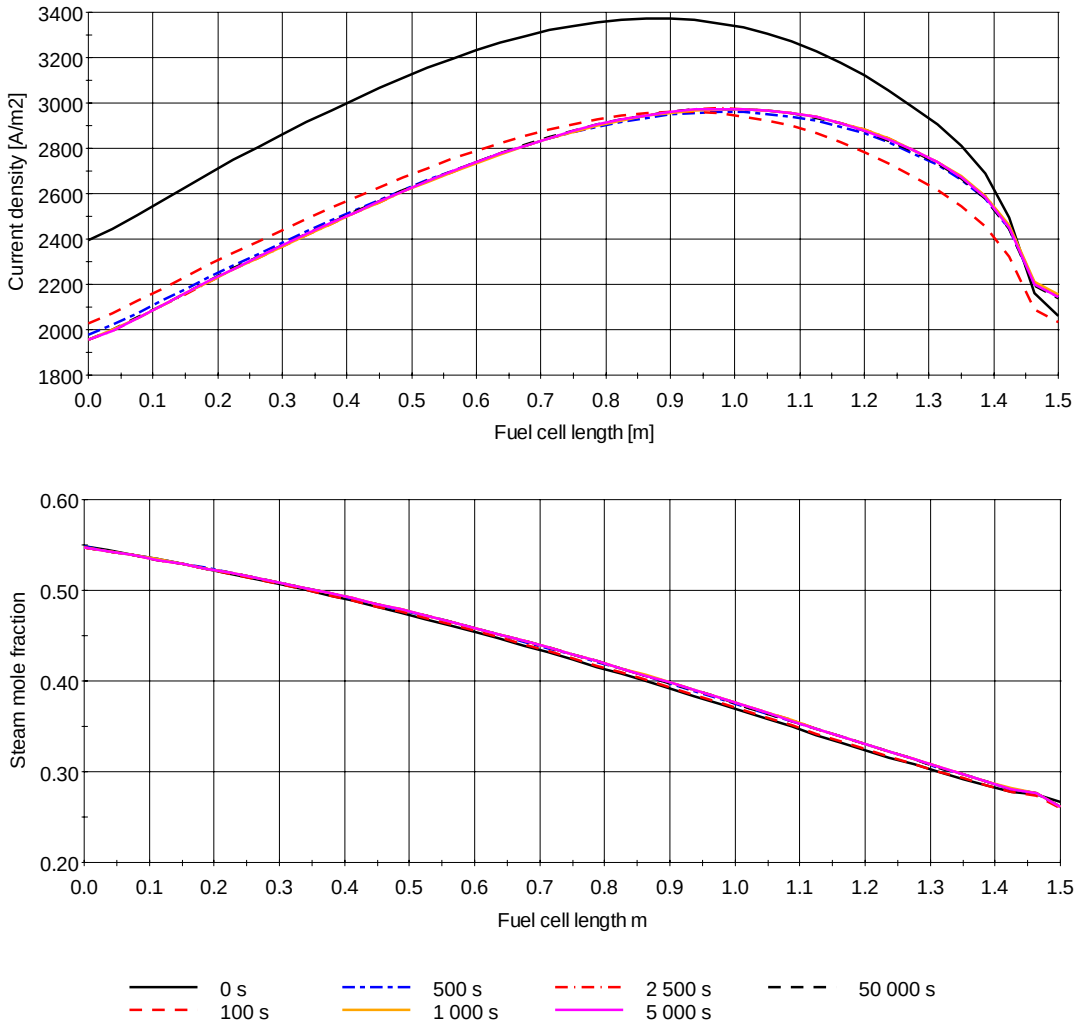

Figure 7-4. Snapshots of the current density profile (top) and steam mole fraction during a load change from 100% to 90% when applying the constant fuel cell temperature strategy.

In Figure 7-4 the upper chart shows snapshots of the current density profile at the same times as for the temperature distribution. The figure shows that already after 100 seconds (80 s after load change) the current density profile is very close to steady-state. At 500 seconds the current density profile is at its steady-state condition, and as seen for the temperature profile, this corresponds very well with the power relaxation time.

The reference case current density profile (0s) shown at the top in Figure 7-4 shows that current density is unevenly distributed and varies between 2100 A/m^2 and 3400 A/m^2. When considering the ageing mechanisms described in Chapter 6.1.2, this implies a more rapid degradation of the electrodes at the location of the maximum current density (fuel cell length = 0.9 m) for the reference case. At part-load, the maximum current density shifts towards the fuel inlet (1.0 m) and at the same time the overall current density is reduced. From the lower chart in Figure 7-4 it can be seen that the steam mole fraction distribution remains fairly constant throughout the load change. Thus, it can be seen that the maximum current density shifts to an area with reduced steam mole fraction at part-load. In combination with the overall reduction in current density, this means that degradation due to nickel agglomeration in the anode and pore formation in the cathode is reduced at part-load.

The reduction in current density leads to less internal heat generation. Thus maintaining a constant mean fuel cell temperature implies balancing the cooling effects from the air flow and prereformer against the internal heat generation. This is indeed what is achieved by the constant mean fuel cell temperature strategy, since this strategy results in reduced air flow, increased stack inlet temperature and reduced cooling by the prereformer. The reason for the increased stack inlet temperature can be found in Figure 7-1. Here it can be seen that the turbine inlet pressure is reduced, thereby causing an increase in TOT. Due to the recuperator, the increased TOT causes the stack air inlet temperature to increase. Furthermore, residence time in the recuperator is increased as a consequence of the reduced air flow, hence facilitating even better heat recovery. When considering the feedback loops shown in Figure 6-1, it can be assumed that the load-line for the constant mean fuel cell temperature strategy represent a combination of the control parameters at which all the feedback loops, except the shaft (which is controlled), have a balancing effect upon the load change with respect to the mean fuel cell temperature.

7.3 Comparison of the Three Load Change Strategies

7.3.1 Reducing Load from 100% to 90%

Figure 7-5 shows normalized plots of mean MEA temperature, fuel flow, shaft speed, power, TIT, turbine inlet pressure and air flow versus time for a load reduction from 100% down to 90%. Results from the constant mean fuel cell temperature strategy are shown at the top (a), the constant TIT strategy in the middle (b) and the constant shaft speed is shown at the bottom (c). The power relaxation times are indicated by a black dashed line. From a first look at the charts, it can be seen that the lowest power relaxation time is found for the constant mean fuel cell temperature strategy. When comparing the power relaxation time from this strategy (430 s) with the two others, it can be seen that the

constant mean fuel cell temperature strategy is 14 times faster than the constant shaft speed strategy (6140 s) and almost 21 times faster than the constant TIT strategy (10795 s). The numerical results of the relaxation time calculations are also shown in Table 7.2. A further investigation of the two slowest strategies reveals that the power reduction proceeds according to two different mechanisms. The first mechanism is the reduction of fuel (and shaft speed in the case of constant TIT). This leads to a 12% and 4% power reduction within the first 80 seconds after the load change for the case of constant TIT and constant shaft speed, respectively. The second mechanism is the temperature adjustment which influences the fuel cell internal loss. This can be seen by the fact that power relaxation times are the same as the relaxation time of their respective mean MEA temperatures. It may therefore be assumed that the power relaxation time depends on the heat capacity of the MEA and the air supply tube as well as the magnitude of the mean temperature change of the materials. However, this is only part of the explanation since the fuel cell also incorporates a balancing thermal feedback loop. The feedback loop is the air supply tube which is identified as number 3 in Figure 6-1, and the balancing effect is due to the counter-current flow configuration and the thermal short cut. Thus, the reason for the substantial relaxation times is due to the combined effect of the material heat capacity and the air supply tube balancing feedback loop. The fact that the relaxation time for the constant TIT strategy is more than one hour longer than that of the constant shaft speed strategy, despite the almost identical changes in mean fuel cell temperature, may be explained by the differences in air mass flow. When the constant shaft speed strategy is applied to the load change, air mass flow increases (Figure 7-5) and thus heat transfer is improved. The opposite occurs when the constant TIT strategy is applied, and hence a higher relaxation time may be expected due to the reduced heat transfer. Although a large part of the relaxation time may be attributed to the heat capacity and the balancing feedback loop of the fuel cell, one must not forget that residence time in the piping system and heat exchangers as well as thermal inertia of the heat exchangers also play an important role.

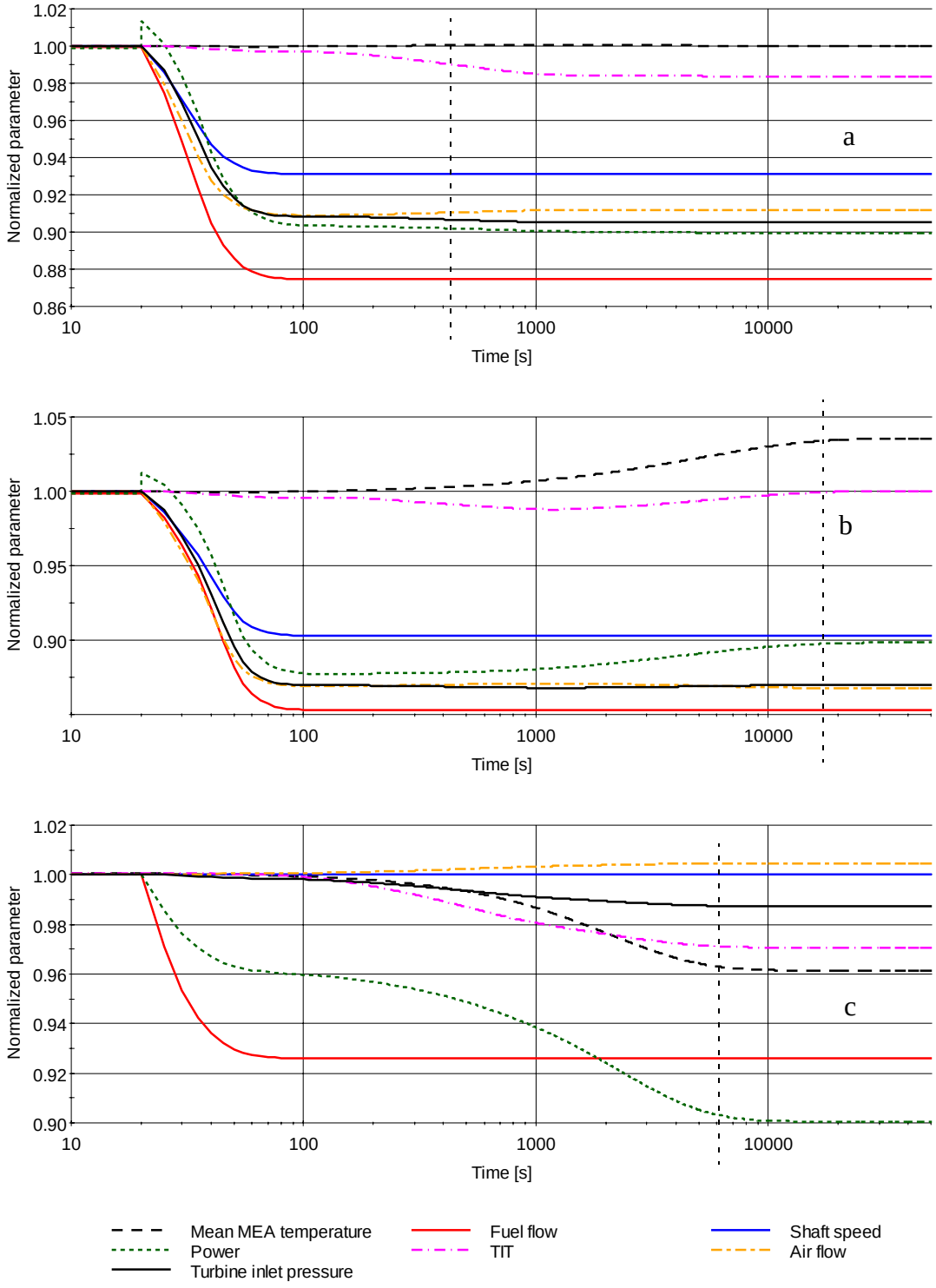

Figure 7-5. Normalized parameters plotted for a load change from 100% to 90% when applying the constant mean fuel cell temperature strategy (a), constant TIT strategy (b) and constant shaft speed (c).

From Figure 7-5 it can be seen that both load change strategies which imply shaft speed reductions (a and b) have a sudden increase in power at the very beginning of the load change. In the case of constant TIT the load is further reduced by 2%-points more than required. While the first effect can be allocated to the shaft speed deceleration, the second effect may be caused by the thermal inertia of the fuel cell stack. The figure shows that the proposed strategy is not sufficient to achieve a constant TIT *during* the load change, but the TIT of the new steady-state condition is the same as prior to the load change. However, the TIT deviation from the target temperature during the load change is no more than 1%. In Figure 7-5 it can also be seen that air flow, turbine inlet pressure and TIT behave quite similar to the mean fuel cell temperature, and hence thermal inertia of the fuel cell is a possible explanation of their respective relaxation times.

Some important parameters with respect to system performance and safety are shown in Figure 7-6. Chart (a) shows efficiencies, SOFC power fraction, voltage, surge margin, degree of prereforming and minimum Gibbs free energy for the carbon deposition reaction when the constant mean fuel cell temperature strategy is applied to the load change. Chart (b) and (c) show the same parameters for the constant TIT and the constant shaft speed strategies, respectively. The power relaxation times are marked by a dashed vertical line in all the figures. If one compares the curves describing the efficiencies for the three cases, it can be seen that part-load efficiency is reduced only in the case of constant shaft speed (c). A comparison with Figure 7-5 shows that this is the only case where the mean fuel cell temperature is reduced at part-load, and this is most probably due to increased air flow in combination with the fuel reduction. This indicates that air flow reduction is important in order to achieve high part-load efficiency. In the same figure it can also be seen that the SOFC power fraction is slightly increased for the constant mean fuel cell temperature and the constant TIT strategies, whereas the constant shaft speed strategy leads to a reduced power contribution from the SOFC. A possible explanation for this behaviour may be increased SOFC losses due to reduced temperature for the case of constant shaft speed. The reduced SOFC power fraction contributes to the net efficiency loss in the case of constant shaft speed. The degree of prereforming shows opposite behaviour when results from the constant shaft speed calculation are compared to the two other strategies. Due to the fact that fuel is reduced for all cases, the reduction in degree of prereforming for the case of constant shaft speed should be attributed to the reduced operating temperature of the fuel cell.

An evaluation of the plots showing the surge margin and the Gibbs free energy for the carbon deposition reveals that all load change strategies operate far from any of these hazards. However, it can be seen that the surge margin increases when the possibility of carbon deposition is reduced and vice versa. This indicates the existence of a safe operating range, where carbon deposition and surge margin represent the upper and lower limits.

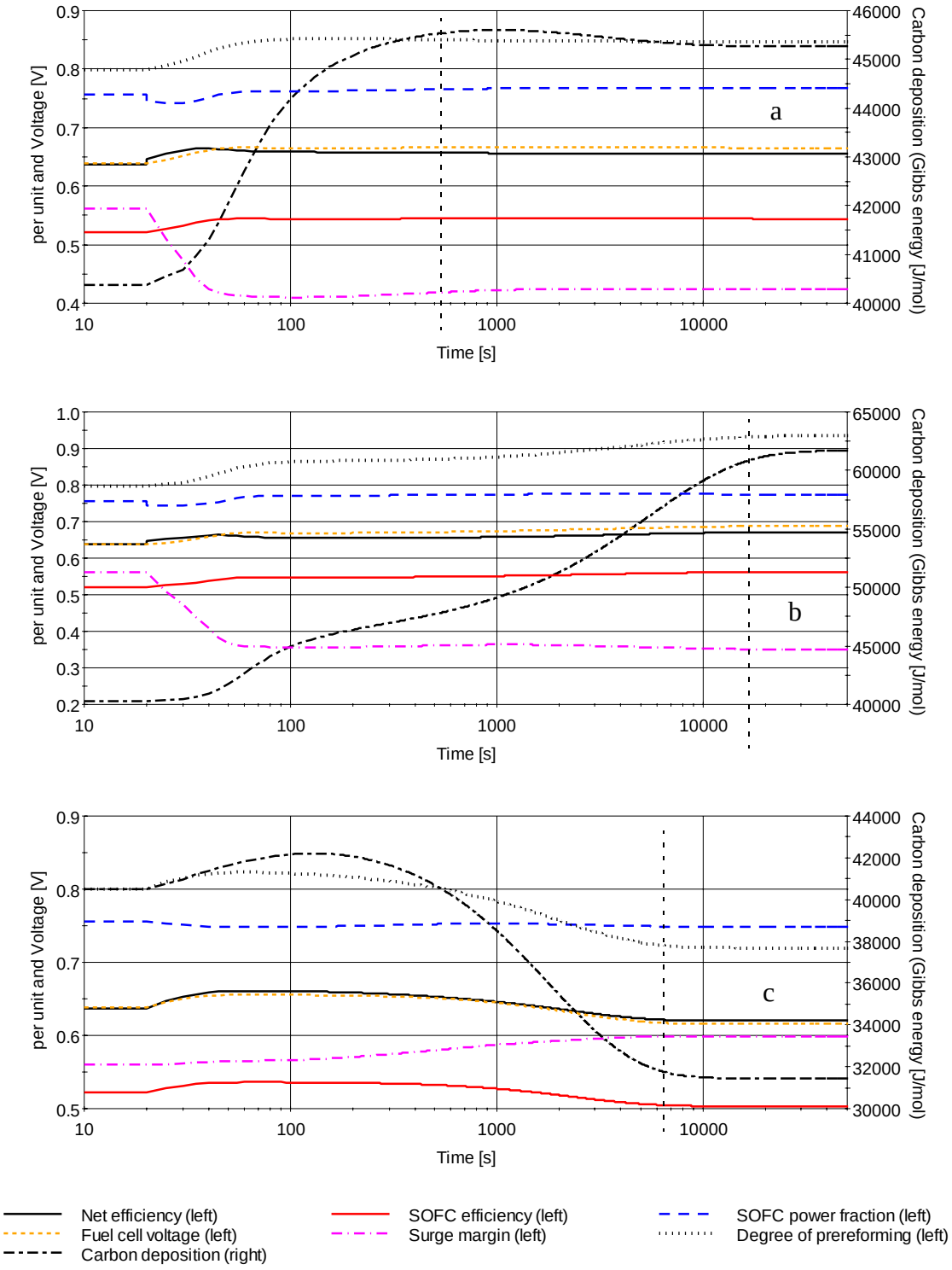

Figure 7-6. Key parameters with respect to performance and safety for the three different load change strategies. Constant mean fuel cell temperature is shown on the top (a), constant TIT in the middle (b) and the chart at the bottom represents the constant shaft speed strategy (c).

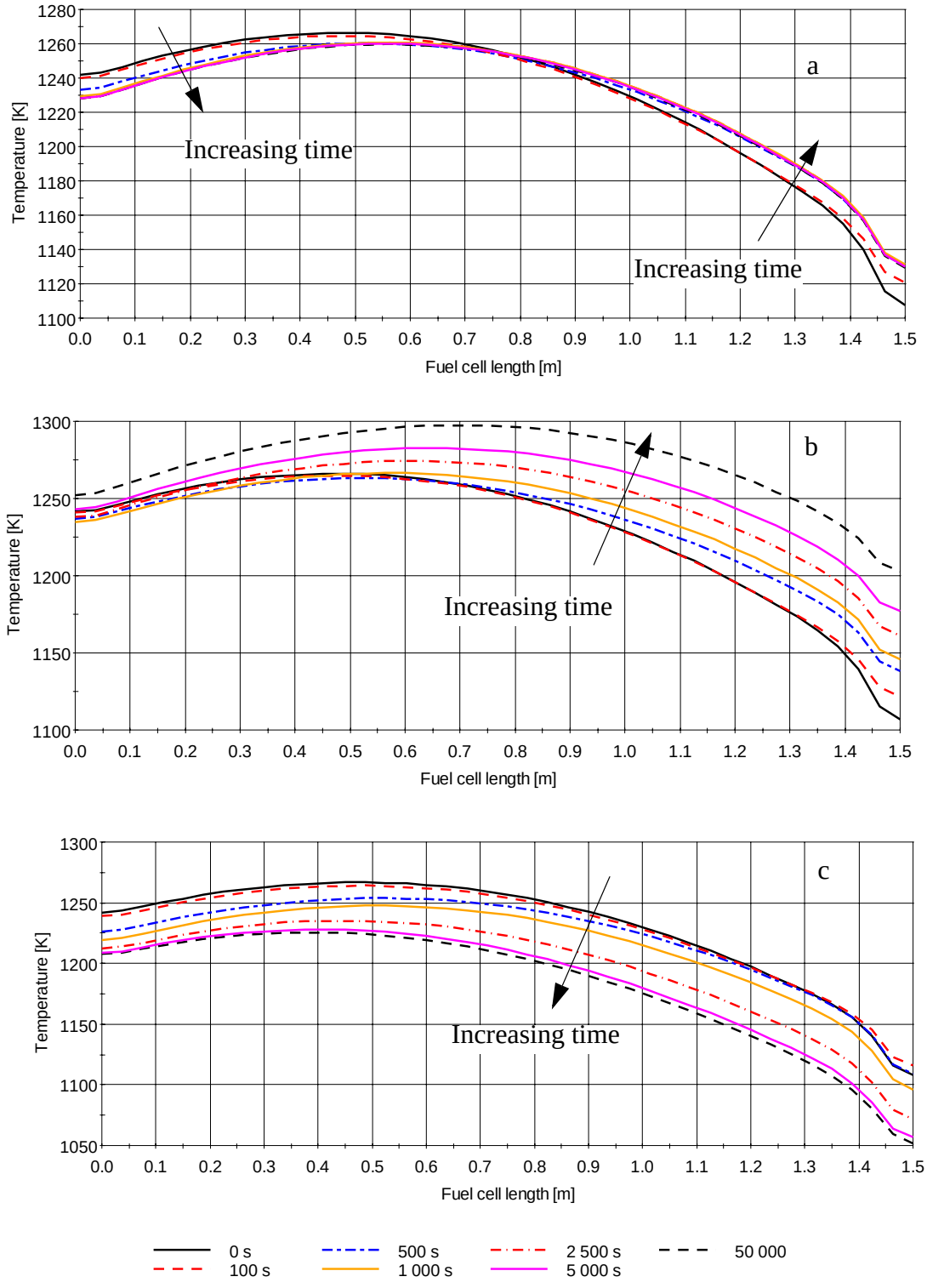

Figure 7-7. Temperature distribution in the fuel cell anode surface at some instances during the load change. Temperatures for the constant mean fuel cell temperature is shown in the top (a), constant TIT in the middle (b) and constant shaft speed at the bottom (c).

Snapshots of the anode surface temperature for the different load change strategies are shown in Figure 7-7. The times reported in the legend refer to the same axis as shown in Figure 7-5 and Figure 7-6. The figure shows that each strategy influences the temperatures in different ways. In the case of constant mean fuel cell temperature (a), the temperature at the fuel inlet (right hand side of the figure) increases, while the temperature at the exit decreases. Thus, there is only a small change in the temperature *profile*, whereas the mean temperature remains unchanged (as expected). In the case of constant TIT (b) the temperature at the fuel inlet increases by 95 K, whereas the temperature at the fuel outlet increases by only 11 K. This suggests that these two strategies (a and b) have a smoothening effect on the fuel cell temperature profile, hence reducing thermal gradients. When comparing the three charts in Figure 7-7, it can be seen that the largest change in the temperature profile is related to the constant TIT strategy, and this may be one of the reasons for the long relaxation time.

Figure 7-8 shows the maximum temperature gradients within the whole MEA, and this figure confirms that temperature gradients are reduced for both the constant mean fuel cell temperature and the constant TIT strategies. In fact, the maximum temperature gradients in the radial direction are reduced by 140 K/m and 289 K/m for the constant mean fuel cell temperature- and the constant TIT strategy, respectively. The corresponding temperature gradients in the axial direction are reduced by 81 K/m and 182 K/m. For the case of constant shaft speed the temperature profile itself remains fairly unchanged, although the mean temperature decreases (Figure 7-7). A glance at Figure 7-8 shows that the maximum radial temperature gradient increases by only 5 K/m, while the corresponding gradient in the axial direction decrease by 33 K/m.

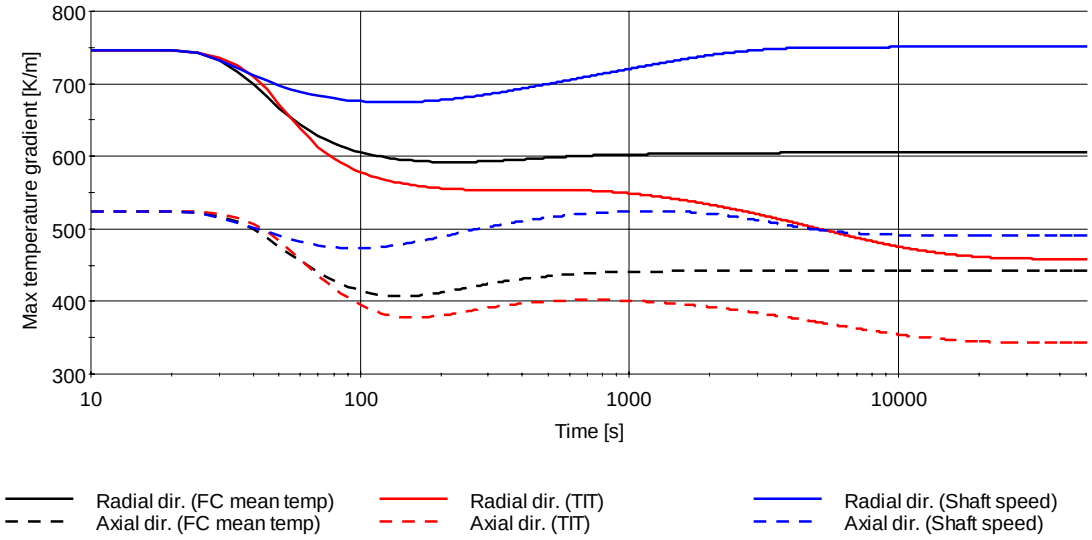

Figure 7-8. Maximum temperature gradients in the MEA during a load reduction from 100% to 90%.

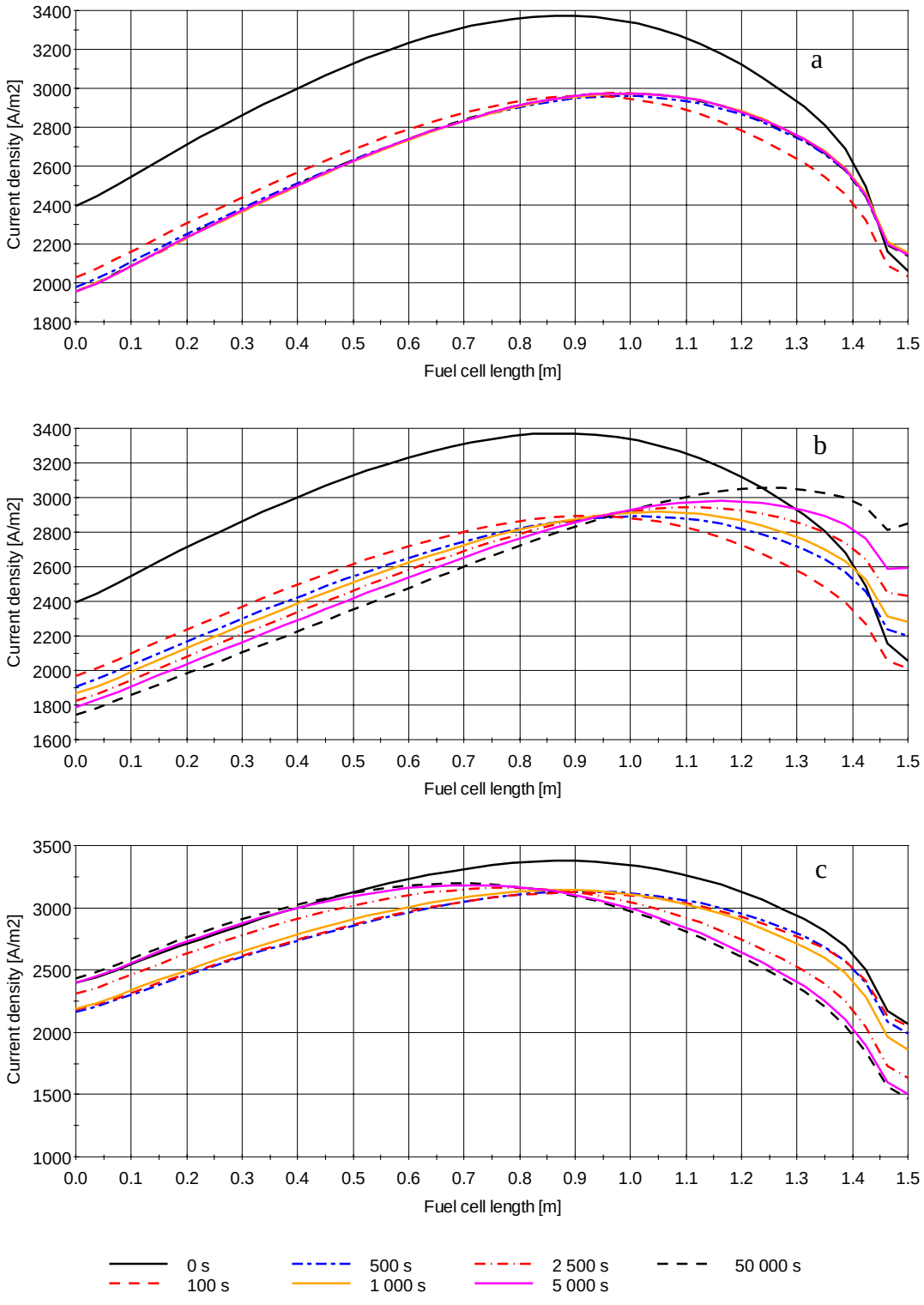

Figure 7-9. Snapshots of the current density distribution from the constant mean fuel cell temperature (a), constant TIT strategy (b) and the constant shaft speed strategy (c).

The reason for the different behaviour in temperature distribution may be found when comparing the results found in Figure 7-5, Figure 7-6 and Figure 7-9 with the results from Figure 7-7 and Figure 7-8. From these figures it can be seen that a load reduction according to the constant mean fuel cell temperature- and the constant TIT strategies (a, b), result in increased degree of prereforming, increased voltage, reduced air flow rate and reduced current density. The effect of increased degree of prereforming is that less unconverted methane enters the fuel cell, and thereby less fuel has to be converted on the fuel cell anode. In combination with the increased voltage, the increased degree of prereforming leads to reduced thermal gradients in the axial direction. Furthermore, reduced current density leads to reduced internal heat generation, and in combination with reduced air flow, this causes a reduction in radial thermal gradients. The opposite can be observed for the case of constant shaft speed. Then air flow is increased while degree of prereforming, voltage and current density are reduced at part-load, hence explaining the transient increase in the maximum axial temperature gradient. Considering the very low increase in maximum radial temperature gradient, the air flow and current density act in the opposite direction and it may therefore seem as if the effect of the air cooling is stronger than that of the current density reduction.

In Figure 7-4 it was shown that the steam mole fraction remained fairly constant for the constant mean fuel cell temperature strategy, despite the load change. This due to the constant fuel utilisation and therefore it also applies to the two other strategies. Hence these graphs are not shown here.

The ageing effects due to current density (pore formation in the electrodes) are reduced at part-load in all the three cases shown in Figure 7-9. This is mainly due to the overall reduction in current density. The highest part-load current density is found for the constant shaft speed strategy (c). This is further combined with a shift in the maximum current density location towards the exit of the fuel cell which is also the location where the highest amount of steam can be found. In fact, most of the current density reduction takes place from fuel cell length = 0.5 m to the bottom. Thus, the upper part of the fuel cell will experience similar current densities as the reference case when operating in part-load. This means that the upper part of the fuel cell is likely to degrade with the same pace at part-load as for the reference case. A consequence of the TIT strategy is that the current density at the fuel inlet increases quite massively, compared to the reference case. At the same time, the other part of the fuel cell experiences a current density reduction. This means that the degradation is likely to proceed more rapidly close to the fuel inlet, but slower in the rest of the fuel cell when operating at part-load. The constant mean fuel cell temperature strategy will experience the least degradation of the three strategies, due to the overall reduction in current density in combination with a maximum current density shift towards a low steam mole fraction area (Chapter 7.2).

7.3.2 Increasing Load from 90% to 100%

Normalized parameters for a load increase from 90% to 100% for the three load change strategies are shown in Figure 7-10. The figure shows that the behaviour of the load increase in general is very similar to the load decrease. A consideration of the power curves shows that there is a power undershooting for the load reduction, where there is a power overshooting for the load decrease and vice versa. The same effect can be seen when investigating the curves representing the other normalized parameters in the same figure and the key parameters seen in Figure 7-11. An analysis of the normalized power curves in Figure 7-10 combined with the numerical results seen in Table 7.2, shows that the main difference between the load increase and load reduction is power relaxation time. In fact, the relaxation time of the constant TIT strategy is 21% less for a load increase than for a load reduction. An opposite behaviour is seen for the two other strategies, as the relaxation times of the constant mean fuel cell temperature strategy and constant shaft speed strategies increase by 21% and 10%, respectively. This means that the power relaxation time depends not only on the load change strategy itself, but also in which direction the load is changed. A comparison of the results from the different load change strategies shows that the constant TIT strategy is the only strategy which implies a reduction in the mean fuel cell temperature upon load reduction. It can also be seen that the two other strategies imply an increase in TIT from part-load to the reference case. If one compares the relaxation times seen in Table 7.2 with Figure 7-5 to Figure 7-12, it can be seen that the maximum relaxation time for each independent strategy coincide with either a permanent or temporary TIT increase. Hence, it makes sense to search for mechanisms related to the TIT in order to explain the differences in relaxation times.

Starting with the TIT strategy, it can be seen from Figure 7-10 that the part-load mean fuel cell temperature is higher than that of the reference case. It can also be seen that moving from 90% load to 100% load implies an increase in the air flow and pressure as well as a reduction in the degree of prereforming. The effect of the increased air flow is improved cooling of the fuel cell, and this is further facilitated by the increased pressure which leads to reduced TOT and therewith also reduced stack inlet temperature. These two mechanisms will initially affect the temperatures close to the top of the fuel cell, i.e. the air supply tube entry. From there on, the temperature change will propagate towards the end of the tube. The reduction in degree of prereforming in the first time period is caused by increased fuel flow, but when the fuel cell cools down, reduced heat transfer from the fuel cell contributes to an even larger decrease in degree of prereforming. The consequence is larger methane content in the fuel entering the fuel cell, and hence improved cooling at the bottom of the tube. This means that reduced degree of prereforming and improved air cooling cools the fuel cell from the top and the bottom at the same time, and hence temperature reaches steady state faster than for the load reduction.

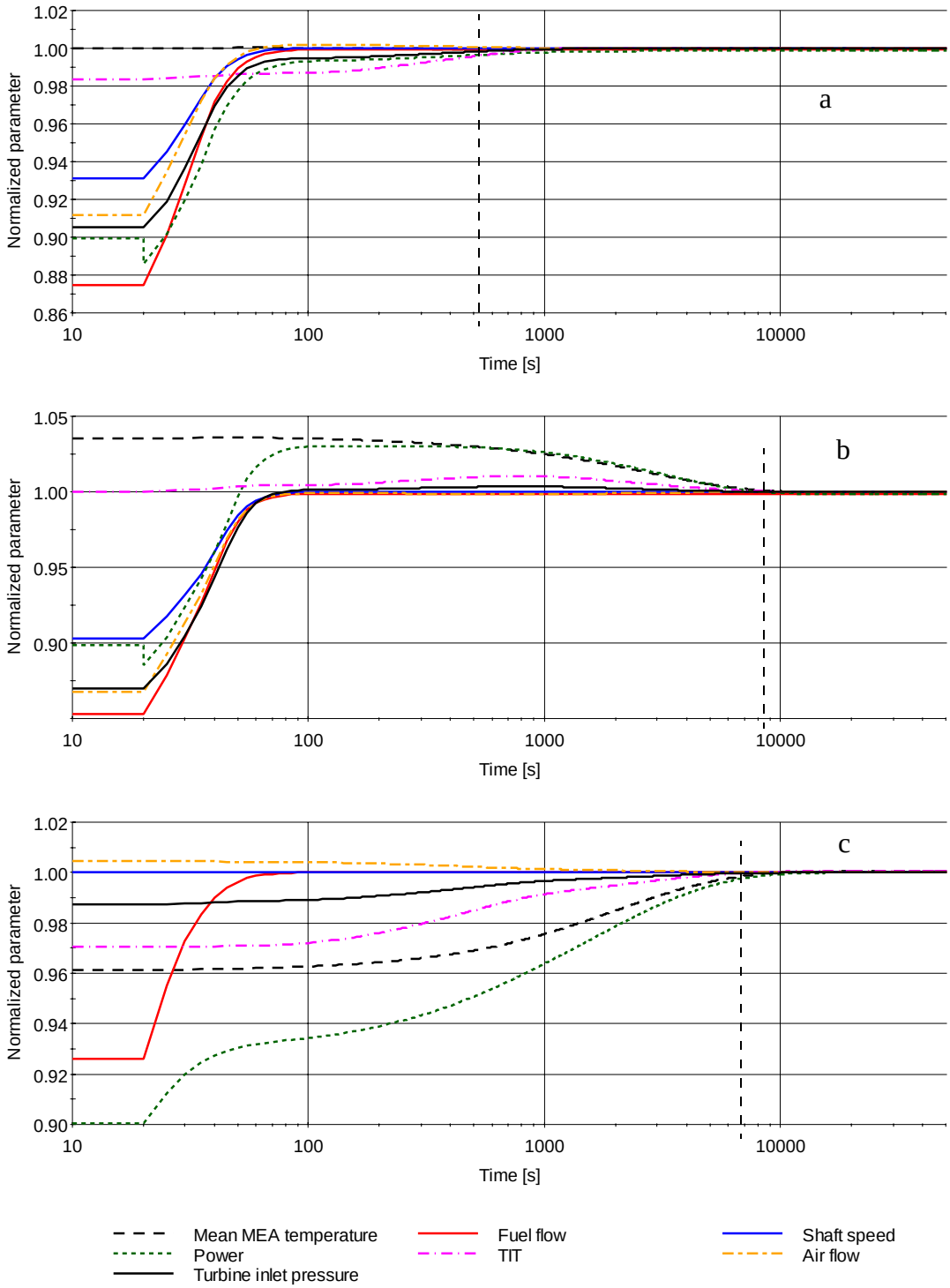

Figure 7-10. Normalized parameters for the three load change strategies when power is increased from 90% to 100%. The constant mean fuel cell temperature strategy is shown at the top (a), the constant TIT strategy in the middle (b), and the constant shaft speed strategy is shown at the bottom (c).

In the case of load increase at constant shaft speed, Figure 7-10 shows an initial power increase of almost 3% during the fuel flow change (the first 50s after the load change). After this period the gradient of the power increase is much lower and there is an asymptotically approach to the new steady state (beware of the logarithmic time axis). From the same figure it can be seen that the part-load air flow rate is higher than for the reference case, and that the part-load pressure is lower than for the reference case. It may further be seen that both the TIT and the mean fuel cell temperature at part-load are lower than for the reference case. Additionally, Figure 7-11 shows that there is an initial reduction in the degree of prereforming as a consequence of the increased fuel flow. From a close look at Figure 7-12 it can be seen that the anode surface temperature actually is reduced by 6 K at the fuel entry 80 seconds after the load change. This occurs despite the voltage reduction, hence indicating a very strong cooling effect from the methane reforming. This suggests that the heating of the fuel cell must fight to overcome the cooling effect from the high air mass flow and increased methane content of the fuel.

An investigation of Figure 7-12 shows that the power relaxation time corresponds quite well with the anode surface temperature relaxation time at the fuel cell exit when the constant mean fuel cell strategy is applied to the load increase. Furthermore, this corresponds well with the relaxation time of the TIT seen in Figure 7-10, and this indicates a connection between the TIT and the anode surface temperature at the fuel cell exit. This part of the fuel cell is indirectly coupled with the entering air of the air supply tube. The temperature of the entering air is further connected to the TIT which depends on the solid temperature of the anode surface at the exit. Hence, the recuperator and air supply tube have a balancing effect upon any temperature change at this location.

Although the relaxation time of the constant mean fuel cell temperature strategy is larger upon a load increase than for a load reduction, it is still the fastest strategy when power is increased. Compared to the two other strategies, the constant mean fuel cell temperature strategy is 13 times faster than the constant shaft speed strategy and more than 16 times faster than the constant TIT strategy (Table 7.2).

Figure 7-11 shows that there is little risk of surge during the load increase. The possibility of carbon deposition is also very low. However, when the constant shaft speed strategy is applied to the load increase, there is a temporary undershooting in the Gibbs free energy of carbon deposition. This coincides with the reduction in degree of prereforming, and it is probably caused by the fuel increase. When the fuel supply is increased, there is a temporary reduction in the steam to carbon ratio until a new steady state has been reached. Hence, it is important not to increase the fuel flow too rapidly, as this might reduce the steam to carbon ratio beyond the limit of carbon deposition.

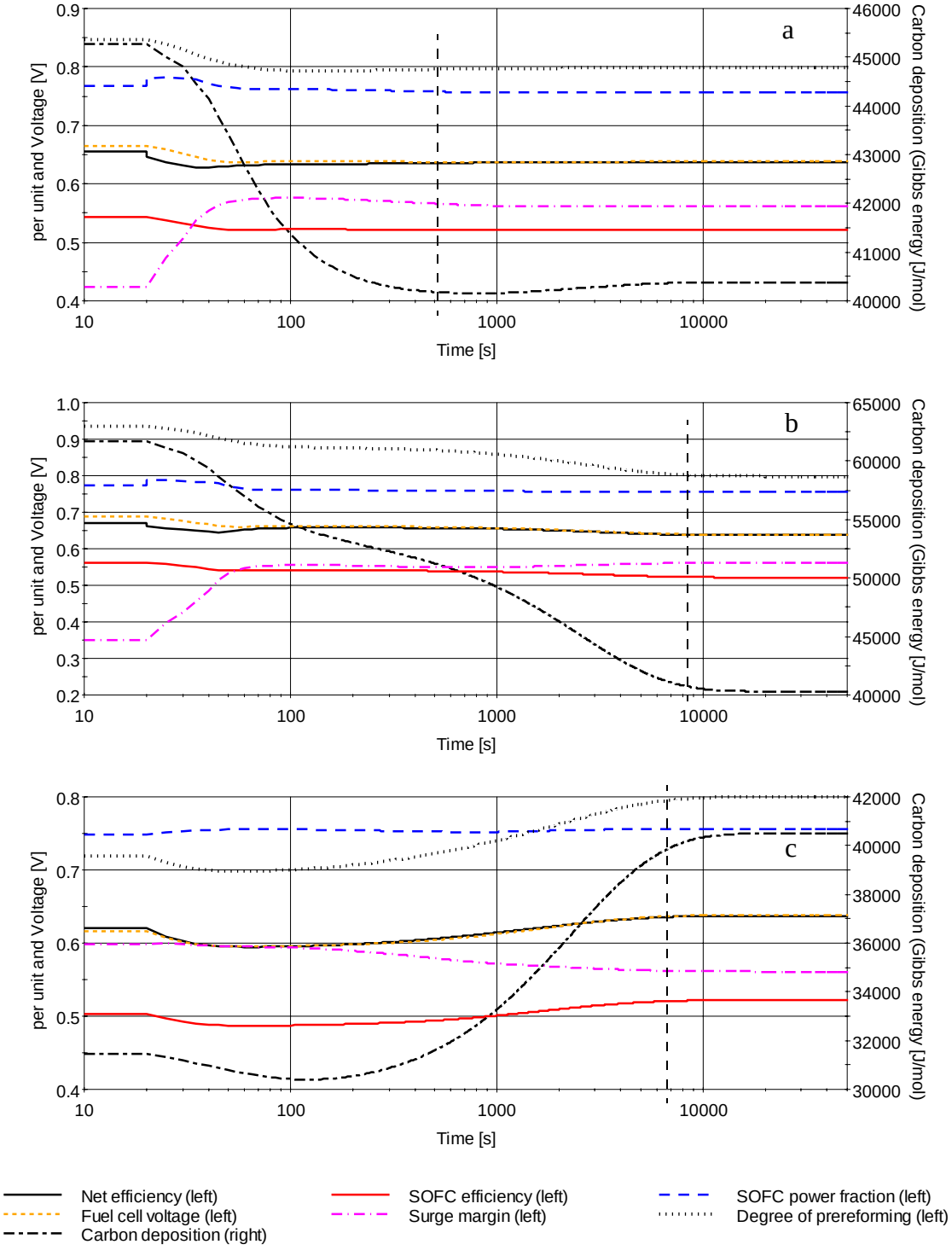

Figure 7-11. Key parameters regarding performance and safety for the three different load change strategies. Results from the constant mean fuel cell temperature strategy are shown at the top (a), the constant TIT strategy in the middle (b) and the results from the constant shaft speed calculation are shown at the bottom (c).

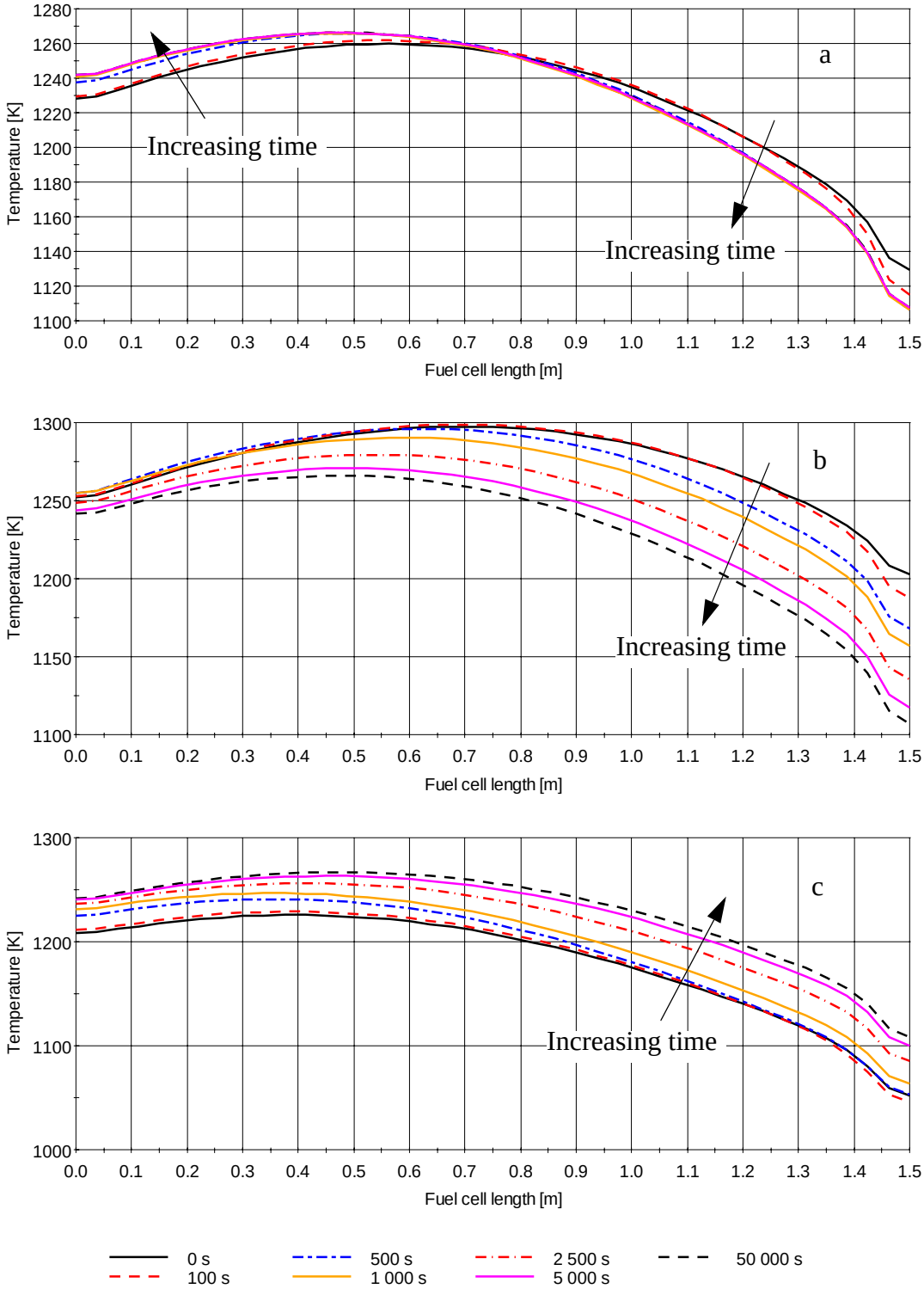

Figure 7-12. Temperature distribution in the fuel cell due to a load increase from 90% to 100% according the constant mean fuel cell temperature strategy (a), the constant TIT strategy (b) and the constant shaft speed (c).

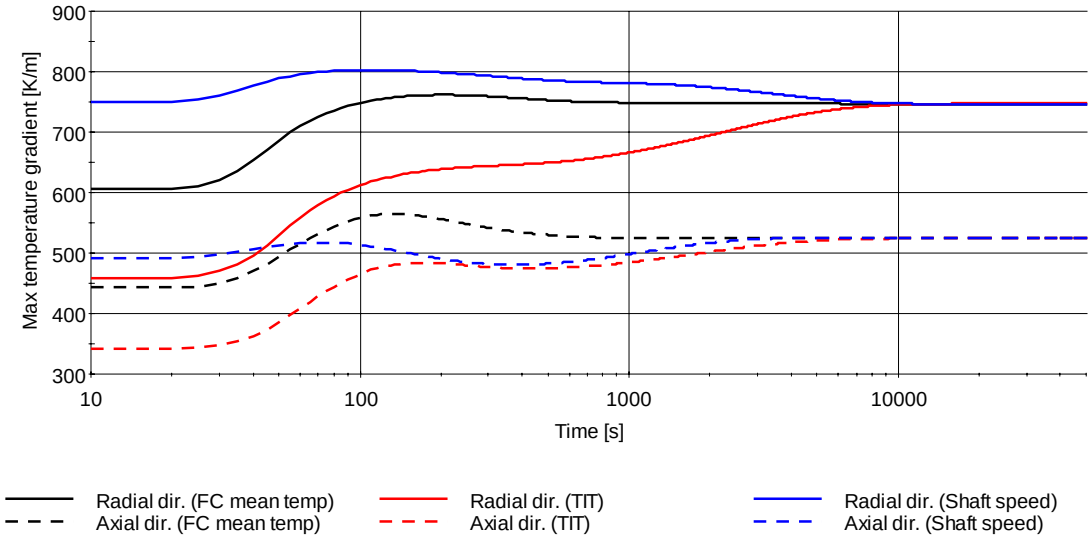

Figure 7-13. Maximum temperature gradients in the MEA when load is changed from 90% to 100%, according to the three different load change strategies.

7.3.3 Reducing Load from 100% to 50%

When power is reduced by as much as 50% according to the constant TIT strategy, one very interesting effect can be observed. In Figure 7-14, which shows the normalized parameters for this load change, it can be seen that the same undershooting of TIT as observed in Figure 7-1 occurs when power is reduced by 50%. However, the TIT never reaches steady-state as it continues to increase with a steadily growing gradient. The calculation shown in Figure 7-14 was stopped at 260,000 seconds, and at this time the maximum fuel cell temperature has already reached 1540 K. In practice such temperatures will cause serious damage to the fuel cell and other parts of the system, and hence this behaviour must be avoided by any means.

The system run-off seen here has previously been observed in the sensitivity study of the heat exchanger size (Chapter 5.3.2). It may thus be assumed that the uncontrolled temperature increase observed here, implies operation in the no-steady-state regime indicated in Figure 1 and Figure 2 in Appendix C. A thorough analysis of the uncontrolled temperature increase seen here will not be given, as it is beyond the scope of this investigation. However, from Figure 7-14 it can be seen that the air flow rate decreases at the same time as the mean fuel cell temperature and TIT increase. The temperature increase may be explained by the reduction in air flow rate which implies better heat recovery in the recuperator in combination with reduced cooling effect in the fuel cell. According to the compressor map in Figure 4-7, increased inlet temperature leads to reduced flow rate, and hence a reinforcing loop is formed by the recuperator (Feedback loop (1) in Figure 6-1.)

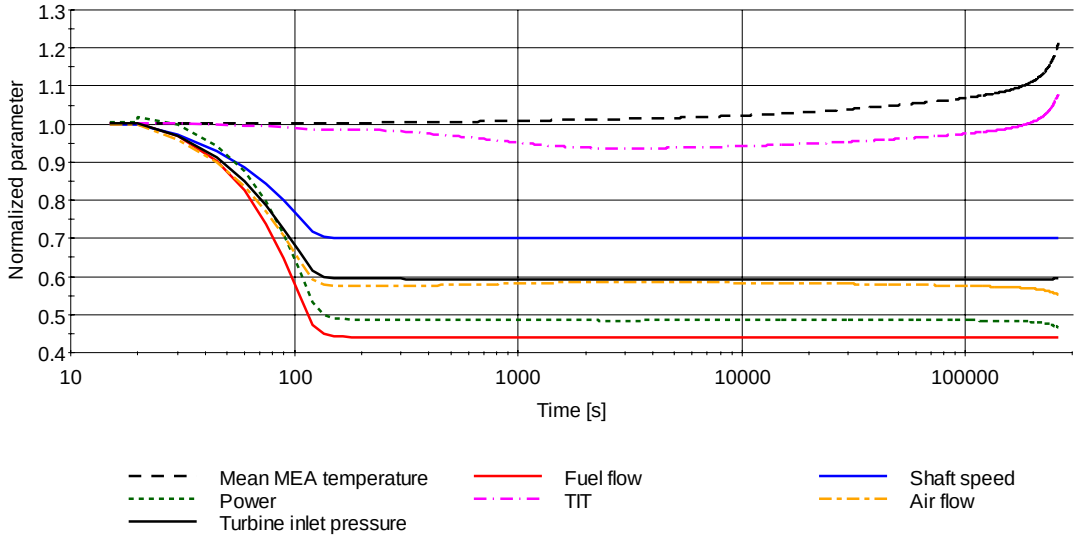

Figure 7-14. Normalized parameters calculated due to a 50% load reduction according to the constant TIT strategy. The sudden temperature increase at 260.000 seconds leads to a excessive fuel cell temperatures.

The most interesting fact about this system run-off is that the steady-state model is able to find a solution for the same combination of the control parameters. This suggests that the steady-state solution is close to, or at the border of the stability limit. Thereby, a very small disturbance in any of the control parameters may shift the operational point into the unstable operational regime. Operation in the unstable regime can also be caused by approaching the new operational point from the wrong direction, i.e. choosing the wrong path to the new load. The latter has been investigated by choosing several paths to this operational point, but none of the attempts were successful. One option may therefore be to approach the 50% load operational point very slowly along the constant TIT load-line. However, this is not an option in the investigation of the strategies shown here, as one of the main purposes is to evaluate the most rapid strategy to load change. It was therefore chosen to implement a safety margin with respect to the TIT. In practice this means that the TIT is kept 3% below the target value at part-load although the constant TIT-strategy is applied to the load change.

Results from the modified constant TIT strategy are shown in the middle (b) of Figure 7-15. The corresponding normalized parameters for the constant mean fuel cell temperature and the constant shaft speed strategies are shown at the top (a) and the bottom (c) in the same figure. The chart showing the constant TIT strategy may seem to follow the same temperature development as seen in Figure 7-14, but it does in fact stabilize at approximately 50000s. The stability was checked by running the calculation for 5000000 seconds, but results from the complete calculation are not shown here due to better comparability with the other charts. Key parameters regarding performance and safety from the same calculations are shown in Figure 7-16, while temperature distribution, temperature gradients and current densities are shown in Figure 7-17 to Figure 7-19.

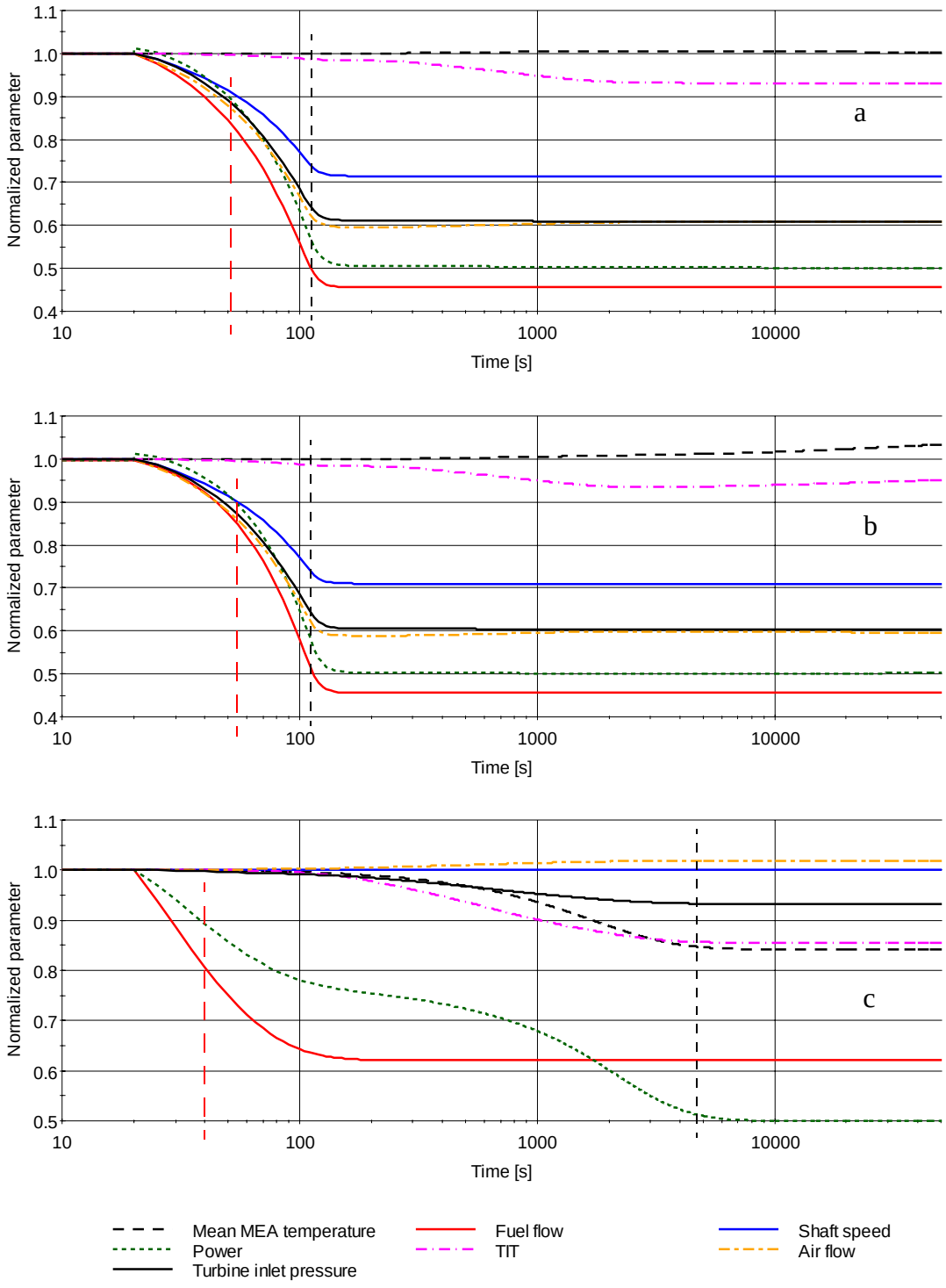

Figure 7-15. Normalized parameters calculated for a 50% load reduction according to the constant mean fuel cell temperature strategy (a), the constant TIT strategy (b) and the constant shaft speed (c).

In Table 7.2 it can be seen that power relaxation times of the constant mean fuel cell temperature strategy and the modified constant TIT strategy are both 115 seconds. This is also indicated in Figure 7-15 by black dashed lines. This is an interesting finding as it suggests that other strategies than the constant mean fuel cell temperature may be just as fast with respect to achieving target load. However, it may be observed that both these strategies imply an almost equal reduction in TIT, but the constant TIT strategy implies a small mean MEA temperature increase at part-load. From Figure 7-16 it can also be seen that the behaviour of the two different strategies are quite similar with respect to performance and safety. Similarities of the two load change strategies may also be found in the anode surface temperature distribution (Figure 7-17), temperature gradients (Figure 7-18) and current density distribution (Figure 7-19). The main difference between the two strategies is that the air flow is slightly lower at part-load for the constant TIT strategy, hence explaining the increased mean MEA temperature.

The red dashed lines in Figure 7-15 indicate the relaxation time for 90% power, and it is quite obvious that it is possible to reach 90% power more rapidly than what was observed in Chapter 7.3.1. Indeed, 90% load is achieved by the constant mean fuel cell strategy already 30 seconds after the initiation of the load change if the control parameters are set to 50% load instead of 90%. This is a relaxation time reduction by 95%, as compared to what was found previously. The same effect can be seen for the two other strategies, as the constant TIT strategy and constant shaft speed strategy reaches 90% load after 30 seconds and 20 seconds respectively. This shows that very low power relaxation times are achievable if the control parameters are initially set beyond target values, and this behaviour is utilised by the control system presented in the paper given in Appendix F.

From Figure 7-15, Figure 7-16, Figure 7-17 and Figure 7-19 it can be seen that the behaviour of a 50% load reduction in general is quite similar to that of a 10% load reduction. The main deviation is the magnitude of the changes of the different parameters, but the connections between them may be described by the same mechanisms as for a small load reduction. As an example it can be seen that part-load efficiency is even higher for the constant TIT and constant mean fuel cell temperature strategies, and even lower for the constant shaft speed strategy. The same applies to the fuel cell voltage and degree of prereforming. With respect to safety, it may be seen that there is a global minimum in the surge margin close to the end of load change when the constant mean fuel cell temperature and constant TIT strategies are applied. The minimum surge margin is just above 20% and from here it increases to approximately 25% at the part-load steady-state. Hence, both strategies can be considered safe, but for an even larger load change the short undershooting of the surge margin may be sufficiently large to go beyond the limit. When considering the numerical values of the part-load steady-state performance of the constant shaft speed strategy it can also be seen that its net efficiency is as low as 51%. This is 19% percentage points less than that of the two other strategies, and almost 13% percentage points less than the reference case net efficiency. It may further be seen that the operating voltage is as low as 0.48 V, and from Figure 7-15 it can be seen that the mean fuel cell temperature is reduced by 16% (=1035 K). Accordingly, it may be assumed that the constant shaft speed strategy is inappropriate for large power reductions.

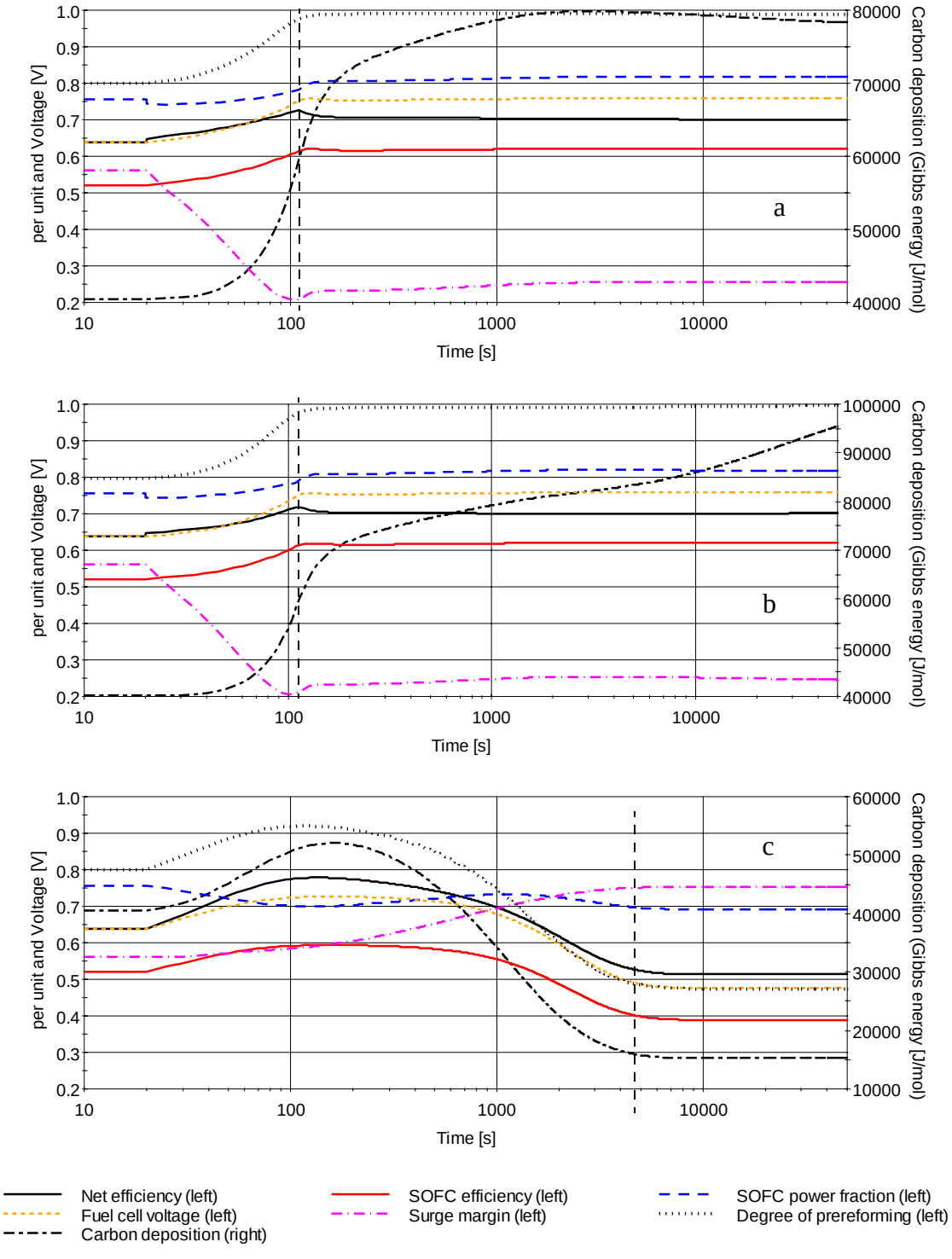

Figure 7-16. Key parameters regarding performance and safety calculated for the constant mean fuel cell temperature strategy (a), the constant TIT strategy (b) and the constant shaft speed (c).

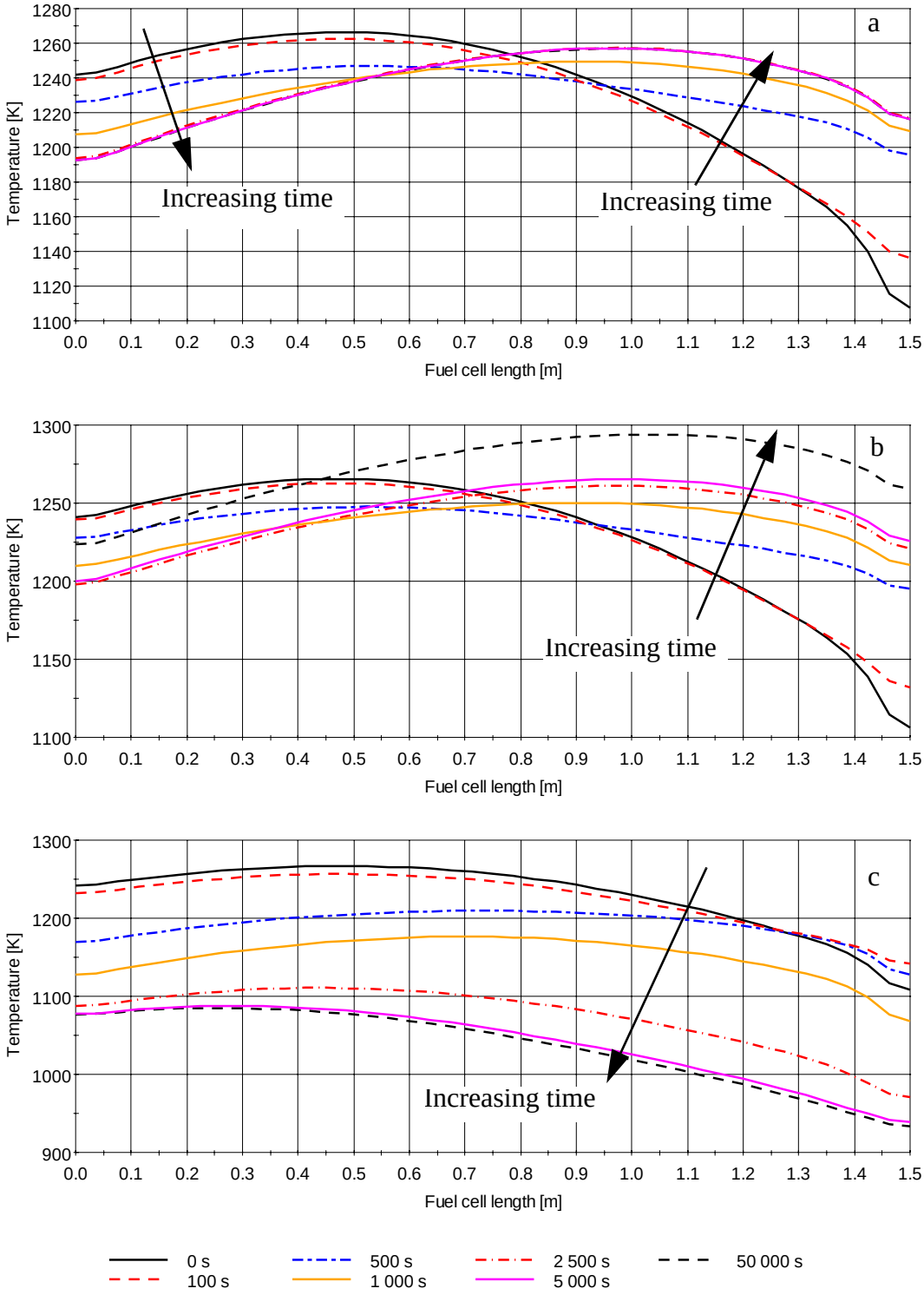

Figure 7-17. Anode surface temperature distribution as a consequence of 50% load reduction according to the constant mean fuel cell temperature strategy (a), the constant TIT strategy (b) and the constant shaft speed strategy (c).

The two upper charts (a and b) in Figure 7-17 and Figure 7-18 indicate a smooth transition from the reference case temperature profile to the part-load temperature profile for both the constant mean fuel cell temperature strategy and constant TIT strategy. Furthermore, the maximum temperature gradients are drastically reduced. The maximum temperature gradients are also reduced when the constant shaft speed strategy is applied, but from Figure 7-18 it can be seen that both gradients fluctuate through a global minimum and local maximum before they reach steady-state. The direct consequence from these types of temperature gradient fluctuations are not known, but it may put extra stress upon the materials in the MEA.

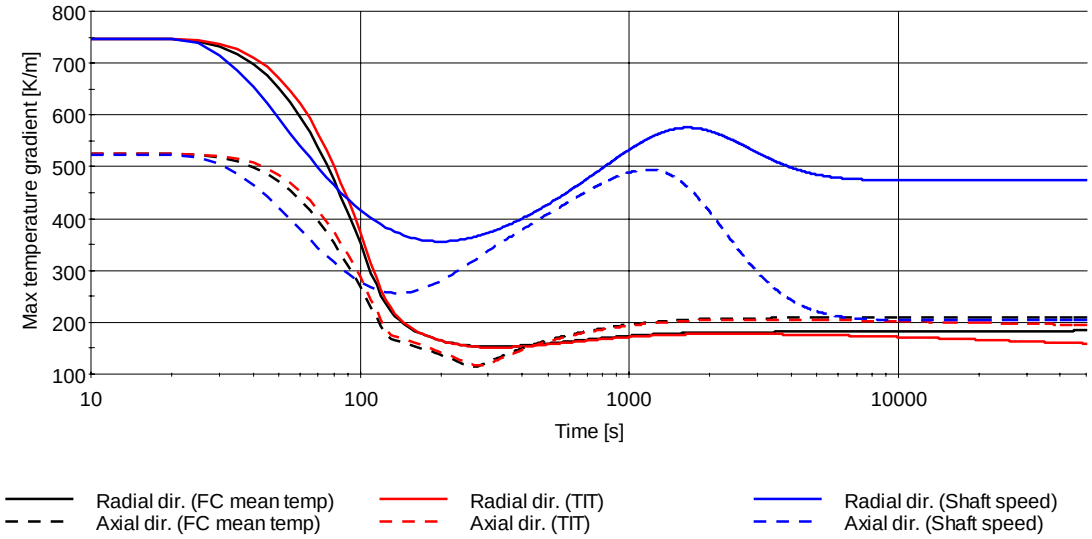

Figure 7-18. Comparison of the temperature gradients in the axial and radial directions during a 50% load reduction for the three different load change strategies.

Figure 7-19 shows snapshots of the current distribution during the load change for the three different load change strategies. A comparison with Figure 7-9 shows that the basic behaviour is the same for both small and large power reductions. Although the current density distribution is changed, one can see that both small and large load changes imply a smoothening of the profiles. For both the constant mean fuel cell temperature and the constant TIT strategy, load increases cause the location of the maximum current density to move towards the fuel inlet (the right hand side of the figure). Presumably, this is mostly due to increased degree of prereforming.

Due to constant fuel utilisation, the steam mole fraction distribution remains fairly unchanged also for large load reductions. Therefore, they are not shown here. Degradation of the electrodes at part-load is likely to be larger for the constant shaft speed strategy than for the two others. This is firstly due to an overall higher current density. Secondly due to relatively high current density at the fuel outlet, and this is where the amount of steam is highest.

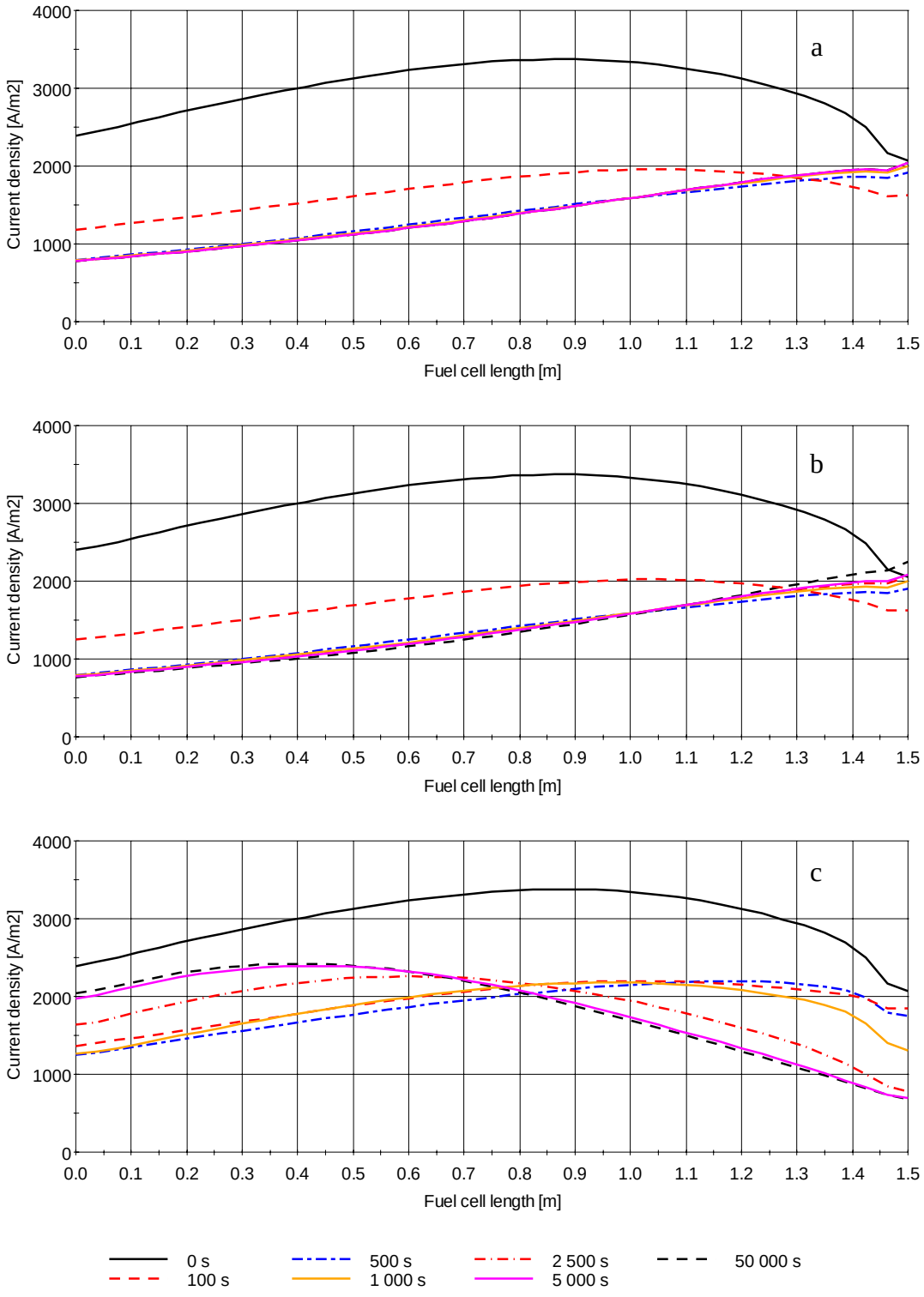

Figure 7-19. Current densities due to a 50% load reduction according to the constant mean fuel cell temperature strategy (a), the constant TIT strategy (b) and the constant shaft speed strategy (c).

7.3.4 Increasing Load from 50% to 100%

From Figure 7-20 it can be seen that the constant mean fuel cell temperature strategy is the quickest strategy, also when load is increased from 50% to 100%. Table 7.2 shows that the power relaxation time of this strategy is 385 seconds. For the constant TIT strategy, the target load is reached already 100 seconds after the load change (the red circle in Figure 7-20 b), but it does not stabilise. It continues to increase for a short while, before it slowly decreases towards the target load. The criterion for the relaxation time is that the load approaches a stable value, and thus the relaxation time for the constant TIT strategy is 3750 seconds. The power overshooting seen for this strategy is most probably due to the high part-load mean fuel cell temperature. The relaxation time for the constant shaft speed it is 5260 seconds. The relaxation times seen for these load changes confirm that the power relaxation time depends on the direction of the load change. This is obviously very important for the constant TIT strategy, as it is almost 33 times slower upon a load increase than for a load reduction.

The key parameters regarding performance and safety are not shown here, as they show the exact opposite behaviour as seen for the load reduction (Figure 7-16). This means that where there is a tumbling during load decrease, where there is a peak during load increase and vice versa. The same effect is seen for the current density distribution, and thus this figure is not shown here either.

With respect to the temperature distribution there is a slightly different behaviour between load reduction and load increase. A comparison of the anode surface temperature plots for the load reduction shown in Figure 7-17 and the corresponding plots for the load increase shown in Figure 7-21, show firstly the that temperature relaxation time is larger for a load increase than for a load decrease. Secondly, it may be seen that heating and cooling of the fuel cell, proceeds from different ends of the fuel cell for the respective load change strategies. As an example, chart (a) in Figure 7-21 shows that the anode surface temperature is at steady-state at the fuel entry already at 500 seconds. At the fuel cell exit, however, it is still 20K away from the target temperature. Similar behaviour can be observed due to a load reduction as shown in Figure 7-17. This suggests that the constant mean fuel cell temperature strategy facilitates a more rapid temperature change at the fuel entry than at the fuel exit. The exact opposite behaviour can be seen for the constant shaft speed strategy (c). For the load reduction shown in Figure 7-17, there is a larger temperature step at the fuel exit than at the inlet at 500 seconds, and vice versa for the load increase (Figure 7-21). The driving mechanisms for this behaviour are the cooling or heating effects from the air flow and degree of prereforming, and it has been discussed previously. However, the consequence of this behaviour is that the transient temperature profiles of the fuel cell stack act different upon a load decrease than for a load increase. The effect becomes apparent when comparing the maximum temperature gradients shown in Figure 7-18 and Figure 7-22. Figure 7-18 shows that both the constant mean fuel cell temperature strategy as well as the constant TIT strategy has a smooth and fast reduction of their respective temperature gradients when load is reduced. In Figure 7-22, however, it may be seen that the maximum temperature gradient in the radial direction for both these strategies reach a maximum at 200 seconds. Thermal gradients when load is changed due to the constant shaft speed strategy show opposite behaviour as the transient

temperature gradients are larger for a load decrease than for a load increase. The same effects are also seen when load is changed between 90% and 100%, although it is to a smaller extent. This suggests a dependency between temperature gradients in the MEA and the load change strategy as well as the direction and the magnitude of the load change. Furthermore, it can be seen that the transient maximum of the radial temperature gradient coincide with a reduction in the degree of prereforming. Due to the endothermic nature of this reaction and the fact that it takes place on the anode surface, it is reasonable to believe that increased reforming on the fuel cell anode cause these thermal gradients. Thus risk of delamination and thermal cracking is larger for load changes where the degree of prereforming is reduced.

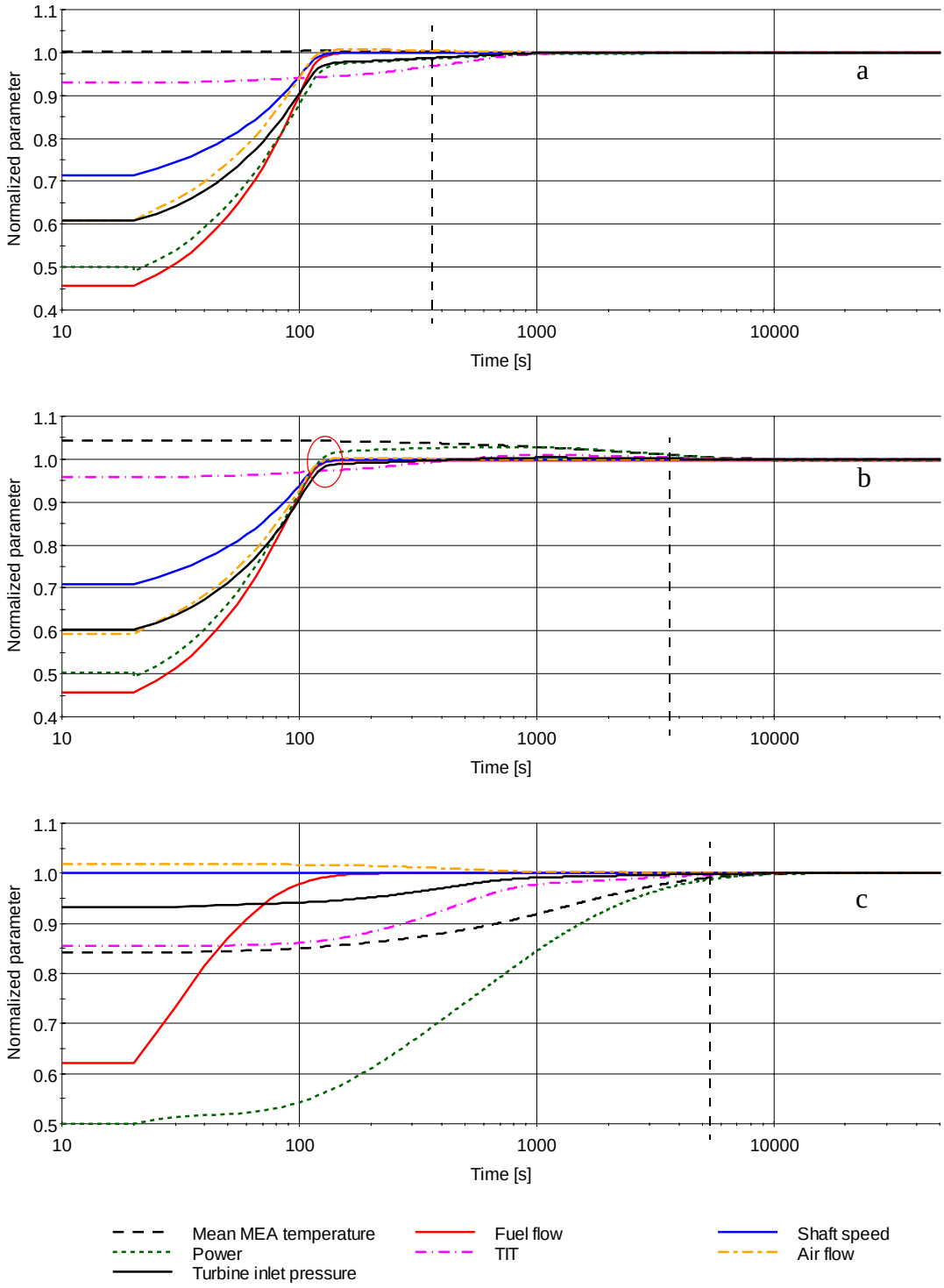

Figure 7-20. Normalized parameters for a 50% load increase by the constant mean fuel cell temperature strategy (a), the constant TIT strategy (b) and the constant shaft speed strategy (c).

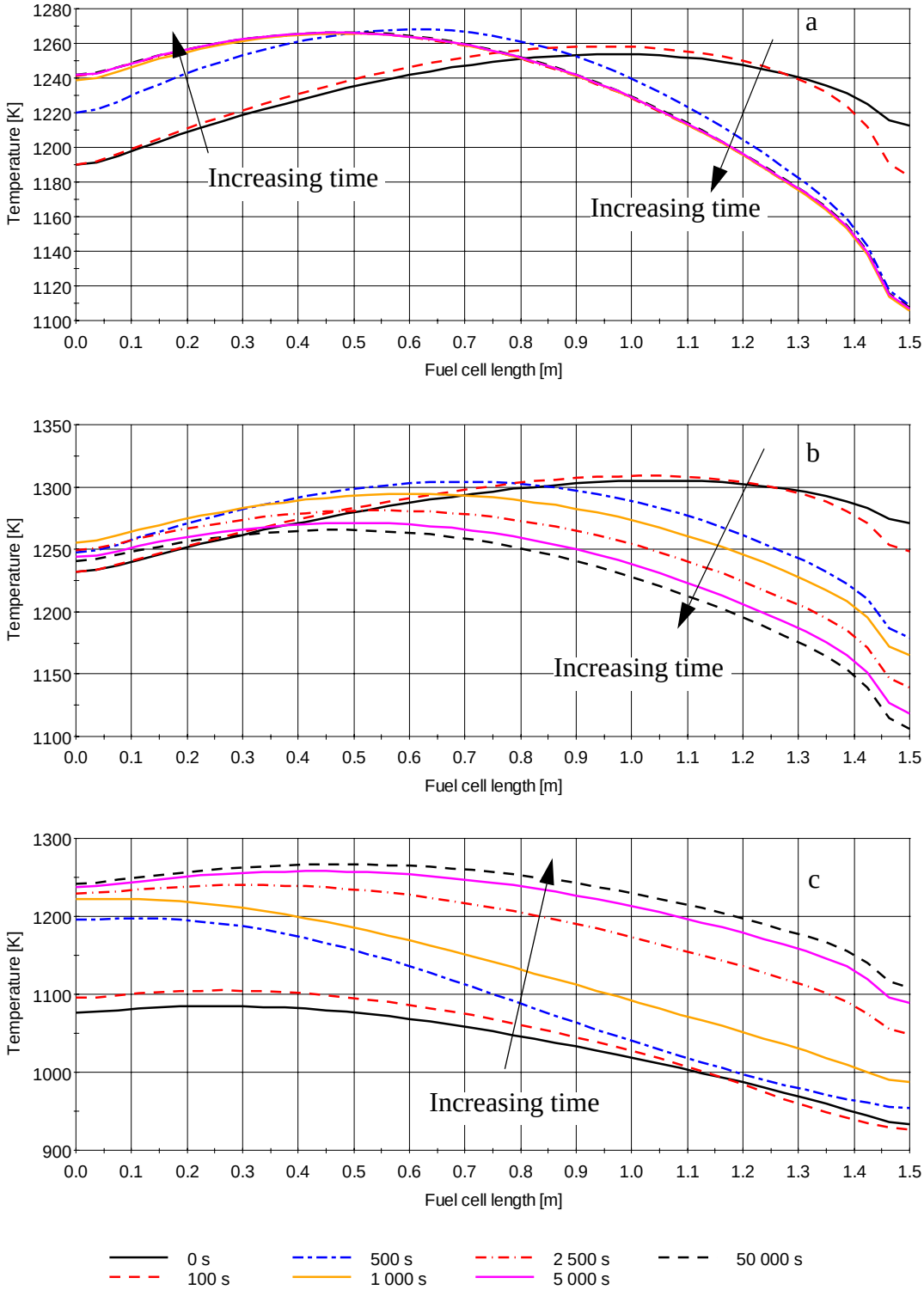

Figure 7-21. Snapshots of the temperature distribution due to a 50% load increase by the constant mean fuel cell temperature strategy (a), the constant TIT strategy (b) and the constant shaft speed strategy (c).

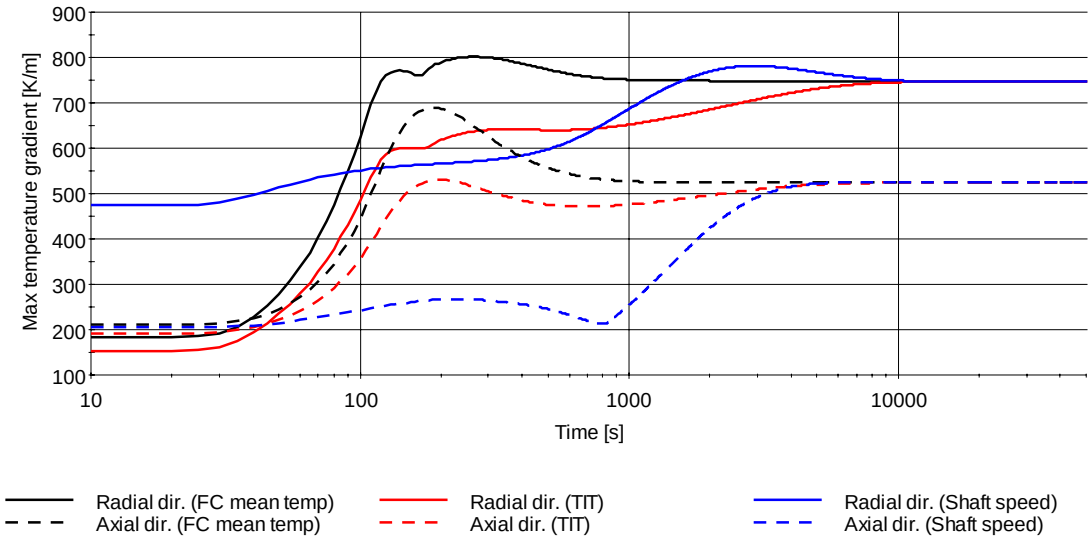

Figure 7-22. Maximum temperature gradients in the MEA when load is changed from 50% to 100%.

7.3.5 Discussion of the Investigated Load Change Strategies

Through the load change strategy investigation it has become quite evident that maintaining a constant mean fuel cell temperature is the best strategy in order to achieve quick load changes. This is also depicted in Table 7.2, which shows power relaxation times for all the strategies investigated in the present work. The constant mean fuel cell temperature strategy has the lowest power relaxation time, irrespective of the direction and magnitude of the load change. Except for the case of 50% load reduction, this strategy is at least one order of magnitude faster than the two other strategies. From Table 7.2 it can also be seen that the constant TIT strategy is the slowest strategy for a small load change, while it is the second fastest for a large load change. There is also a dependency on the load change direction, as it can be seen that a load increase is generally slower than a corresponding load reduction. It has further been found that there is a strong relationship between power and fuel cell temperature. Thus power relaxation time mainly mirrors the temperature change of the fuel cell. This is concurrent to the findings in [Achenbach, 1994]. Reduced relaxation time may therefore be achieved by efficient control of the heating or cooling duty of the air flow and the prereformer. However, relaxation times may be further reduced by utilising an advanced control system, which initially sets the control parameters beyond the target values and then slowly adjusts the control parameters to their steady-state values. An example of such a control system is proposed in the paper which is reproduced in Appendix C, and it is investigated in the paper which is reproduced in Appendix F.

The investigation has shown that both the constant mean fuel cell temperature strategy and the constant TIT strategy facilitate enhanced part-load efficiency, while the opposite is observed for the constant shaft speed strategy. The difference in part-load efficiency

can be as high as 19%-points between the constant shaft speed strategy and the constant mean fuel cell temperature strategy. The constant shaft speed strategy should therefore not be implemented on power plants intended for long-term part-load operation.

Table 7.2: Comparison of the investigated load change strategies

	Strategy	Relaxation time [s]	Comment
10% load reduction	FC temperature	430	Power overshooting, improved efficiency.
	TIT	10,795	Power under- & overshooting. Improved efficiency.
	Shaft speed	6,140	Almost constant efficiency
10% load increase	FC temperature	520	Initial power undershooting.
	TIT	8,620	Short power undershooting, followed by overshooting
	Shaft speed	6,775	
50% load reduction	FC temperature	115	High degree of prereforming
	TIT	115	TIT-condition not fulfilled at part-load!
	Shaft speed	4,685	Transient thermal gradient peaking. Very low part-load efficiency
50% load increase	FC temperature	385	Transient thermal gradient peaking
	TIT	3,760	Power overshooting. Transient thermal gradient peaking
	Shaft speed	5,260	Large temporary reduction in degree of prereforming

The load change analysis has shown that none of the presented strategies are exposed to either compressor surge or carbon deposition in any of the investigated load change cases. However, in the case of 50% load reduction a temporary undershooting of the surge margin steady-state value was found in those strategies involving variations in shaft speed. Surveillance of this limitation is thus particularly important for very large load reductions. For the constant shaft speed strategy, it was found that the risk of carbon deposition was higher for a load increase than for a load reduction. Thus, a very large and very fast load increase according to this strategy may lead to carbon formation on the anode. However, a very rapid increase in fuel supply could cause carbon deposition for all the strategies, due to the anode exhaust gas recirculation. Due to this loop, steam to carbon ratio will always be reduced when fuel is increased, and if the fuel feed is too rapidly, carbon deposition may occur.

Investigation of the anode surface temperature profiles has shown that heating and cooling of the fuel cell is mainly controlled by the air flow when the constant shaft speed strategy is applied. The degree of prereforming dominates the temperature change for the two other strategies. This means that the fuel cell is mainly heated or cooled from the top of the tube when the constant shaft speed strategy is applied. For the two other strategies, temperature changes propagate from the bottom of the tube towards the top. In Chapter 5.3.2 it was found that the degree of prereforming has a large effect on the temperature distribution. Thus it is likely that a change in the initial (design case) degree of prereforming will have the largest effect upon behaviour of the constant mean fuel cell temperature strategy and the constant TIT strategy. However, designing the system for a different degree of prereforming is not likely to change the fact that the constant mean fuel cell temperature strategy has the lowest relaxation time and that the constant shaft speed strategy has the highest relaxation time. This is because the constant shaft speed strategy implies larger fuel cell temperature changes than the constant mean fuel cell strategy, and it has been shown that the power relaxation time depends on the magnitude of the mean fuel cell temperature change.

With respect to the thermal gradients there is a transient maximum for the constant shaft speed strategy when load is reduced, but smooth transition upon load increase. The opposite can be observed for the two other strategies. This is concurrent with reduced degree of prereforming, and hence it can be assumed that a load increase which implies a reduction in the degree or prereforming can lead to high transient thermal gradients. The direct consequence of these thermal gradients is difficult to analyse without a full 3D-analysis of the fuel cell tube stresses. In such an analysis it is also of great importance that residual stresses are included, but more material data are needed. However, from the presented analysis it can be concluded that a load increase according to the constant mean fuel cell temperature strategy or the constant TIT strategy are more risky than a corresponding load reduction. The constant shaft speed strategy has shown similar behaviour with respect to large load changes, but for the opposite direction. Thus the largest transient thermal gradients in the MEA are found for a load reduction, while a corresponding load increase is less exposed to large thermal gradients.

From an analysis of the distributions of current density and steam mole fraction, it has been found that the constant shaft speed strategy is likely to lead to more rapid degradation at part-load than the two other strategies. This is because the maximum current density is found at a location in the fuel cell which also has a large steam mole fraction. These are conditions which promote both nickel agglomeration in the anode and pore formation in the cathode. The constant mean fuel cell temperature strategy is the strategy which is likely to experience the least degradation of the three strategies, as it has the lowest overall part-load current density. Furthermore, this strategy causes the maximum current density location to shift towards the fuel inlet, and this is where the lowest steam mole fraction is found.

The most risky behaviour found in this investigation is related to large load reductions for the constant TIT strategy. If no measures are taken, this strategy will eventually cause excessive fuel cell temperatures, which may lead to a system break down. From the comparison of the steady-state model and the dynamic model, it may seem as if the TIT

strategy implies operation at, or close to the system stability limit at low loads. However, the strategy may be applied to small load changes in the vicinity of the reference case (design load) without risk.

The analysis has shown that the constant shaft speed strategy leads to the largest power relaxation time and the most rapid fuel cell degradation at part-load. The comparison with the two other strategies has further shown that air flow rate control is of great importance with respect to safety and rapid load change capability. This means that a SOFC/GT power plant could be operated at constant shaft speed, if air flow rate control systems are implemented, i.e. VIGV, air bypass or compressor blow off. In fact, these systems could facilitate operation at constant mean fuel cell temperature, despite the constant shaft speed. Thereby, similar behaviour as seen for the constant mean fuel cell temperature strategy may be achieved. However, the exact behaviour of such systems are not known, and they should be subject for further research. Nevertheless, it is believed that variable shaft speed facilitates a broader operational range, as it is able to increase air flow rate also above the design load. This is necessary to supply adequate fuel cell cooling when operating above 100% load.

When evaluating the results in this chapter it is important to remember that they are produced by a model, incorporating only one single fuel cell tube model. Furthermore, this fuel cell is placed close to the prereformer wall, and the prereformer will need to reform exactly the same amount of fuel that is supplied to the fuel cell. In a real system not every fuel cell can be placed next to the prereformer wall, and accordingly there will be temperature gradients throughout the stack. Thus, it is not likely that the presented model represents the exact behaviour of an actual SOFC/GT system. Still, one can assume that the *trends* seen in the presented analysis also apply to real fuel cell systems. As an example, it is not likely that the constant mean fuel cell temperature strategy will be able to impose a constant mean temperature for each individual fuel cell tube in a real stack, but it may be able to achieve a constant mean *stack* temperature. It is also very likely that this strategy will be the quickest and safest load change strategy for a real system.

7.4 Suggestions for Safe Operation

Executing load changes over a long time-period is probably the safest approach for SOFC/GT systems. If this policy is applied to one of the strategies discussed in this chapter it means moving towards the target operation point near to the steady-state load-line. Recalling Chapter 7.1.2, the load-line of a strategy represents the combination of control parameters which fulfils the load change strategy requirement at steady-state. Accordingly, transient thermal gradient maxima as seen in Figure 7-18 and Figure 7-22 may be omitted.

However, the presented analysis has shown that rapid load changes in SOFC/GT systems also can be executed at low risk. Both the constant TIT strategy as well as the constant mean fuel cell temperature strategy is able to achieve target load within a very short period, independent of the load change magnitude. If system behaviour is well-known, it is even possible to reduce time to target load below the relaxation times seen in Table 7.2. For instance it has been seen that the constant mean fuel cell strategy is affiliated by an

undershooting of the target load. If the exact behaviour is known in advance, a very rapid load change can be achieved by first setting the set-point of the controller beyond the target steady-state value, and then slowly adjusting to the steady-state set-point. This procedure is often called feedback control, and it is often used in control-system engineering. Allowing the fuel utilisation to deviate temporarily from the 85% used in this analysis may further reduce power relaxation time. However, it is believed that the constant mean fuel cell temperature strategy is safer than the TIT strategy. This is mostly because of the uncontrolled temperature escalation which the constant TIT strategy may be exposed to at low loads. Nevertheless, the constant mean fuel cell temperature may also be exposed to this hazard, as the presented dynamic analysis is inadequate to totally exclude this possibility. Accordingly, it is important that a SOFC/GT control system is able to unveil initial signs of system run-off. As seen in Figure 7-14, pressure and air flow reduction combined with increasing TIT and fuel cell temperature at fixed shaft speed, can be signals showing an early stage of a temperature escalation. Fuel reduction, increased shaft speed or heat exchanger bypassing are some actions which may be able to prevent this event. It is further important that the control system is able to adjust to system degradation and changes in fuel flow composition. If not, it can be very risky to operate close to the system stability limit.

8 Conclusions and Suggestions for Further Work

8.1 Conclusions

The aim of this work was to develop a dynamic SOFC/GT modelling tool, adequate for transient analysis and control system strategy investigations. An advanced dynamic SOFC/GT model comprising of a plate-fin recuperator and a shell-tube heat exchanger for air preheating, an anode exhaust gas recycling loop for steam/carbon-ratio control, a fuel gas prereformer for syngas production and a combustion chamber has been presented. The SOFC design is similar to the tubular fuel cells developed by Siemens Westinghouse. The SOFC and both the heat exchangers are spatially distributed models. In addition, performance maps are used to calculate part-load performance of the compressor and turbine. Gas turbine transients are accounted for by a shaft model which includes moment of inertia.

Calibration of the SOFC model has shown conformity between model predicted and experimental results. SOFC and system properties have been investigated by means of a sensitivity study. The study showed that material properties have a high influence on activation polarisation and diffusion losses, but that the overall impact of these losses on system performance is relatively small at normal operating conditions. The analysis also revealed that the degree of prereforming has a large influence on the temperature distribution of the fuel cell. In fact, increased degree of prereforming leads to flattening of the axial fuel cell temperature profile. Recuperator size proved to influence both system performance as well as stability. At part-load, an excessively large recuperator appeared to recover too much heat and thus caused an uncontrolled temperature rise beyond SOFC material limitations.

The SOFC/GT model capabilities have been demonstrated by a dynamic study, incorporating three different load change strategies; constant mean fuel cell temperature, constant turbine inlet temperature (TIT) and constant shaft speed. The study indicated a large degree of path dependency with power response time as well as risk of malfunctions. A strong dependency between the fuel cell temperature and power was found, and a general conclusion is that the less the fuel cell temperature is changed; the lower is the power relaxation time. This makes temperature control of the fuel cell highly important, not only with respect to safety, but also in order to be able to respond to rapidly changing load demands.

The constant mean fuel cell temperature strategy represents the most rapid load change method. Load changes according to this strategy proved to represent the least thermal cycling of the fuel cell stack, and this is also the explanation for the rapid load change capabilities when compared to the two other strategies. Low degree of thermal cycling also implies that this strategy is less exposed to thermal cracking and delamination. However, this strategy exhibited larger thermal gradients in the membrane electrode assembly (MEA) during transients than at steady-state when load was increased from 50% to 100%. This was also found for the constant TIT strategy, and for both strategies the increased thermal gradients was concurrent with a reduction in degree of prereforming

Thus, special care must be taken when degree of prereforming is reduced during rapid and large load increases. At part-load, the constant mean fuel cell temperature strategy lead to the least exposure towards factors which are known to promote fuel cell degradation. Both the constant mean fuel cell strategy and the constant TIT strategy had a smaller surge margin during load reduction transients than at steady-state part-load operation. Nevertheless, both strategies stayed within safe distance from surge during the all the simulations.

The constant TIT strategy proved to be the slowest strategy for small load changes, but it was the second best for large load changes. However, this strategy did actually reach target load more rapidly than the constant mean fuel cell temperature, but it went beyond the target load and it took a long time to reach steady-state. At very low load (50%) the TIT-requirement for this strategy had to be adjusted in order not to run into unstable operation. If not corrected for, operation at low load might eventually lead to gas temperatures beyond material limitations.

The constant shaft speed strategy needed the most time to adapt to a new load. Large load reductions according to the constant shaft speed strategy also implied operation at very low fuel cell temperatures. Furthermore, this strategy lead to the highest part-load current density and thus degradation is likely to be more rapid for this strategy than for the two others. The constant shaft speed strategy also implies lower part-load efficiencies than the two other strategies. The low part-load efficiency was caused by an increased air flow rate which resulted in very low fuel cell temperatures and thus also low voltage. Therefore, this strategy is considered unsuitable for large load reductions, unless air flow rate control systems are implemented. Variable inlet guide vanes (VIGV), air bypass or compressor blow off are methods which can be used to enhance controllability and performance for systems operating at constant shaft speed.

The discrepancy between the three strategies proved mainly to be caused by different air flow, degree of prereforming and voltage, thus emphasising the importance of thermal management of the SOFC. Reduced response time may therefore be achieved by efficient control of the heating or cooling duty of the air flow and the prereformer.

The power relaxation time for all the above mentioned load change strategies can be further reduced by feedback control, i.e. temporarily setting the control parameters for larger load changes than required, and slowly adjusting the parameters as the power production approaches target load. Such an advanced control system is demonstrated in the paper given in Appendix F.

Irrespective of which load change strategy is applied to the SOFC/GT system, it is important that the control system is able to detect early stage signs of system-run off, compressor surge, carbon deposition and that it facilitates temperature control of the fuel cell. It is further important that it is able to account for system degradation, as well as variations in the fuel composition.

The main contributions from the presented work are the following:

- Compared to previously published work, a more detailed, flexible and dynamic SOFC/GT system model has been developed.
- Three different load change strategies have been investigated and evaluated.
- It has been shown that SOFC/GT systems are suitable for rapid load change operation, provided the implementation of an adequate control system.
- The constant mean fuel cell temperature strategy is the most appropriate load change strategy in this aspect.

8.2 Suggestions for Further Work

The presented SOFC/GT system model has a higher detailing level than what has been reported in the open literature, especially concerning the spatial distribution of the tubular SOFC model. However, the presented analysis has revealed that more effort should be put into model refinement of some of the components. The strong dependency between SOFC temperature distribution and degree of prereforming calls for a more accurate model of the prereformer. Indeed, such a model is developed and it is briefly described in Appendix F, but a thorough cycle analysis is still lacking. More material and geometrical data are needed in order to perform an adequate analysis. Further work should also include an investigation of the influence of different fuels and fuel processing methods, as the presented analysis is based only on steam reforming of methane.

A further enhancement of the SOFC model could be the implementation of several SOFC tubes, representing different locations within the stack. This can be accomplished by using several instances of the SOFC model with different boundary conditions. It is further suggested that the simplified ejector model in the presented model is exchanged with a more detailed ejector model. Thereby, it should be possible to investigate the influence of the dynamic behaviour of the ejector upon system dynamics. It would also facilitate the prediction of anode exhaust backflow. Such a model has been developed and is utilised in the papers given in Appendix E and Appendix F. However, more geometrical and performance data are needed in order to perform a thorough system analysis.

Although good agreement between the SOFC model and the experimental data was achieved by the model calibration, even better agreement could be achieved if more material data of the fuel cell and experimental data were available. Especially, if one considers the large number of references which have been used to acquire a complete set of data for the fuel cell model. Accurate data on material strength, durability and thermal expansion factors are of special interest, as these data would facilitate a more comprehensive investigation of the consequences of thermal cycling. It is further important to procure experimental data from a complete SOFC/GT cycle in order to verify the overall system model.

The present dynamic SOFC/GT system model can be utilized in more comprehensive dynamic studies than what has been demonstrated in this work. An extension of the present work could include operation over a larger load range as well as load change between part-load operation points. Furthermore, the presented model can be utilised to

test control systems, and this may give better information on how to operate these types of systems.

For further work it is also suggested that similar studies as described here, are undertaken on other configurations of the SOFC/GT system. In this study, the shaft speed has been used to control the air flow rate, but variable inlet guide vanes (VIGV), air bypass or compressor blow off are methods which can be utilised. If for instance VIGV are employed, the constant shaft speed strategy may prove to be more rapid and safe than what has been observed in this work due to better fuel cell temperature control. VIGV can further be used in combination with variable shaft speed. Two-shaft turbines should also be included in an extended analysis.

References

[Achenbach, 1994] Achenbach, E., Riensche, E., Methane/steam reforming kinetics for solid oxide fuel cells, Journal of Power Sources, 52 (1994) 283-288

[Achenbach, 1995] Achenbach, E., *Response of a solid oxide fuel cell to load change*, Journal of Power Sources 57 (1995) 105-109.

[Ali, 2001] Ali, S. A., Moritz, R. R, *"A Turbogenerator for Fuel Cell/Gas Turbine Hybrid Power Plant"* Proceedings of ASME TURBO EXPO 2001, June 4-7, 2001, New Orleans, Luisiana, USA, 2001-GT-0524.

[Atkinson, 2000] Atkinson, A., Selcuk, A., *Mechanical behaviour of ceramic oxygen ion-conducting membranes*, Solid State Ionics 134 (2000) 59-66.

[Bossel, 1992] Bossel, Ulf G., *Final report on SOFC data, Facts and Figures*, Swiss Federal Institute of Energy, Operating Task II, Berne, April 1992.

[Campanari, 2000] Campanari, S., *Full load and part-load performance prediction for integrated SOFC and microturbine systems*, Journal of Engineering for Gas Turbines and Power, 2000, Vol. 122, p 239-246.

[Campanari, 2004] Campanari, S., Iora, P., *Definition and sensitivity analysis of a finite volume SOFC model for tubular geometry*. Journal of Power Sources 132 (2004) 113-126.

[Chan, 2001] Chan, S. H., Khor, K. A., Xia, Z. T., *A complete polarization model of a solid oxide fuel cell and its sensitivity to the change of cell component thickness*, Journal of Power Sources, 93 (2001) 130-140.

[Chan, 2002] Chan, S. H., Ho, H. K., Tian, Y., *Modelling of simple hybrid solid oxide fuel and gas turbine power plant*, Journal of Power Sources, 109 (2002) 111-120.

[Chan, 2003a] Chan, S. H., Ho, H. K., Tian, Y., *Multi-level modeling of SOFC-gas turbine hybrid system*, International Journal of Hydrogen Energy, 28 (2003) 889-900.

[Chan, 2003b] Chan, S. H., Ho, H. K., Tian, Y., *Modeling for part-load operation of solid oxide fuel cell-gas turbine hybrid power plant*, Journal of Power Sources, 114 (2003 213-227.

[Cheremisinoff, 1986] Cheremisinoff, N. P., *Handbook of Heat and Mass Transfer, Volume 2: Mass Transfer and Reactor Design*, Gulf Publishing Company, 1986.

[Costamagna, 1998] Costamagna, P., Honegger, K., *Modelling of Solid Oxide Heat Exchanger Integrated Stacks and Simulation at High Fuel Utilisation*, Journal of Electrochemical Society, Vol. 145, No 11, pp 1995-4007.

[Costamagna, 2001] Costamagna, P., Magistri, L., Massardo, A. F., *Design and part-load performance of a hybrid system based on a solid oxide fuel cell reactor and a micro gas turbine*, Journal of Power Sources, 96 (2001) 352-368.

[Cussler, 1997] Cussler, E. L., *Diffusion - Mass Transfer in Fluid Systems 2nd Ed*, Cambridge University Press, 1997.

[Divisek, 1994] Divisek, J., de Haart, L. G. J., Holtappels, P., Lennartz, T., Malléner, W., Stimming, U., Wippermann, K., *The kinetics of electrochemical reactions on high temperature fuel cell electrodes*, Journal of Power Sources, 49 (1994) 257-270.

[Gemmen, 2000] Gemmen, R. S., Rogers, W., A., Prinkey, M. T., *Application of a Computational Fluid Dynamics Code to Fuel Cells - Integrated SOFC Fuel Cell and Post Oxidizer*. Fluent, Technical Notes TN128.

[Gemmen, 2005] Gemmen, R. S., Johnson, C. D., *Effect of load transients on SOFC operation - current reversal on loss of load*, Journal of Power Sources - ***In Press!***

[George, 2000] George, R. A., *Status of tubular SOFC field demonstrations*, Journal of Power Sources, 2000, Vol. 86, p 134-139.

[gPROMS, 2004] *gPROMS Introductory User Guide*, Process Systems Enterprise Ltd., Release 2.3.1, June 2004.

[Haynes, 2002] Haynes, C., *Simulating process settings for unslaved SOFC response to increases in load demand*, Journal of Power Sources 109 (2002) 365-376.

[Hermann, 2002] Hermann, F., Pålsson, J., Mauss, F., *Combustor Design Analysis for SOFC Off-gases.* Fifth European Solid Oxide Fuel Cell Forum, 1.-5. July 2002, Lucerne, Switzerland.

[Inui, 2003] Inui, Y., Yanagisawa S., Ishida, T., *Proposal of high performance SOFC combined power generation system with carbon dioxide recovery*, Energy Conversion and Management, 44 (2003) 597-609.

[Jenne, 2002] Jenne, M., Zähringer, T., *Sulzer Hexis SOFC systems for biogas and heating oil*, Proceedings of the 5th European Fuel Cell Forum, 1-5 July, 2002, Lucerne, Switzerland, Vol. 1, p 461-466.

[Jiang, 2004] Jiang, S. P., Chan, S. H., *A review of anode materials development in solid oxide fuel cells*, Journal of Materials Science, 39 (2004) 4405-4439.

[Jørgensen, 2000] Jørgensen, M, J., Holtappels, P., Appel C. C., *Durability test of SOFC cathodes*, Journal of Applied Electrochemistry 30: 411-418, 2000.

[Karoliussen, 1993] Karoliussen, H., *Matematisk modellering av fastoksid brenselcelle*, Doctoral Thesis at Department of Technical Electrochemistry, Norwegian Institute of Technology, 1993.

[Kays, 1984] Kays, W. M., London, A. L., *Compact Heat Exchangers,* McGraw-Hill, 1984.

[Khandkar, 1999] Khandkar, A., Hartvigsen, J., Bangovan, S., Rowley, D., Privette, R., Tharp, M., *Status and progress in SOFCo's planar SOFC development*, The 6th International Symposium on Solid Oxide Fuel Cells, Oct. 17-22, 1999.

[Kimijima, 2002] Kimijima, S., Kasagi, N., *Performance evaluation of gas turbine-fuel cell hybrid micro generation system*, Proceedings of ASME TURBO EXPO 2002, GT-2002-30111.

[Kordesch, 1996] Kordesch, K., Simader, G., *Fuel Cells and Their Applications,* VCH - Weinheim, 1996.

[Kuchonthara, 2003] Kuchonthara, P., Bhattacharya, S., Tsutsumi, A., *Combinations of solid oxide fuel cell and several enhanced gas turbine cycles*, Journal of Power Sources, 124 (2003) 65-75.

[Kurzke, 2004] Kurzke, J., *Compressor and Turbine Maps for Gas Turbine Performance Computer Programs - Component Map Collection 2*, Joachim Kurzke, Dachau, 2004

[Larminie, 2000] Larminie, J., Dicks, A., *Fuel Cell Systems Explained.* John Wiley & Sons Ltd., 2000.

[Larrain, 2003] Larrain, D., Van Herle, J., Maréchal, F., Favrat, D., *Thermal modelling of a small anode supported solid oxide fuel cell*, Journal of Power Sources 118 (2003) 367-374.

[Lehnert, 2000] Lehnert, W., Meusinger, J., Thom, F., *Modelling of gas transport phenomena in SOFC anodes*, Journal of Power Sources 87 (2000) 57-63.

[Lowrie, 2000] Lowrie, F. L., *Room and high temperature failure mechanisms in solid oxide fuel cell electrolytes.* Journal of the European Ceramic Society, 20 (2000) 751-760.

[Lu, 2005] Lu, Y., Schaefer, L., Li, P., *Numerical study of a flat-tube high power density solid oxide fuel cell. Part I. Heat/mass transfer and fluid flow.* Journal of Power Sources, In Press, Uncorrected Proof!

[Magistri, 2002] Magistri, L., Bozzo, R., Costamagna, P., Massardo, A. F., *Simplified versus detailed SOFC reactor models and influence on the simulation of the design point performance of hybrid systems,* ASME TURBU EXPO 2002, GT-2002-30653.

[Magistri, 2003] Magistri, L., Bozzolo, M., Tarnowski. O., Agnew, G., Massardo, A. F., *Design and off-design analysis of a MW hybrid system based on Rolls-Royce integrated planar SOFC,* Proceedings of ASME TURBO EXPO 2003, GT2003-38220.

[Magistri, 2004a] Magistri, L., Transino, F., Costamagna, P., *Transient Analysis of Solid Oxide Fuel Cell Hybrids: Part A Fuel Cell Models*, Proceedings of ASME TURBO EXPO 2004, GT2004-53842.

[Magistri, 2004b] Magistri, L., Ferrari, M., Traverso, A., Costamagna, P., Massardo, A. F., *Transient Analysis of Solid Oxide Fuel Cell Hybrids: Part C Whole Cycle Model*, Proceedings of ASME TURBO EXPO 2004, GT 2004-53845.

[Mills, 1995] Mills, A. F., *Heat and Mass Transfer*, IRWIN, Irwin Heat Transfer Series, 1995

[Minh, 1995] Minh, N. Q., Takahashi, T., 1995. *Science and Technology of Ceramic Fuel Cells.* Elsevier 1995.

[Mogensen, 1993] Mogensen, M., Lindegaard, T., *The kinetics of hydrogen oxidation on a Ni-YSZ SOFC electrode at 1000C.* Proceedings of the Third International Symposium on Solid Oxide Fuel Cells, p 484-93

[Mogensen, 2002] Mogensen, M., Jensen, K. V., Jørgensen, M. J., Primdahl, S., *Progress in understanding SOFC electrodes*, Solid State Ionics 150 (2002) 123 - 129.

[Multiflash, 2001] Multiflash Command Reference, Infochem Computer Services Ltd., V 3.0 15 Feb. 2001.

[Nakajo, 2005] Nakajo. A., *Simulation of thermal stresses in tubular SOFC*, Master thesis performed at Institute of Energy Sciences of Swiss Federal Institute (Lausanne), 2005.

[NASA, 2005] http://science.nasa.gov/headlines/y2003/18mar_fuelcell.htm, vitisted at 26.04.05

[Nisancioglu, 1989] Nisancioglu, Kemal, *Natural gas fuelled solid oxide fuel cells and systems - ohmic losses*, International Energy Agency, Workshop on Mathematical Modelling, Charmey, Switzerland, July 2.-6., 1989.

[Oh, 1996] Oh, M., Pantelides, C. C., *A modelling and Simulation Language for Combined Lumped and Distributed Parameter Systems*, Computers Chem. Eng., Vol 20, No 6/7, p 611-633, 1996

[Onuma, 2000] Onuma, S., Kaimai, A., Kawamura, K., Nigara, Y., Kawasa, T., Mizusaki, J., Tagawa, H., *Influence of the coexisting gases on the electrochemical reaction rates between 873 and 1173 K in a CH_4/Pt/YSZ system.* Solid State Ionics 132 (2000) 309-331.

[Ota, 2003] Ota, T., Koyama, M., Wen, C., Yamada, K., Takahashi, H., *Object-based modelling of SOFC-system: dynamic behaviour of micro-tube SOFC*, Journal of Power Sources 118 (2003) 430-439.

[Padullés, 2000] Padullés, J., Ault, G. W., McDonald, J. R., *An integrated SOFC plant dynamic model for power systems simulation*, Journal of Power Sources 86 (2000) 495-500.

[Pålsson, 2000] Pålsson, J., Selimovic, A., Sjunnesson, L., *Combined solid oxide fuel cell and gas turbine systems for efficient power and heat generation*, Journal of Power Sources 86 (2000) 442-448.

[Pålsson, 2001] Pålsson, J., Selimovic, A., *Design and off-design predictions of a combined SOFC and gas turbine system*, Proceedings of ASME TURBO EXPO 2001, 2001-GT-0379.

[Pålsson, 2002] Pålsson, J., 2002, *Thermodynamic Modelling and Performance of Combined Solid Oxide Fuel Cell and Gas Turbine Systems*, Doctoral Thesis, Lund University, ISSN 0282-1990.

[Rao, 2001] Rao, A. D., Samuelsen, G. S., *A Thermodynamic analysis of tubular sofc based hybrid systems*, Proceedings of ASME TURBO EXPO 2001, 2001-GT-0522.

[Rechenauer, 1992] Rechenauer, Ch., Achenbach, E., *Dreidimensionale mathematische Modellierung des stationären und instationären Verhaltens oxidkeramischer Hochtemperatur-Brennstoffcellen,* Diss. RWTH-Aachen 1992, Berichte des Forschunszentrum Jülich; 2753.

[Reid, 1987] Reid, R. C., Prausnitz, J. M., Poling, B. E., *The Properties of Gases and Liquids.* McGraw-Hill, New York, 1987.

[Riensche, 2000] Riensche, E., Achenbach, E., Froning, D., Haines M. R., Heidug, W. K., Lokurlu, A., von Adrian, S., *Clean combined-cycle SOFC power plant - cell modelling and process analysis*, Journal of Power Sources, 86 (2000) 404-410.

[Rohsenow, 1998] Rohsenow, W. M., Hartnett, J. P., Cho, Y. I., *Handbook of Heat Transfer*, 3rd Ed. McGrav-Hill. 1998.

[Saravanamuttoo, 2001] Saravanamuttoo, H. I. H., Rogers, G. F. C., Cohen, H., *Gas Turbine Theory*, 5th Ed., Prentice Hall, 2001

[Saunders, 2002] Saunders, G. J., Kendall, K., *Reactions of hydrocarbons in small tubular SOFCs,* Journal of Power Sources, Vol. 106, 2002, p 258-263.

[Selimovic, 2002] Selimovic, Azra, *Modelling of Solid Oxide Fuel Cells Applied to the Analysis of Integrated Systems with Gas turbines*, Doctoral Thesis, 2002, Lund University, Division of Thermal Power and Engineering, Department of Heat and Power Engineering.

[Singhal, 2002] Singhal, S. C., *Review - Solid oxide fuel cells for stationary, mobile and military applications,* Solid State Ionics, 152-153 (2002) 405-410.

[Singhal, 2003] Singhal, S. C., Kendall, K., *High Temperature Solid Oxide Fuel Cells - Fundamentals, Design and Applications*, Elsevier Ltd., 2003

[Song, 2004] Song, T., W., Sohn, J. L., Kim, J. H., Kim, T, S., Ro, S. T., Suzuki, K., *Parametric studies for a performance analysis of a SOFC/MGT*

hybrid power system based on a quasi-2D model, Proceedings of ASME TURBO EXPO 2004, GT2004-53304.

[Stiller, 2006] Cristoph Stiller, Doctoral Thesis, Department of Energy and Process Engineering, NTNU, Trondheim, Norway, to be submitted in December 2005.

[Tanaka, 2000] Tanaka, K., Wen, C., Yamada, K., *Design and evaluation of combined cycle system with solid oxide fuel cell and gas turbine.* Fuel 79 (2000) 1493-1507.

[Thorud, 2004] Thorud, B., Stiller, C., Weydahl, T., Bolland, O., Karoliussen, H., *Part-load and load change simulation of tubular SOFC systems,* Proceedings of the 6th European Solid Oxide Fuel Cell Forum, Vol. 2.

[Traupel, 1966] Traupel, W., Thermische Turbomaschinen, Erster Band, Thermodynamisch-strömungstechnische Berechnung, 2 Auflage, Springer-Verlag, 1966.

[Tu, 2005] Tu, H., Stimming, U., *Advances, aging mechanisms and life-time in solid oxide fuel cells,* Journal of Power Sources 127 (2005) 284-293.

[Ulfsnes, 2006] Ragnhild Ulfsnes, Doctoral Thesis, Department of Energy and Process Engineering, NTNU, Trondheim, Norway, to be submitted in December 2005.

[Veyo, 2003] Veyo, S. E., Lundberg, W. L., Vora, S. D., Litzinger, K. P., *Tubular SOFC hybrid power system status,* Proceedings of ASME TURBO EXPO 2003, GT2003-38943.

[Waldbillig, 2005] Waldbillig, D., Wood, A., Ivey, D. G, *Thermal analysis of the cyclic reduction and oxidation behaviour of SOFC anodes,* Solid State Ionics 176 (2005) 847-859.

[Winkler,2000] Winkler, W., Hagen, L., *Layout of SOFC-GT cycles with electric efficiencies over 80%,* Proceedings of the 4th European Fuel Cell Forum, 1-5 July, Lucerne, Switzerland, Vol. 1, p 413-420.

[Winkler,2002] Winkler, W., Lorenz, H., *The Design of stationary and mobile solid oxide fuel cell-gas turbine systems,* Journal of Power Sources, Vol. 105, 2002, p 222-227.

[Yakabe, 2001] Yakabe, H., Ogiwara, T., Hishinuma, M., Yasuda, I., *3-D model calculation for planar SOFC,* Journal of Power Sources, 102 (2001) 144-154.

[Yakabe, 2004] Yakabe, H., Baba, Y., Sakurai, T., Yoshitaka, Y., *Evaluation of the residual stress for anode-supported SOFCs,* Journal of Power Sources 135 (2004) 9-16.

[Yi, 2003] Yi, Y., Smith, T. P., Brouwer, J., Rao, A. D., Samuelsen, G. S., *Simulation of a 220 kW hybrid SOFC gas turbine system and data comparison,* Solid Oxide Fuel Cells VIII (SOFC VIII), Proceedings

of the International Symposium, The Electrochemical Society. Vol. 2003-7, p 1442-1454.

[Yi, 2004] Yi, Y., Rao, A. D., Brouwer, J., Samuelsen, S. G., *Analysis and optimization of a solid oxide fuel cell and intercooled gas turbine (SOFC-ICGT) hybrid cycle*, Journal of Power Sources, 134 (2004) 77-85.

[Ødegård, 1995] Ødegård, R., Johnsen, E., Karoliussen, H., Methane reforming on Ni/Zirconia SOFC anodes, Proceedings of the 4th International Symposium on Solid Oxide Fuel Cells, Yokohama, Japan, June 18-23, 1995.

Appendix A - Paper I

Finite-volume modelling and hybrid-cycle performance of planar and tubular solid oxide fuells

Christoph Stiller, Bjørn Thorud, Steinar Seljebø, Øistein Mathiesen, Håvard Karoliussen, Olav Bolland

Journal of Power Sources, Vol 131, 2005, p 227 - 240

Available online at www.sciencedirect.com
SCIENCE DIRECT®
Journal of Power Sources 141 (2005) 227–240
JOURNAL OF POWER SOURCES
www.elsevier.com/locate/jpowsour

Finite-volume modeling and hybrid-cycle performance of planar and tubular solid oxide fuel cells

Christoph Stiller*, Bjørn Thorud, Steinar Seljebø, Øistein Mathisen, Håvard Karoliussen, Olav Bolland

Department of Energy and Process Engineering, Norwegian University of Science and Technology, Kolbjorn Hejes vei 1B, Trondheim N-7491, Norway

Received 18 February 2004; received in revised form 14 July 2004; accepted 27 September 2004
Available online 23 November 2004

Abstract

The paper describes two 2D steady-state models for solid oxide fuel cells (SOFC) with planar and tubular geometries fuelled by methane. Following a description of the basic geometries and general premises the approaches, assumptions and simplifications for the calculation of ohmic resistance, convective, conductive and radiative heat transfer are given. The modeling approach of the chemical reactions and molar and thermal balances are depicted in detail with the intention to allow for reproduction of the models. The required boundary conditions and input parameters of the models are also discussed. Relying on models, a bottoming GT cycle is introduced and specified and a base case for operation defined. The influence of pressure ratio, air inlet temperature, air flow rate and anode gas recycling are investigated in a parameter study. For both designs air flow rate and pressure ratio are the most important parameters considering the system performance, but for the tubular system these parameters have less impact than for the planar design. Based on the parameter study, a near-optimum case is defined specifically for both systems and the conditions in the fuel cells are investigated. The cycle balance is different in both systems, as the tubular fuel cell requires a lower air inlet temperature. Both fuel cell systems achieve above 65% electric efficiency.

Keywords: SOFC; Tubular; Planar; Model; Hybrid

1. Introduction

Combined solid oxide fuel cells and gas turbine (SOFC)/GT cycles promise to achieve high electric efficiencies even for small-scale systems with power output below 10 MW and hence have a certain potential in decentralized power generation concepts. However, there is a lot of uncertainty about the best layout of the fuel cell and the hybrid cycle in terms of feasibility, performance, economics and controllability. This paper compares the performance of the two most common SOFC geometries, namely planar and tubular, in a gas turbine hybrid cycle. It describes the configuration of the fuel cells and gives a comprehensive and reproducible description of the approach, assumptions and methods used for the steady-state models of the different geometries. After a validation of the fuel cell models, their implementation into the gas turbine cycle simulation is described, and the performance of combined cycles with planar and tubular SOFCs are studied and compared. Departing from a base case, the sensitivities to certain process parameters are studied and discussed and operational options and constraints are derived. The maximum efficiency under near-optimum operation is estimated.

2. Fuel cell models

2.1. Fuel cell geometries and modeling premises

The investigated planar SOFC is a cross-flow, electrolyte-supported cell. A previously in-house developed repeat

Abbreviations: CV, control volume; FU, fuel utilization; GT, gas turbine; PEN, positive electrode–electrolyte–negative electrode; SOFC, solid oxide fuel cell; TIT, turbine inlet temperature

* Corresponding author. Tel.: +47 7359 3723; fax: +47 7359 8390.
E-mail address: Christoph.stiller@ntnu.no (C. Stiller).

0378-7753/$ – see front matter © 2004 Elsevier B.V. All rights reserved.
doi:10.1016/j.jpowsour.2004.09.019

Nomenclature

Symbols

A	area (m^2)
A_{act}	active cell area (m^2)
co	gas component
c_p	specific heat capacity ($J\,K^{-1}\,mole^{-1}$)
D_h	hydraulic diameter (m)
E^{rev}	reversible potential (V)
F	Faraday constant ($96485\,C\,mole^{-1}$)
I	total CV current (A)
J	lumped parameter
L	length (m)
n	molar flow ($mole\,s^{-1}$)
Nu	Nusselt number
p	pressure (Pa)
$\dot{Q}$	radiative heat flow (W)
R	universal gas constant ($8.314\,J\,K^{-1}\,mole^{-1}$)
r	radius (m)
$r_{...}$	reaction rate ($mole\,s^{-1}$)
$R_{1...}R_5$	heat resistivity of planar model building blocks (kW^{-1})
$R_{p,i}$; $R_{p,j}$	solid heat resistivity of planar model in i- and j-direction (kW^{-1})
$R_{t,ax}$	axial heat resistivity of tubular model (kW^{-1})
$R_{t1...}R_{t6}$	radial chain heat resistivity of tubular model (kW^{-1})
R_Ω	ohmic resistance (Ω)
T	temperature (K)
T_{black}	temperature of black body receiving radiation energy for the pre-reformer
U	cell voltage (V)

Greek letters

α	convective heat transfer coefficient ($W\,m^{-2}\,K^{-1}$)
δ	thickness (m)
ΔH	enthalpy change ($J\,mole^{-1}$)
ε	emissivity (0.8)
η	overpotential (V)
λ	heat conduction efficient ($W\,m^{-1}\,K^{-1}$)
ρ	specific resistance ($\Omega\,m$)
σ	Stefan–Boltzmann-constant ($5.67 \times 10^{-8}\,W\,m^{-2}\,K^{-4}$)

Indexes

a	anode
a_1	cathode air (tubular model)
a_2	injector air
air	air (planar)
c	cathode
co	gas component counter
e	electrolyte
electro	electrochemical reaction
f	fuel
i, j	counter for CV number in i- and j-direction
ic	interconnect
inj	injector
irrad	irradiation
p	planar
preref	pre-reformer
rad	radiation
ref	reforming reaction
s	solid (tube material)
shift	shift reaction
t	tubular

element geometry with a size of 3.8 mm × 3.8 mm [1] has been used as control volume. In order to scale the cell to the standard size of 100 mm × 100 mm, a matrix of 26 × 26 repeat elements is required. The resulting length of the cell is 98.8 mm. The tubular geometry is based on the current Siemens–Westinghouse technology [2], which is a cathode-supported, 1.5 m long and 22 mm diameter vertical tube. The air enters an inner tube (injector) from the top, is preheated while flowing downwards to the end of the tube where it turns and flows upwards between the cathode and the injector tube. The fuel is correspondingly fed from outside the tube and flows upwards. Fig. 1 shows the control volume of the planar and the tubular cell, together with the respective key dimensions and the materials. The tube interconnect that penetrates the anode and electrolyte is not shown here.

The following assumptions, simplifications and premises were chosen for the proposed models:

1. The fuel is partially pre-reformed methane.
2. Internal reforming at the anode. Kinetics of the reforming reaction are respected while the shift reaction is always at equilibrium.
3. A pre-reformer is thermally integrated by radiation from the edges of the cells for the planar design and radiation from the solid in the tubular design. The pre-reformer itself is not integrated in the SOFC model, but the required amount of heat is an input variable.
4. Single-cell setup is considered, i.e. adiabatic boundaries except the pre-reformer are assumed.
5. The electrochemical kinetics is limited to activation overpotential, i.e. no diffusion overpotential is calculated.
6. In the planar model, each CV has one temperature node respectively for solid, air and fuel temperature. The tubular model has additionally temperature nodes for the injector air and the injector tube.
7. Heat conduction is calculated in two dimensions in the planar model, neglecting heat flow in the stacking direction. The tubular model features heat conduction in axial direction as well as radiation between the concentric tubes.

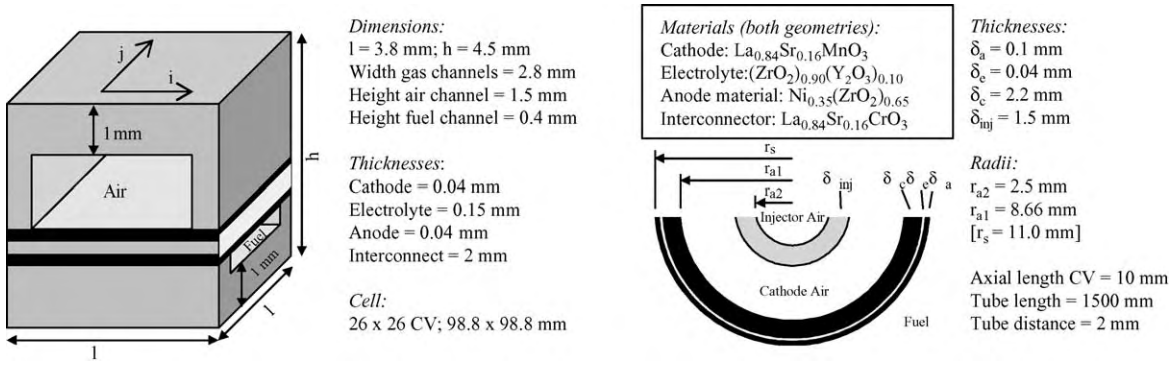

Fig. 1. Basic geometries of planar and tubular fuel cell control volume.

8. Radiation inside the planar cell is not included. In the tubular cell, radiation between the solid and the injector tube is modeled.

Similar work has been performed by Selimovic [3], Campanari [4] and some other SOFC researchers. The models present a common approach for finite-volume modeling of SOFC, detailed enough to give information about the internal behaviour of the cell and lean enough to be implemented into a hybrid system model and be solved within a reasonable calculation time.

2.2. Ohmic resistance

The ohmic resistance consists of the electronic current resistance in the interconnect and electrodes, and the ionic resistance in the electrolyte. The latter is the most dominating in both concepts.

In the planar model, the electronic resistance of anode, cathode and interconnect is low compared to the electrolyte resistance [5] and can be regarded as temperature independent within the given operating conditions. The material specific values for a temperature of 1173 K from Bossel [5] have been used to calculate the resistance of the layers. Conductivity and resistance for one CV as well as the temperature dependency of the electrolyte is listed in Table 1.

Even though in the tubular model, the same materials as for the flat plate model are applied, the properties given in literature are different due to unlike production techniques. Therefore, mostly temperature dependant resistances have been chosen for the tubular model. Also, the geometry is more complex than for the flat plate design. Although the tube is modeled in 2D, effects from current flowing in the 3rd direction (tangential) are accounted for by using the analytical expression for ohmic resistance of a control volume of the tube developed by Nisancioglu [6]. The expression is given in Eqs. (1)–(3), describing the so-called transmission line model. For further explanation, it is referred to the work of Niscanscioglu [6].

$$R_\Omega(\Omega) = L_{CV}\left(\frac{\left(\left(\frac{\rho_a}{\delta_a}\right)^2+\left(\frac{\rho_c}{\delta_c}\right)^2\right)\cosh(J_e)+\frac{\rho_a\rho_c}{\delta_a\delta_c}(2+J_e\sinh(J_e))}{2\left(\frac{1}{\rho_e\delta_e}\right)^{1/2}\left(\frac{\rho_a}{\delta_a}+\frac{\rho_c}{\delta_c}\right)^{3/2}\sinh(J_e)}+\frac{\sqrt{\rho_{ic}\delta_{ic}\left(\frac{\rho_c}{\delta_c}\right)}}{2\tanh(J_{ic})}\right) \quad (1)$$

where

$$J_e = \frac{L_e}{2}\sqrt{\frac{1}{\rho_e\delta_e}\left(\frac{\rho_a}{\delta_a}+\frac{\rho_c}{\delta_c}\right)} \quad (2)$$

and

$$J_{ic} = \frac{L_{ic}}{2}\sqrt{\frac{1}{\rho_{ic}\delta_{ic}}\frac{\rho_a}{\delta_a}} \quad (3)$$

with the terms $\rho_{ic}\delta_{ic} = 0.002\,\Omega\,cm^2$ (taken from Nisancioglu [6]); $\rho_e = 8.78\times10^{-3}\,e^{9165/T}\,\Omega\,cm$ (taken from Ota [7]); $\rho_a = 2.99\times10^{-3}\,e^{-1395/T}\,\Omega\,cm$ (taken from Ota [7]); $\rho_c = 7.99\times10^{-3}\,e^{601/T}\,\Omega\,cm$ (taken from Ota [7]); $L_{CV} = 1$ cm (axial length of CV); $L_e = 6.16$ cm (circumferential length of electrode); $L_{ic} = 0.6$ cm (circumferential length of interconnect) and the thickness δ to be taken from Fig. 1.

Table 1
Ohmic resistances for the planar model

Layer	Conductivity (S m^{-1})	CV resistance (Ω)
Anode	30.39×10^3	91.24×10^{-6}
Cathode	12.87×10^3	215.2×10^{-6}
Interconnect	3.11×10^3	44.53×10^{-3}
Electrolyte	$33.4\times10^3\,e^{(-10300/T)}$	$3.11\times10^{-4}\times e^{(10300/T)}$

Table 2
Nusselt numbers and hydraulic diameters

	Planar model		Tubular model			
	Air side	Fuel side	Inner air, injector	Outer air w.r.t. injector	Outer air w.r.t. cathode	Fuel, anode
Nu	4[a]	6.2[a]	4.36[b]	10[b]	7[b]	1.8[b]
D_h (mm)	1.953	0.7	5	9.328	9.328	11.3

[a] Taken from [10].
[b] Taken from [8].

2.3. Convective and conductive heat transfer

The heat transfer in the models is implemented by applying an electrical analogy, i.e. by calculation of thermal resistances.

The convective heat transfer coefficients α for all gas–solid interfaces are determined via the Nusselt number:

$$\alpha = \frac{Nu\lambda}{D_h} \tag{4}$$

The flow is assumed to be laminar and entrance effects have been neglected. Table 2 shows the Nusselt numbers *Nu* and hydraulic diameters D_h of the flow channels. Note that flow in annular ducts has different Nusselt numbers with respect to the inner and outer surface [8].

The heat conduction coefficients λ of the gases are calculated separately for the temperature and gas composition of each control volume using the polynomic formulae from Bossel [5] for each gas species.

Thermal conductivities of the solids are considered to be constant and their values are listed in Table 3.

The cells are assumed to operate under adiabatic conditions, thus heat conduction between adjacent cells is neglected. Only heat conduction between adjacent CVs, thus in *i*- and *j*-direction, is modeled. Due to its low thickness, the PEN structure is neglected in terms of heat conduction. For the heat transfer in *i*- and *j*-direction, the thermal resistance of a CV is calculated by dividing the interconnect into basic rectangular building blocks and calculating a total resistance of the circuit. The building block model, the resulting circuit in *i*-direction (*j* direction analogous) and the resulting total resistance equations are shown in Fig. 2.

In the tubular model, heat transfer in the radial direction is calculated by using an electrical analog circuit with conductive and convective resistances in series, shown in Fig. 3. The respective temperatures in the anode, electrolyte and cathode layer are regarded as uniform in each specific control volume. To calculate conduction into axial direction of the solid, the center temperature with respect to thermal resistance is chosen (i.e. the temperature at the radius where thermal resistance to inner and outer surface of the solid are equal). In

Table 3
Heat conduction coefficients

	Planar model	Tubular model			
	Interconnect	Anode	Electrolyte	Cathode	Injector
λ ($W m^{-1} K^{-1}$)	3.5[a]	3[a]	2[a]	3[a]	6.84[b]

[a] Taken from [5].
[b] Taken from [10].

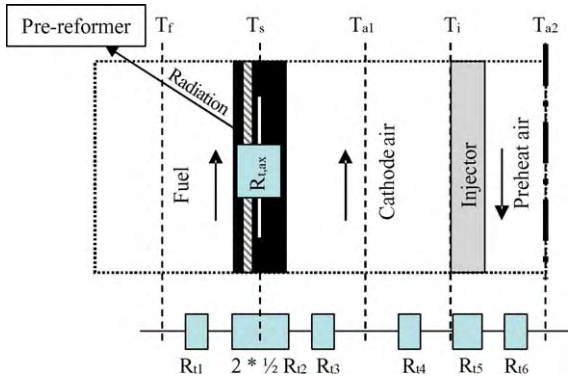

Fig. 3. Tubular radial heat conduction model.

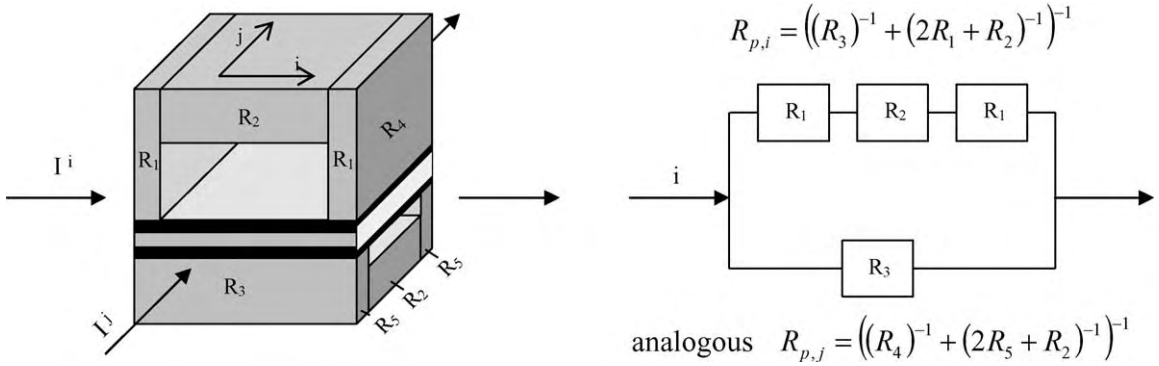

Fig. 2. Planar heat conduction model.

the injector tube, the outside temperature is used to calculate the radiation between injector and cathode. Axial heat conduction is only considered for the solid, not for the injector tube. The effect of interconnect and circumferential heat conduction is not considered.

2.4. Radiation

In order to reduce calculation time for the planar model, radiation between adjacent CVs was neglected. Even though the impact is lower than for the tubular model due to the small channel height, neglecting this phenomenon will according to Yakabe [9] lead to a steeper temperature profile and a shift of the maximum temperature upstream of the fuel flow. However, it is assumed that this effect does not seriously affect the key results, such as fuel utilization, efficiency and power output. Thus the model should still be able to produce reasonable results for use in combination with other processes, such as a gas turbine process. However, the energy demand of the pre-reformer is covered by radiation from the edges of the cell (i.e. the outermost CVs) towards a fictive black body with a uniform temperature. During the calculation, the black body temperature is adjusted iteratively until the radiative cell loss equals the pre-reformer duty. In order to be physically feasible, the black body temperature must be higher than or at least equal to the pre-reformer temperature.

The tubular geometry shows high temperature differences between the solid and the injector tube. Therefore, the tubular model includes radiation between the injector tube and the cathode. In this case, the control volumes of the tube represent a 10 mm high slice of the tube, and by pre-calculations it has been found that 95% of the radiative heat exchange occurs within the same CV and with the CVs lying above and underneath the CV in consideration. To reduce calculation time the remaining radiative heat exchange has been neglected. The implementation is shown in Fig. 1 with shape factors obtained from Incropera and Dewitt [10]. Note that the cathode has a shape factor of 34% to itself. Consequently only 66% of the radiation originating from the cathode occurs in the heat balance.

To reduce calculation time the pre-reformer heat duty is included as constant sink term in the tube solid heat balance, although this effect is of radiative character. Thus, all CVs deliver the same heat flow to the pre-reformer. To exclude a violation of the second law of thermodynamics, it is checked that the required temperature of the recipient for obtaining the required heat flow does not fall below the pre-reformer temperature.

2.5. Reactions and molar balances

Methane in the fuel is reformed at the entrance of the fuel cell in a reaction with steam, using nickel as catalyst:

$$CH_4 + H_2O \rightleftarrows CO + 3H_2 \tag{5}$$

The reaction rate of this reaction can, according to Rechenauer and Achenbach [11], be calculated by the following expression:

$$r_{CH_4}(\text{mole s}^{-1}) = 4274\,(\text{mole m}^{-2}\,\text{bar}^{-1}\,\text{s}^{-1})\,\text{e}^{-82\,(\text{kJ mole}^{-1})/RT}\,p_{CH_4}A_{\text{act}} \tag{6}$$

with the active area of $1.444 \times 10^{-5}\,\text{m}^2$ for the planar and $5.76 \times 10^{-4}\,\text{m}^2$ for the tubular CV. The carbon monoxide produced by methane reforming reacts with steam to form carbon dioxide and hydrogen:

$$CO + H_2O \rightleftarrows CO_2 + H_2 \tag{7}$$

At the SOFC operating temperature this reaction is very fast and assumed always to be in equilibrium. The equilibrium constant is determined with linear approaches for the Gibbs free energy found in standard literature. Due to a rather high steam to carbon ratio (~2–3) no carbon deposition is considered. A check whether this assumption is fair is however included.

Both carbon monoxide and hydrogen can theoretically participate in the electrochemical reactions, but for simplicity only the hydrogen reaction is considered.

$$H_2 + \tfrac{1}{2}O_2 \rightarrow H_2O \tag{8}$$

The reaction rate of the electrochemical reaction can be calculated by using the formulae (9)–(11):

$$U = E^{\text{rev}} - R_\Omega I - \eta \tag{9}$$

Table 4
Molar balance equations

Species	Planar model	Tubular model	Equation
CH_4	$n^{i,j}_{CH_4} = n^{i-1,j}_{CH_4} - r_{CH_4}$	$n^{i}_{CH_4} = n^{i-1}_{CH_4} - r_{CH_4}$	(26)
CO	$n^{i,j}_{CO} = n^{i-1,j}_{CO} + r_{CH_4} - r_{CO}$	$n^{i}_{CO} = n^{i-1}_{CO} + r_{CH_4} - r_{CO}$	(27)
CO_2	$n^{i,j}_{CO_2} = n^{i-1,j}_{CO_2} + r_{CO}$	$n^{i}_{CO_2} = n^{i-1}_{CO_2} + r_{CO}$	(28)
H_2	$n^{i,j}_{H_2} = n^{i-1,j}_{H_2} + 3r_{CH_4} - r_{H_2} + r_{CO}$	$n^{i}_{H_2} = n^{i-1}_{H_2} + 3r_{CH_4} - r_{H_2} + r_{CO}$	(29)
H_2O	$n^{i,j}_{H_2O} = n^{i-1,j}_{H_2O} - r_{CH_4} - r_{CO} + r_{H_2}$	$n^{i}_{H_2O} = n^{i-1}_{H_2O} - r_{CH_4} - r_{CO} + r_{H_2}$	(30)
O_2	$n^{i,j}_{O_2} = n^{i,j-1}_{O_2} - 0.5r_{H_2}$	$n^{i}_{O_2} = n^{i-1}_{O_2} - 0.5r_{H_2}$ (cathode air)	(31)
N_2	$n^{i,j}_{N_2} = n^{i,j-1}_{N_2}$	$n^{i}_{N_2} = n^{i-1}_{N_2}$ (cathode air)	(32)

$$\eta = 2.83 \times 10^{-4}\,(\Omega\,\mathrm{m}^2)\,\frac{I}{A_{\mathrm{act}}}\mathrm{e}^{8360\,(\mathrm{K})/T} \tag{10}$$

$$r_{\mathrm{H_2}} = \frac{I}{2F} \tag{11}$$

In Eq. (9) the current is calculated from a set operating voltage, open circuit potential, sum of the ohmic and ionic resistances and activation overpotential. The latter is approximated in Eq. (10), taken from Selimovic [3]. The reaction rate of H_2 can then be calculated by applying Faradays law as in Eq. (11). Being the most common approach for SOFC modeling, no diffusion overpotential has been regarded.

Applying these reactions and considering the gas flows into the CVs at anode and cathode side of the cell, the molar balance equations for all occurring species are determined as shown in Table 4.

2.6. Heat balances

In the planar model, heat balances are calculated for the air, fuel and solid (i.e. interconnect). Air flows in the *j*-direction, while fuel flows in the *i*-direction as depicted in Fig. 1.

Heat balance of the air is given by:

$$\alpha_{\mathrm{air}} A_{\mathrm{c}}(T_{\mathrm{air}}^{i,j} - T_{\mathrm{s}}^{i,j}) = \sum_{\mathrm{co}}^{\mathrm{co_{air}}}(c_{\mathrm{p,co}}(T_{\mathrm{air}}^{i,j-1})n_{\mathrm{co}}^{i,j-1}T_{\mathrm{air}}^{i,j-1} - c_{\mathrm{p,co}}(T_{\mathrm{air}}^{i,j})n_{\mathrm{co}}^{i,j}T_{\mathrm{air}}^{i,j}) \tag{12}$$

In words, the convective heat transport between air and solid material equals the sum of the heat capacity flows of all species into the CV minus the sum of the heat capacity flows of all species out of the CV.

The fuel heat balance is analogous; however, the fuel flows orthogonally to the air:

$$\alpha_{\mathrm{f}} A_{\mathrm{a}}(T_{\mathrm{f}}^{\mathrm{i,j}} - T_{\mathrm{s}}^{\mathrm{i,j}}) = \sum_{\mathrm{co}}^{\mathrm{co_f}}(c_{\mathrm{p,co}}(T_{\mathrm{f}}^{i-1,j})n_{\mathrm{co}}^{i-1,j}T_{\mathrm{f}}^{i-1,j} - c_{\mathrm{p,co}}(T_{\mathrm{f}}^{i,j})n_{\mathrm{co}}^{i,j}T_{\mathrm{f}}^{i,j}) \tag{13}$$

Due to the electrical analogy the heat balance in the solid is given by:

$$\begin{aligned}&\frac{2T_{\mathrm{s}}^{i,j} - T_{\mathrm{s}}^{i+1,j} - T_{\mathrm{s}}^{i-1,j}}{R_{\mathrm{p},i}} + \frac{2T_{\mathrm{s}}^{i,j} - T_{\mathrm{s}}^{i,j+1} - T_{\mathrm{s}}^{i,j-1}}{R_{\mathrm{p},j}} \\ &\quad + \alpha_{\mathrm{air}} A_{\mathrm{c}}(T_{\mathrm{s}}^{i,j} - T_{\mathrm{air}}^{i,j}) + \alpha_{\mathrm{f}} A_{\mathrm{c}}(T_{\mathrm{s}}^{i,j} - T_{\mathrm{f}}^{i,j}) \\ &= -r_{\mathrm{CH_4}}\Delta H_{\mathrm{ref}} - r_{\mathrm{CO}}\Delta H_{\mathrm{shift}} \\ &\quad - r_{\mathrm{H_2}}(\Delta H_{\mathrm{electro}} + 2UF) - \dot{Q}_{\mathrm{p,preref}}^{i,j}\end{aligned} \tag{14}$$

In words, the heat conduction in *i*- and *j*-direction plus the convection to air and fuel equals the heat conversion of reforming, shift and electrochemical reaction and the radiation to the pre-reformer. The latter is only different from zero at the edges of the cell (thus, $i = 1$, $i = 26$, $j = 1$ or $j = 26$) and where $T_{\mathrm{s}}^{i,j} > T_{\mathrm{black}}$ and is in these cases

$$\dot{Q}_{\mathrm{p,preref}}^{i,j} = \varepsilon\sigma A_{\mathrm{s}}((T_{\mathrm{s}}^{i,j})^4 - (T_{\mathrm{black}})^4) \tag{15}$$

with an emissivity of $\varepsilon = 0.8$. The tubular model is more complex, as it comprises three separate gas channels and furthermore includes radiation between the injector tube and the cathode.

The heat balance for the fuel is analogous to the planar model, however one-dimensional:

$$\frac{T_{\mathrm{f}}^{i} - T_{\mathrm{s}}^{i}}{R_{\mathrm{t1}}} = \sum_{\mathrm{co}}^{\mathrm{co_f}}(c_{\mathrm{p,co}}(T_{\mathrm{f}}^{i-1})n_{\mathrm{co}}^{i-1}T_{\mathrm{a}}^{i-1} - c_{\mathrm{p,co}}(T_{\mathrm{f}}^{i})n_{\mathrm{co}}^{i}T_{\mathrm{f}}^{i}) \tag{16}$$

The heat balance for the tube solid is extended by the radiation and irradiation terms and the pre-reformer duty:

$$\begin{aligned}&\frac{2T_{\mathrm{s}}^{i} - T_{\mathrm{s}}^{i+1} - T_{\mathrm{s}}^{i-1}}{R_{\mathrm{t,ax}}} + \frac{T_{\mathrm{s}}^{i} - T_{\mathrm{f}}^{i}}{R_{\mathrm{t1}} + \frac{1}{2}R_{\mathrm{t2}}} + \frac{T_{\mathrm{s}}^{i} - T_{\mathrm{a1}}^{i}}{R_{\mathrm{t3}} + \frac{1}{2}R_{\mathrm{t2}}} \\ &\quad + \dot{Q}_{\mathrm{s,rad}}^{i} - \dot{Q}_{\mathrm{s,irrad}}^{i} \\ &= -r_{\mathrm{CH_4}}\Delta H_{\mathrm{ref}} - r_{\mathrm{CO}}\Delta H_{\mathrm{shift}} - r_{\mathrm{H_2}}(\Delta H_{\mathrm{electro}} + 2UF) \\ &\quad - \dot{Q}_{\mathrm{t,preref}}\end{aligned} \tag{17}$$

where the radiative terms according to Fig. 4 can be expressed as:

$$\begin{aligned}\dot{Q}_{\mathrm{s,rad}}^{i} &= (0.3 + 2 \times 0.1 + 2 \times 0.08)\varepsilon\sigma A_{\mathrm{s}}(T_{\mathrm{s}}^{i})^4 \\ &= 0.64\varepsilon\sigma A_{\mathrm{s}}(T_{\mathrm{s}}^{i})^4\end{aligned} \tag{18}$$

and

$$\begin{aligned}&\dot{Q}_{\mathrm{s,irrad}}^{i} \\ &= \varepsilon\sigma[A_{\mathrm{inj}}(0.64(T_{\mathrm{inj}}^{i})^4 + 0.18(T_{\mathrm{inj}}^{i-1})^4 + 0.18(T_{\mathrm{inj}}^{i+1})^4) \\ &+ A_{\mathrm{s}}(0.1(T_{\mathrm{s}}^{i-1})^4 + 0.1(T_{\mathrm{s}}^{i+1})^4)]\end{aligned} \tag{19}$$

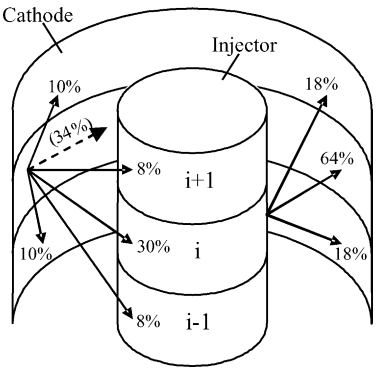

Fig. 4. Distribution of radiation energy between three adjacent control volumes in the tubular system.

with an emissivity of $\varepsilon = 0.8$. The pre-reformer duty $\dot{Q}_{\mathrm{t,preref}}$ is an input parameter, which must be determined externally to correspond with the pre-reformer inlet and outlet fuel composition enthalpies.

The heat balance for the cathode air between injector and cathode is:

$$\frac{T^i_{\mathrm{a1}} - T^i_{\mathrm{s}}}{R_{\mathrm{t3}} + \frac{1}{2}R_{\mathrm{t2}}} + \frac{T^i_{\mathrm{a1}} - T^i_{\mathrm{inj}}}{R_{\mathrm{t4}}} = \sum_{\mathrm{co}}^{\mathrm{co_{a1}}} (c_{\mathrm{p,co}}(T^{i-1}_{\mathrm{a1}}) n^{i-1}_{\mathrm{co}} T^{i-1}_{\mathrm{a1}} - c_{\mathrm{p,co}}(T^i_{\mathrm{a1}}) n^{\mathrm{i}}_{\mathrm{co}} T^i_{\mathrm{a1}}) \quad (20)$$

The heat balance for the injector tube is

$$\frac{T^i_{\mathrm{inj}} - T^i_{\mathrm{a1}}}{R_{\mathrm{t4}}} + \frac{T^i_{\mathrm{inj}} - T^i_{\mathrm{a2}}}{R_{\mathrm{t5}} + R_{\mathrm{t6}}} + \dot{Q}^i_{\mathrm{inj,rad}} - \dot{Q}^i_{\mathrm{inj,irrad}} = 0 \quad (21)$$

and again includes radiation and irradiation:

$$\dot{Q}^i_{\mathrm{inj,rad}} = (0.64 + 2 \times 0.18)\varepsilon\sigma A_{\mathrm{inj}} (T^i_{\mathrm{inj}})^4 = \varepsilon\sigma A_{\mathrm{inj}} (T^i_{\mathrm{inj}})^4 \quad (22)$$

and

$$\dot{Q}^i_{\mathrm{inj,irrad}} = \varepsilon\sigma A_{\mathrm{s}} (0.3(T^i_{\mathrm{s}})^4 + 0.08(T^{i-1}_{\mathrm{s}})^4 + 0.08(T^{i+1}_{\mathrm{s}})^4) \quad (23)$$

The gas composition in the injector is constant, as no reactions occur. Its heat balance is:

$$\frac{{T_{\mathrm{a2}}}^i - {T_{\mathrm{inj}}}^i}{R_{\mathrm{t5}} + R_{\mathrm{t6}}} = \sum_{\mathrm{co}}^{\mathrm{co_{a2}}} (c_{\mathrm{p,co}}({T_{\mathrm{a2}}}^{i+1}) n_{\mathrm{co}} {T_{\mathrm{a2}}}^{i+1} - c_{\mathrm{p,co}}({T_{\mathrm{a2}}}^i) n_{\mathrm{co}} {T_{\mathrm{a2}}}^i) \quad (24)$$

A check whether carbon deposition occurs can be included into the model by investigating the Gibbs energy of the reactions:

$$2\mathrm{CO} \rightleftarrows \mathrm{C} + \mathrm{CO_2} \text{ and } \mathrm{CH_4} \rightleftarrows \mathrm{C} + 2\mathrm{H_2} \quad (25)$$

If the Gibbs energy is less than or equal to zero, coking can theoretically occur. However, as the reactions are rather slow, small negative Gibbs energy values could possibly be tolerated. Nevertheless, Gibbs energy of zero was assumed to be the lower boundary for the carbon-deposition-free regime.

2.7. Boundary conditions and input parameters

The model requires temperature, pressure, composition and molar flow of the incoming gas streams as boundary conditions and therefore input parameters. The radiation heat from the cell edges to the pre-reformer is also a boundary condition which needs to be set according to the incoming (pre-reformed) fuel stream properties. This can be done by regarding the pre-reformer as a Gibbs reactor.

A further input parameter is the cell voltage, through which the current is determined by Eq. (9). The fuel utilization (FU), i.e. the fraction of fuel that is utilized by the fuel cell, is determined by evaluating Eq. (11) for each CV together with the solved heat balance equations.

In some cases it may be more desirable to define the fuel utilization instead of the operating voltage. This can be reached by a simple iteration routine, which modifies the voltage until the desired FU is reached. The electric current is a function of fuel flow, inlet concentration and fuel utilization and is thus also an implicit input parameter of the model.

In order to reduce calculation time both planar and tubular models do not consider special stacking particularities, i.e. except the specified heat exchange with the pre-reformer, the cell boundaries are adiabatic. This idealization means that indefinite stacks are modeled.

2.8. Numerical method and implementation

The implementation of the models results in a set of connected non-linear equations and some ancillary equations. The system is solved with the Newton–Raphson iteration procedure taken from Engeln-Muellges and Uhlig [12], which uses the partial derivatives of the equations to approach the solution.

The models have been implemented in Fortran 90, under the objective to integrate them into the flowsheet simulation software PRO/II by Simsci.

2.9. Type of results

The following results can be achieved with the SOFC models:

- Fuel utilization/voltage: depending on the running mode, one is an input parameter and the other one a result.
- Power output and global energy efficiency of the cell.
- Carbon deposition check: the CVs where carbon deposition is likely to occur.
- Black body temperature: the temperature an imaginary black body must have to receive the radiative heat flow that is required by the pre-reformer.
- Arrays of values for each CV (two-dimensional for the planar, one-dimensional for the tubular model)
  - Molar flow of all components.
  - Temperatures of air, fuel, solid (additional preheating air and injector for tubular model).
  - Temperature gradients in *i*- and *j*-direction of the planar and in axial direction of the tubular cell.
  - Electric current.
  - Molar amount of CO processed by the water gas shift reaction.

These results allow for a detailed study of the operation conditions of the fuel cells.

2.10. Model validation

The planar model has been validated against the models of Rechenauer [11] and Selimovic [3] using the input values of the IEA Benchmark Test [13]. The air and fuel flow rate were in both cases adjusted to the exact values selected by each compared model. The comparison in Table 5 shows that the planar model produces similar results in all shown parameters and a voltage deviation at identical fuel utilization and current density in the range of 2%.

The tubular model was validated using the experimental data and assumptions published by Campanari [4] for an atmospheric and a pressurized system. The input parameters and fuel utilization values of the experimental data have been simulated with the model, giving voltage and power as result. Input parameters and results are shown in Table 6. While the atmospheric case matches very well with a voltage deviation of only 0.8%, there is quite a high deviation in the pressurized case (13.3% in terms of voltage). However, the results are sensitive to the inlet temperature and fuel composition, which Campanari chose from a different work than the experimental results. If air and fuel inlet temperature for the model are increased by 90 K in case of the pressurized system, the voltage values match. As no complete set of input parameters and experimental results for tubular fuel cells was found in literature, we consider the exactness of the model as sufficient for the meanwhile. Once measurement data has been published, it is easy to calibrate the model to the data using parameter estimation.

Table 5
Validation of the planar model

	Rechenauer	Planar model	Selimovic	Planar model
Pressure (bar)	1	1	1	1
Fuel flow rate (mole s^{-1})	1.872×10^{-4}		1.784×10^{-4}	
Air flow rate (mole s^{-1})	3.047×10^{-3}		2.901×10^{-3}	
Inlet fuel and air temperature (K)	1173			
Fuel utilization (%)	85			
Inlet fuel composition (molar fraction)				
H_2	0.2626			
H_2O	0.4934			
CH_4	0.1710			
CO	0.0294			
CO_2	0.0436			
Voltage (V)	0.682	0.7	0.658	0.669
Voltage deviation (%)	2.64	2.64	1.67	1.67
Power (W)	20.46	21.12	19.74	19.02
Max. current density (A m^{-2})	4800	4570	6039	5798
Min. current density (A m^{-2})	1100	1260	804	1665
Max. solid temperature (°C)	1061	1036	1130	1063
Min. solid temperature (°C)	823	845	741	849
Max. temperature gradient (K mm^{-1})	7.09	8.95	n.a.	

Table 6
Validation of the tubular model

	Atmospheric (plant A)	Tubular model	Pressurized (plant B)	Tubular model
Pressure (bar)	1.05	1.05	3.5	3.5
Fuel flow per tube (mole s^{-1})	1.511×10^{-3}		2.287×10^{-3}	
Air flow per tube (mole s^{-1})	1.055×10^{-2}		1.290×10^{-2}	
Inlet fuel temperature (K)	823		860	
Inlet air temperature (K)	1104		1048	
Fuel utilization (%)	69		69	
Inlet fuel composition (molar fraction)				
H_2	0.258		0.226	
H_2O	0.284		0.334	
CH_4	0.11		0.131	
CO	0.057		0.057	
CO_2	0.228		0.241	
N_2	0.063		0.011	
Voltage (V)	0.69	0.695	0.639	0.564
Voltage deviation (%)	0.72	0.72	13.3	13.3
Power (W)	104.8	105.6	157.0	138.6

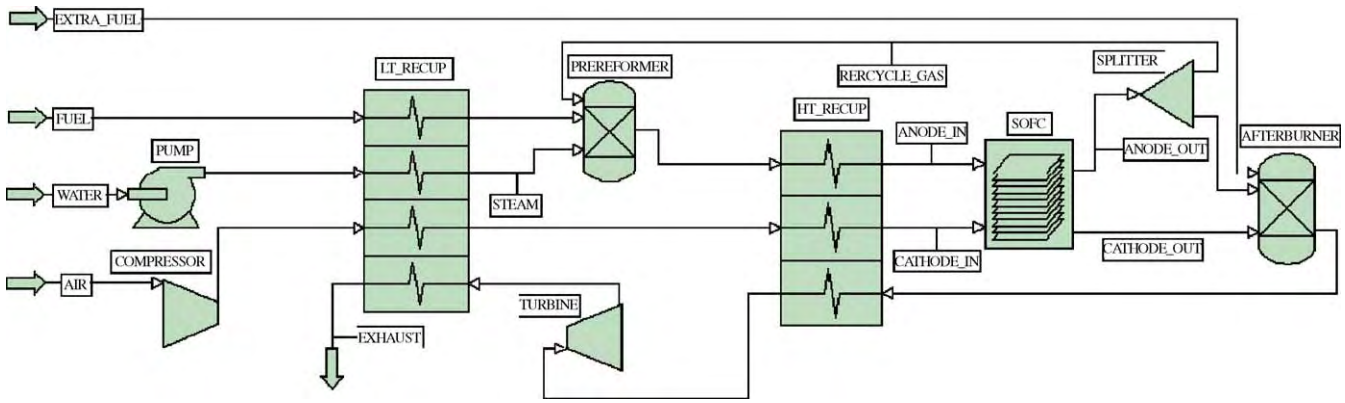

Fig. 5. Applied gas turbine cycle.

3. Hybrid cycle performance simulation

3.1. SOFC/GT cycle design and simulation premises

The modeled SOFC/GT cycle is illustrated in Fig. 5. The GT cycle and balance of plant equipment is implemented in PRO/II, where Fortran-based SOFC models are implemented as a user added subroutine in the flowsheet. The gas streams of the SOFC are defined by linking of the SOFC model in the flowsheet. The heat duty to the pre-reformer as well as voltage respectively fuel utilization of the SOFC models are entered via an entry form and can also be linked to process variables. Methane is partially reformed in a pre-reformer, which is modeled as a Gibbs reactor and thermally connected to the fuel cell. The operation temperature of the pre-reformer is controlled to equilibrium temperature of the desired pre-reforming level.

The cycle comprises two-stage cascaded heat recuperation, anode gas recycling and an afterburner for the unspent and possibly additional fuel. The pressure of the recycle gas is raised to the fresh fuel gas level by an ejector (not displayed). Losses in the ejector are not included in the energy balance of the system, as the fuel is assumed to be delivered directly from a high-pressure grid.

Table 7 summarizes the setup of the GT cycle. Most assumptions were taken from Pålsson [14]. The specifications that are most significant for the cycle or subject to changes during the parameter studies are shown below in Table 8.

The fuel cell input parameters, such as gas composition, pressure and temperature of the streams ANODE_IN and CATHODE_IN (Fig. 5) and the duty of the pre-reformer, are calculated in the PRO/II model and sent to the Fortran submodule. The solver operation mode and one further input parameter (operation voltage or fuel utilization level) must be specified in the SOFC module itself to be transferred to the Fortran routine.

The most important operational constraints for the planar SOFC are the maximum allowable temperature (T_{max}) of 1300 K [3] and the maximum temperature gradient in the area of 5 K mm^{-1} [11] to avoid thermal cracking of the cell. The tubular SOFC is less sensitive to this effect since the tubes can expand freely and the temperature is more uniform. Another issue is to avoid operational modes where coking can occur.

Table 7
GT cycle setup

Item (Fig. 5)	Specification
EXTRA_FUEL	100% Methane; 288 K/20 bar
AIR	288 K/1 bar
WATER	283 K/1 bar
COMPRESSOR	81% Adiabatic efficiency
TURBINE	84% Adiabatic efficiency; outlet pressure 1.1 bar
PRE-REFORMER	Gibbs reactor; pressure drop 2%; operating temperature 800–900 K (controlled to achieve desired pre-reforming degree); heat demand supplied by fuel cell
AFTERBURNER	Gibbs reactor; pressure drop 5%; complete combustion; coupled with HT_RECUP for heat transfer
SOFC	User added subroutine; pressure drop 2%; radiative heat loss is the PRE-REFORMER heat demand; specification of either operating voltage or fuel utilization
LT_RECUP	Pressure drop 2% for inlet air and exhaust (rest 0); cold products outlet 50 K below hot product inlet (1st and 2nd law check)
HT_RECUP	Pressure drop cold side 2% (hot side is coupled with AFTERBURNER), cold product temperature specified (fuel cell specifications)

Table 8
Base case parameters

Parameters	Planar	Tubular
Pressure (bar)	3	3
Steam to carbon ratio[a]	2.5	2.5
Fuel utilization (%)	85	85
Recirculation degree (%)	0	0
Fuel inlet temperature (K)	1123	1123
Air inlet temperature (K)	1123	923
Fuel flow per active cell area (mole m^{-2} s^{-1})	4.5×10^{-3}	3.8×10^{-3}
Air excess ratio, λ	6	4
Pre-reforming degree (%)	30	50

[a] Molar flow of steam divided by molar flow of methane in the fresh fuel entering the pre-reformer.

Table 9
Operational data at base case

System	Parameter	Planar system	Tubular system
Fuel cell	Efficiency (LHV, %)[a]	62.5	52.5
	Voltage[b] (V)	0.700	0.616
	Max. temperature (K)	1272	1130
GT cycle	TIT (K)	747	1185
	Spec. turbine power production[c] (%)	55	69
	Spec. compressor power consumption[c] (%)	48	37
SOFC/GT cycle	Total efficiency (LHV, %)	58.5	63.1

[a] Based on the fuel taking part in the electrochemical reaction.
[b] Voltage is a result of the model when a certain fuel utilization is determined.
[c] Ratio between power of compressor/turbine and fuel cell power.

3.2. Setup of a base case

As a starting point for parameter variations, a base case is defined. Table 8 shows the base case assumptions for the parameters that are of high importance for the cycle thermodynamics and fuel cell operation. The values represent typical values for SOFCs. A recirculation degree of zero has been chosen for calculation time reasons. Due to the nature of the different designs, some values differ for the planar and tubular model:

- The air inlet temperature of the tubular fuel cell lies well below the one of the planar SOFC in order to achieve the designated internal cooling effect of the preheating injector air.
- The fuel flow rate has been adapted geometry-specifically (i.e. fuel flow per m^2 s) in order to achieve comparable points in the operation ranges of the fuel cells. A value from Rechenauer [11] was chosen for the planar cell and a value from Yi [15] for the tubular cell.
- The tubular model is known to tolerate lower air excess ratios due to the ability of the tubes to tolerate higher thermal gradients by expanding freely. Therefore an air excess of 4 has been chosen for the tubular model.
- The pre-reforming degree of the tubular cell must be comparably high due to problems with the convergence of the model.

Table 9 shows main operational data of the fuel cell and the GT cycle for the base case. The listed fuel cell efficiency is based on the fuel taking part at the electrochemical reaction, i.e. without considering the fuel utilization. Power production and consumption by the gas turbine and compressor is given specifically as percentage of the fuel cell stack power. The power supplement of the GT cycle in relation to the fuel cell can thus be seen as the difference between specific turbine and compressor power. It is visible that in the planar system, the net power output from the GT cycle is very low and the system efficiency is below the fuel cell efficiency. This is mainly due to the low turbine inlet temperature. The tubular fuel cell has a lower efficiency due to the higher ohmic resistance, which leads to a higher heat production. The additional amount of heat is however spent on internal preheating of the incoming air flow. This in turn reduces the duty of the high temperature recuperator, which leads to a higher turbine inlet temperature (TIT) and therewith a higher output of the GT cycle.

3.3. Parameter study

A parameter study was performed by varying only one parameter at a time while keeping the others at their base case values. Figs. 6 and 7 shows the system efficiency for the planar design (left) and the tubular design (right) as a function of the varied parameters. The *y*-axis covers the same range

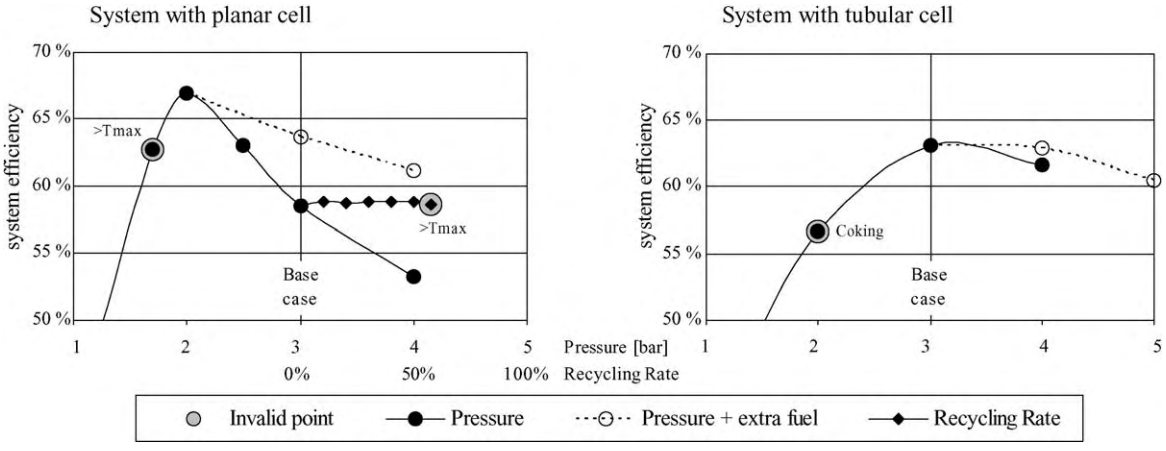

Fig. 6. Dependency of system efficiency on pressure and recycling rate.

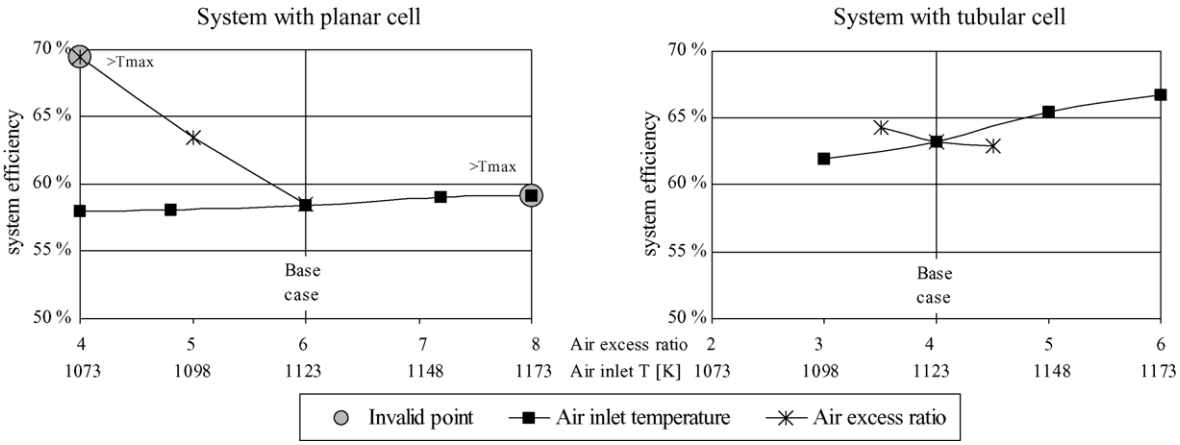

Fig. 7. Dependency of system efficiency on air inlet temperature and air excess ratio.

of values for all diagrams. The *x*-axis has been designed to show the base case value of each parameter and system in the middle, while the gradient is the same for each parameter. Figs. 8 and 9 show the gas turbine cycle power supplement to the fuel cell power in the same manner.

As can be seen from the bold line of Fig. 8, the turbine power output of the planar system decreases strongly at a pressure higher than 2 bar. That is because the TIT decreases due to a shift of the heat recovery duty towards the high-temperature recuperator. This can be countered by adding extra fuel to the afterburner. The dashed line in Figs. 6 and 8 shows the performance at a TIT controlled to 1173 K by this method. It can be seen that the power production of the planar system can be strongly increased at the cost of only a slight decrease in efficiency by adding extra fuel. For the tubular system, this effect is also present, however it is weaker. The system power output is furthermore increased slightly by the fuel cell efficiency increase at higher pressure.

Reducing the air flow rate would cause a high gain in efficiency of the planar system due to reduced heat and energy losses (see Fig. 6, left). However, the high excess air is required for cooling reasons, hence the maximum temperature is exceeded for an air excess ratio of 4. The tubular cell has better internal heat management and can thus be operated at a lower air excess ratio. This fact compensates for the lower efficiency of the tubular SOFC stack.

The air inlet temperature strongly influences the average temperature in the cell. Thus, a higher air inlet temperature has a positive influence on the reaction kinetics and results in higher fuel cell efficiency. This causes the tubular system efficiency to increase with increasing fuel cell air inlet temperature as can be seen in Fig. 7. In the planar system, this effect is partially compensated by the decreasing TIT caused by a higher heat transfer in the high-temperature recuperator. Regarding the internal temperature charts of the fuel cell, it turns out that the maximum local temperature of the SOFC can be effectively controlled by the air inlet temperature.

The influence of the recycling rate on the planar system efficiency is rather low. However it should be mentioned that anode gas recycling rate has practical advantages as it reduces the system complexity by providing steam and also decreases internal temperature gradients of the fuel cell. The recycling rate could not be checked in the tubular case due to solver stability reasons, but the same tendency could be expected.

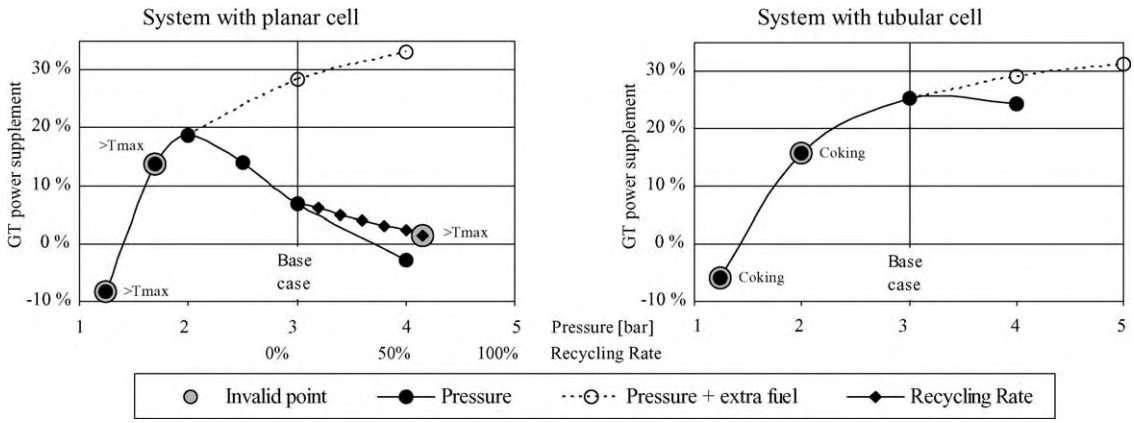

Fig. 8. Dependency of gas turbine power supplement on pressure and recycling rate.

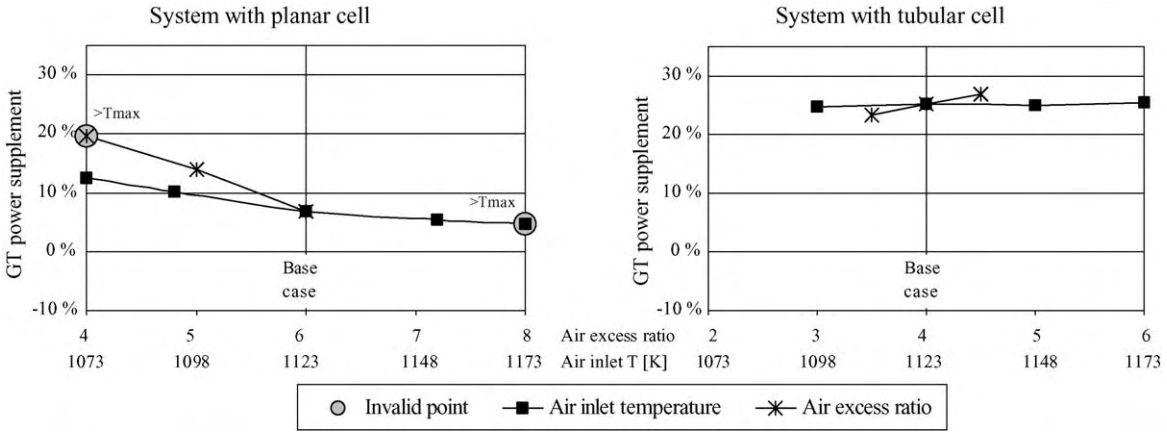

Fig. 9. Dependency of gas turbine power supplement on air inlet temperature and air excess ratio.

3.4. Near-optimum case

In accordance with preliminary studies, the pressure of the planar system has been reduced to 2 bar and the air inlet temperature of the tubular system is raised to 973 K in order to study a near-optimum case. Base case parameters have been assumed for the remaining values. For the planar system, the maximum local temperature in the cell is at its limit. Simulations with a combination of lower air inlet temperature and lower air excess ratio did not show significant efficiency improvements. Table 10 shows relevant operational data at the near-optimum point.

Fig. 10 displays charts for solid temperature, current density, hydrogen and methane of the planar fuel cell at near-optimum operation. The temperature distribution shows that the maximum local temperature occurs at the air outlet and near the fuel outlet. Close to the outlet of the fuel flow, temperature decreases due to decreasing electrochemical reaction

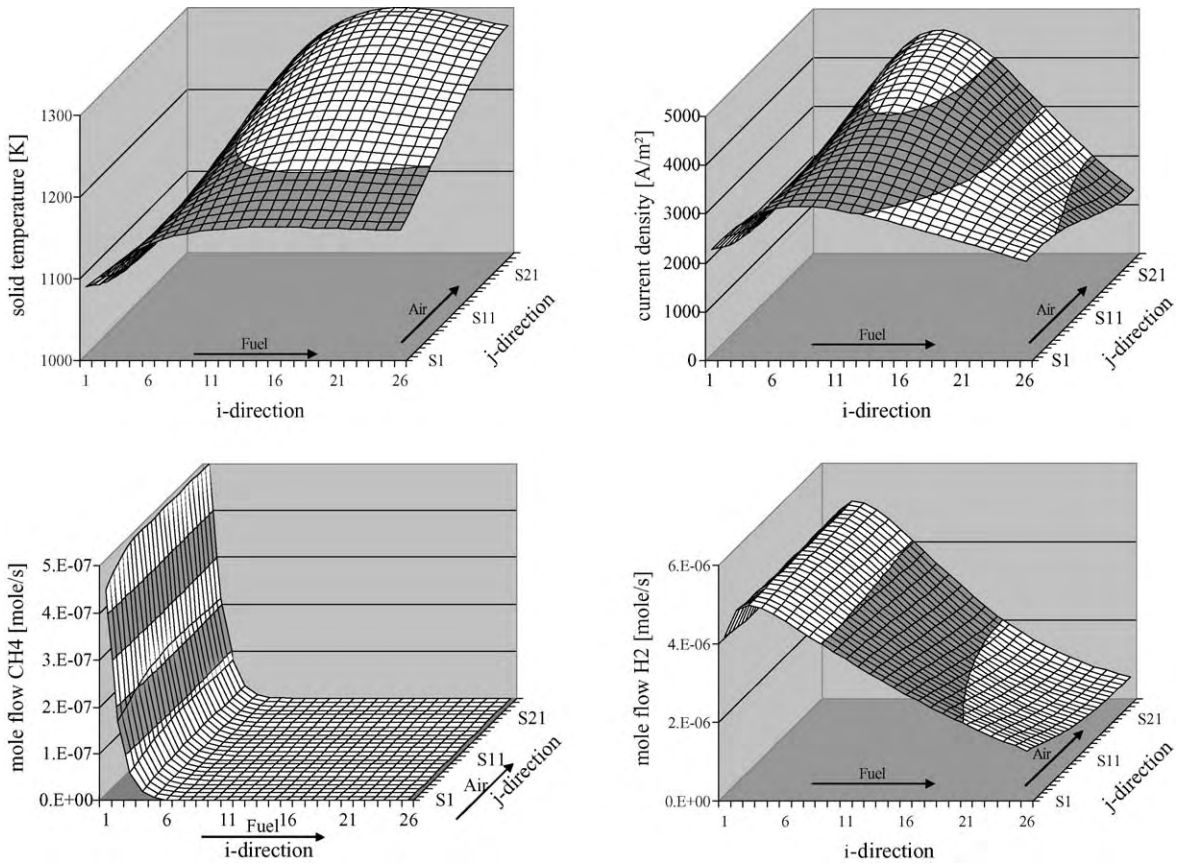

Fig. 10. Temperature, current density, H_2 and CH_4 molar flow fields for the planar cell at near-optimum case.

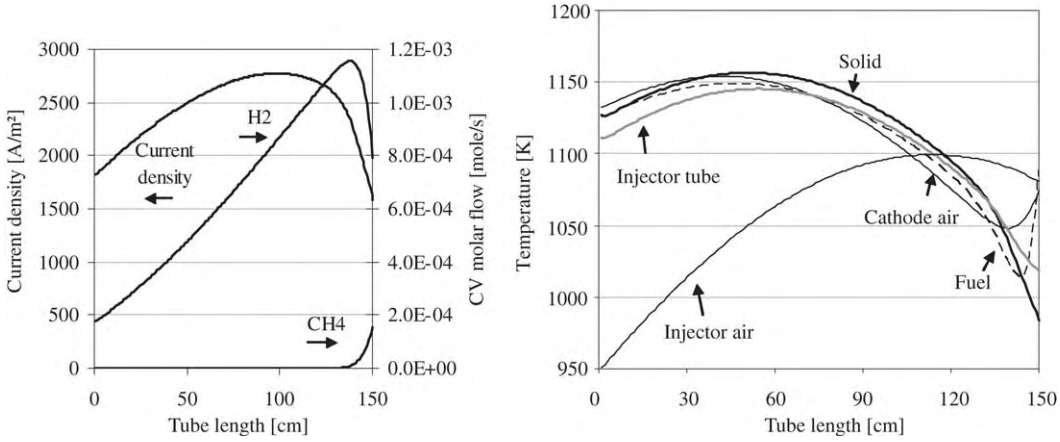

Fig. 11. Temperatures, current density, H_2 and CH_4 molar flow fields for the tubular cell at near-optimum case.

Table 10
Operational data at near-optimum case

System	Parameter	Planar system	Tubular system
Fuel cell	Efficiency (LHV, %)	62.5	54.7
	Voltage (V)	0.705	0.641
	Max. temperature (K)	1300	1175
GT cycle	TIT (K)	1191	1220
	Spec. turbine power[a] (%)	51	68
	Spec. compressor power[a] (%)	28	35
	Total efficiency (LHV, %)	66.9	66.7

[a] Ratio between power of compressor/turbine and fuel cell power.

rate, cooling by the air and the radiation to the pre-reformer. The figure also shows that most of the methane is reformed at the inlet. The hydrogen mole flow decreases steadily towards the fuel outlet. The current density as a measure for the electrochemical reaction is mainly influenced by the temperature (through the ohmic resistivity) and the amount of hydrogen (through the Nernst equation). Thus the maximum lies between the hydrogen and the temperature maximum.

Fig. 11 shows parameters in the tubular cell. The injector air flows to the right (downwards), while the reacting gases flow to the left (upwards) in these diagrams. It can be seen that the injector air is effectively cooling the cell in the upper section, while it provides some heat for the reforming reaction in the lower section. Hydrogen and methane mole flows and the current density behave similar to the planar model in *i*-direction.

4. Conclusions

The current paper describes two steady-state finite volume models for planar and tubular fuel cells. Although several simplifications and assumptions have been done during the development of the models, they provide reasonable results. This has been proven for the planar model by validation against the models from Selimovic [3] and Rechenauer [11]. A validation of the tubular model against Campanari [4] shows a certain divergence at high-pressure. However, no complete set of parameters from one source was found in literature, making a proper validation impossible.

It has been shown that hybrid systems can achieve efficiencies above 65% with the planar as well as the tubular geometry SOFC. The main difference between the planar and the tubular system for the gas turbine cycle is the internal pre-heating of the air in the tubular system, permitting a lower air inlet temperature. The thereby reduced amount of high-temperature heat in the pre-heating section allows for a higher-pressure ratio at acceptable turbine inlet temperatures. The tubular system's ability to be operated at lower air excess ratio lowers the exhaust gas losses and increases the afterburner temperature, improving the effectiveness of the GT cycle. These effects compensate for the lower efficiency of the tubular fuel cell stack, which is caused by its higher ohmic resistivity.

The introduction of additional fuel to the afterburner increases the turbine inlet temperature and therewith the GT cycle yield. The efficiency of both systems at higher pressures can be raised by this method. In case of the planar system, the power supplement of the GT cycle can be significantly increased. This effect could play a roll for the power output control of hybrid systems capable of pressure variation.

References

[1] H. Karoliussen, et al., SOFC stack modeling with internal reforming, in: Proceedings of the fourth IEA Workshop on SOFC, Lausanne, Switzerland, August, 1992.
[2] K. Hassmann, SOFC power plants, the Siemens–Westinghouse approach, Fuel Cells 1 (2001) 1.
[3] A. Selimovic, SOFC Modelling for SOFC/GT Combined Cycle Simulations, Licenciate Thesis, Lund University, Sweden, 2000.
[4] S. Campanari, P. Iora, Definition and sensitivity analysis of a finite volume SOFC model for a tubular cell geometry, J. Power Sources 132 (2004) 113–126.
[5] U.G. Bossel, Final Report on SOFC Data, Facts and Figures, Swiss Federal Office of Energy, Berne, 1992.

[6] K. Nisancioglu, Natural Gas Fuelled Solid Oxide Fuel Cells and Systems, Swiss Federal Office Of Energy, 1989, p. 96.
[7] T. Ota, M. Koyama, C. Wen, K. Yamada, H. Takahashi, Object-based modeling of SOFC system: dynamic behavior of micro-tube SOFC, J. Power Sources 5249 (2003) 1–10.
[8] W.M. Rohsenow, J.P. Hartnett, Y.I. Cho, Handbook of Heat Transfer, third ed., McGraw-Hill, 1998.
[9] H. Yakabe, et al., 3-D model calculation for planar SOFC, J. Power Sources 102 (2001) 144–154.
[10] F.P. Incropera, D.P. Dewitt, Fundamentals of Heat and Mass Transfer, fifth ed., Wiley and Sons Inc., 2002.
[11] C. Rechnenauer, E. Achenbach, Dreidimensionale mathematische Modellierung des stationären und instationären Verhaltens oxidkeramischer Hochtemperatur-Brennstoffzellen, Doctoral Thesis, Forschungszentrum Jülich, Germany, 1993.
[12] G. Engeln-Muellges, F. Uhlig, Numerical Algorithms with C, Springer-Verlag, 1996.
[13] E. Achenbach, International Energy Agency, Annex II, Modelling and Evaluation of Advanced SOFC, Subtask A: Numerical Modelling, Experimental Data Base and Validation, Activity A2: Stack Modelling, 1995.
[14] J. Pålsson, Thermodynamic Modelling and Performance of Combined SOFC and GT Systems, Doctoral Thesis, Lund University, Sweden, 2002.
[15] Y. Yi, T.P. Smith, J. Brouwer, A.D. Rao, G.S. Samuelsen, Simulation of a 220 kW hybrid SOFC gas turbine system and data comparison, in: Proceedings of the Electrochemical Society, vol. 7, 2003.

Appendix B - Paper II

Part-load and load change simulation of tubular SOFC systems

Bjørn Thorud, Christoph Stiller, Torleif Weydahl, Olav Bolland, Håvard Karoliussen

The 6th European Solid Oxide Fuel Cell Forum, 28. June-2. July, Lucerne Switzerland

Proceedings Vol 2, p 716-729

Part-Load and Load Change Simulation of Tubular SOFC Systems

Bjørn Thorud[1], Christoph Stiller[1], Torleif Weydahl[2], Olav Bolland[1], Håvard Karoliussen[1]

[1] Norwegian University of Science and Technology, N-7491 Trondheim
[2] SINTEF Energy Research, N-7491 Trondheim

Abstract

A quasi two-dimensional dynamic model for tubular type solid oxide fuel cell has been developed. The model has been linked together with a model for a prereformer, an anode gas recirculation and mixing chamber and an afterburner. Examinations of part-load and dynamic behaviour of a SOFC system intended for use in hybrid cycles have been performed. Steady-state part-load behaviour is presented in performance maps by a novel method. In addition to power output and efficiency, the maps also provide information about key temperatures and temperature gradients in the fuel cell solid. The maps may be used to predict key parameters for part-load operation and furthermore to evaluate part-load strategies. In addition, dynamic behaviour for load changes between 55 and 100% load was examined. Results from the dynamic behaviour simulations show that air utilisation should be set constant during load changes.

Introduction

A large number of models (1)-(3) and a demonstration plant (4) have proven that a solid oxide fuel cell (SOFC) integrated with a gas turbine has a potential for high efficiency electricity production with low environmental emissions. However, these types of systems face a large number of challenges when operated in either dynamic or part-load mode. The gas turbine has good dynamic properties compared to the SOFC, but part-load performance can be rather poor. The SOFC is generally able to respond quickly to load changes (5), but it might be destroyed or seriously degraded during dynamic operation. This is mainly due to thermally induced stresses caused by different thermal expansion coefficients in the cell materials. Due to these differences in behaviour, matching system components for part-load operation can be a challenge.

Results from part-load operation modelling have already been discussed by some authors. Costamagna et al. (6) investigated a hybrid system using a dimensionless tubular SOFC model. They simulated a hybrid system with fixed gas-turbine shaft speed. In such a system, power output can only be controlled by varying the fuel flow. In the simulations they assumed constant fuel utilisation (FU) and varied the air flow rate according to the amount supplied by the compressor. These simulations showed large variations in air utilisation (AU) and loss of efficiency for fixed shaft speed when operating at part-load. For variable shaft speed, however, AU and FU as well as stack inlet temperatures could remain fairly constant in part-load operation with only a small penalty on system efficiency. This effect was mainly due to increased recuperator efficiency owing to reduced air flow rate.

Campanari et al. (7) also used a dimensionless tubular SOFC model to investigate the hybrid system. For constant shaft speed they suggested to reduce AU and current density while keeping the air flow rate constant. This approach will reduce power output of the SOFC as well as the turbine inlet temperature (TIT) and consequently the power output of the gas turbine. For variable shaft speed they suggested to reduce air flow rate and current density to maintain a constant AU. With this approach a constant TIT could be maintained, provided that the stack inlet temperature was kept constant. However, a reduction in air flow rate leads to pressure reduction, which increases turbine outlet temperature (TOT) and thus the recuperator outlet temperatures. In order to maintain a constant TIT the current density has to be reduced further.

Chan et al. (8) also investigated a dimensionless tubular SOFC-type in a hybrid system. In their system, power is reduced by shifting the load from the stack to the gas turbine at almost constant system fuel consumption, which results in reduction of the system efficiency. This method also implies that a stack bypass should be implemented for both fuel and air. Due to the low efficiency at part-load, Chan et al. state that this method is meant for short term load reduction only. The aim is to maintain a relatively high stack temperature while keeping the different components matched.

Pålsson et al. (9) used a 2-dimensional planar SOFC model for their part-load studies. The design case was set to the point where the compressor flow matched the cooling requirement of the SOFC stack. They also introduced an air heater/cooler prior to the stack entry in order to meet the requirements for the air inlet temperatures at part-load operation. Air cooling was introduced to prevent exceeding maximum hot spot temperature in the stack. In their calculations, they kept TIT constant and varied the turbine shaft speed. At part-load operation, increased stack FU and low part-load efficiency of the gas turbine led to an increased power contribution from the SOFC. Due to the problems associated with matching the system components, they concluded that the load range for hybrid systems should be limited to 55 – 100%, corresponding to a load variation of the gas turbine of 20 – 100%.

Kimijima and Kasagi (10) studied part-load of a 30 kW simple recuperated cycle using a dimensionless SOFC model. Variable and fixed shaft speed is compared. The FU is kept constant, even though it is mentioned that the FU could be increased at part-load operation. They conclude that variable shaft speed operation is favourable in terms of part-load performance; however the higher turbine exhaust temperature could cause problems.

All above mentioned authors have identified inlet and outlet gas temperatures as well as air and fuel utilisation of the SOFC as important parameters for part-load operation of hybrid systems. Maintaining a constant stack operation temperature is important to avoid thermal cracking, but this might be difficult to achieve at reduced pressure as the turbine outlet temperature increases and consequently the recuperator outlet temperatures.

In the present work, focus is on the stack and prereformer, while keeping in mind that these components should be fitted into a hybrid system. Novel stack performance maps are introduced to illustrate the relationships between the most important parameters: AU, FU, air flow rate, maximum and mean solid temperatures, solid temperature gradients, efficiency and power output. The performance maps represent a more comprehensive and generalised presentation of SOFC performance than previously published. Based on these maps, strategies for part-load operation of the SOFC system are proposed. Finally, dynamic simulations have been performed to investigate the behaviour when system load is changed.

Model description

The SOFC model is a quasi two-dimensional dynamic model of a solid oxide fuel cell tube, similar to that of Siemens Westinghouse. This type of design has been described by other authors as in (11) and (12). The model also incorporates a prereformer, an afterburner and a recirculation and mixing chamber. Part of the anode exhaust gas is mixed with fresh fuel in the mixing chamber in order to supply steam to the steam reforming and shift reaction. The prereformer is modelled as a Gibbs reactor, thermally connected to the fuel cell tube. The consumed heat is supplied by radiation from the anode surface, adjusted by a shape factor to meet 30% prereforming degree for the design case. The remaining anode exhaust gas is completely combusted together with the cathode air in the afterburner. The prereformer, the afterburner and the recirculation and mixing chamber are all non-dimensional models. The fuel cell, however, is a discretised model where gas flows are treated as 1D plug flows. The solid structures are modelled by a 2D discretisation scheme in the axial and radial direction, neglecting effects in the circumferential direction. A flow sheet of the simulated system is shown to the left in Flow sheet of the simulated system (left) and break down of the cell geometry (right).. A break-down of the cell geometry can be seen to the right in the same figure. The numbers in the figure (right) refer to the equations for the thermal model which are listed in figure 1.

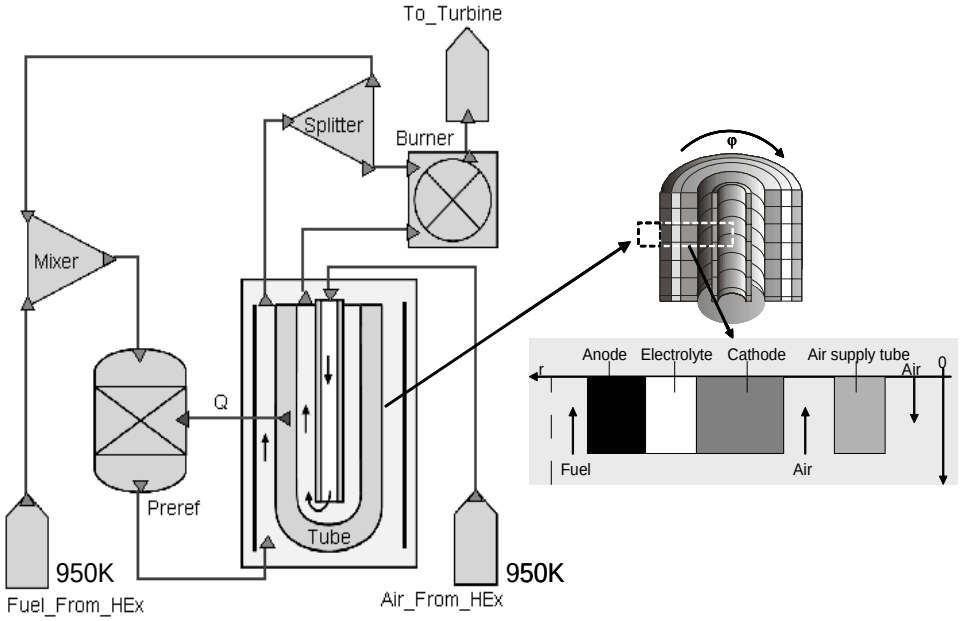

Figure 1: Flow sheet of the simulated system (left) and break down of the cell geometry (right).

Heat transfer between the fuel cell tube walls and the fluids are calculated using Newton's law of cooling. The heat transfer coefficients are calculated from Nusselt numbers for laminar flow and for constant heat flux. Thermal radiation is incorporated between the air supply tube and the cathode surface by using a shape factor for radiation between two tubes, neglecting axial effects and absorption in the air. To reduce calculation time, the solid structure of the anode, electrolyte and the cathode is treated as one single material with weighted mean values for the thermal and electrical properties. The total thickness

of anode and electrolyte (0.14 mm) is very small compared to the cathode (2.2 mm) for this type of fuel cell. Therefore the heat sources and sinks related to the electrochemical and methane reforming kinetics are located at the anode surface. For steam reforming kinetics, Achenbach's approach is used (14), while the water-gas shift reaction is assumed to be always in equilibrium. Electrochemical oxidation of CO is neglected in the model. The local electrical potential is calculated by the Nernst equation, an approach for polarisation losses by Karoliussen et al. (15) and an analytical expression for the ohmic resistance developed by Nisancioglu (16). Diffusion losses are not included. The model is implemented in the modelling tool gPROMS (13) (PSE Ltd).

Ref no in Figure 1	**Equation**	**Comment**
1	$\frac{\partial\left(T_{air}c_p\rho_{air}\right)}{\partial t}+v_{air}\frac{\partial\left(T_{air}c_p\rho_{air}\right)}{\partial z}=\frac{2\alpha}{r_{AST,i}}\left(T_{AST}-T_{air}\right)$	Heat transfer between air supply tube and air within the tube
2	$\frac{dT}{dt}=\frac{k}{c\cdot\rho}\nabla^2\cdot T$	Heat conduction in solid structures (Air supply tube and SOFC membrane)
3	$\frac{\partial\left(T_{air}\rho_{air}c_{p,air}\right)}{\partial t}+v_{air}\frac{\partial\left(T_{air}\rho_{air}c_{p,air}\right)}{\partial z}=$ $\frac{2r_{AST,o}\alpha_{AST,o}}{\left(r_{c,i}^2-r_{AST,o}^2\right)}\left(T_{AST,o}-T_{air}\right)+\frac{2r_{c,i}\alpha_{c,i}}{\left(r_{c,i}^2-r_{AST,o}^2\right)}\left(T_{c,i}-T_{air}\right)$	Heat transfer between air supply tube, cathode air and cathode
4	$\frac{\partial\left(T_{fuel}\rho_{fuel}c_{p,fuel}\right)}{\partial t}+v_{fuel}\frac{\partial\left(T_{fuel}\rho_{fuel}c_{p,fuel}\right)}{\partial z}$ $=\frac{2\alpha_{fuel}r_{a,o}}{\left(\left(r_{a,o}+\Delta r\right)^2-r_{a,o}^2\right)}\left(T_{a,o}-T_{fuel}\right)$	Heat transfer between anode surface and fuel

Table 1: Equations for heat transfer in the SOFC tube.

T	**Temperature [K]**	**k**	**Thermal conductivity [W/mK]**
c/c_p	Heat capacity [J/kgK]	α	Convective heat transfer coeff. [W/m^2K]
ρ	Density [kg/m^3]	Δr	Thickness of fuel plenum [m]
V	Gas velocity [m/s]	r	Radius [m]

Table 2: Nomenclature

AST	Air Supply Tube	c	Cathode
a	Anode	i	Inner radius
o	Outer radius		

Table 3: Subscripts

Steady state part-load simulations

The goal of the present work is to produce a generalised part-load performance map for the tubular SOFC, which enables identification of potential part-load strategies. AU and FU as well as air and fuel flow rates have previously been identified as important performance parameters (6) - (10). However cell behaviour as a function of these parameters has so far not been presented. In this study we have evaluated a strategy were either AU or FU is kept constant. Performance maps have been produced for these two cases through a number of steady state simulations. The reference for all part-load simulations is a non optimised design case with similar parameter values as used in (4) - (9). The parameters are listed in table 4.

Parameter	**Comment**	**Value**
Fuel flow	Pure methane	$3.8 \cdot 10^{-4}$ mole/s
Fuel inlet temperature	Prereformer inlet, before mixing with recycled anode exhaust gases	950 K
Air flow rate	$\lambda = 4$ (air excess ratio), dry air	$1.448 \cdot 10^{-3}$ mole/s
Air inlet temperature	Air supply tube inlet	950 K
Fuel utilisation	$FU = \frac{I}{2F \cdot 4\dot{n}_{CH_4}}$, current divided by fresh fuel flow	85 %
Air utilisation	$AU = \frac{I}{4F \cdot \dot{n}_{O_2}}$, current divided by oxygen flow into the fuel cell	21.25 %
Pressure	Varies with air flow rate	4 bar
Steam/Carbon ratio	Anode exhaust gas recycling	2.5

Prereforming degree	Amount of fresh fuel being reformed in the prereformer	30 %
Electric power	Gross (voltage times current)	136 W
Efficiency	$Eff = \frac{Power}{\left(LHV_{in} - LHV_{out}\right)_{cell}}$	48%
Mean solid temperature	Arithmetic average of membrane	1032 K
Turbine inlet temperature	After complete adiabatic combustion in burner	1150 K

Table 4: Main parameters for the design case

In the first case AU was kept constant at 21.25%. FU was varied between 67 and 97%, while air flow rate was varied between 30 and 100% of the design air flow rate. Fuel flow and operation voltage were adjusted to achieve the selected AU and FU. In the second case, FU was kept constant at 85%. AU was varied between 15 and 30%, while air flow rate was varied between 30 and 100%. As for the previous case, fuel flow and operational voltage were adjusted to achieve the selected AU and FU.

Air flow rate is a characteristic parameter for gas turbine systems. Therefore the air flow rate was varied in order to facilitate the use of these performance maps in hybrid system evaluations. Due to the identification of variable shaft speed as an important property of the gas turbine in hybrid systems (6) - (10), system pressure for both calculations has been varied proportionally to air flow rate. This is assumed to be a sufficient approximation of part-load gas turbine behaviour, and it is also verified by the calculations of Kimijima et al. (10).

In a hybrid system the fuel cell inlet temperatures are expected to vary with the operation point due to changes in compressor and recuperator efficiency. It is difficult to predict these variations without simulating the whole hybrid cycle. However, air inlet temperature can partly be controlled by for example introducing additional fuel to the afterburner or implementing a recuperator bypass. Furthermore, it is desirable in terms of SOFC performance and in order to avoid thermal cracking, to operate the cell at a constant temperature level. Thus a constant system air inlet temperature was assumed in all calculations. The fresh fuel inlet temperature is assumed to be the same as the air inlet temperature.

Steady state part-load results and discussion

Performance maps, based on part-load calculations are shown in figure 2 - 4. In principle, all parameters could be plotted in one single map for either constant AU or FU, but in order to increase readability of the maps, the information has been split up into three maps for each case. Part-load performance maps can also be produced for other values of AU and FU than the ones shown above. A full map, however, would be a three-dimensional map with AU, FU and air flow rate as coordinates, which only can be handled electronically.

System part-load performance at constant FU can shortly be summarized as following:

- Efficiency increases at reduced power, partly due to reduced ohmic losses.
- Mean and maximum solid temperatures as well as TIT and air outlet temperature show similar behaviour. They decrease at reduced AU and air flow rate which may be due to increased cooling effect.

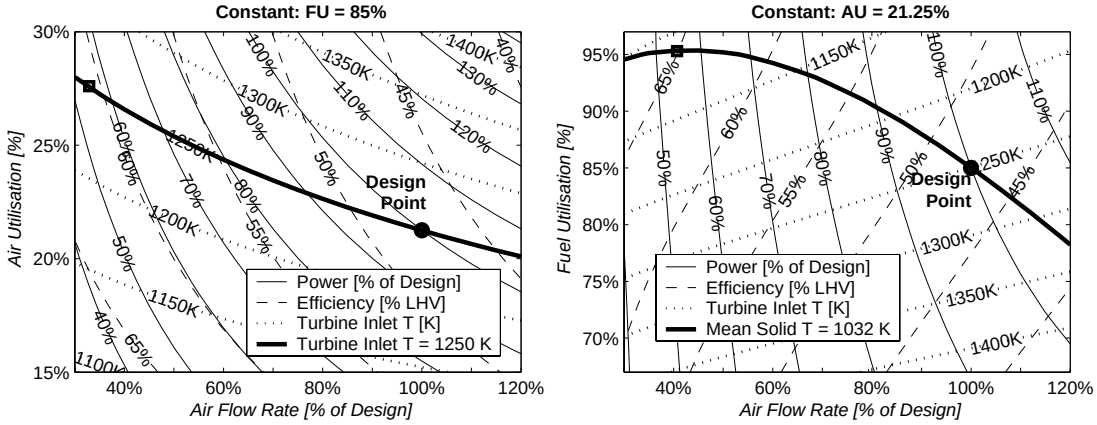

Figure 2: Power, efficiency and TIT.

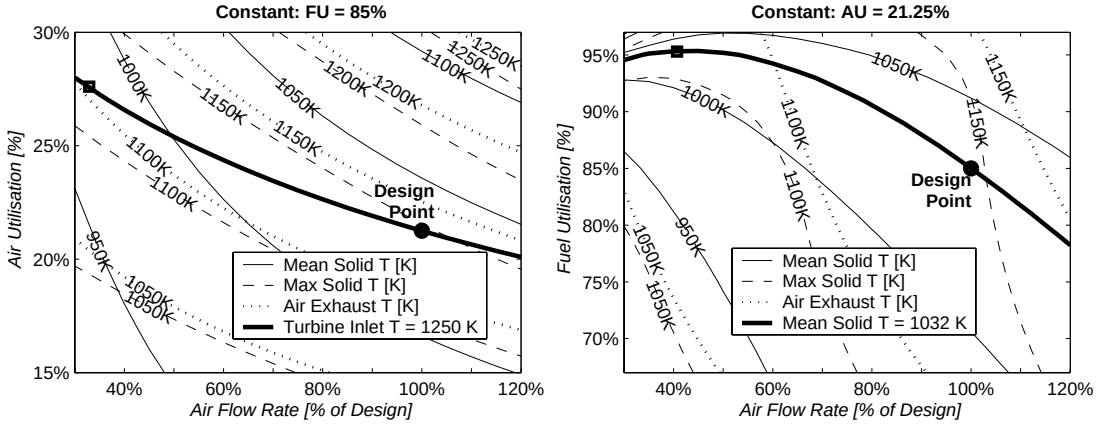

Figure 3: Mean and max solid and air exhaust temperature

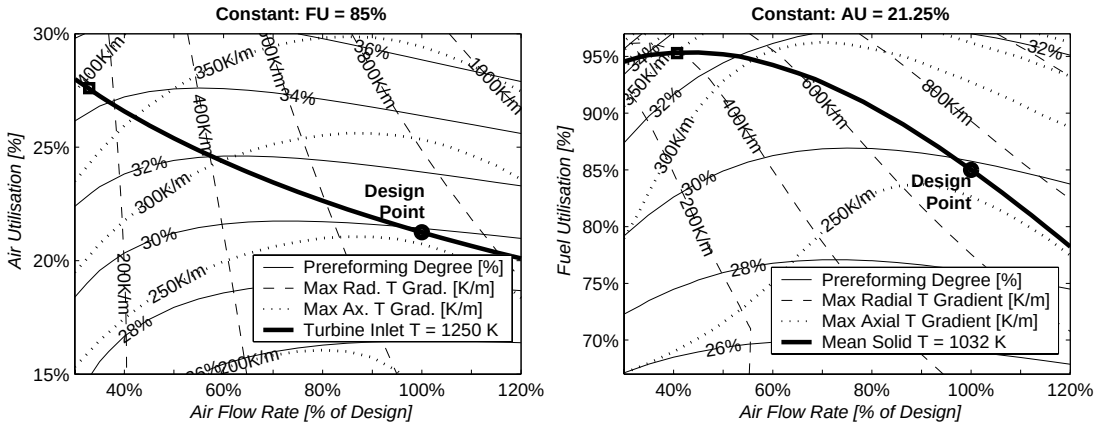

Figure 4: Prereforming degree and radial and axial temperature gradients.

- Axial temperature gradients increase towards higher air utilisation and reduced air flow rate.
- Radial temperature gradients decrease at reduced load.
- Prereforming degree is reduced at lower air utilisation. This may be caused by increased cooling and thus less heat supply to the prereformer.

It can be seen from figure 3 (left) that maintaining a constant solid temperature in part-load is a poor strategy if a constant FU should be maintained. In this case, a reduced air flow rate will hardly influence power output. Behaviour would be similar for constant maximum solid temperature and air exhaust temperature due to the parallel nature of the iso-lines.

A strategy following constant TIT, as mentioned by Pålsson et al. (3) proves to be more interesting in this case. As can be seen in figure 2 (left; bold line), power is reduced sufficiently at reduced air flow rate, while efficiency increases. Figure 4 (left) shows an increase in axial temperature gradients, while radial gradients are reduced.

System part-load performance for constant AU can shortly be summarised as following:

- Efficiency increases at reduced air flow rate, partly due to reduced current density and thereby reduced ohmic losses.
- Mean and maximum solid temperatures decrease with the air flow rate.
- TIT decreases with increasing FU as less fuel is burned in the afterburner.
- Power depends mainly on the air flow rate, as the fuel to air ratio is constant in the simulated range.
- Radial temperature gradients decrease at reduced air flow rate and load.
- For constant air flow rate, axial temperature gradients decrease with FU. Reducing air flow rate at constant FU decreases axial gradients to a certain point where a further reduction in air flow rate leads to an increase in the gradients.

Maintaining a constant TIT results in less favourable part-load behaviour for constant AU, as the mean solid temperature is more reduced than in the constant FU case. For constant AU, keeping the mean solid temperature constant proves to be a better strategy. In this case, both FU and efficiency increase at reduced power and air flow rate. There is also a large reduction in radial temperature gradients, however, at the expense of increased axial gradients.

The following example demonstrates the use of the performance maps. We assume that operation parameters for 55% load with the same TIT and FU as for the design point are desired. The iso-line for TIT=1250K can be found in figure 2 (left) and projected onto figure 3 and figure 4 (Bold line in the figures to the left). The operational point is found in the middle between the 50 and 60% load iso-lines and the projected iso-line for constant TIT. The axes coordinates show approximately 35% air flow rate and 27% AU (Square in figure 2, left). The dashed iso-lines show that in this case efficiency will be slightly above 60%. Projecting this point onto the other figures reveals the other operational parameters.

Pressure and temperature sensitivity studies were performed. They showed that pressure mainly influences prereforming degree and thermal gradients, while influence on the other system parameters is rather low. This justifies the assumption of linear pressure

dependence on air flow rate. Fuel and air inlet temperatures, however, proved to significantly influence power output and cell temperatures. Hence the performance maps are only valid for small deviations of the fuel and air inlet temperatures.

Dynamic simulations

A study on dynamic performance of the single cell system shown in figure 1 (left) was performed. The intention of this study was to investigate dynamic behaviour without the use of an advanced control strategy. Load reduction for both AU and FU was simulated to reduce power from 100% to 55%. For the constant AU case, FU and air flow rate were controlled to move linearly towards the target point over a period of 100 s (From design point to square in figure 2 (right)). AU and air flow rate were controlled in the same manner for the constant FU case. Load increase was simulated in the opposite direction between the same points. The results are shown in figure 5 and figure 6. The data have been plotted against a logarithmic time scale to comprise both short and long term effects.

Figure 5 (left, above) shows that the target power is reached almost within the 100 s period of the load change when constant FU is maintained. As predicted by the part-load diagram in figure 4 (left), there is an increase in maximum axial temperature gradients and a reduction in the maximum radial gradients. The maximum axial temperature gradient peaks slightly above the final value after approximately 2,000 s and then it gradually adjusts to the new steady state value. The TIT peaks for a short period at almost 100K above the final value after 100 s and it takes 10,000 s before it stabilises at the steady state value. The temporary oscillation may be explained by the gas residence time in the fuel cell and pressure reduction due to the reduced flow rate. Prior to reaching the peak, more fuel exits than enters the cell and thus more fuel is burned in the afterburner. When this surplus fuel is combusted, the TIT gradually adjusts to the steady state value. A final steady state is reached after app. 20,000 s (5.6 hours).

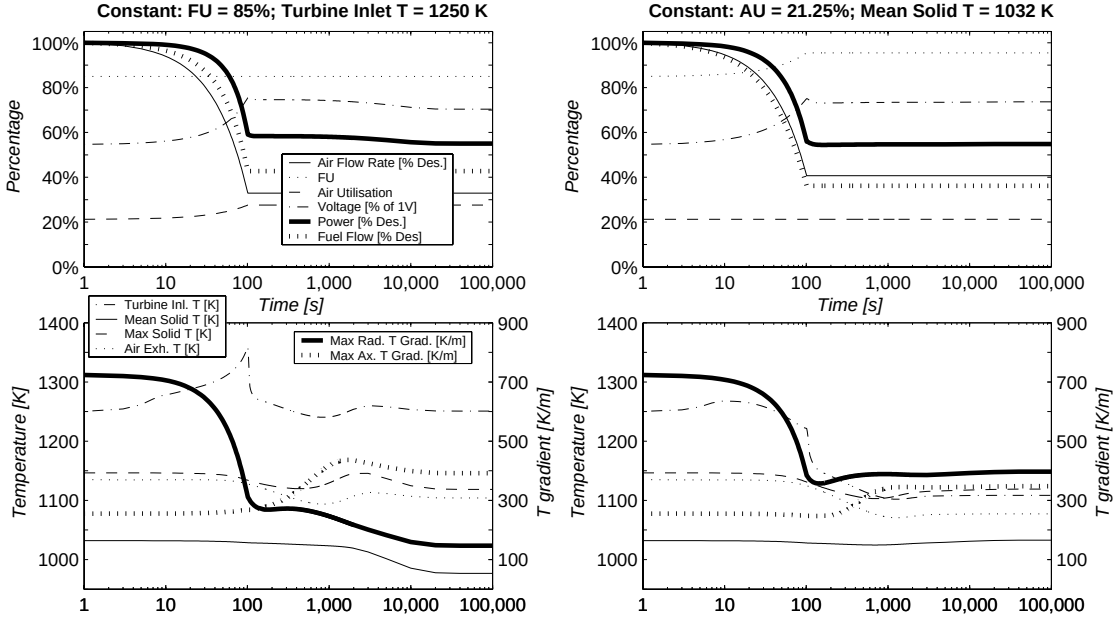

Figure 5: Dynamic behaviour at load decrease from 100 to 55% for constant FU (left) and AU (right). Time is given in seconds on a logarithmic scale.

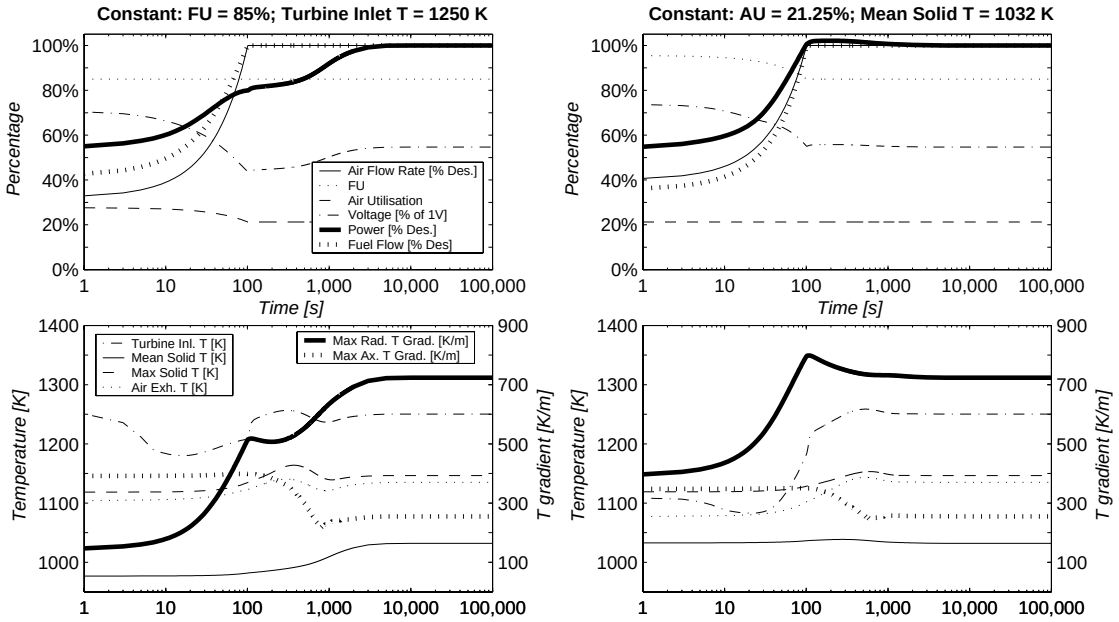

Figure 6: Dynamic behaviour at load increase from 55% to 100% for constant FU (left) and AU (right). Time is given in seconds on a logarithmic scale.

The same load change but with a constant AU and mean solid temperature shows a more rapid adjustment to the new operational point, and almost all parameters show an asymptotical approximation to steady state. The TIT has only a marginal peak in this case. Steady state is reached after app. 3,000 s.

Figure 6 (left) shows that load increase for constant FU takes app 5,000 s to reach steady state. All parameters seem to reach the final value at the same time as power. However, maximum radial temperature gradient, maximum solid temperature and the air exhaust temperature show local and global peak values. The axial maximum temperature gradient slightly undershoots its final value at about 800 s.

Behaviour while maintaining a constant AU is shown to the right in the same figure. Again, this strategy shows a more rapid adjustment than for constant FU. Power, FU and voltage are nearly stable directly after the load change ramp. The temperatures are somewhat delayed in their response, and it takes them about 1,000 s to asymptotically adjust to the new values. The maximum radial gradient peaks with app 50K above the final value at the end of the load change.

For all the dynamic simulations there seems to be a connection between the power and the radial temperature gradient. This is also shown by an observation of the performance maps in Power, efficiency and TIT. to Prereforming degree and radial and axial temperature gradients.. The relationship may be explained by the heat production released in the electrochemical reaction which scales with the power and the heat flow through the cell solid. The dynamic simulations also show that thermal response is slower than the power production response. This can be explained by thermal inertia and low thermal conductivity of the cell materials.

Although the start and the end points for the simulations for constant FU are at the iso-line for constant TIT, there are large variations of this parameter during the load change. This is a dynamic effect which cannot be predicted by interpretation of the steady state

performance maps. The start and end point, however, have the same temperature, as predicted in figure 2 (left). In a hybrid cycle this behaviour may influence turbine output. Hence, further investigation is needed.

Load change at constant AU was performed between two points at the iso-line for mean solid temperature. As can be seen from figure 5 and figure 6 (right), mean solid temperature remains rather constant during the load change. This behaviour may be explained by thermal inertia of the solid material.

Conclusions

A novel method for presenting part-load performance as a function of utilisation factors and air flow rate has been presented. The performance maps can be used to predict thermal gradients, mean solid temperature, air exhaust temperature, TIT as well as power and efficiency for a system of a tubular SOFC with prereformer, afterburner and exhaust gas recirculation, operating at steady-state. The maps may also be used as a first approximation for development of control strategies during load change. Sensitivity studies show a strong dependency on inlet temperatures and this fact must be considered when operating a hybrid system.

Dynamic simulations for both load increase and reduction, following a simple ramp parameter change, have been performed for constant AU and FU. The simulations show that maintaining constant AU during load change has a faster response and relaxation than if constant FU is maintained.

Further work will include extension of the model to a full hybrid cycle and further investigation of control strategies.

Acknowledgements

Hanne Marie Kvamsdal from SINTEF and Rolf Jarle Aaberg from Statkraft are acknowledged for their contribution. We also thank the Norwegian Research Council, Shell Technology Norway and Statkraft for their financial support.

References

(1) A. D. Rao, G. S. Samuelsen, A Thermodynamic Analysis of Tubular SOFC Based Hybrid Systems, Proceedings of ASME TURBO EXPO 2001, June 4-7, 2001, New Orleans, Luisiana. (2001-GT-0522)

(2) S. H. Chan, H. K. Ho, Y. Tian, Modeling for part-load operation of solid oxide fuel cell-gas turbine hybrid power plant, Journal of Power Sources, 114 (2003) 213-227.

(3) Jens Pålsson, Azra Selimovic, Lars Sjunnesson, Combined Solid Oxide Fuel Cell and Gas Turbine Systems for Efficient Power and Heat Generation, Journal of Power Sources, 86 (2000) 442-448.

(4) Stephen E. Veyo, Wayne L. Lundberg, Shailesh D. Vora, Kevin P. Litzinger, Tubular SOFC Hybrid Power System Status, Proceedings of ASME TURBO EXPO 2003, June 16-19, 2003, Atlanta, Georgia, USA. (GT2003-38943)

(5) Elmar Achenbach, Response of a Solid Oxide Fuel Cell to a Load Change, Journal of Power Sources, 57 (1995) 105-109)

(6) P. Costamagna, L. Magistri, A. F. Massardo, Design and part-load performance of a hybrid system based on a solid oxide fuel cell reactor and a micro gas turbine, Journal of Power Sources, 96 (2001) 352-368.

(7) Stefano Campanari, Full Load and Part Load Performance Prediction for Integrated SOFC and Microturbine Systems, Journal of Engineering for Gas Turbines and Power, Apr. 2000, Vol 122, pp 239-246.

(8) S. H. Chan, H. K. Yo, Y. Tian, Modelling for Part Load Operation of Solid Oxide Fuel Cell-Gas Turbine Hybrid Power Plant, Journal of Power Sources, 114 (2003), 213-227.

(9) Jens Pålsson, Azra Selimovic, Design and Off-Design Predictions of a Combined SOFC and Gas Turbine System, Proceedings of ASME TURBO EXPO 2001, June, 4-7, New Orleans, Luisiana, USA, (2001-GT-0379)

(10) Kimijima, S., Kasagi, N., Performance Evaluation of Gas Turbine-Fuel Cell Hybrid Micro Generation System, Proceedings of ASME Turbo Expo 2002, Amsterdam, Netherlands, June 2002

(11) A. D. Rao, G. S. Samuelsen, Analysis Strategies for Tubular Solid Oxide Fuel Cell Based Hybrid Systems, Journal of Engineering for Gas Turbines and Power, July 2002, Vol 124, 503-509.

(12) Riensche, E, Achenbach, E, Froning, D., Haines, M. R., Heidug, W. K., Lokurlu, A., von Adrian, S., Clean Combined-Cycle SOFC Power Plant-Cell modelling and Process Analysis.

(13) gPROMS (General PROcess Modelling and Simulation tool), v.2.3.0, Process Systems Enterprise Ltd., London, http://www.psenterprise.com/

(14) Achenbach, E., Riensche, E., Methane/steam reforming kinetics for solid oxide fuel cells, Journal of Power Sources, 52 (1994), 283-288.

(15) Karoliussen H., Nisancioglu K., Solheim A., Ødegård R., SOFC Stack Modeling with Internal Reforming, Proceedings of the 4th IEA Workshop on SOFC, Lausanne, Switzerland, August 1992.

(16) Nisancioglu, Kemal, Ohmic losses, IEA, Workshop on Mathematical Modelling, Proceedings on natural gas fuelled solid oxide fuel cells and systems, Charmey, Switzerland, July 2-6, 1989.

Appendix C - Paper III

Safe Dynamic Operation of a Simple SOFC/GT Hybrid System

Christoph Stiller, Bjørn Thorud, Olav Bolland

Published at:

ASME TURBO EXPO 2005, Reno-Tahoe, Nevada USA, June 6-9, 2005

Proceedings of GT2005
ASME Turbo Expo 2005: Power for Land, Sea and Air
June 6-9, 2005, Reno-Tahoe, Nevada, USA

GT2005-68481

SAFE DYNAMIC OPERATION OF A SIMPLE SOFC/GT HYBRID SYSTEM

Christoph Stiller
Tel. +47 735 937 23
Christoph.Stiller@ntnu.no

Bjørn Thorud
Tel. +47 735 939 34
Bjorn.Thorud@ntnu.no

Olav Bolland
Tel. +47 735 916 04
Olav.Bolland@ntnu.no

The Norwegian University of Science and Technology (NTNU)
Department of Energy and Process Engineering (EPT)
Kolbjørn Hejes vei 1B
N-7491 Trondheim, Norway

ABSTRACT

The current work shall prove the feasibility and show methods to safely operate a simple SOFC/GT hybrid system under part-load and load change. Dynamic and steady state studies on a detailed model of a SOFC/GT hybrid system have been performed. A design point is selected. Steady-state part-load behaviour is shown by means of performance maps. An operation line with fairly constant temperatures in the upper part-load regime and an almost constant efficiency down to app. 25% part-load is proposed and the dynamic behaviour of the system on rapid load changes is investigated. Strategies for the dynamic controlling of power by manipulating fuel flow are shown that might enable the system to adapt to a new setpoint power quite quickly.

Keywords: SOFC, Hybrid System, Dynamic Model, Part-load

INTRODUCTION

A large amount of modelling work [1-4] and a demonstration plant [5] have proven that a solid oxide fuel cell (SOFC) integrated with a gas turbine (GT) has a potential for high efficiency electricity production with low environmental emissions. However, these types of systems face many challenges when it comes to load change and part-load operation. A gas turbine alone has good dynamic properties compared to the SOFC, but part-load performance can be rather poor. In any operational point, compressor surge must be prevented. A SOFC is generally able to respond quickly to load changes [6], but it might be destroyed or seriously degraded either due to thermally induced stresses caused by different thermal expansion coefficients in the cell materials or from carbon deposition at the anode. Another phenomenon that may occur during load change is backflow of gas from the burner to the anode cycle. These incidents must not occur in any operation instance.

Results from part-load operation modelling have already been discussed by some authors. Costamagna et al. [7] investigated a hybrid system using a non-dimensional tubular SOFC model. In all simulations they assumed constant fuel utilisation (FU). If shaft speed was assumed constant, power output could only be controlled by varying the fuel flow. These simulations showed large variations in air utilisation (AU) and loss of efficiency for fixed shaft speed when operating at part-load. For variable shaft speed, however, AU and FU as well as SOFC inlet temperatures could remain fairly constant in part-load operation with only a small penalty on system efficiency. This effect was mainly due to increased recuperator efficiency owing to reduced air flow rate.

Campanari [8] also used a non-dimensional tubular SOFC model to investigate the hybrid system. Assuming constant FU of 80%, for constant shaft speed they suggested reducing AU and current density for part-load. This approach will reduce power output of the SOFC as well as the turbine inlet temperature (TIT) and consequently the power output of the GT. For variable shaft speed they suggested to reduce air flow rate and current density to maintain a constant AU. However, a reduction in air flow rate leads to pressure reduction and therewith higher turbine outlet temperature (TOT) and thus higher recuperator outlet temperatures. They concluded that for maintaining constant TIT, the current density has to be reduced further.

Chan et al. [3] also investigated a non-dimensional tubular SOFC-type in a hybrid system. In their system, power is reduced by shifting the load from the SOFC to the GT through introducing fuel to the combustor, which results in strong reduction of the system efficiency. This method also implies

that a SOFC bypass should be implemented for both fuel and air. Due to the low part-load efficiency, they state that this method is mainly for short term load reduction. The aim was to maintain a relatively high SOFC temperature.

Pålsson and Selimovic [9] used a 2-dimensional planar SOFC model for part-load studies. Design point was set where the compressor flow matched the cooling requirement of the SOFC. They introduced an air heater/cooler prior to the SOFC entry in order to meet the requirements for the air inlet temperatures at part-load operation. TIT was kept constant and shaft speed was varied. At part-load operation, increased FU and low GT part-load efficiency led to increased power contribution from the SOFC. Due to the problems associated with matching of the system components, they concluded that the load range for hybrid systems should be limited to 55 – 100%, corresponding to a load variation of the GT of 20 – 100%.

Kimijima and Kasagi [10] studied part-load of a 30 kW simple recuperated cycle using a non-dimensional SOFC model. Variable and fixed shaft speed operations are compared. FU is kept constant, even though it is mentioned that FU could be increased at part-load operation. They conclude that variable shaft speed operation is favourable in terms of part-load performance; however the higher TOT could cause problems.

All above mentioned authors have identified inlet and outlet gas temperatures as well as air and fuel utilisation of the SOFC as important parameters for part-load operation of hybrid systems. Maintaining a constant SOFC operation temperature is important to avoid thermal cracking, but this might be difficult to achieve at reduced pressure as the TOT increases and consequently the recuperator outlet temperatures.

We have recently investigated a SOFC system with recycle and pre-reformer to be fitted into a hybrid system [11]. Performance maps were introduced to illustrate the relationships between the most important SOFC parameters over air flow and either FU or AU, while keeping the other of the two latter parameters constant. Based on these maps, it was found out that strategies with fairly constant temperatures in the SOFC seem feasible. Due to the lack of a GT model, SOFC inlet temperature was assumed constant and the pressure was assumed proportional to the air flow. This was the main limitation of this work.

The current work presents a detailed dynamic model of a tubular SOFC system integrated into a simple recuperated GT cycle. It shall prove the feasibility and show methods to operate such a system in part-load and load change without any of the critical phenomena to occur. The system is designed for a certain nominal performance. The selection of the design point is discussed and vital parameters are highlighted. Furthermore, part-load behaviour as a function of the controllable parameters, i.e. fuel flow and shaft speed, is investigated. The dependency of crucial system parameters on the controllable parameters is displayed in steady state performance maps. From the maps, valid ranges of the controllable parameters and advantageous operation lines are derived. Applying the derived operation lines, transient behaviour of the crucial parameters during load-changes is investigated. Considering steady state and transient results, a strategy for safe operation of the investigated system is proposed. Finally, an overview on further opportunities is given.

NOMENCLATURE

Abbreviations

FU	- Fuel utilisation
GT	- Gas turbine
HEX	- Heat exchanger
RFF	- Fuel flow relative to design point
RP	- Net power relative to design point
RPM	- Rounds per minute
RSS	- Shaft speed relative to design point
SM	- Surge margin
SOFC	- Solid oxide fuel cell
TIT	- Turbine inlet temperature
TOT	- Turbine outlet temperature

SOFC AND GT-CYCLE MODEL

The investigated hybrid cycle is shown in Fig. 1. The ducts account for time delay of the flows under transient conditions. The SOFC system design (inside the vessel in Fig. 1) is similar to that of Siemens-Westinghouse. This type of design has been described by other authors [12, 13]. The model incorporates pre-reformer, afterburner and recirculation and mixing chamber, where part of the anode exhaust gas is admixed to the fresh fuel in an ejector in order to supply steam to the steam reforming and shift reaction. Required valves for start-up, shut-down and failure have not been included. The whole model is implemented in the equation based modelling tool gPROMS [14]. The sub-models comprise the following:

- The SOFC model is spatially discretised and fully dynamic in terms of gas transport and heat transfer, allowing the study of temperature distributions. Gas flows are treated as 1D plug flows, while the solid structures are modelled by a 2D discretisation scheme in axial and radial direction, neglecting effects in the circumferential direction. The model accounts for the effects of internal reforming, activation and concentration polarisation, ohmic resistance and pressure losses. A more detailed description of the model is given in Appendix 1.
- As the temperature distribution inside the pre-reformer is of minor interest, it is modelled as a non-dimensional Gibbs equilibrium reactor where reforming and water-gas shift reactions take place. It is thermally connected to the fuel cell tube. The consumed heat is supplied by radiation from the anode surface, adjusted by a shape factor to meet a certain pre-reforming degree at the design case. Gas residence time in the pre-reformer is accounted for by ducts up- and downstream the pre-reformer.
- The afterburner is non-dimensional and adiabatic and completely combusts the remaining anode exhaust gas together with the cathode air. By mixing cathode and anode exhaust streams, it causes pressure equalisation of these flows upstream.
- The afterburner exhaust is preheating the inlet air by a counter-flow tube-shell set-up, where the tube is the prolongation of the fuel cell air supply tube. The model accounts for thermal inertia, pressure loss and gas residence times. The approaches are equal to the SOFC model.

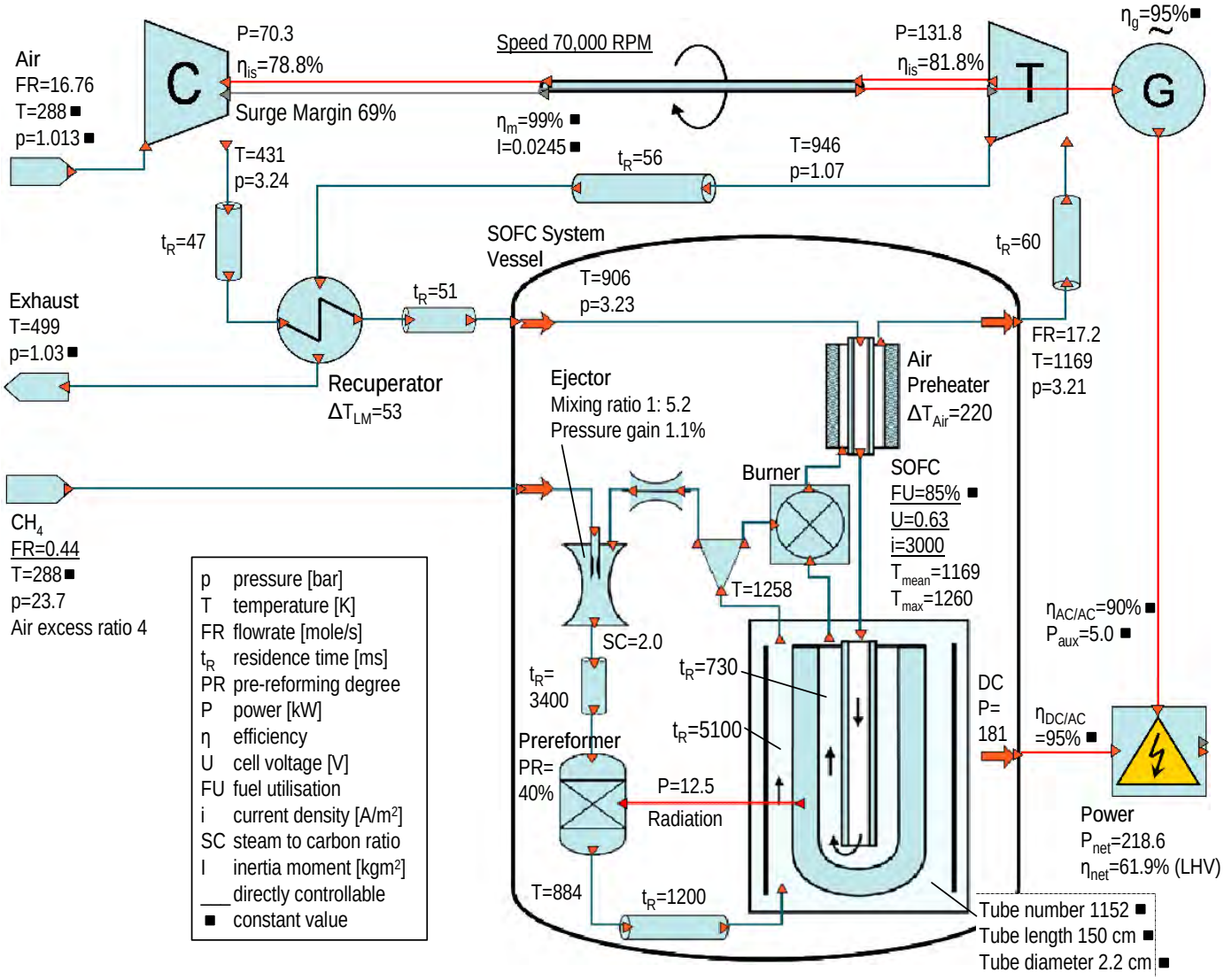

Figure 1: Cycle layout and design point values (square-marked values remain always constant).

- The pressure loss in the anode loop is overcome by an ejector. High induced (recycle) flow rates at low pressure differences are typically achieved by subsonic mixing ejectors. The actuating flow is accelerated to supersonic speed in a Laval nozzle before it enters the mixing chamber. The ejector model is based on section-wise momentum balances and has been validated against data from Marsano et al. [15]. Pressure losses are included by a fixed throttle valve.
- The ducts are adiabatic and frictionless. Their only purpose is to account for gas residence time.
- The HEX is a stack of counter-flow plate-fin type. A 2-dimensional distributed model is applied that accounts for thermal inertia, pressure loss and gas residence times. The approaches are equal to the SOFC model.
- Generator and power electronics account for transformation efficiencies which are assumed to be constant. A constant power sink accounts for power consumption of auxiliaries and transformation efficiency decrease at low load.
- The compressor is based on the performance map of a small centrifugal research compressor by the German Aerospace Centre [16]. The map is understood as a generic radial compressor map and therefore it has been scaled in terms of reduced mass flow, pressure ratio and shaft speed to fit the design case. The map has been modelled using polynomials of 4th and 5th order for reduced mass flow, pressure and efficiency as functions of reduced shaft speed and operation (β) line. A surge margin (SM) is calculated as follows:

$$SM = \frac{\pi_{surge}\left(\dot{m}\right) - \pi\left(\dot{m}, n\right)}{\pi\left(\dot{m}, n\right)} \quad (1)$$

where $\pi\left(\dot{m}, n\right)$ is the actual pressure ratio at the actual mass flow and reduced shaft speed and $\pi_{surge}\left(\dot{m}\right)$ is the surge pressure ratio at the actual mass flow. An iso-line representation of the compressor characteristics is shown in Appendix 2.

- The turbine is based on the performance map of a small radial turbine [16] which is, similar to the compressor map, scaled to fit the design case. An ellipse approach has been used for the relationship between reduced mass flow, reduced shaft speed and operation (β) line. Pressure ratio and efficiency have been modelled through polynomials. An iso-line representation of the turbine characteristics is shown in Appendix 2.
- The shaft model includes acceleration/deceleration of the shaft through moment of inertia of the moving parts:

$$\frac{d\omega}{dt} = \frac{P_B}{I \cdot \omega} \quad (2)$$

Where ω is the angular shaft speed in [rad·s^{-1}], I is the moment of inertia in [kg·m^2], and P_B is the power balance

$$P_B = \eta_m P_{Turb} - P_{Comp} - P_{Gen} \text{ in [W]}. \quad (3)$$

The resulting whole model consists of approximately 9,000 algebraic and 2,000 state variables. The simulations were performed on a 2.5 GHz Intel Pentium-4 processor PC. Calculation time for a steady state point was approximately 5-10 seconds. The solver for dynamic calculations uses flexible time increments, thus calculation time depends on the momentary fluctuation rate of the variables. A calculation time of about 5 minutes was required for the dynamic performance studies shown below.

DESIGN POINT

Before part-load behaviour can be studied, a design point has to be defined. All relevant cycle data are displayed in Fig. 1. Most of the data are similar to recent literature on hybrid cycles [3,7,8,10] and public data from Siemens-Westinghouse. Values in the figure marked with a square are constant during all simulations. The design point and system dimensioning is furthermore based on the following assumptions:

- The system size is determined based on the Siemens-Westinghouse stack design which incorporates 1152 tubular cells [17].
- Pure methane is supplied as fuel.
- A length of 0.5 m was chosen for the air preheat tube, yielding a temperature increase of 220 K at design point.
- The ducts have a length of 1 m and are dimensioned for gas velocities around 20 m/s at design point. The residence times are calculated utilising the ideal gas law. Therefore they will vary slightly in other operation points. Residence times before and after the pre-reformer account for the actual pre-reformer residence time.
- The fuel utilisation (FU) is determined from current and fuel flow, as these parameters can be measured in a real system. Setting FU constant hence means maintaining a constant ratio of current to fuel flow. While this in steady state provokes a constant content of combustibles in the anode exhaust gas, the content may vary during dynamic operation due to pressure change and gas transport delay. Due to the variations of the heating value of the exhaust gas, this may cause severe oscillations in burner temperature during load change. The common fuel utilisation value of 85% has been chosen.
- The ejector has been dimensioned for supplying a steam to carbon ratio of 2 in the design point. The difference in static pressure of induced and actuating gas flow in the mixing zone is vital for the ejector performance. According to Johannesen [18], a lower actuating flow pressure than induced flow pressure, causes a strong reduction in induced flow rate, while a higher actuating flow pressure does not significantly increase induced fluid flow rate. For being able to reduce the fuel flow rate for part-load operation while maintaining a high recycle ratio, the inlet pressure of the actuating fluid at design point must be high. A value of 23.7 bar was chosen for design point.
- The recuperator is dimensioned in order to achieve a high amount of heat recuperation at tolerable size and pressure drop.
- The rotating parts of turbine, compressor, generator and shaft have together a moment of inertia of 0.025 kg·m^2. This is equivalent to a rotating mass of 20 kg and a mean radius of 5 cm. The moment of inertia influences the power output during shaft acceleration and deceleration.
- The generator is assumed to have a constant efficiency of 95%. The power electronics have constant efficiencies of 90% for AC/AC and 95% for DC/AC conversion. In order to account for power consumption of auxiliaries and the decreasing conversion efficiencies at load reduction, a constant sink term of 5 kW was applied.

STEADY-STATE PERFORMANCE

With the given design, three degrees of freedom remain for off-design operation:

1. Shaft speed variation
2. Fuel flow variation
3. Fuel utilisation/Current/Voltage variation.

Variation of the shaft speed can be controlled by the power electronics, i.e. generator power. Dependent on the power balance at the shaft, it runs steadily, accelerates or decelerates.

Fuel flow variation can be achieved by a control valve. For the dynamic simulations we assume that the flow rate can instantaneously be adjusted to a desired value.

Fuel utilisation and current are coupled via the fuel flow rate, while current and voltage are coupled via the fuel cell characteristics. However, large variations in FU are not recommendable, as low FU leads to low steam content in the anode recycle and high TIT, while high FU leads to steep internal temperature gradients in the fuel cell. Therefore, we chose to operate at constant FU by setting the current proportional to the fuel flow rate.

The remaining free parameters, shaft speed and fuel flow, may be varied independently from each other within certain limits. Each combination determines a certain operation point of the system. Thus, two-dimensional matrices of the interesting process parameter steady state values over the two free parameters can be produced and displayed in performance maps. We have previously introduced similar maps for a SOFC stack system [11]. In that work we used air utilisation and air flow rate as free parameters. Due to absence of a GT cycle model, in that work simplified assumptions for gas inlet temperature and operating pressure had to be made. These data

are in the present work being calculated by the GT cycle model, representing a more comprehensive study.

For easy reading, we give dimensionless values for shaft speed (RSS) and fuel flow (RFF), related to the design point values. RSS is varied between 65% and 105%, representing the valid range for the compressor and turbine map. RFF is varied between 15% and 110%.

Figure 2 and 3 show the steady-state behaviour of the parameters of interest as a function of RSS and RFF. For easier reading, each diagram shows only the fields of three parameters.

The blinded out area on the upper left (low shaft speed and high fuel flow) represents an area where no steady state exists. Transient experiments have shown that the temperature in this regime is steadily climbing far beyond the valid ranges and furthermore eventually causing compressor surge. This is because enhanced effectiveness of the heat recuperation loop and lower air excess ratio at lower airflow causes TIT to increase. Concurrently, the increased TIT causes decrease of airflow, originating from compressor and turbine characteristics.

In the lower right area (high shaft speed and low fuel flow), the cell is cooled down strongly and therefore the voltage is low. As it is not recommendable to operate in this regime, it is blinded out for cell voltages lower than 0.3 V.

A first result from the performance map is that reducing fuel flow at constant shaft speed (and therewith fairly constant air flow), i.e. going down a vertical line from design point, results in a strong reduction in temperatures and therewith efficiencies.

The figures also show that a load reduction by linearly reducing fuel flow and air flow will lead into the unstable region. Remaining in the stable regime therefore implies larger percentual reduction in fuel flow than air flow. This is a consequence of the lower pressure ratio at reduced shaft speed which results in an increased TOT. The same behaviour is also confirmed in a study by Costamagna et al. [7].

Surge margin and steam to carbon ratio do not reach any alarming values in the shown operation range.

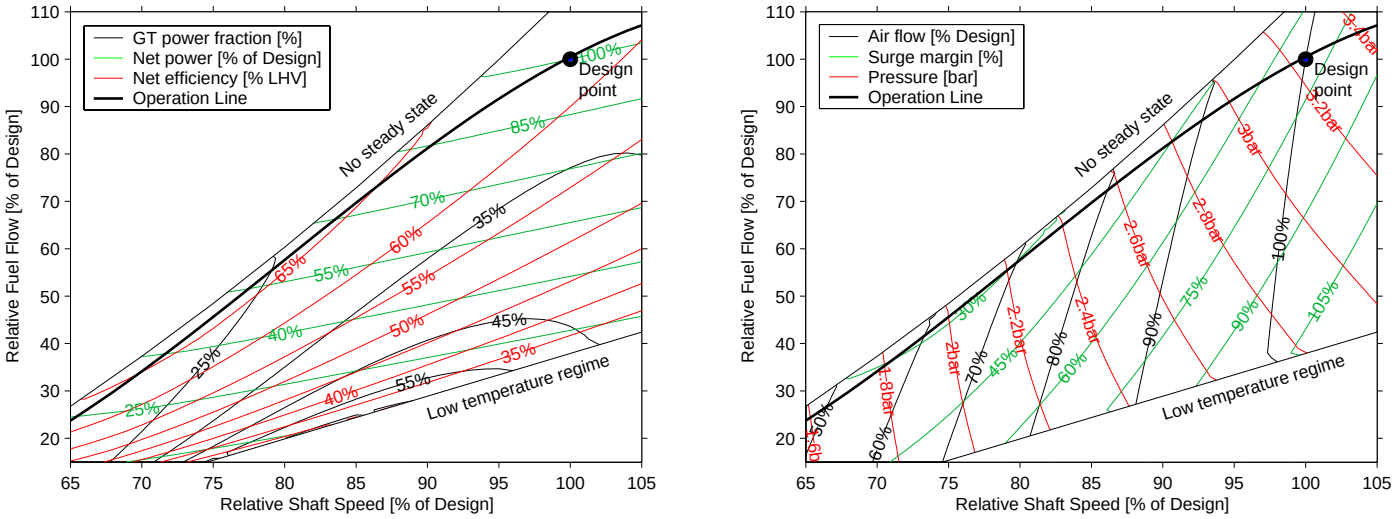

Figure 2: Power parameters (left) and turbomachinery parameters (right) in steady state.

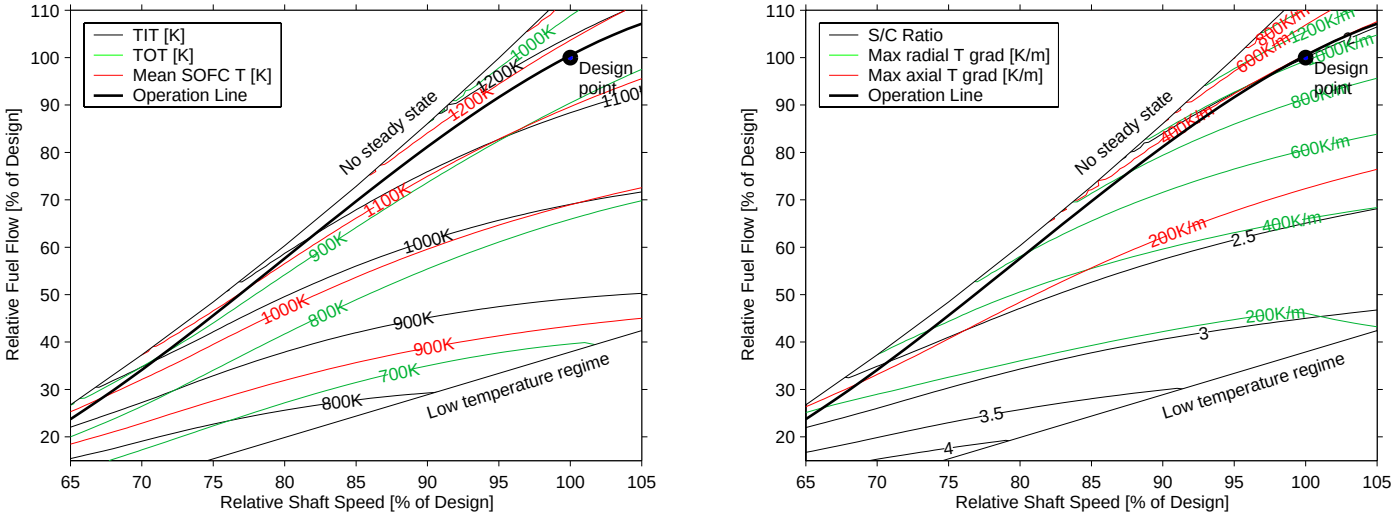

Figure 3: Significant temperatures (left) and steam to carbon ratio and SOFC temperature gradients (right) in steady state.

STEADY-STATE OPERATION LINE

The main parameter of interest for the power plant is simply the power output. Using the performance maps, we find lines of constant dimensionless net power in Fig. 2. For a certain desired power in steady state, each point of its line is basically a valid operation point. However, in order to decide which point is optimal, the following objectives need to be considered:

1. High efficiency
2. Safe operation: Distance from invalid regimes and alarming values for safety-relevant parameters.
3. Fairly constant SOFC temperature level

The latter point is the most restrictive requirement, as thermal cycling affects the lifetime of SOFCs. It is also the most important in terms of load following behaviour and thermal gradients in the fuel cell during dynamic operation.

From Fig. 3 can be seen that isolines of the most significant temperatures are almost parallel and linear in the area of interest.

At a given current, the mean SOFC temperature is strongly influencing voltage and thus power output of the SOFC. Due to high thermal inertia, the SOFC is quite slow in reaching a new steady temperature state after a load change, causing power to vary over a long time. The most favourable operation line in terms of quick load following would therefore be along a line of constant mean SOFC temperature. However, in Fig. 3 (left, red lines), it can be seen that reducing shaft speed at constant mean SOFC temperature results in approaching the regime where no steady state exists. We assume there is an indifferent regime close to the steady-state boundary, where the same values of air and fuel flow may cause different operation temperatures depending on the initial temperatures. However, if no reliable temperature feedback to the control system exists, the system cannot be operated safely in this regime. Hence the temperature *must* be decreased when strongly decreasing the load. The proposed operation line therefore follows a line of constant mean SOFC temperature for relative shaft speed between 90 and 100%. Below 90%, the operation line departs from the constant mean SOFC temperature line and instead pursues a parallel line to the steady-state border down to the minimum RSS of 65%. The resulting operation line can be developed as a 3rd order polynomial and is plotted in the maps. Its equation is

$$RFF = -7.21 \cdot RSS^3 + 17.31 \cdot RSS^2 - 11.45 \cdot RSS + 2.34 \quad (4)$$

With this strategy, a fairly constant mean SOFC temperature of app. 1170K can be maintained in a range of relative net power (RP) from 80% to 105%. The minimum part load operation at 65% RSS yields a relative power of 24% and a mean SOFC temperature of 970K. Knowing a desired output power (in steady state), the required shaft speed can be estimated through

$$RSS = 0.674 \cdot RP^3 - 1.08 \cdot RP^2 + 0.930 \cdot RP + 0.478 \quad (5)$$

The net LHV-based efficiency increases from 62% at design point to 66% at relative power of 50% and decreases again to 63% at minimum part load. TIT decreases from 1170K at design point slowly to app. 930K at minimum part load. This decrease helps in keeping the surge margin wide. Trends and values of all other parameters can be estimated from the performance maps. Including an air bypass around the SOFC system may facilitate constant mean SOFC temperature over the whole range. This will be studied further.

The shown behaviour certainly depends on the characteristics of all applied components and assumptions of the cycle. The displayed quantitative data represent only the current system. However, the trends are expected to be similar in a real system. Hence, the demonstrated methods can be applied on a real system, once an accurate model of its true behaviour is available.

DYNAMIC PERFORMANCE

In the following study, the control parameters of fuel flow and shaft speed are changed between several points and the behaviour of the crucial system parameters is investigated. There is no controller including a feedback loop of measured output parameters as normally found in control system designs. The purpose of this method is to show the straight, non-controlled behaviour of the system following a load change.

In order to study dynamic load changes, a strategy for changing shaft speed and fuel flow is required. Speed changes of the shaft are calculated by its inertia and power balance; see Eq. (2) and (3). In case of reduced generator load the shaft accelerates, and vice versa. We manipulate the shaft power balance in a way that the shaft acceleration/deceleration is either a constant value or zero:

$$\frac{P_B}{I \cdot \omega} = \frac{d\omega}{dt} = R \cdot \mathrm{sgn}\left(N_{Setpoint} - N\right) \quad (6)$$

where $N_{Setpoint}$ is the setpoint shaft speed in [s^{-1}] and R is the shaft speed change rate in [rad·s^{-2}]. The sgn function yields

1 if $N < N_{Setpoint}$;
0 if $N = N_{Setpoint}$;
-1 if $N > N_{Setpoint}$.

Therewith the shaft speed is either constant at setpoint or moving linearly towards a new setpoint. The value of 52.4 rad·s^{-2}, corresponding to a speed change rate of 500 RPM per second, is set for R. This approach only represents a theoretical investigation method; for practical speed control systems, additional requirements apply.

The relative fuel flow is coupled to the actual relative shaft speed via the operation line Eq. (4), i.e. a speed change will result in fuel flow following an approximate ramp function.

The time from initiation of a load change until the new steady state is reached, called relaxation time, is an important parameter in dynamic studies. Figure 4 shows relaxation behaviour for a quick load change between 100% and 24% RP (respectively 100% and 65% RSS). At time equals 1, the shaft speed setpoint is changed by a step.

As can be seen from Fig. 4, with the reset of the setpoint shaft speed at time equals 1, power performs an immediate step into the inverse direction due to the shaft deceleration/acceleration. It takes very long until the power reaches its steady value after the load changes, calling for a control strategy incorporating feedback loops for exact load following.

The surge margin has a minimum during load decrease and a maximum during increase. This behaviour is different from regular gas turbine cycles. It is caused by the fairly constant TIT during speed change, which is caused by thermal inertia of the air preheater inside the SOFC system.

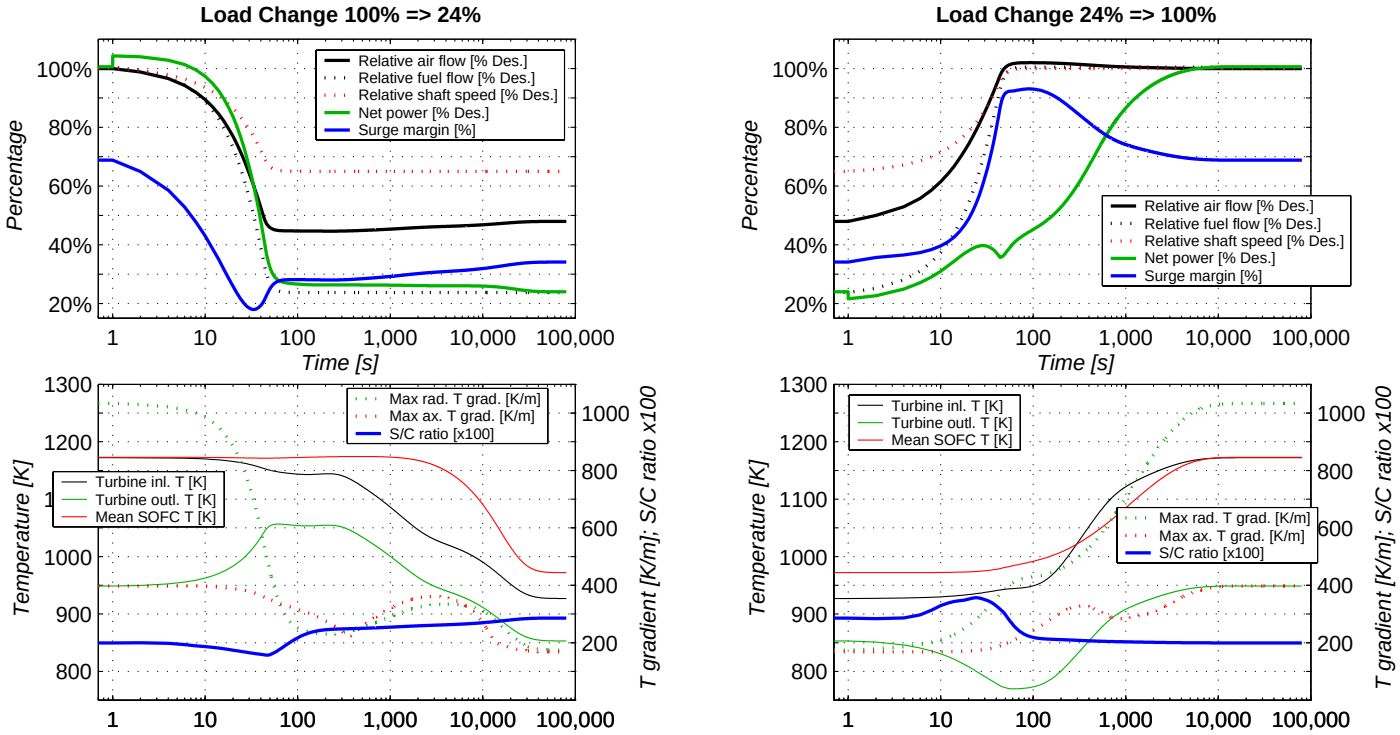

Figure 4: Load change between 24% and 100% (left: decrease; right: increase).

The maximum temperature gradients in the cell show unsteadiness along the relaxation time, indicating that the cell temperature profile is changing and the location of maximum gradients are moving. However, no global minima or maxima can be observed during the relaxation process.

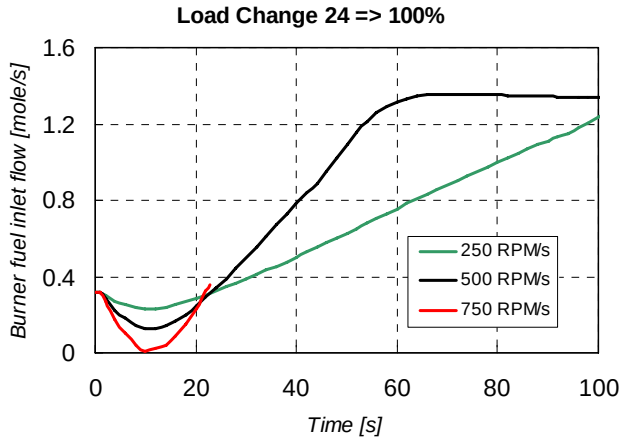

Figure 5: Burner fuel flow at different speed change rates

During load decrease, the steam to carbon ratio reaches a minimum of 1.8 after approximately 50 seconds, but this is not regarded as a critical value. During load increase, the anode exhaust gas recycle ratio increases temporarily to a very high value. This represents a danger, as it may cause backflow from the burner to the anode exhaust gas recycle loop. Thereby the anode may be exposed to oxygen. Figure 5 shows the fuel flow into the burner for a load increase at different speed change rates. The minima occur because during load change, the pressure is increasing and with it the gas mass in the fuel cell. Hence, less gas is leaving the cell than entering it during pressure increase. Furthermore, more fuel is being introduced, improving ejector performance. Anode backflow is hence restricting the maximum possible speed/pressure increase rate.

Another problem with quick pressure increase is the temporarily high depletion of the anode outlet gas due to the constant current to fuel flow ratio. In other words, the “true” fuel utilisation may temporarily come very close to 100% and the voltage must be decreased to very low values in order to keep the current to fuel flow ratio constant. The simulation with 750 RPM/s in Fig. 5 could not be finished due to numerical problems associated to this phenomenon. It may in practice lead to fuel cell degradation or burner extinguishing. However, it can be omitted by a more sophisticated current/voltage control (i.e. setting a minimum boundary for the voltage). The break in the power curve during load increase at a time of app. 50 seconds (see Fig. 4) is also a result of a temporarily too low voltage.

Table 1 lists the time required from the setpoint reset until the margin of ± 2% of the new steady state value of power and radial gradient has been reached for load change between three different points. The maximum radial thermal gradient is taken as a measure for the thermal steady state, simply because it shows the strongest variation of all temperature-related parameters. Steady power is always reached somewhat quicker.

It can be observed that between 80% and 100% relative net power, steady state is reached quicker. This is because of the fairly constant mean SOFC temperature in this regime, with the SOFC comprising the highest thermal inertia in the system. Beside the mean SOFC temperature, relaxation time is strongly influenced by the end point of the load change. Higher load end points cause quicker relaxation as a consequence of the higher gas and energy turnover. This has been reported previously by

Achenbach [6] and is the reason why load increases relax generally faster than load decreases.

Table 1: Relaxation times for load changes.

Relaxation time [s]		to 24%	to 80%	to 100%
From RP=24%	Power		5400	3800
	Radial Grad.		11000	6200
From RP=80%	Power	26000		360
	Radial Grad.	38000		2650
From RP=100%	Power	28000	40	
	Radial Grad.	40000	5300	

CONTROL STRATEGY

The dynamic performance study revealed slow relative power change and long time until power steady state is reached when moving along the proposed operation line. This might be sufficient for a power plant connected to the grid. However, a remote power plant without grid connection is required to follow load curves very quickly, thus load compensation units such as batteries or large capacitors would be required.

On the other hand, other methods of operating the hybrid cycle may be advantageous. At present, the fuel flow, which influences power output to great extent and which can be controlled quite quickly, is coupled to the rather slowly moving parameter of shaft speed via Eq. (4). Furthermore, during a load change, the system may be operated at any combination of RSS and RFF, as long as the end point is within the stable regime of the performance maps.

In an advanced control strategy, the setpoint shaft speed could be directly coupled to the setpoint power output via Eq. (5), ensuring that the system in steady state is always on the proposed operation line.

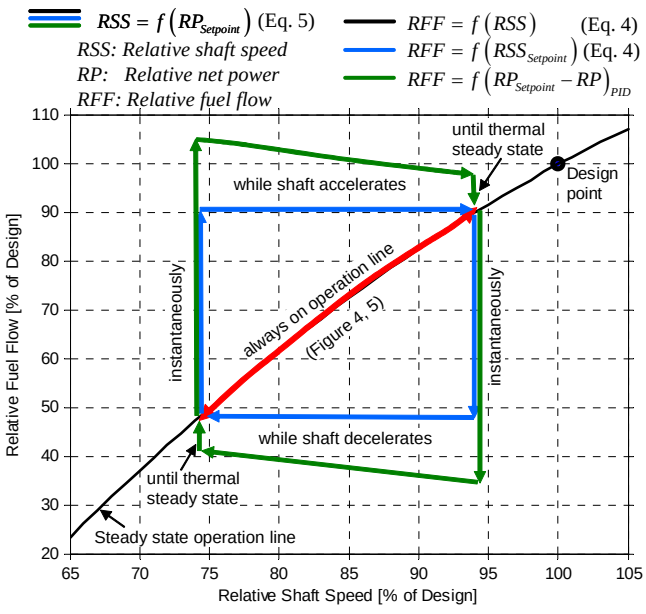

Figure 6: Control strategies for fuel flow.

The fuel flow could then be coupled to the setpoint shaft speed instead of the actual shaft speed in the same way as in Eq. (4), resulting in a much faster power change. The most efficient way though would be to control fuel flow by comparing the feedback measured actual power with the setpoint power.

Figure 6 shows the proposed strategies in a RFF-over-RSS diagram (same as Fig. 2 and 3). The red line indicates the movement of the parameters if fuel flow is coupled to actual shaft speed (strategy pursued for the above dynamic performance study). The blue lines indicate the movement of parameters if fuel flow is coupled to setpoint shaft speed, and the green lines sketch the possible behaviour if the power output is controlled a feedback loop. With the latter strategy, it should be possible to follow load curves with a very short delay between setpoint and actual power. However, the mentioned critical phenomena could be a restriction to very quick load variation with the proposed system.

Where quick load following is required, alternative systems with constant shaft speed and other means to control the air flow, such as variable inlet guide vanes or an air bypass, may be even more suitable, as these control means can be manipulated much quicker than the inertia-affected shaft speed. Another option would be introduction of an auxiliary burner in the current system directly upstream the turbine for quick TIT control.

CONCLUSIONS

A powerful full dynamic model of a simple hybrid system has been developed and the hybrid system performance has been characterised. The following main conclusions can be drawn:

1. The system power is mainly controlled by fuel flow, shaft speed and current.
2. Setting the ratio of current to fuel flow (and therewith fuel utilisation) constant, the part-load behaviour of the system shows the presence of unstable regimes (no steady state exists) at high fuel flow and low shaft speed, and regimes with very low SOFC temperatures at high shaft speed and low fuel flow.
3. In steady-state part-load, the air-to-fuel ratio must increase in order not to operate in an unstable regime.
4. Operation lines with constant mean SOFC temperature exist, but approximate the unstable regime. An operation line is proposed where the mean SOFC temperature is constant in a load range from 80% to 100%. Below 80% load, temperature must decrease if no temperature feedback controller is applied.
5. Load changes in the regime of constant mean SOFC temperature reach a new thermal steady state quite quick, while it takes much longer when the temperature is varied.
6. The effect of gas from the burner flowing back into the anode cycle restricts the pressure increase rate under load increase.
7. Quicker load changes may be performed when the fuel flow and SOFC current are varied quicker than the shaft speed.
8. With the present tool, a coherent design for control of the whole system may be developed.

The depicted quantitative data are only valid for the studied model. However, the qualitative trends are expected to be similar in a genuine system. Hence, the demonstrated

methods can be applied on a real system, given that relevant data of its behaviour are available.

ACKNOWLEDGMENTS

We thank the Norwegian Research Council, Shell Technology Norway and Statkraft for their financial support.

REFERENCES

[1] Stiller, C., Thorud, B., Seljebø, S., Mathisen, Ø., Karoliussen, H., Bolland, O., 2004, "Finite-volume modeling and hybrid-cycle performance of planar and tubular solid oxide fuel cells", accepted for publication in Journal of Power Sources

[2] Rao, D., Samuelsen, G. S., 2001, "A thermodynamic analysis of tubular SOFC based hybrid systems", ASME Paper 2001-GT-0522.

[3] Chan, S. H., Ho, H. K., Tian, Y., 2003, "Modeling for part-load operation of solid oxide fuel cell-gas turbine hybrid power plant", Journal of Power Sources **114** 213-227.

[4] Pålsson, J., Selimovic, A., Sjunnesson, L., 2000, "Combined solid oxide fuel cell and gas turbine systems for efficient power and heat generation", Journal of Power Sources **86** 442-448.

[5] Veyo, S.E., Lundberg, W.L. Vora, S.D., Litzinger, K.P., 2003, "Tubular SOFC hybrid power system status", ASME Paper 2003-GT-38943.

[6] Achenbach, E., 1995, "Response of a solid oxide fuel cell to load change", Journal of Power Sources **57** 105-109.

[7] Costamagna, P., Magistri, L., Massardo, A.F., 2001, "Design and part-load performance of a hybrid system based on a solid oxide fuel cell reactor and a micro gas turbine", Journal of Power Sources **96** 352-368.

[8] Campanari, S., 2000, "Full load and part load performance prediction for integrated SOFC and microturbine systems", Journal of Engineering for Gas Turbines and Power **122** 239-246.

[9] Pålsson, J., Selimovic, A., 2001, "Design and off-design predictions of a combined SOFC and gas turbine system", ASME Paper 2001-GT-0379.

[10] Kimijima, S., Kasagi, N., 2002, "Performance evaluation of gas turbine-fuel cell hybrid micro generation system", ASME Paper 2002-GT-30111.

[11] Thorud, B., Stiller, C., Weydahl, T., Bolland, O., Karoliussen, H., 2004, "Part-load and load-change simulation of tubular SOFC systems", 6th European Solid Oxide Fuel Cell Forum, Lucerne, Switzerland.

[12] Rao, A.D., Samuelsen, G.S., 2002, "Analysis strategies for tubular solid oxide fuel cell based hybrid systems", Journal of Engineering for Gas Turbines and Power **124** 503-509.

[13] Song, T.W., Sohn, J.L., Kim, J.H., Kim, T.S., Ro, S.T., Suzuki, K., 2004, "Parametric studies for a performance analysis of a SOFC/MGT hybrid power system based on a quasi-2D model", ASME Paper 2004-GT-53304.

[14] gPROMS (General Process Modelling and Simulation Tool), v.2.3.3, Process Systems Enterprise Ltd., London, http://www.psenterprise.com/

[15] Marsano, F., Magistri, L., Massardo, A.F., "Ejector performance on a solid oxide fuel cell anodic recirculation system", Journal of Power Sources **129** 216-228.

[16] Kurzke, J., 2004, "Compressor and turbine maps for gas turbine performance computer programs – Component Map Collection 2", Joachim Kurzke, Dachau, Germany

[17] Yi, Y., Smith, T.P., Brouwer, J., Rao, A.D., Samuelsen, G.S., 2003, "Simulation of a 220 kW hybrid SOFC gas turbine system and data comparison", Electrochemical Society Proceedings **2003-7** 1442-1454.

[18] Johannesen, N. H., 1951, "Ejector Theory and Experiments", Dissertation, Danish Academy of Technical Sciences, Copenhagen, Denmark.

[19] Achenbach, E., Riensche, E., 1994, "Methane/steam reforming kinetics for solid oxide fuel cells", Journal of Power Sources **52** 283-288.

[20] Karoliussen, H., Nisancioglu, K., Solheim, A., Ødegård, R., 1992, "SOFC stack modeling with internal reforming", 4th IEA Workshop on SOFC, Lausanne, Switzerland.

[21] Nisancioglu, K, 1989, "Ohmic losses", Natural gas fuelled solid oxide fuel cells and systems, IEA Workshop on Mathematical Modelling, Charmey, Switzerland.

[22] Reid, R.C., Prausnitz, J.M., Poling, B.E., 1987, *The properties of gases and liquids*, McGraw-Hill, New York.

[23] Mills, A.F., 1995, *Heat and Mass Transfer*, Irwin, Chicago.

APPENDIX 1 – SOFC MODEL

Table 2: Equations for heat transfer in the SOFC tube.

Ref. no in Fig. 7	Equation	Comment
1	$\frac{\partial\left(T_{air}c_p\rho_{air}\right)}{\partial t}+v_{air}\frac{\partial\left(T_{air}c_p\rho_{air}\right)}{\partial z}=\frac{2\alpha}{r_{AST,i}}\left(T_{AST}-T_{air}\right)$	Heat transfer between air supply tube and air within the tube
2	$\frac{dT}{dt}=\frac{k}{c\cdot\rho}\nabla^2\cdot T$	Heat conduction in solid structures (Air supply tube and SOFC membrane)
3	$\frac{\partial\left(T_{air}\rho_{air}c_{p,air}\right)}{\partial t}+v_{air}\frac{\partial\left(T_{air}\rho_{air}c_{p,air}\right)}{\partial z}=$ $\frac{2r_{AST,o}\alpha_{AST,o}}{\left(r_{c,i}^2-r_{AST,o}^2\right)}\left(T_{AST,o}-T_{air}\right)+\frac{2r_{c,i}\alpha_{c,i}}{\left(r_{c,i}^2-r_{AST,o}^2\right)}\left(T_{c,i}-T_{air}\right)$	Heat transfer between air supply tube, cathode air and cathode
4	$\frac{\partial\left(T_{fuel}\rho_{fuel}c_{p,fuel}\right)}{\partial t}+v_{fuel}\frac{\partial\left(T_{fuel}\rho_{fuel}c_{p,fuel}\right)}{\partial z}$ $=\frac{2\alpha_{fuel}r_{a,o}}{\left(\left(r_{a,o}+\Delta r\right)^2-r_{a,o}^2\right)}\left(T_{a,o}-T_{fuel}\right)$	Heat transfer between anode surface and fuel

Nomenclature	T	Temperature [K]	k	Thermal conductivity [W/mK]
	c/c_p	Heat capacity [J/kgK]	α	Convective heat transfer coeff. [W/m^{2}K]
	ρ	Density [kg/m^3]	Δr	Thickness of fuel plenum [m]
	v	Gas velocity [m/s]	r	Radius [m]
	t	Time [s]	z	Axis direction [m]
Subscripts	AST	Air Supply Tube	c	Cathode
	a	Anode	i	Inner radius
	o	Outer radius		

Figure 7 shows a break-down of the cell geometry. The numbers refer to the equations for the thermal model which are listed in Table 2. The following features are included:

- Heat transfer between the fuel cell tube walls and the fluids are calculated using Newton's law of cooling. Heat transfer coefficients are calculated from Nusselt numbers for laminar flow and for constant heat flux.
- Thermal radiation is incorporated between the air supply tube and the cathode surface by using a shape factor for radiation between two tubes, neglecting axial spreading effects and absorption in the gas.
- To reduce calculation time, the solid structure of the anode, electrolyte and the cathode is treated as one single material with weighted mean values for the thermal and electrical properties.
- As the total thickness of anode and electrolyte (0.14 mm) is very small compared to the cathode (2.2 mm), heat sources and sinks related to the electrochemical and methane reforming kinetics are located at the anode surface.
- For steam reforming kinetics, Achenbach's approach is used [19], while the water-gas shift reaction is assumed to be always in equilibrium.
- The local electrical potential is calculated by the Nernst equation, an approach for polarisation losses by Karoliussen et al. [20], an analytical expression for the ohmic resistance developed by Nisancioglu [21] and diffusion losses. For the latter, Knudsen-diffusion is applied using diffusion coefficients determined from the Fuller method [22] and correction factors for multi-component diffusion coefficient calculation. Electrochemical oxidation of CO is neglected.
- Friction losses in the air delivery tube, cathode and anode channels are accounted for by the Reynolds number approach and under the assumption of laminar flow [23].

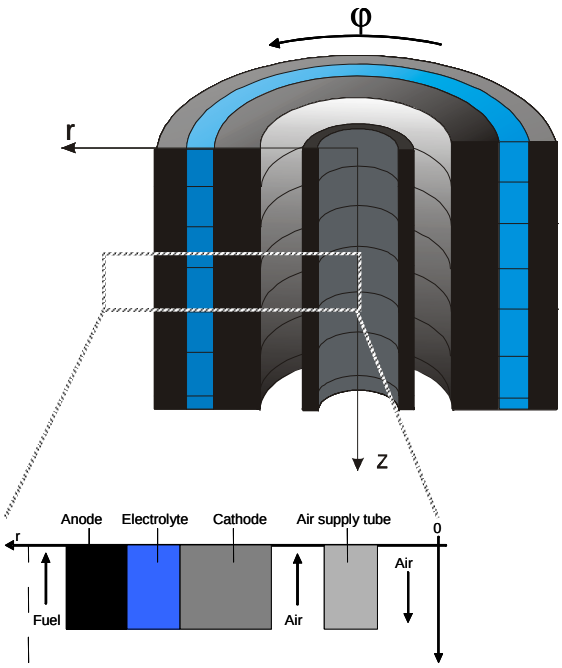

Figure 7: Break down of the cell geometry.

APPENDIX 2 – COMPRESSOR AND TURBINE MAP

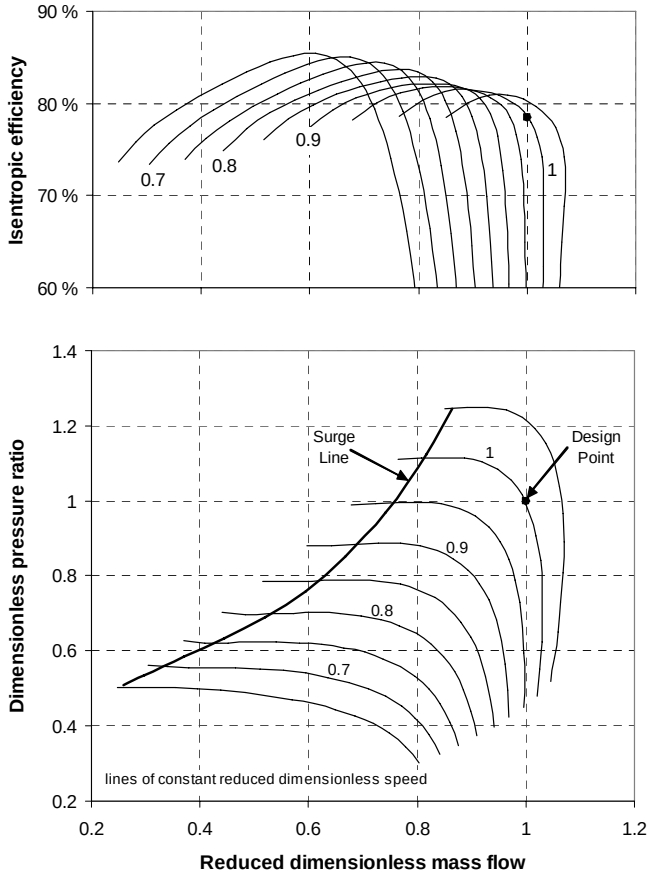

Figure 8: Normalized compressor map.

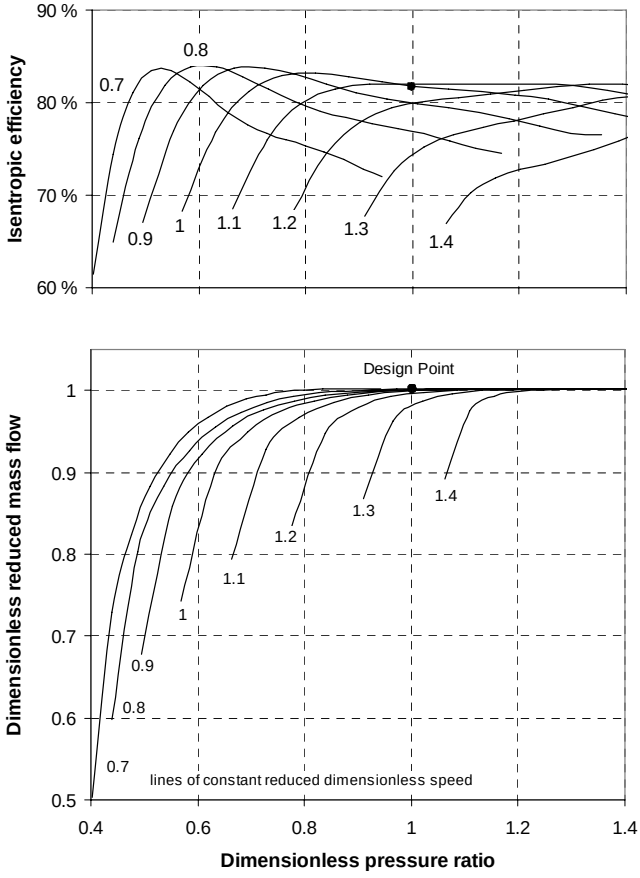

Figure 9: Normalized turbine map.

Appendix D - Paper IV

Control-Relevant SOFC Modelling and Model Evaluation

Rambabu Kandepu, Lars Imsland, Bjarne A. Foss, Christoph Stiller, Bjørn Thorud, Olav Bolland

Proceedings of ECOS 2005, the 18th Conference on Efficiency, Cost, Optimization, Simulation and Environmental Impact of Energy Systems, Vol 3, p 1139-1146.

Trondheim, Norway, June 20-22, 2005.

Proceedings of ECOS 2005
Trondheim, Norway
June 20–22, 2005

CONTROL-RELEVANT SOFC MODELING AND MODEL EVALUATION

Rambabu Kandepu[*], Lars Imsland[*], Bjarne A. Foss[*]
Department of Engineering Cybernetics

Christoph Stiller[†], Bjørn Thorud[†] and Olav Bolland[†]
Department of Process Engineering

Norwegian University of Science and Technology
7491 Trondheim, Norway

ABSTRACT

In this paper, a dynamic, lumped model of a Solide Oxide Fuel Cell (SOFC) is described, as a step towards developing control relevant models for a SOFC integrated in a gas turbine process. Several such lumped models can be aggregated to approximate the distributed nature of important variables of the SOFC. The model is evaluated against a distributed dynamic tubular SOFC model. The simulation results confirm that the simple model is able to capture the important dynamics of the SOFC. It is concluded that the simple model can be used for control and operability studies of the hybrid system.
Keywords: SOFC, control relevant, fuel cells, modeling

INTRODUCTION

Solid Oxide Fuel Cells (SOFC) integrated in Gas Turbine (GT) cycles (often denoted hybrid systems) is a promising concept for production of efficient and low-polluting electrical power. The SOFC can produce electric power at an electrical efficiency of about 55%, and when it is combined with a GT, studies show that the net electrical efficiency can be increased up to 70% [8]. The hybrid system uses natural gas as fuel and the percentage of pollutant flue gases is low compared to conventional power production from fossil fuels.

Due to the tight integration between the SOFC and the GT in a hybrid system, dynamic operability (and hence control) of the process is a challenge. It is important not only to design a good control system, but also to choose a process design that together with the appropriate control structure allows satisfying disturbance rejection and part load operation. Such a design procedure is usually called a integrated process design, see eg. van Schijndel [15]. To be able to design control structures and analyze dynamic behavior, it is very beneficial to have low complexity models of the components of the hybrid system. Such models are also valuable for online optimization. The aim of this article is to develop a low complexity mechanistic SOFC dynamic model which includes the relevant dynamics for operation in a hybrid system. There are several dynamic, distributed models reported in the literature. For example, Achenbach [1] developed a three dimensional, dynamic, distributed model for a planar SOFC stack. Chan et al. [4, 3], Thorud et al. [14], Stiller et al. [12] and Magistri et al. [10] all developed distributed, dynamic tubular SOFC models for designs similar to that of Siemens Westinghouse, for use in hybrid systems. In this paper, a simple, lumped, dynamic model of the SOFC based on mass and energy balances, with methane as fuel, is developed. The modeling approach proposed by Padulles et al. [11] for use in power systems simulation has some similarities with the approach described in this paper, however, therein hydrogen is used as fuel and only mass balances are considered.

The paper is outlined as follows: First a simple control relevant SOFC model is described with no regard to the geometric layout (tubular or planar). Extension of the simple lumped model towards capturing the distributed nature of the process by aggregating single volumes is explained next. Both SOFC models are evaluated against a distributed tubular SOFC model [14] with a considerably higher complexity. The two models are simulated for different realistic scenarios and the corresponding simulation results are presented. Applicability and shortcom-

[*] {Rambabu.Kandepu,Lars.Imsland,Bjarne.A.Foss}@itk.ntnu.no
[†] {Christoph.Stiller,Bjorn.Thorud,Olav.Bolland}@ntnu.no

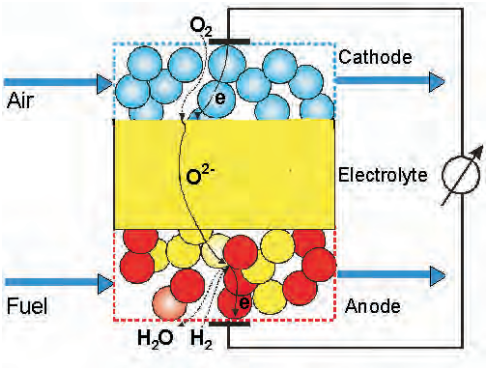

Figure 1: SOFC operation

Table 1: Reactions at anode and cathode

At anode	
Reaction	Reaction rate (r_j^{an})
$H_2+O^{2-} \rightarrow H_2O+2e^-$	r_1^{an}
$CH_4+H_2O \Leftrightarrow CO+3H_2$	r_2^{an}
$CO+H_2O \Leftrightarrow CO_2+H_2$	r_3^{an}
$CH_4+2H_2O \Leftrightarrow CO_2+4H_2$	r_4^{an}
At cathode	
Reaction	Reaction rate (r_j^{an})
$\frac{1}{2}O_2+2e^- \rightarrow O^{2-}$	r_1^{ca}

ings of the low complexity model are discussed. A nomenclature can be found at the end of the paper.

PROCESS DESCRIPTION

The Solid Oxide Fuel Cell (SOFC) is a device which converts chemical energy of a fuel directly into electrical energy [7]. The basic components of the SOFC are anode, cathode and electrolyte (conceptually illustrated in Figure 1). The electrolyte material is zirconia stabilized with the addition of a small percentage of yttria (Y_2O_3). The anode material is a zirconia cermet. The most common cathode material is strontium-doped lanthanum manganite. Fuel is supplied to the anode and air is supplied to the cathode. At the cathode-electrolyte interface, oxygen molecules accept electrons coming from the external circuit to form oxide ions, see Table 1 for reactions. The electrolyte layer allows only oxide ions to pass through and at the anode-electrolyte interface, hydrogen molecules present in the fuel react with oxide ions to form steam and electrons get released. These electrons pass through the external circuit and reach the cathode-electrolyte layer, and thus the circuit is closed. To increase the amount of power generated, a number of cells can be connected in series/parallel. This is known as stacking of cells. Also, there are mainly two types of SOFCs depending on the geometry; tubular and planar. The operating pressure can be from one bar to 15 bars. It is found that SOFCs show enhanced performance with increasing cell pressure [7]. The operating temperature of the SOFC is around 800-1000$^\circ C$. The high temperature and pressure operating conditions of the SOFC make it advantageous to combine the SOFC with a gas turbine (GT) to get a hybrid system with an high efficiency [8]. Due to the high operating temperature, an advantage is that several types of fuels can be used. In this paper methane is used as fuel. Because of the electrochemical reactions, there is a production of steam, and partial recirculation of this steam is used to reform methane into hydrogen. Typically, one third of the fuel is reformed (for example, in a pre-reformer) before it enters the SOFC and the remaining part is reformed within the SOFC. Table 1 gives the list of reactions that take place at anode and cathode and the corresponding reaction rates notation.

MODELING

The dynamic model of a single SOFC is developed using two mass balances; one for anode volume and the other for cathode volume, and one overall energy balance. In all of the streams from/to the SOFC, the following components can be present; Nitrogen (N_2), Oxygen (O_2), Hydrogen (H_2), Methane (CH_4), Steam (H_2O), Carbonmonoxide (CO), and Carbondioxide (CO_2). A number is assigned to each of these components to simplify the notation:

i	1	2	3	4	5	6	7
comp.	N_2	O_2	H_2	CH_4	H_2O	CO	CO_2

Model assumptions

The following main assumptions are made in developing the model.

1. All the physical variables are assumed to be uniform over the SOFC, resulting in a lumped model.

2. There is sufficient turbulence and diffusion within the anode and the cathode for perfect mixing to occur (CSTR).

3. The gas temperatures within the SOFC are assumed to be the same as the solid; i.e. the thermal inertia of the gases is neglected.

4. For the energy balance, pressure changes within the SOFC are neglected.

5. All gases are assumed to be ideal.

Mass balances

Two mass balances; one for the anode volume and one for the cathode volume are used:

$$\frac{dN_i^{an}}{dt} = \dot{N}_i^{in,an} - \dot{N}_i^{out,an} + \sum_{j=1}^{n_{rx}^{an}} a_{ij}^{an} r_j^{an}, \qquad (1)$$
$$i = 1,...,7, \;\; n_{rx}^{an} = 4$$

$$\frac{dN_i^{ca}}{dt} = \dot{N}_i^{in,ca} - \dot{N}_i^{out,ca} + \sum_{j=1}^{n_{rx}^{ca}} a_{ij}^{ca} r_j^{ca}, \qquad (2)$$
$$i = 1,...,7, \;\; n_{rx}^{ca} = 1$$

The reaction rates corresponding to the electrochemical reactions (r_1^{ca}, r_1^{an}) are directly related by the current,

$$r_1^{an} = I/(2F) = r_1^{ca} \qquad (3)$$

and the reaction rates corresponding to the reforming reactions are calculated as proposed by Xu [16]

$$r_2^{an} = \frac{k_2}{p_{H_2}^{an^2.5}} \left(p_{CH_4}^{an} p_{H_2O}^{an} - \frac{p_{H_2}^{an^3} p_{CO}^{an}}{K_2} \right) / (DEN)^2$$
$$r_3^{an} = \frac{k_3}{p_{H_2}^{an}} \left(p_{CO}^{an} p_{H_2O}^{an} - \frac{p_{H_2}^{an} p_{CO_2}^{an}}{K_3} \right) / (DEN)^2 \qquad (4)$$
$$r_4^{an} = \frac{k_4}{p_{H_2}^{an^3.5}} \left(p_{CH_4}^{an} p_{H_2O}^{an^2} - \frac{p_{H_2}^{an^4} p_{CO_2}^{an}}{K_4} \right) / (DEN)^2$$

In (4), DEN is given by

$$DEN = 1 + K_{CO}^{ads} p_{CO}^{an} + K_{H_2}^{ads} p_{H_2}^{an} + K_{CH_4}^{ads} p_{CH_4}^{an} \qquad (5)$$
$$+ K_{H_2O}^{ads} p_{H_2O}^{an} / p_{H_2}^{an}$$

and k_2, k_3 and k_4, the rate coefficients for the reforming reactions, are calculated by

$$k_j = A_{kj} \exp(\frac{-E_j}{RT}), \quad j = 2,3,4 \qquad (6)$$

The equilibrium constants for the reforming reactions K_2, K_3 and K_4 are given by

$$K_2 = \exp(-26830/T + 30.114) \quad [bar^2]$$
$$K_3 = \exp(4400/T - 4.036 \quad [-] \qquad (7)$$
$$K_4 = \exp(-22430/T + 26.078) \quad [bar^2]$$

In (5), $K_{CO}^{ads}, K_{H_2}^{ads}, K_{CH_4}^{ads}$ and $K_{H_2O}^{ads}$ are the adsorption constants, which are calculated by

$$K_i^{ads} = A_{K^{ads}i} \exp(\frac{-\Delta\overline{h}_i^{ads}}{RT}), \quad i = H_2, CH_4, H_2O, CO \qquad (8)$$

It is assumed that the exhaust flows at the anode and cathode outlets can be described by the choked exhaust flow equation. This means that the mass flow rate of the exhaust flow at the anode (cathode) depends on the pressure difference between the pressure inside the anode (cathode) and the pressure at the outlet [11]:

$$\dot{m}_{out,an} = \sqrt{k_{an}(p_{an} - p_{out,an})} \qquad (9)$$
$$\dot{m}_{out,ca} = \sqrt{k_{ca}(p_{ca} - p_{out,ca})}$$

The partial pressures, volume, and temperature are assumed to be related by the ideal gas equation, for instance at the anode,

$$p_i^{an} V_{an} = N_i^{an} RT \qquad (10)$$

Energy balance

The energy balance accounts for the whole SOFC volume, and is given by [13, 9]:

$$C^s \frac{dT}{dt} = \sum_{i=1}^{N} \dot{N}_i^{in,an} (\Delta\overline{h}_i^{in,an} - \Delta\overline{h}_i)$$
$$+ \sum_{i=1}^{N} (\dot{N}_i^{in,ca} (\Delta\overline{h}_i^{in,ca} - \Delta\overline{h}_i) \qquad (11)$$
$$- \sum_{j=1}^{M} \Delta\overline{h}_j^{rx} r_j^{an} - P_{DC} - P_{rad} - P_{cond}$$

In this equation, the temperature changes of gases are neglected as they are fast compared to the temperature changes of the solid and by assuming that these fast changes of gas temperatures do not influence the dynamics of the overall process. Hence the energy balance gives a dynamic equation for the temperature changes of the SOFC solid.
In (11), P_{DC} represents the amount of DC power produced by the SOFC, P_{cond} represents the conduction heat loss from SOFC to the surroundings and P_{rad} represents the amount of radiation heat given from the SOFC. As the SOFC operating temperature is higher than that of the surroundings, there is always some loss due to radiation. It can be calculated by [6]

$$P_{rad} = A\delta\varepsilon\sigma(T^4 - T_{sur}^4) \qquad (12)$$

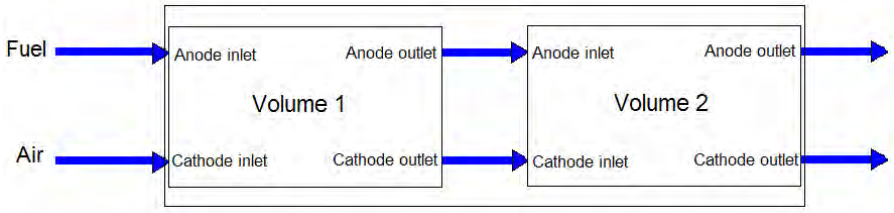

Figure 2: Aggregation mechanically

In (12), A is the surface area, δ is shaping factor, T_{sur} represents the surroundings temperature, ε is the emissivity of the SOFC surface and σ is the *Stefan-Boltzmann constant* ($\sigma = 5.67 \times 10^{-8}\text{W/(m}^2\text{.K}^4)$). The amount of DC power from the SOFC is given by

$$P_{DC} = VI \tag{13}$$

Voltage

The operating cell voltage is given by

$$V = E^{OCV} - V_{loss} \tag{14}$$

where the open circuit voltage of the cell is given by the *Nernst equation* [7],

$$E^{OCV} = E^o + \frac{RT}{2F} \ln \left(\frac{p_{H_2}^{an} p_{O_2}^{an^{0.5}}}{p_{H_2O}^{an}} \right) \tag{15}$$

where E^o is the EMF at standard pressure. V_{loss} is the voltage loss, as explained below.

Voltage loss

When the cell is operated, there are voltage losses coming from different sources; activation losses, concentration losses and ohmic losses [7]. Activation losses are caused by the limited reaction rate on the surface of the electrodes. Ohmic losses are due to the electrical resistance of the electrode material and the various interconnections, as well as the resistance of the electrolyte. The ohmic losses are responsible for the largest part of the voltage losses. The concentration losses result from the change in concentration of the reactants at the surface of the electrodes as the fuel is used. Stiller et al. [12], Thorud et al. [14], Campanari et al. [2], and Magistri et al. [10] used rather complex empirical functions to calculate the ohmic and activation losses. In this simple model the total voltage loss is approximated by a first order function of cell temperature and current. This function is obtained by curve fitting the simulated data obtained from a distributed model [14], where an active area of 834cm^2 is used to calculate the different voltage losses. Thus total voltage loss is calculated by

$$V_{loss} = f(I,T) \tag{16}$$

MODEL AGGREGATION

In a real SOFC, temperature and pressure vary over the SOFC volume. The distributed nature cannot be represented by using the ”one volume” model. By connecting many volumes in a sequential manner it is possible to approximate the distributed nature of the variables. The whole structure with all the volumes represent a single cell. So, if many volumes are connected, each volume can be represented by a scaled-down model. In principle, it is possible to connect any number of volumes, but for simplification, an example is considered where a single SOFC model is obtained by connecting two scaled-down models as shown in Figure 2. The two volumes are selected such that the first volume is represented by a scaled-down model by scaling down the ”one volume” model volume and heat capacity constants by 1/3. The second volume is represented by a scaled-down model obtained by scaling down the ”one volume” model constants by 2/3. Electrically, the two scaled-down models are connected in parallel (Figure 3). Ideally, the voltage across each of the volumes should be the same and the total current is divided between the two volumes. Then probably, most of the current will be produced from the second volume, as mainly reforming reactions take place in the first volume. In the present work it is assumed that the first volume supplies 1/3rd of the total current and the second volume supplies the remaining current. With this assumption, there is a small voltage difference between the two volumes. Developing a strategy for dividing the currents among the volumes when a SOFC is represented by many volumes is a part of further work. The basic point is

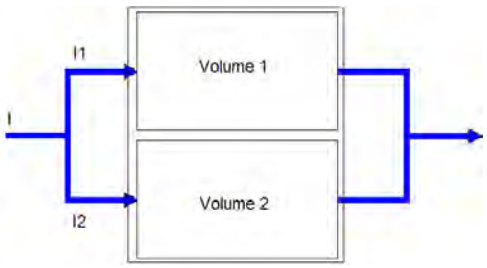

Figure 3: Electrical aggregation

to show that it is possible to approximate the distributed nature of the variables by aggregating the scaled-down models.

MODEL EVALUATION

As no experimental data is available to the authors for evaluating the simple model, the model is evaluated with an available detailed model. The detailed model [14] is a quasi two-dimensional dynamic model of a SOFC tube, similar to that of Siemens Westinghouse. It is a discretized model where gas flows are treated as 1D plug flows. The solid structures are modeled by a 2D discretization scheme in the axial and radial direction, neglecting effects in the circumferential direction. Both the simple and the detailed models are developed using gPROMS [5]. For solving the detailed model gPROMS uses about 1300 differential equations, where as for the simple model it uses 15 differential equations.

Figure 4 shows the comparison set up used for the simulation. Here the main aim is to evaluate the simple model against the detailed model [14]. The simulations are performed in such a way that the same input conditions are applied to the two SOFC models. Fuel is supplied to the pre-reformer which reforms about 30% of methane. The pre-reformer outlet gas is supplied to the anode inlet and air is supplied to the cathode inlet. Some part of the anode flue gas is recycled back to the pre-reformer to supply steam required by the reforming reactions. The other part of the anode flue gas and the cathode flue gas are supplied to a combustor where the remaining fuel is burnt and the resultant gas mixture will be the exhaust gas. The SOFC and pre-reformer are thermally connected by radiation. The details of the models of the other components used in the process shown in Figure 4 are not discussed here. The values of important parameters of the simple model are given in Table 2. The values of important variables at steady state are given in Table 3. Table 4 shows

Table 2: Model parameters

Anode volume	$1.032\times10^{-5}\mathrm{m}^3$
Cathode volume	$4.3\times10^{-5}\mathrm{m}^3$
C^s	800J/K
k_{an}	$1.9\times10^{-3}\mathrm{kg}^2\mathrm{s}^{-2}\mathrm{Pa}^{-1}$
k_{ca}	$4.2\times10^{-3}\mathrm{kg}^2\mathrm{s}^{-2}\mathrm{Pa}^{-1}$

Table 3: Steady state values

methane flow rate	4.50×10^{-4}kg/s
methane inlet temperature	950K
Air flow rate	1.44×10^{-2}kg/s
Air inlet temperature	950K
Current	250A
Anode pressure	3bar
Cathode pressure	3bar
Cell voltage	0.56V
Cell power	141W
Cell temperature	1113K
air utilization	0.21
fuel utilization	0.7

the simulation scenarios used for comparing the dynamic behavior of the two models.

SIMULATION RESULTS

Simulations are made for two comparison schemes; first, the simple SOFC model with one volume is compared to the distributed tubular SOFC model [14], and second, the simple SOFC with two volumes is compared to the distributed tubular SOFC model. SOFC mean solid temperature, cell voltage and cell power of the simple model and the detailed model are compared in each comparison scheme. Figures 5-7 show simulation results of the first comparison scheme and Figures 8-9 show simulation results of the second comparison scheme.

Table 4: Simulation details

Time(min)	Disturbance
90	fuel flow is decreased by 20%
180	fuel flow is increased back to 100%
270	air flow is decreased by 20%
360	air flow is increased back to 100%
450	current is decreased by 20%
540	current is increased back to 100%

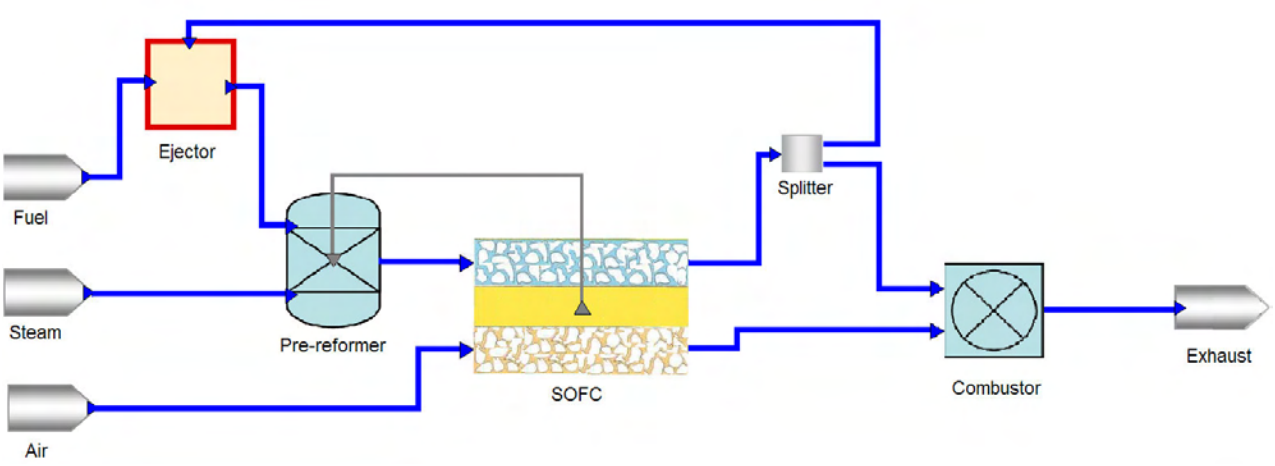

Figure 4: SOFC system

DISCUSSION

One volume SOFC model

Figure 5 shows the mean temperatures of the simple and the detailed SOFC models. At nominal steady state there is a temperature difference of about 120K between the two mean SOFC temperatures. This can be explained as follows. For both SOFC models, since inlet massflows and current are the same, the energy balance should ensure that the energy in the outlet massflow (and hence outlet temperature) is approximately[1] the same for both models. In a SOFC, the maximum temperature region is at the outlets of the anode and the cathode. Since the simple model is a bulk model, the exit temperature is equal to the mean temperature. For the detailed model, SOFC temperature is a distributed variable and the mean temperature is certainly less than the exit temperature. It is verified that the maximum temperature of the detailed model at the nominal steady state is approximately equal to the mean temperature of the simple SOFC model. From Figure 5, it is clear that both the models exhibit similar dynamics for the disturbances applied during the simulation. Figure 6 shows the voltages of the two models during the simulation. Here also both models show the same dynamic changes in the voltages for all the disturbances applied. Here the simple model has higher voltage than the detailed model which is also mainly because of the higher mean solid temperature of the simple SOFC model. Refering to (16), when temperature increases the voltage loss decreases. Hence the simple SOFC voltage given

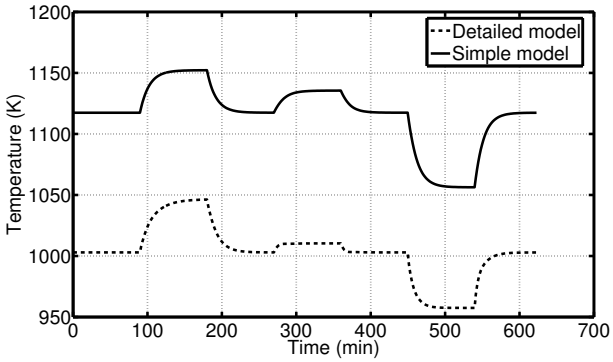

Figure 5: Comparison of mean solid temperatures of the simple model with one volume and the detailed model for different disturbances

by (14) is higher than that of the detailed SOFC model at the nominal steady state. Figure 7 shows a comparison of power production of the two models during the simulation. Since the voltage of the simple SOFC model is higher than that of the detailed model and the current is the same in both models, the power produced by the simple SOFC model is higher.

Two volume SOFC model

Figure 8 shows the comparison of the mean temperatures of the two SOFC models. Now, the simple SOFC is represented by aggregation of two volumes. The simple SOFC solid mean temperature is given by the average of the temperatures of the two volumes. The difference between the two mean temperatures at the nominal steady state is reduced to 51K as supposed to 120K. The dynamics of the two

[1] A slight difference in voltage and hence produced DC power gives a small temperature difference.

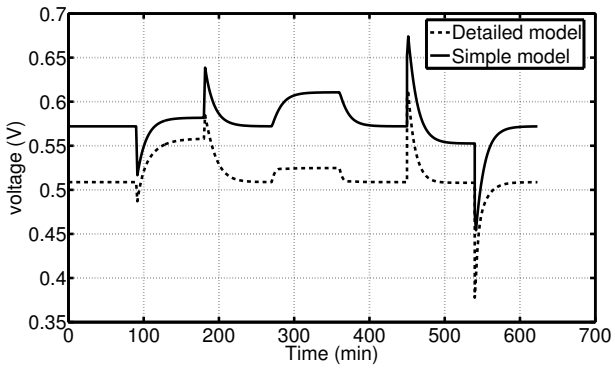

Figure 6: Comparison of voltages of the simple model with one volume and the detailed model for different disturbances

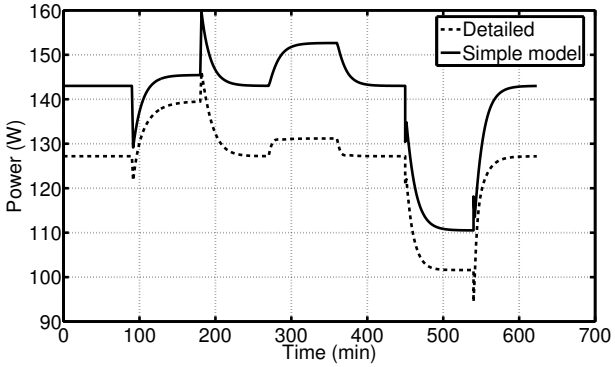

Figure 7: Comparison of power production of the simple model with one volume and the detailed model for different disturbances

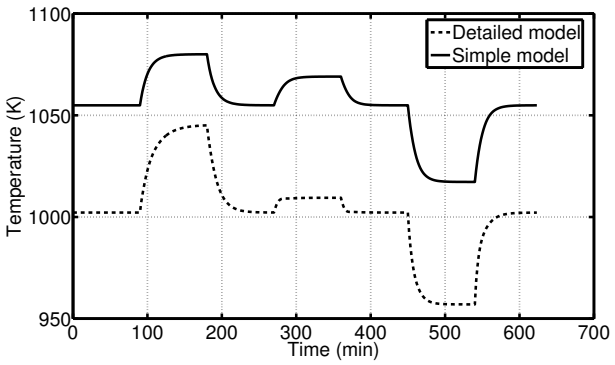

Figure 8: Comparison of mean solid temperatures of the simple model with two volumes and the detailed model for different disturbances

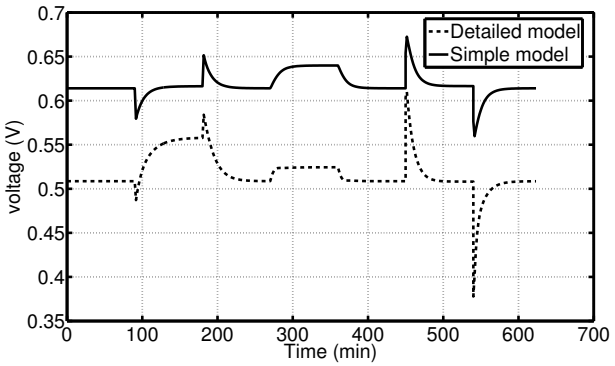

Figure 9: Comparison of voltages of the simple model with two volumes and the detailed model for different disturbances

volume model is similar to that the dynamics of the one volume model for all the disturbances. Figure 9 shows the comparison of the voltages of the two models, for the two volume model the average voltage is plotted. There is a small voltage difference of 0.1V between the two volumes and this is caused by the somewhat crude approximate distribution of currents between the two volumes. Developing a strategy for a more accurate distribution of currents between two or more volumes is a topic for future work.

CONCLUSION AND FURTHER WORK

From the simulation results, it is quite clear that even though there is some steady state offset, important variables of the simple and the detailed models show similar dynamic behavior during the simulations. It can therefore be concluded that the simple model is able to capture the overall dynamics of the SOFC. This model will hence be used for further studies on control and operability of the hybrid system, i.e. an SOFC integrated in a GT cycle.

If the one volume model is too crude, it is possible to aggregate a number of volumes. The results herein however indicate that a one volume model may suffice in many cases.

Further work includes developing the simple models of the other components in the SOFC-GT hybrid system, looking at how different design decisions affect controllability and developing an optimizing control structure for safe and part load operation.

Acknowledgments

Financial support from The Gas Technology Center, NTNU-SINTEF is acknowledged.

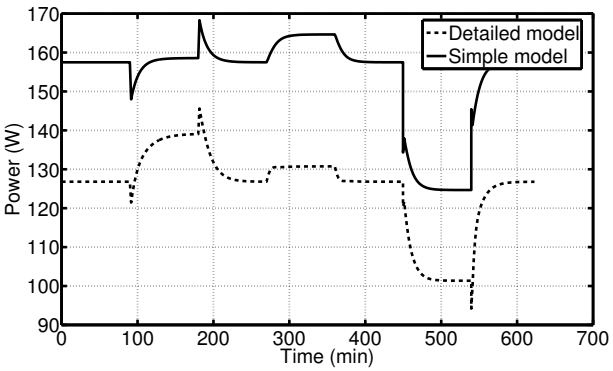

Figure 10: Comparison of powers of the simple model with two volumes and the detailed model for different disturbances

NOMENCLATURE

a_{ij}	stoichiometric matrix
A	SOFC surface area
A_{k_i}, $A_{K^{ads}}$	pre-exp. factors for k_i
C^s	solid heat capacity
DEN	denominator
E	activation energy
E^o	EMF at standard temperature and pressure
E^{OCV}	open circuit voltage
F	Faraday's constant
I	current
k_2, k_3, k_4	rate coefficients for reforming reactions
k_{an}, k_{ca}	choked flow constants
K_j	equilibrium constant for reaction j
K_i^{ads}	adsorption constant for component i
$\dot{m}$	mass flow rate
n_{rx}	number of reactions
N	number of moles
p	pressure
P	power
r_j	reaction rate of reaction j
R	universal gas constant
T	temperature
V_{an}, V_{ca}	volumes
V	voltage
$\Delta\overline{h}$	molar specific enthalpy
$\Delta\overline{h}^{rx}$	molar specific enthalpy change of reaction
$\Delta\overline{h}^{ads}$	enthalpy change of adsorption
δ	shaping factor

Subscripts and superscripts

i	chemical component
j	reaction
an	anode
ca	cathode
in	inlet
out	outlet
rad	radiation
$cond$	conduction

REFERENCES

[1] E. Achenbach. Three-dimensional and time-dependent simulation of a planar solid oxide fuel cell stack. *Journal of Power Sources*, 1994.

[2] S. Campanari. Thermodynamic model and parametric analysis of a tubular sofc module. *Journal of Power Sources*, 2004.

[3] S.H. Chan, H.K. Ho, and Y. Tian. Modelling of a simple hybrid solid oxide fuel cell and gas turbine power plant. *Journal of Power Sources*, 2002.

[4] S.H. Chan, H.K. Ho, and Y. Tian. Multi-level modeling of sofc-gas turbine hybrid system. *International Journal of Hydrogen Energy*, 2003.

[5] gPROMS (2004). gPROMS introductory user guide. *Process Systems Enterprise Ltd.*, 2004.

[6] F. P. Incropera and D. P. De Witt. *Fundamentals of Heat and Mass Transfer*. Wiley, USA, 2002.

[7] J. Larminie and A. Dicks. *Fuel Cell Systems Explained*. Wiley, England, 2003.

[8] J. Pålsson, A. Selimovic, and L. Sjunnesson. Combined solid oxide fuel cell and gas turbine systems for efficient power and heat generation. *Journal of Power Sources*, 2000.

[9] M. D. Lukas, K. Y. Lee, and H. Ghezel-Ayagh. An explicit dynamic model for direct reforming carbonate fuel cell stack. *IEEE Transactions on Energy Conversion*, 16(3), September 2001.

[10] L. Magistri, F. Trasino, and P. Costamagna. Transient analysis of a solid oxide fuel cell hybrids part a: fuel cell models. *Journal of Power Sources*, 2004.

[11] J. Padulles, G.W. Ault, and J. R. McDonald. An integrated sofc dynamic model power systems simulation. *Journal of Power sources*, pages 495–500, 2000.

[12] C. Stiller, B. Thorud, S. Seljebø, Ø. Mathisen, H. Karoliussen, and O. Bolland. Finite-volume modeling and hybrid-cycle performance of planar and tubular solid oxide fuel cells. *Journal of Power Sources*, 141:227–240, 2005.

[13] P. Thomas. *Simulation of Industrial Processes For Control Engineers*. Butterworth-Heinemann, Wobourn, MA, USA, 1999.

[14] B. Thorud, C. Stiller, T. Weydahl, O. Bolland, and H. Karoliussen. Part-load and load change simulation of tubular sofc systems. *Fuel Cell Forum, Lucerne, 28 June-2 July 2004*, 2004.

[15] J. van Schijndel and E. N. Pistikopoulos. Towards the integration of process design, process control, and process operability: Current status and future trends. *In the proceedings of FOCAPD '99, Breckenridge, Colorado, USA*, 1999.

[16] J. Xu and G. F. Froment. Methane steam reforming, methanation and water-gas shift: I. intrinsic kinetics. *AIChE Journal*, 1989.

Appendix E - Paper V

Planar and Tubular Solid Oxide Fuel Cells - Comparison of Transient Process Behaviours

Miriam Kemm, Christoph Stiller, Azra Selimovic, Bjørn Thorud, Tord Torisson, Olav Bolland

Accepted for publication at Solid Oxide Fuel Cells IX, May 15-20 2005, Québec City, Canada

ACCEPTED DRAFT
Planar And Tubular Solid Oxide Fuel Cells – A Comparison of Transient Process Behaviors

Miriam Kemm[a], Christoph Stiller[b], Azra Selimovic[a], Bjørn Thorud[b], Tord Torisson[a], Olav Bolland[b]
[a] Lund Institute of Technology (LTH), Dept. of Heat and Power Engineering,
P.O. Box 118, SE-221 00 Lund, Sweden
[b] Norwegian University of Science and Technology (NTNU), Dept. of Energy and Process Engineering, Kolbjørn Hejes vei 1B, N-7491 Trondheim, Norway

ABSTRACT

Two typical configurations of Solid Oxide Fuel Cells (SOFC) are planar cross-flow and tubular counter-flow. Even though their performance is based on the same physical principles, their operation characteristics and parameters vary considerably due to different geometries.
The goals of this paper are to detect the particularities of the cell geometries at transient operation and to identify their applicability for stationary power generation. This has been achieved by investigating the thermal and electrochemical performance of a planar and a tubular cell at different operation modes, i.e. load change, start-up, and shut-down.
As the most relevant results of the transient SOFC analysis, the comparison of relaxation times and transient temperature gradients within the cell as well as the transients of the power density are presented and discussed. Relaxation times for different processes are shorter for the planar geometry, caused by its compactness. However, due to its longer spatial extension the tubular geometry is more advantageous concerning the level of temperature gradients within the cell.

INTRODUCTION

Due to its low emission and highly efficient operation, the fuel cell is considered to be a promising technology for future energy supply. In the field of stationary power generation, the Solid Oxide Fuel Cell (SOFC) turned out to be the most suitable candidate of all types of fuel cells. Its high operation temperature enables the use of natural gas as fuel and it facilitates a higher electrical net efficiency than for low-temperature fuel cells. When compared to the Molten Carbonate Fuel Cell, the SOFC has the advantage of no corrosion at the electrolyte and consequently longer lifetime of the cell.
However, especially the high operation temperature of the SOFC poses a challenge for the material of all cell components. A non-uniform temperature distribution within the cell during steady state and transient operation causes thermal stresses, which can cause micro-cracks when becoming too high (1). Another disadvantage related to the high

operation temperature is long start-up and shut-down times making the SOFC less suitable for vehicle propulsion. Further, long relaxation times for load changes occur, which can result in difficulties if strongly fluctuating load profiles need to be followed.
The temperature distribution within the cell as well as transient behavior depends strongly on the geometry of the cell. The most established geometries today are the planar and the tubular.
Some of the authors have previously compared steady state behavior of planar and tubular cells implemented into a hybrid cycle (2). In the current paper, transient simulations, i.e. load change, start-up, and shut-down, have been performed for the planar cross-flow and the tubular counter-flow SOFC geometry. Their particular transient behavior has been investigated in terms of temperature, thermal gradients, and power density to compare their applicability for stationary power generation application.

SOFC GEOMETRIES

The investigated planar geometry is an electrolyte-supported cell with ceramic interconnects. The cell has an active area of 95 cm^2 and 18 fuel and air channels, respectively, which are arranged in cross-flow (3). The tubular geometry is based on the Siemens-Westinghouse technology (4), which is a cathode-supported 1.5 m long vertical tube with a diameter of 22 mm. The incoming air is heated up by flowing downwards an inner tube (injector). At the closed end of the tube, the air turns and enters the air channel between the cathode and the outer injector wall. The fuel flows co-currently to the air outside of the tube. Figure 1 shows the control volumes of each cell geometry.

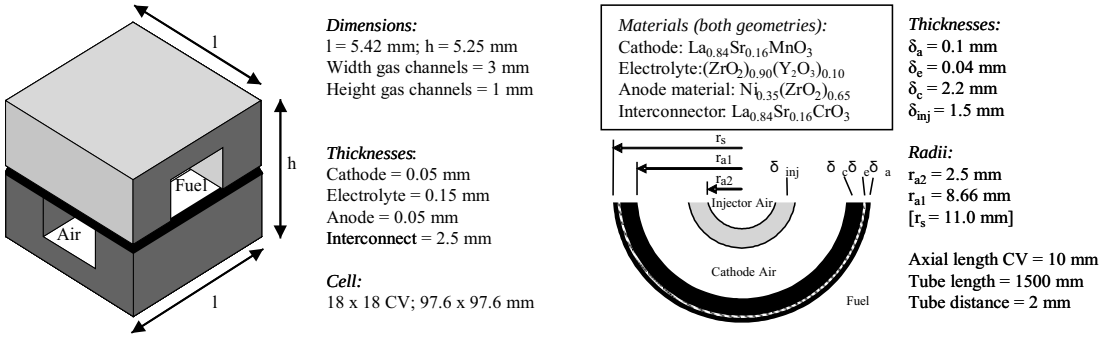

Figure 1: Basic geometries of planar and tubular fuel cell control volume.

In Table 1, the particularities of the different cell geometries are presented. Of special interest are the total heat capacities, which, related to the active area, strongly affect the dynamic behavior of the cells. It is also worth noting that the current and gas flow paths are quite different for both cells: the tubular cell has only one channel for each gas and therefore the flow path of the gas is 15 times longer than for the planar cell which has 18 parallel channels. This particularity is the main reason for the different transient behaviors, which will be discussed later.

Table 1: Geometry of the planar and the tubular model.

	Planar geometry	Tubular geometry
Anode thickness	0.05 mm	0.10 mm
Electrolyte thickness	0.15 mm	0.04 mm
Cathode thickness	0.05 mm	2.20 mm
Interconnector thickness	2.5 mm	(0.6) mm
Thickness of air injector wall	n.a.	1.5 mm
Gas flow arrangement	Cross flow	Counter flow
Internal preheating	not applicable	Airflow
Active area	95 cm^2	834 cm^2
Number of air channels	18	1
Cross-sectional area fuel channel	0.54 cm^2	2.11 cm^2
Number of fuel channels	18	1
Cross-sectional area air channel	0.54 cm^2	1.85 cm^2 0.196 cm2 (injector)
Flow path length	9.76 cm	150 cm
Total heat capacity of the solid material	113 J/K	471 J/K
Electric current flow path	Perpendicular to MEA	Perpendicular to electrolyte, longitudinal to anode and cathode

MODELING

The models used for the investigations are 2-dimensional distributed transient models. The planar model has been developed at LTH. It is based on the finite volume method and has been implemented in FORTRAN. The tubular model is developed at NTNU and it has been implemented in gPROMS, based on the finite difference method. The models are described in depth by Selimovic (5) and Thorud (6).

Both models solve the voltage balance, the mass, and the energy balances of the gas phase, as well as the energy balance of the solid phase for each node. As results the distribution of temperature, current density, the gas flows and the concentrations are calculated.

Calculations performed by Haynes (7) have shown that electrochemical and electrical changes within the cell, as well as alternations in gas concentrations and temperature, respond very fast in comparison to the temperature in the solid structure. Based on these results and own performed simulations, thermal inertia of the gases was neglected in this study. Both models account for convective heat transfer of the gases and conductive heat transfer within the solid structure. Additionally, the tubular model includes radiation between the injector wall and the cathode. Radiation emerging in the gas channels of the planar cell was neglected since the impact was assumed to be low due to the small channel sizes. However, neglecting this phenomenon will according to Yakabe (8) lead to a steeper temperature profile.

Both steady-state models were benchmarked against other existing models (3,9) and show good agreement. The transient simulations results of the models concur qualitatively with results found in literature (10).

To enable a comparison of the two cell geometries, property data from Bossel (11) have been utilized for materials and gases in both models.
The maximum values of the tubular cell temperature gradients will be displayed in axial and radial direction. For the planar model, the gradients in air and fuel direction have been merged to an effective gradient according to Pythagoras' theorem presented in equation [1]. The maximum value of this effective gradient will be displayed.

$$\left(\frac{dT}{dxy}\right)_{eff} = \sqrt{\left(\frac{dT}{dx}\right)^2 + \left(\frac{dT}{dy}\right)^2} \qquad [1]$$

DESIGN POINT

In the design point, both cells are operated at a mean temperature of 950 °C and are fuelled with 30 % pre-reformed natural gas. The fuel flow for the planar model is chosen to meet a fuel utilization of 85 % and an average current density of 2500 A/m^2. The airflow is adjusted in order to limit the maximum solid temperature to 1050 °C.

With these input data and the resulting voltage, a power density of 1730 W/m² has been calculated. Fuel and air flow of the tubular cell have been chosen to meet the same fuel utilization, power density and maximum temperature as the planar cell. Due to the different current-voltage characteristics of the cells, the resulting current density and voltage are different for both models, although the power densities are equal.
This operation point is defined as design points for all further investigations. Operation data connected to the design point can be found in Table 2.

Table 2: Design point data of the planar and tubular cell.

	Planar model	Tubular model
Power density in W/m^2	1730	1730
Fuel utilization in %	85	85
Maximum solid Temperature in K	1323	1323
Air inlet temperature in K	1173	1023
Fuel inlet temperature in K	1173	1173
Air excess ratio*	8.8	3.5
Voltage in V	0.692	0.7191
Fuel flow in kg/h**	0.00794	0.0672
Air flow in kg/h	0.314	1.058

* based on inlet fuel flow

** Fuel composition is 26.3% hydrogen, 17.1% methane, 49.3% steam, 2.9% carbon monoxide and 4.4% carbon dioxide

Within the tubular cell heat is transferred from the solid structure to the incoming air flowing through the air injector tube. This arrangement is beneficial compared to the planar cell geometry since it leads to a considerable flattening of the temperature profile. Furthermore, lower air inlet temperatures are feasible and therewith the demand of air mass flow for cell cooling is reduced.

LOAD CHANGE PERFORMANCE

To investigate the load change behavior of the two geometries, the voltages corresponding to the steady state power density of 100 % (design point), 75 %, and 50 % were altered with the help of a step function. The voltages differ for the two designs and they are shown on the x-axis in Figure 2 where the power density (solid lines) and current density (dotted lines) are plotted. Different flow paths of the cells mainly cause the difference in current-voltage characteristic between the two designs.

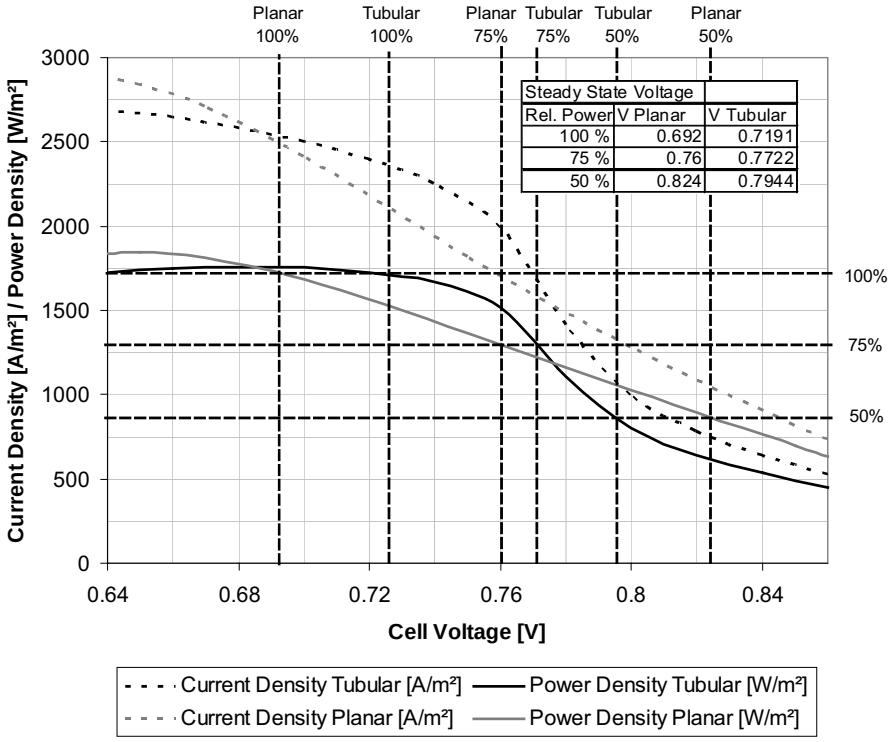

Figure 2: Current and power density characteristics design and part load points for planar and tubular cell.

Figure 3 presents the load change behavior of the two cell geometries when the power density is decreased from design point to 50 % part load. At time t = 0, the voltages are increased corresponding to the steady state values for a power density of 50 % following a step function. All other input data are held constant.

The relaxation time for the tubular geometry is about eight times longer (12000 sec) as for the planar geometry (1500 sec). This is due to a much higher temperature change of the tubular model between the two operation points.

Maximum temperature gradients decrease proportional to the temperatures and thus have its highest values at the design point. The maximum temperature gradients are by far higher for the planar cell than for the tubular. This can be explained by the cross-flow gas channel arrangement of the planar cell geometry, leading to a variation in reaction rates within the cell and thus a non-uniform temperature distribution. Further, the planar cell geometry is much more compact than the tubular. Investigations concerning the principal stresses caused by thermal gradients for the planar cell geometry have been performed by some of the authors (12). The paper shows that the thermal stresses developing in the cross-flow planar cell geometry at this operation point would exceed the material

strength of the electrolyte given by Montross (13). For the tubular geometry the maximum radial temperature gradient is higher than the axial. The radial gradients occur due to heat conduction in radial direction, which is a consequence of the heat sources and sinks caused by the chemical reactions and the duty between the air channels. Previous studies (6) have shown that the radial gradients correlate fairly proportionally with the current. Due to the long gas channels arranged in co-flow and the temperature smoothing by air preheating in the tubular cell, the axial temperature gradients reach lower values as the radial.

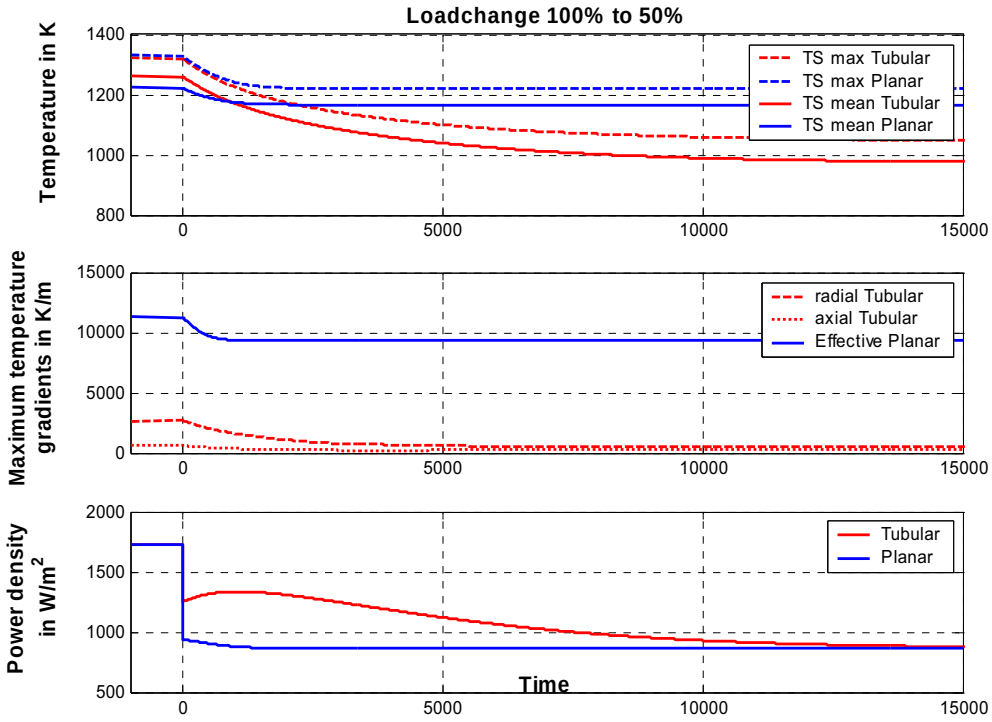

Figure 3: Load change from 100 % to 50 % power density.

The sudden increase in voltages causes an immediate decrease in power densities. The power density curves for the planar and the tubular geometries differ quite considerably. The power density of the planar geometry drops immediately and then decreases slightly due to a decrease in temperature. The sudden power density drop of the tubular geometry, however, is minor compared to the planar cell geometry and followed by a small increase before decreasing to the final value. The difference in power density drop arises from the different voltage-current characteristics, as already mentioned above. The tubular cell's power density behavior is caused by the changing temperature profile longitudinal to the cell. The current-voltage behavior of the cell is not only dependent on the mean temperature, but also on the correlation between temperature and hydrogen distribution. Thus, even at a constant mean temperature, different temperature distributions along the cell will influence the current distribution and therewith the losses.

The increase of power densities from 50 % to 100 % by decreasing the accordant voltages is presented in Figure 4. Comparing the process to the decrease of power density

investigated above, the transient behavior for the planar geometry is reversed. However, the time needed to come to steady state is increased (2000 sec), since the elevated reaction rates at 100 % power densities cause even higher temperature gradients which need more time to develop.
The temperature and thermal gradient behavior of the tubular geometry is similar as for the corresponding reverse case. The design power density is already reached after about 1000 seconds but increases slightly before decreasing again and coming to steady state after about 5000 seconds. As for the load decrease, this is also a consequence of the changing temperature profile along the cell.

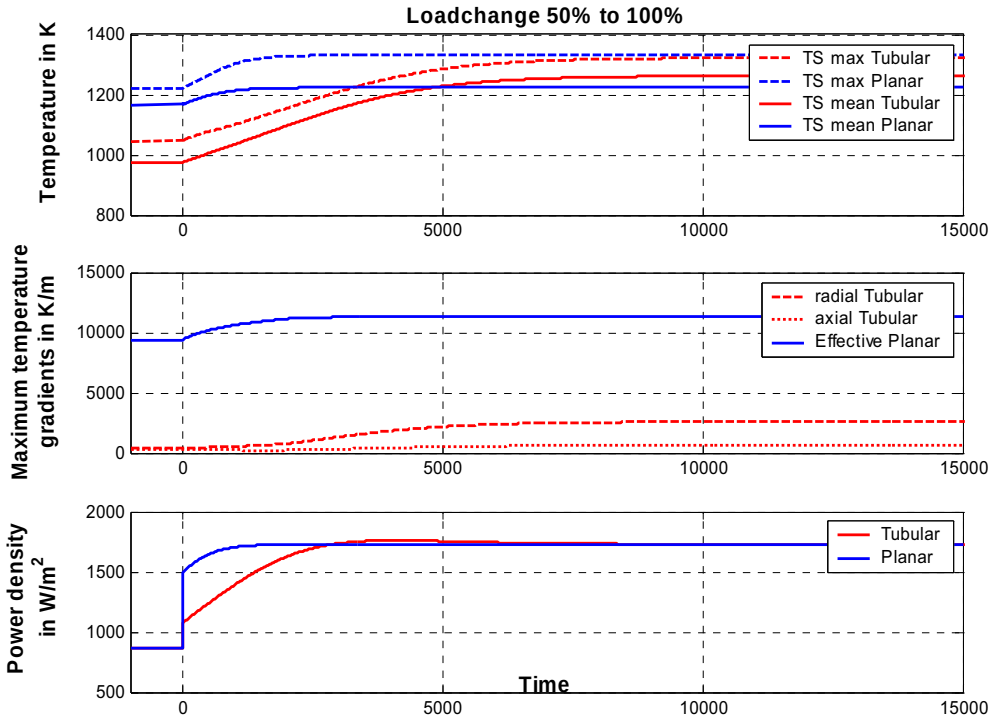

Figure 4: Load change from 50 % to 100 % power density.

Table 3: Relaxation times for different load changes.

Relaxation time in sec	To 100 %		To 75 %		To 50 %	
	Planar	Tubular	Planar	Tubular	Planar	Tubular
From 100 %			2000	17000	1500	12000
From 75 %	2000	5000			1500	12000
From 50 %	2000	5000	2000	17000		

In Table 3, a summary of the relaxation times of all the investigated load change cases is presented. The planar cell responds faster than the tubular for all investigated cases, due to its highly compact geometry and steadier mean temperature throughout the operation range. As already presented by Achenbach (14), it can be seen that the relaxation time is mainly influenced by the end point of a load change and almost independent of the size of load change step.

START-UP PERFORMANCE

To enable the operation of a SOFC, the temperature of the solid cell structure has to be increased from ambient temperature to a level of about 1000 K. This may be done by feeding preheated Nitrogen into the gas channels. The temperatures of the entering gases are successively increased to maintain a constant temperature difference of 100 K to the gases leaving the cell. This assumption is pragmatic in case the inlet gas is heated recuperatively by the outlet gas and a constant power supplementary heater. The utilization of an electric heater has been reported by George (15).
Due to the similar sizes of flow areas for air and fuel channels in both models, equal gas flow rates for fuel and air channels have been chosen. The gas flow rates are set close to the particular design molar flow rates of the air, thus 0.3 kg/h for the planar and 1 kg/h for the tubular model. These values conform well to the specific total heat capacities of the cells resulting in similar start-up duration for both cells.
When both gases have reached a temperature level of 1023 K, fuel and air, according to the base cases, are fed into the cells to start electrochemical reactions. The voltages are set to the design point values. The gas inlet temperatures (except air inlet of the tubular cell) are further increased in the same manner, until the design point value of 1173 K is reached. Due to the variation in reaction rates within the cells, non-uniform temperature fields develop until steady state is reached. The schematic of the heat up process is sketched in Figure 5.

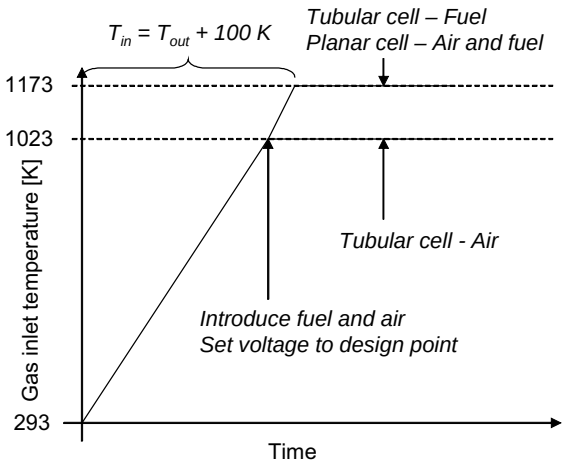

Figure 5: Schematic of the Start-up procedure

The behavior of the cells during start-up process can be seen in Figure 6. The duration of the heat up process where no chemical reactions take place is about 1 hour for the planar cell and 1 hour and 15 minutes for the tubular cell. The temperature profile of the planar cell is diagonally symmetric due to the symmetry of the cell structure and the equal gas flows. Higher temperature gradients arise in the planar cell. This is caused by the compact cross-flow arranged gas channels resulting in high temperature difference between the gas inlets and the fuel-air outlet corner. The tubular cell has co-flow arranged gas channels, considerably higher channel length, and internally counter-flowing preheated air, which results in low axial gradients.
The progress of the planar cell's maximum temperature gradient during the heating up shows a good matching to a similar start-up procedure simulated by Rechenauer (16), even though the absolute values are lower in the present study. For the tubular cell, no data on start-up have been found.

Generally, the gradients during any operation do not exceed the values at the design point for both models. However, at low temperatures the fuel cell's tolerance of thermal gradients could be lower, as the residual stresses between the membrane layers tend to be higher.
When starting the electrochemical reactions by feeding fuel and air into the gas channels, the power densities increase instantaneously. Although the planar cell has a mean temperature of about 950 K in comparison to 920 K in the tubular cell when electrochemical reactions are started, this instantaneous power density increase is minor for the planar geometry. This may be explained by the different performance characteristics of the two cell geometries.

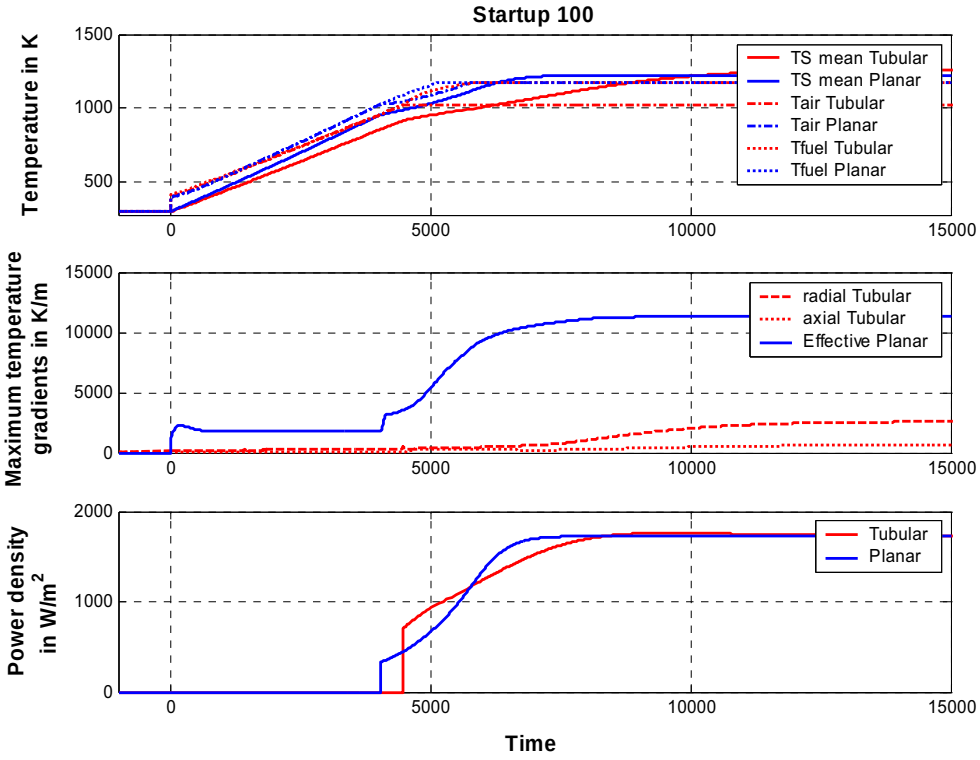

Figure 6: Start-up performance of the cells.

Times to reach steady state differ slightly for both models due to a power density overshoot of the design point for the tubular geometry, as already observed for load change operations. The planar geometry needs about 2 hours in total to reach steady state, while the tubular one reaches 100 % power density after 2 hours and 20 minutes but overshoots the design point slightly, resulting in a prolongation of the relaxation process.

SHUT-DOWN PERFORMANCE

The shut-down strategy used to anneal the cell to ambient temperature is almost contrariwise to the start-up process. The gases entering the cell are substituted by nitrogen. The same flow rates as for the heat up procedure are used and the inlet

temperatures are kept 100 K under the outlet gas temperature until a temperature level of 293 K is reached.
As expected and shown in Figure 7, the steepness of both models´ temperatures is the same as for heatup. Accordingly, the tubular cell temperature decreases slower than the planar, causing only a time difference of about 10 minutes. The shut-down takes thus about 1.5 hours for both geometries. It is quicker than the start-up as no steady state relaxation has to be awaited.

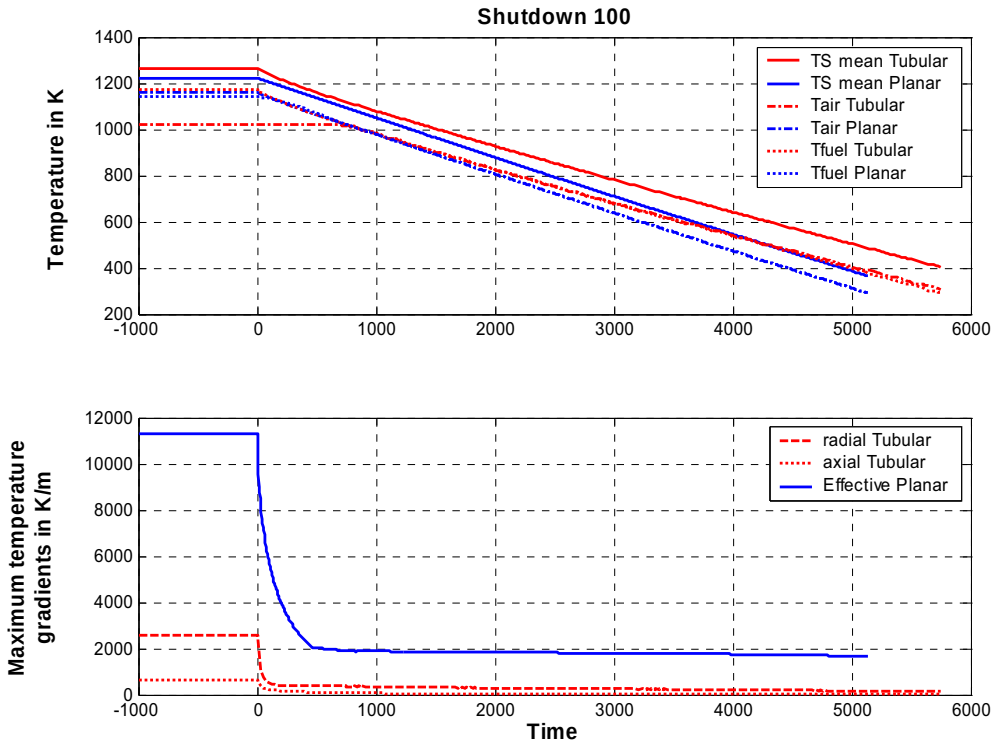

Figure 7: Shut-down performance of the cells

CONCLUSIONS

The transient behavior of the planar and tubular cell geometries has been investigated by simulating load changes, start-up and shut-down processes.

Considering the relaxation times for the investigated cases, the planar cell geometry adapts faster to new operating conditions. This is significant for load change processes where the tubular cell geometry needs between 2.5 and 8.5 times as long as the planar one, depending on the end point of load change For start-up and shut-down processes, the differences in relaxation times for the two cell geometries are almost negligible.

When looking at operational demands of the cell materials during transient processes, the tubular cell geometry is less complicated due to lower maximum thermal gradients occurring within the cell. For the defined design point, the planar cell geometry causes about 4.6 times higher maximum thermal gradients than the tubular. No higher gradients than in the design point could be observed during any dynamic operation.

Generally, the models show very different behavior in terms of current-voltage characteristics and relaxation times even though all kinetics and thermophysical properties have been equalized. The reasons for this are the different electric and gas flow paths, the internal cooling of the tubular cell and the different heat capacities of the solids.

For further work, the impact of the thermal gradients and the temperature levels on the two cell geometries has to be investigated.

ACKNOWLEDGEMENTS

The Swedish Energy Administration, Sydkraft utility, Shell Technology Norway, Statkraft and the Norwegian Research Council are greatly acknowledged for funding this work.

REFERENCES

1. A. Selcuk, G. Merere, A. Atkinson, *Journal of Material Science*, **36**, pp. 1173 – 1182, (2001).
2. Stiller, B. Thorud, S. Seljebø, Ø. Mathisen, H. Karoliussen, O. Bolland, *Journal of Power Sources*, in press.
3. E. Achenbach, H. Nabielek, *IEA Programme on R,D&D on Advanced Fuel Cells, development* Final Report of Activity A2, Report of Research Center Julich, (1996).
4. K. Hassmann, *(2001) Fuel Cells*, 1, No.1.
5. A. Selimovic, *(2002) Doctoral Thesis*, Lund Institute of Technology, ISRN LUTMDN/TMHP-02/1002-SE; ISSN 0282-1990.
6. B. Thorud, C. Stiller, T. Weydahl, O. Bolland, H. Karoliussen, *6th European Solid Oxide Fuel Cell Forum*, Lucerne, Switzerland, (2004).
7. C. Haynes, *Journal of Power Sources*, **109**, pp 365 – 376, (2002).
8. H. Yakabe, T. Ogiwara, M. Hishinuma, I. Yasuda, *Journal of Power Sources*, **102**, pp. 144-154, (2001).
9. S. Campanari, P. Iora, *Journal of Power Sources*, **132**, pp. 113-126, (2004).
10. E. Achenbach, *Journal of Power Sources*, **57**, pp 105-109, (1995).
11. U.G. Bossel, in *Facts and Figures*, Final Report on SOFC data", IEA report, Operating task II, Swiss Federal Office of Energy, Berne, CH, 1992.
12. A. Selimovic, M. Kemm, T. Torisson, M. Assadi, submitted to *Journal of Power Sources*.
13. C. S. Montross, H. Yokokawa, M. Dokiya, *British Ceramic Transactions*, **101**, (2000).
14. E. Achenbach, *Journal of Power Sources*, **49**, pp 333-348, (1994).
15. Raymond A. George, *Journal of Power Sources*, **86**, pp. 134-139, (2000).
16. Ch. Rechnenauer, E. Achenbach, *Doctoral Thesis*, Forschungszentrum Jülich, Germany, (1993).

Appendix F - Paper VI

Control Strategy for a Solid Oxide Fuel Cell and Gas Turbine Hybrid System

Christoph Stiller, Bjørn Thorud, Olav Bolland, Rambabu Kandepu, Lars Imsland

Submitted to the Journal of Power Sources

Control Strategy for a Solid Oxide Fuel Cell and Gas Turbine Hybrid System

Christoph Stiller*, Bjørn Thorud, Olav Bolland

Department of Energy and Process Engineering

e-mail christoph.stiller@ntnu.no; bjorn.thorud@ntnu.no, olav.bolland@ntnu.no

Rambabu Kandepu, Lars Imsland

Department of Engineering Cybernetics

e-mail rambabu.kandepu@ntnu.no, lars.imsland@ntnu.no

Norwegian University of Science and Technology

NO-7491 Trondheim, Norway

* Corresponding author, tel. 0047-735-93723, fax 0047-735-98390

Abstract

The paper presents a multi-loop control strategy for a SOFC/GT hybrid system. First, a detailed dynamic model of the system is presented and its part-load performance is studied. Objectives for control are discussed, the main issue being a fairly constant fuel cell temperature under all conditions. Based on the system configuration and part-load performance, input and output variables of the control system are detected. Control cycles are introduced and their design is discussed. The response of the resulting system on load changes, external disturbances as well as malfunction and degradation incidents is investigated. The system behaves stable under all incidents. Errors in fuel flow measurement or assumed fuel quality provoke permanent fuel cell temperature changes. For a degraded system, it may be advisable to readjust the control system to the new characteristics.

Keywords

SOFC, hybrid cycle, modelling, part-load, control

Abbreviations

SOFC	solid oxide fuel cell
GT	gas turbine
FU	fuel utilisation
AU	air utilisation
TIT	turbine inlet temperature
TOT	turbine outlet temperature
IIR	indirect internal reforming

1 Introduction

A large amount of modelling work [1]-[4] and a demonstration plant [5] have proven that a solid oxide fuel cell (SOFC) integrated with a gas turbine (GT) has a potential for high efficiency electricity production with low environmental emissions. The good scalability of such systems makes them especially advantageous for distributed generation systems. Provided that quick load following is feasible, stand alone power generation is a possible application.

However, SOFC/GT hybrid systems face many challenges when it comes to load change and part-load operation. A gas turbine alone has good dynamic properties, but part-load performance can be rather poor. In any operation point, compressor surge must be prevented. A SOFC is generally able to respond quickly to load changes [6], but it might be destroyed or seriously degraded either due to thermally induced stresses caused by different thermal expansion coefficients in the cell materials or from carbon deposition at the anode. Another phenomenon that may occur during load change is backflow of gas from the burner to the anode cycle, exposing the anode to oxygen. These incidents must not occur in any operation instance. Furthermore, in terms of high efficiency and low degradation of the fuel cell due to thermal cycling, the fuel cell temperature should remain fairly constant during operation. The fulfilment of the mentioned tasks requires a comprehensive control strategy.

Results from part-load operation modelling have already been discussed by some authors. Costamagna et al. [7] investigated a hybrid system using a non-dimensional tubular SOFC model. In all simulations they assumed constant fuel utilisation (FU). If shaft speed was assumed constant, power output could only be controlled by varying the fuel flow. These simulations showed large variations in air utilisation (AU) and loss of efficiency for fixed shaft speed when operating at part-load. For variable shaft speed, however, AU and FU as well as SOFC inlet temperatures could remain fairly constant in part-load operation with only a small penalty on system efficiency. This effect was mainly due to increased recuperator efficiency owing to reduced air flow rate.

Campanari [8] also used a non-dimensional tubular SOFC model to investigate the hybrid system. Assuming constant FU of 80%, for constant shaft speed they suggested reducing AU and current density for part-load. This approach will reduce power output of the SOFC as well as the turbine inlet temperature (TIT) and consequently the power output of the GT. For variable shaft speed they suggested to reduce air flow rate and current density to maintain a constant AU. However, a reduction in air flow rate leads to pressure reduction and therewith higher turbine outlet temperature (TOT) and thus higher recuperator outlet temperatures. They concluded that for maintaining constant TIT, the current density has to be reduced further.

Chan et al. [3] also investigated a non-dimensional tubular SOFC-type in a hybrid system. In their system, power is reduced by shifting the load from the SOFC to the GT through introducing fuel to the combustor, which results in strong reduction of the system efficiency. This method also implies that a SOFC bypass should be implemented for both fuel and air. Due to the low part-load efficiency, they state that this method is mainly for short term load reduction. The aim was to maintain a relatively high SOFC temperature.

Pålsson and Selimovic [9] used a 2-dimensional planar SOFC model for part-load studies. Design point was set where the compressor flow matched the cooling requirement of the SOFC. They introduced an air heater/cooler prior to the SOFC entry in order to meet the requirements for the air inlet temperatures at part-load operation. TIT was kept constant and shaft speed was varied. At part-load operation, increased FU and low GT part-load efficiency led to increased power contribution from the SOFC. Due to the problems associated with

matching of the system components, they concluded that the load range for hybrid systems should be limited to 55 – 100%, corresponding to a load variation of the GT of 20 – 100%.

Kimijima and Kasagi [10] studied part-load of a 30 kW simple recuperated cycle using a non-dimensional SOFC model. Variable and fixed shaft speed operations are compared. FU is kept constant, even though it is mentioned that FU could be increased at part-load operation. They conclude that variable shaft speed operation is favourable in terms of part-load performance; however the higher TOT could cause problems.

Some of the authors of the present work have recently presented a complex model of a SOFC/GT system [11]. Performance maps were introduced to illustrate the variations of the most important parameters over the two degrees of freedom, namely shaft speed and fuel flow. Based on these maps, it was found that strategies with fairly constant temperatures in the SOFC seem feasible but require a feedback control system for safe operation. Responses of the non-controlled system on variations of shaft speed and fuel flow were briefly studied.

All above mentioned authors have identified inlet and outlet gas temperatures as well as air and fuel utilisations of the SOFC as important parameters for part-load operation of hybrid systems. Maintaining a constant SOFC operation temperature is important to avoid thermal cracking, but this might be difficult to achieve at reduced pressure as the TOT and consequently the recuperator outlet temperature increases.

Few studies on control layout and load-following of high temperature fuel cell systems and hybrid systems have been published. Zhu and Tomsovic [12] have studied the load-following of microturbine and fuel cell system models, however not as a hybrid system but as separate systems coupled together in a power network. Response time of approximately 10 and 30 s were observed for load increase in the microturbine and SOFC system, respectively. The slow SOFC response was mainly due to the slow dynamics of the fuel processor. It was concluded that load-following in a network is to be provided mainly by microturbine systems. Jurado [13] designed a control system for a molten carbonate fuel cell indirectly integrated into a gas turbine. Controllers for the gas turbine and fuel cell are introduced; however no coupling between these is established. Both references do not regard the thermo- and gas-dynamical processes during and subsequent to load changes.

The aim of the current work is to present a comprehensive control layout for a hybrid system. A detailed dynamic model of a tubular SOFC system integrated into a simple recuperated GT cycle as the basis for the investigation is described. The steady state behaviour of the system is displayed in performance maps. Next, control objectives and the nature of disturbances influencing the system are discussed. A combined feedback-feedforward control layout is introduced. From the performance maps, an appropriate operation line is selected and the feedforward section is tuned to it. Feedback controller tuning is discussed. As a result, the responses of the controlled system to certain load changes and disturbances are studied.

2 Hybrid cycle model

The investigated hybrid cycle is shown in Figure 1. The SOFC system design (inside the vessel in Figure 1) is similar to that of Siemens-Westinghouse [14][15]. The model incorporates indirect internal reformer (IIR), afterburner and recirculation and mixing chamber, where part of the anode exhaust gas is admixed to the fresh fuel in an ejector in order to supply steam to the steam reforming and shift reaction. Required valves for start-up, shut-down and failure have not been included.

Figure 1

Since the last study [11] with this hybrid cycle model, the reforming section has been improved. Furthermore, heat loss from the stack by radiation has been added and the activation and diffusion potential models have been refined. The models are described below.

2.1 SOFC

The SOFC model is spatially discretised and fully dynamic in terms of gas transport and heat transfer, allowing the study of temperature distributions. Gas flows are treated as 1D plug flows

$$\frac{\partial c_i}{\partial t} + v_g \frac{\partial c_i}{\partial z} = \sum_j r_{i,j} \tag{1}$$

The solid structures are modelled by a 2D discretisation scheme in axial and radial direction, neglecting effects in the circumferential direction. Heat conduction in solid structures is calculated by

$$\frac{dT_s}{dt} = \frac{k_s}{c_s \cdot \rho_s} \nabla^2 T_s \tag{2}$$

Internal reforming is implemented using the kinetic approach of Achenbach [16] for steam-methane reforming, while the water-gas shift reaction is assumed to be always in equilibrium. The model calculates the local electrical potential balance, accounting for the effects of activation (Butler-Volmer) and diffusion potentials (Fick's Law and Knudsen diffusion) and ohmic resistance. The constants used in the Butler-Volmer equation have been estimated based on measurement data from Singhal [17]. For the heat transfer between the solids and the gases, Newton's law of cooling is applied in the following way:

$$\frac{\partial \left(T_g c_{p;g} \rho_g \right)}{\partial t} + v_g \frac{\partial \left(T_g c_{p;g} \rho_g \right)}{\partial z} = \frac{2h}{r_s} \left(T_s - T_g \right) \tag{3}$$

Spatially discretised radiation heat exchange is included between the cathode surface and the air supply tube. Furthermore, the anode radiates to the IIR to supply heat for the reforming reaction, and to the casing wall, leading to heat loss to the environment. Friction losses in the gas channels are accounted for by the Reynolds number approach.

2.2 Anode recycle loop and reformers

In order to supply steam for the reforming process, a certain part of the anode exhaust gas must be recycled. The suction of the recycle stream and the mixing with the fresh fuel is performed by an ejector. High induced (recycle) flow rates at low pressure differences are typically achieved by subsonic mixing ejectors. The actuating flow is accelerated to supersonic speed in a Laval nozzle before it enters the mixing chamber. The ejector model is based on section-wise momentum balances and has been validated against data from Marsano et al.[18]. Pressure losses are included by a fixed throttle valve.

Before entering the anode cycle, the gas leaving the ejector is passing two reformers: An adiabatic pre-reformer and an internal indirect reformer (IIR).

The pre-reformer is modelled as a non-dimensional Gibbs equilibrium reactor where reforming and water-gas shift reactions take place. It is meant for cracking any higher hydrocarbons in the fuel gas and reform a part of the methane until an equilibrium is reached. To account for reaction kinetics, a difference between the actual outlet temperature and the equilibrium temperature of 20K is assumed.

The IIR is situated downstream the pre-reformer and it is based on Gibbs equilibrium. The gas is assumed to be reformed while it flows downwards rectangular ducts. The duct walls are coupled to the fuel cell anode by radiation which is computed as distribution in the flow direction. A view factor is adjusted in the design calculation to meet the desired reforming degree. Gas residence time in the reformer is accounted by the same approach used in the SOFC model (Equation 1).

2.3 Burner and recuperators

The burner is modelled non-dimensionally and adiabatically and completely combusts the remaining anode exhaust gas together with the cathode air. By mixing cathode and anode exhaust streams, it causes pressure equalisation of these flows upstream.

The burner exhaust is preheating the inlet air by a counter-flow tube-shell set-up, where the tube is the prolongation of the fuel cell air supply tube. The model accounts for thermal inertia, pressure loss and gas residence times, using the same approaches as in the SOFC model.

The recuperator heat exchanger is a stack of counter-flow plate-fin type. A 2-dimensional distributed model is applied that accounts for thermal inertia, pressure loss and gas residence times. The recuperator model is based on data and relations from Kays [19].

2.4 Gas turbine

The gas turbine model features map-based steady state turbomachinery, a shaft model accounting for rotating mass inertia, power electronics and ducts.

The compressor is based on the performance map of a small centrifugal research compressor by the German Aerospace Centre, found in a map collection from Kurzke [20][19]. The map is understood as a generic radial compressor map and therefore it has been scaled in terms of reduced mass flow, pressure ratio and shaft speed to fit the design case. The map has been modelled using polynomials of 4th and 5th order for reduced mass flow, pressure and efficiency as functions of reduced shaft speed and operation (β) line. A surge margin (SM) is calculated as follows:

$$SM = \frac{\pi_{surge}\left(\dot{m}\right) - \pi\left(\dot{m}, n\right)}{\pi\left(\dot{m}, n\right)} \tag{4}$$

where $\pi\left(\dot{m}, n\right)$ is the actual pressure ratio at the actual reduced mass flow and reduced shaft speed and $\pi_{surge}\left(\dot{m}\right)$ is the surge pressure ratio at the actual reduced mass flow.

The turbine is based on the performance map of a small radial turbine [20][19] which also is scaled to fit the design case. An ellipse approach has been used for the relationship between reduced mass flow, reduced shaft speed and operation (β) line. Pressure ratio and efficiency have been modelled by a polynomials approach.

Generator and power electronics account for transformation efficiencies which are assumed to be constant. A constant power sink accounts for power consumption of auxiliaries and transformation efficiency decrease at low load.

The shaft model includes acceleration/deceleration of the shaft through moment of inertia of the moving parts:

$$\frac{d\omega}{dt} = \frac{P_b}{I \cdot \omega} \tag{5}$$

Where ω is the angular shaft speed in *rad* s^{-1}, I is the moment of inertia in *kg* m^2, and P_b is the power balance

$$P_b = \eta_m P_{turb} - P_{comp} - P_{gen} \quad \text{in } W. \tag{6}$$

The ducts are adiabatic and frictionless. Their only purpose is to account for gas residence time in the piping.

2.5 Complete model

The complete model is implemented in gPROMS [16], a process modelling tool based on an equation oriented solver. The strength of the equation oriented approach is that there is no fixed input-output structure. In fact, a certain number and combination of variables must be specified in order to achieve a valid equation system, but many degrees of freedom remain in choice of variables. As an example, either voltage or current of the fuel cell model may be specified.

The resulting system model consists of approximately 14,000 algebraic and 2,300 state variables. The simulations were performed on a 2.5 GHz Intel Pentium-4 processor PC. Calculation time for a steady state point was approximately 5-10 seconds. The solver used for dynamic calculations (SRADAU) varies time increments, thus calculation time depends on the occurrence of discontinuities and momentary fluctuation rate of the variables. A calculation time of about 5 minutes was required for the load change studies shown below, while the load profile simulation required about 20 hours.

3 Design case and steady-state part-load behaviour

Before part-load behaviour can be studied, a design point has to be defined. All relevant cycle data are displayed in Figure 1. Most of the data are similar to recent literature on hybrid cycles [3][7][8][10] and public data from Siemens-Westinghouse. Values in the figure marked with a square are constant during all simulations. The design point and system dimensioning is furthermore based on the following assumptions:

- The system size is determined based on the Siemens-Westinghouse stack design which incorporates 1152 tubular cells [22] and 16 indirect internal reformers.
- Pure methane is supplied as fuel.
- The view factor for the radiation from the anode surface to the IIR is equal for each cell and has been adjusted to achieve a reforming degree of 80%. Despite the fact that the numbers are usually in the range of 30-50%, such a high number has been chosen in order to flatten the profile of temperature and current density in the cell. Furthermore, Song et al. [15] report that the IIR exhaust gas includes only a small amount of unreformed methane at the Siemens-Westinghouse configuration.
- The view factor for the radiation from the anode surface to the stack casing and the thermal conductivity of the stack casing have been adjusted in order to obtain a heat loss of 10 kW at design point.
- A length of 0.5 m was chosen for the air preheat tube, yielding a temperature increase of 208 K at design point.
- The ducts have a length of 1 m and are dimensioned for gas velocities of app. 20 m/s at design point. The residence times are calculated utilising the ideal gas law. Therefore they will vary slightly in other operation points. Residence times before and after the pre-reformer account for the actual pre-reformer residence time.

- The fuel utilisation (FU) is determined from current and fuel flow, as these parameters can be measured in a real system. Setting FU constant hence means maintaining a constant ratio of current to fuel flow. While this in steady state provokes a constant content of combustibles in the anode exhaust gas, the content may vary during dynamic operation due to pressure change and gas transport delay. Due to the variations of the heating value of the exhaust gas, this may cause severe oscillations in burner temperature during load change. The common fuel utilisation value of 85% has been chosen.
- The ejector has been dimensioned for supplying a steam to carbon ratio of 2 in the design point. The difference in static pressure of induced and actuating gas flow in the mixing zone is vital for the ejector performance. According to Johannesen [23], a lower actuating flow pressure than induced flow pressure, causes a strong reduction in induced flow rate, while a higher actuating flow pressure does not significantly increase induced fluid flow rate. For being able to reduce the fuel flow rate for part-load operation while maintaining a high recycle ratio, the inlet pressure of the actuating fluid at design point must be high. A value of 23.7 bar was chosen for design point. It is assumed that natural gas is available at this pressure, and hence there is no need for a fuel compressor.
- The recuperator is dimensioned in order to achieve a high amount of heat recuperation at tolerable size and pressure drop.
- The total moment of inertia for the rotating parts (turbine, compressor, generator and shaft) is assumed to be 0.025 $kg \cdot m^2$. This is equivalent to a rotating mass of 20 kg and a mean radius of 5 cm. The moment of inertia influences the power output during shaft acceleration and deceleration.
- The generator is assumed to have a constant efficiency of 95%. The power electronics have constant efficiencies of 90% for AC/AC and 95% for DC/AC conversion. As a comparison, von Spakovsky et al. [24] report values of 92 to 95% for DC/AC conversion for a 5 kW system. In order to account for power consumption of auxiliaries and the decreasing conversion efficiencies at load reduction, a constant power loss of 5 kW was applied.

With the given design and assuming a constant fuel utilisation in steady state operation, two degrees of freedom remain for off-design operation, most pragmatically expressed by the parameters of fuel and air flow rate. Fuel flow can be controlled by a flow control valve. The air flow can be controlled through the gas turbine system in various ways, such as variable shaft speed, variable compressor inlet guide vanes or variable compressor bleed. Their effect on the system is very similar. Shaft speed variation was chosen for the current work, as this is the option maintaining the highest efficiencies and the lowest pressure changes when reducing air flow. The shaft speed is controllable through the power that is produced by the generator.

The free parameters air and fuel flow may be varied independently from each other within certain limits. Each combination determines a certain operation point of the system. Figure 2-4 show the steady-state behaviour of the parameters of interest as a function of fuel flow (FF) and air flow (AF) relative to their design values. Similar maps have been introduced for a SOFC stack system [25] and a full hybrid system [11].

Figure 2

Figure 3

Figure 4

The blinded out area on the upper left (low air and high fuel flow) represents an area where no steady state operation exists. Transient simulations have shown that the temperature in this regime is steadily climbing far beyond the valid ranges and furthermore eventually causing compressor surge. This is because enhanced effectiveness of the heat recuperation loop and lower air excess ratio at lower airflow causes TIT to increase.

In the lower right area (high air and low fuel flow), the fuel cell is cooled down strongly and therefore the voltage is low. As it is not recommendable to operate in this regime, it is blinded out for cell voltages lower than 0.3 V.

A first result from the performance map is that reducing fuel flow at constant air flow, i.e. going down a vertical line from the design point, results in a strong reduction in temperatures and therewith efficiencies.

The figures also show that a load reduction by linearly reducing fuel flow and air flow will lead into the unstable region. Remaining in the stable regime therefore implies larger relative reduction in fuel flow than air flow. This is a consequence of the lower pressure ratio at lower shaft speed which results in an increased TOT. The same behaviour is also confirmed in a study by Costamagna et al. [7].

Surge margin and steam to carbon ratio do not reach any alarming values in the shown operation range.

4 Control design

4.1 Control objectives

A suitable control strategy for normal operation must meet the following objectives:

- Safe operation of the system: Incidents which may cause damage to the fuel cell or other components must be avoided. Such incidents are compressor surge or cell degradation due to thermal cracking or too high temperatures, carbon deposition and therewith blocking of the anode, and backflow of gas from the burner to the anode cycle, exposing the anode to oxygen. Compressor surge can occur in case of too high turbine inlet temperature. The occurrence of thermal cracking is coupled to the temperature and therewith stress profile in the cell. A model for thermal stress calculation in tubular SOFC has been developed recently at NTNU [26], however it is very computationally expensive and revealed a high degree of uncertainty and sensitivity to exact material properties. Carbon deposition becomes likely with too low temperatures and too low amount of steam at the cell inlet. Anode backflow has been observed with the model used here during sharp pressure increases [11], therewith restricting the maximum allowed pressure increase rate.
- Quick load following and high efficiency: The selected control strategy should make it possible to follow a load profile quickly and accurately and furthermore maintain a high efficiency of the system in part-load operation.
- Long lifetime of the fuel cell: In addition to thermal cracking, the fuel cell may be degraded through thermal fatigue and high local heat production rates [24]. The effect of thermal fatigue may be reduced by reducing the thermal cycling amplitude, hence by maintaining the mean cell temperature as constant as possible throughout any part-load operation. Local heat production may be controlled by limiting the current drawn from the cell.

- Governing external influences: The system must react on external disturbances and adapt to changes in subcomponent performance, caused for example by fuel cell degradation or compressor fouling.

4.2 Analysis of the system

The hybrid cycle model is strongly non-linear and cannot be easily linearised due to its complexity. Therewith most of the common controllability analysis techniques are not applicable [27]. However, having mapped the part-load behaviour, the system response is not so difficult to predict and thus the system is analysed manually.

The system has only one outer control variable, which is power. However, a certain operation strategy must be implemented, and thus also fuel utilisation, air flow and SOFC temperature have to be controlled. The manipulated variables are current, fuel flow and generator power.

There is strong interaction among the manipulated and controlled variables. However, as the required time scales are very different for the different control issues, a multi-loop control design may be applied without resulting in instabilities:

- Power is controlled by manipulating SOFC current due to its quick dynamics (magnitude of less than one second)
- Fuel utilisation must hence be controlled by manipulating the fuel flow (magnitude of few seconds).
- Air flow is controlled by manipulating the generator power and thus adjusting the shaft speed (magnitude of 1 minute)
- Cell temperature is controlled by adjustment of the air flow setpoint (very slow)

The mentioned control loops are explained in detail in the following sections. The resulting control system is sketched in Figure 5.

Figure 5

It must be pointed out that the control strategy presented here is adapted to the behaviour of the described system. Even though the shown equations and parameters are only valid for this system, it is expected that the control strategy can be adapted to a real system once data of its true behaviour are available.

4.3 SOFC power controller

The fuel cell can respond very quickly to load changes, as it is only limited by the electrochemical reaction restoring the charge which has been drained by the load [12]. Typically, time constants of below 1 s are assumed for a change in current [12][24]. For the primary control of power, it is therefore reasonable to manipulate the fuel cell current. We assume that this is being done in an instantaneous way by the power electronics subsystem which is determining the operation point on the current-voltage line of the fuel cell. However, there are some limitations that prohibit the arbitrary movement on this line:

- The fuel utilisation must be kept within certain bounds. A too low FU leads to low steam content in the anode recycle and high TIT and therewith the risk of carbon deposition and compressor surge. A too high FU on the other hand leads to steep internal temperature gradients in the fuel cell and therewith advances thermal cracking. It is chosen to vary fuel utilisation in the range from 75% to 90%.
- The cell voltage must not drop under a certain level, as there is a maximum power output at an intermediate voltage (app. 0.5-0.6 V, depending on the operation state).

Lower voltage causes decreasing power in spite of increasing current and is unfavourable. A minimum voltage of 0.52V is chosen.

The outcome is a multi-mode controller which switches between the modes of "*normal operation*", "*maximum FU*", "*minimum FU*" and "*minimum voltage*" to fulfil all above limitations. In "*normal operation*" mode, the current is manipulated so that the desired power of the whole system is produced. Small load steps in the range of some kW can be followed instantaneously, while for larger steps, the controller switches to the mode "*maximum FU*" or "*minimum voltage*" in case a load increase and "*minimum FU*" in case of a decrease.

4.4 Fuel utilisation control

After a load change, the fuel utilisation must be reset to its static value of 85%. This is achieved simply by an indirect acting integral controller (integral time constant of 10 s), to which the fuel utilisation error serves as input and which manipulates the setpoint of the fuel flow valve. If the SOFC power controller is in "*normal operation*" mode, it will remain in this mode and the fuel utilisation will be reset to its static value. If it is in "*maximum FU*" mode, i.e. during a larger load increase, at first the error remains constant and the fuel utilisation controller will increase the fuel flow in a perfect ramp function. At the point where the SOFC power controller can satisfy the power demand, it switches back to "*normal operation*", and the fuel flow ramp flattens to finally reach the new steady value. Zhu and Tomsovic [12] have previously shown a control strategy where fuel utilisation is reaching a high boundary during load increase.

4.5 Air flow control

The above mentioned controllers fix the fuel flow. From the performance maps (Figure 2-4) it can be seen that a fuel flow change should not be undertaken without a corresponding change in air flow, or else the system will advance to unfavourable conditions. In Figure 3 it can also be seen that a constant mean solid temperature is achievable over a load range from 40% to app. 105%. Moreover, this operation line features a very high efficiency in part-load. From the map data, a characteristic line for the air flow as a function of fuel flow or power can be developed which supplies a setpoint to the air flow controller. However, the fuel flow will tend to overshoot the target values during load changes. This might cause instability in the system if fuel flow is taken as input to the air flow setpoint calculation. Hence, the produced power as a stabilised parameter is chosen. The result is a characteristic function for the air flow setpoint (AF_{Setp}) as a polynomial function of power (P) at constant mean solid temperature of the shape $AF_{Setp} = f(P)$.

The setpoint together with the measured signal forms the error for the air flow feedback controller, which is an indirect acting proportional-integral-differential (PID) type. It manipulates the generator power through sending a power setpoint to the power electronics. We assume the power electronics to be able to instantaneously adjust the power drawn from the generator to this value.

Given a constant generator power, the system is at an unstable equilibrium. Departing from steady state, for example a step increase of the generator power will lead to deceleration of the shaft speed. No new equilibrium will be found within the valid bounds of shaft speed. By trial-and-error tuning, it has been found that a PID type controller with a high gain of ~8, an integral time constant of ~18 s and a differential time constant of ~0.8 s is able to control the shaft speed and air flow reliably, stably and quickly. However, a too quick change of the air flow rate is not desirable, as this may lead to anode backflow, inverse reaction of system power due to high amplitudes in generator power and instability due to interference with the

fuel utilisation control. In order to slow down the air flow change rate, the air flow setpoint signal is smoothened by a rate limiter.

Air flow and shaft speed are directly coupled. Nevertheless, for example a change in air density may lead to a higher required shaft speed for maintaining a certain air flow rate. Therefore the shaft speed must be monitored and overspeed protection must be provided.

4.6 Temperature control

The above mentioned strategy is under ideal conditions able to follow a load line while maintaining safe operation and constant temperature. However, the strategy does not yet assure a stable cell temperature upon external disturbances as well as changes in system characteristics through degradation, or measurement errors. Especially in the low load regime, the cell temperature is very sensitive to the fuel flow. A small error of 1-2 percentage points (caused by valve measurement error or varying fuel quality) may lead to steady state temperature change of 50 K, even though it must be noted that the temperature advances very slowly to its new steady value (in the magnitude of hours to days). As the control strategy must also ensure temperature stability, an additional feedback loop is required.

An effective way to control the temperature by only slightly influencing power is manipulating the air flow (see almost horizontal power iso-lines in Figure 2). An obstacle is that the mean cell temperature cannot be measured conveniently. However the related temperature of the fuel leaving the cell (*TF*) can be measured, for example in the recirculation plenum.

An implicit relationship between the two temperatures is established by again determining a characteristic line. It has been detected that apart from the load, the relationship is dependent on the ambient air conditions. The setpoint of *TF* is hence calculated as a second order polynomial function of power, ambient pressure and ambient temperature; $TF_{Setp} = f(P, p_{\infty}, T_{\infty})$. The coefficients of this function have been fitted using the least squares method on simulation results with constant mean cell temperature.

The error from setpoint and measured fuel temperature is fed into a slow, direct acting integral controller (integral time constant of 20,000 s). A quicker controller would react too strongly on load change dynamics which provoke a temporary error in fuel temperature. The controller output signal is added to the air flow setpoint entering the air flow controller. This method of controlling a non-measurable variable indirectly by a measurable one is called inferential control [27].

5 System response results

5.1 Small load change

Small distributed networks supplying private households are assumed to have a maximum step change of power of about 10 kW (4.7% power). Figure 6 and Figure 7 show the system response to a load decrease respectively increase of this step size around design condition over a logarithmic time axis. At the power decrease, the setpoint power is reached after less than one second without the SOFC power controller reaching the "*minimum FU*" limit. At the load increase, the SOFC power controller switches to "*maximum FU*" for approximately 3 seconds before the setpoint power is reached. Air flow advances gently to the new point of the characteristics, while the fuel flow varies in order to keep the fuel utilisation at its setpoint value. The values are fairly steady after app. 20 s. The cell temperature variation of app. 2 K is due to the temporary mismatch between air and fuel flow and hence an unbalance between

heat input and cooling. This effect diminishes with greater time constants and is supported by the temperature control.

Figure 6

Figure 7

5.2 Large load change

For industrial applications, larger load changes than the above may occur. In the following, the system response to a load change of 100 kW (from rated power down to 53%) is investigated and shown in Figure 8 and Figure 9. The setpoint power is reached after app. 11 and 57 s at the load decrease and increase respectively. The slower response at power increase is due to the lower deviation of fuel utilisation from its setpoint. It is furthermore technically required due to the danger of backflow from the burner into the anode recirculation system during pressure increase (this being not an issue at pressure decrease). A faster load increase may be achievable through higher gain of the fuel utilisation controller. Furthermore, the mean cell temperature reaches a minimum of 29 K below the design point app. 1100 s after the load decrease and a maximum of 35 K above design point app. 600 s after the load increase. This is due to the same reason as mentioned above. The presented control strategy is hence able to stabilise the mean cell temperature in a bandwidth of 65 K under strong and quick load fluctuation.

Figure 8

Figure 9

5.3 Load profile

To demonstrate the stability of the cell temperature during load following, the system is exposed to a randomly generated 24 hour load profile. It implies at an average of 24 random steps per hour with a maximum size of 10 kW. Furthermore, a day-night variation covering the full load range of 40% to 105% is superposed. Figure 10 shows the load line and the mean SOFC temperature. Under these conditions, the observed bandwidth of the temperature is app. 40 K. The strongest deviations result from steep load increase and decrease.

Figure 10

5.4 Ambient pressure and temperature change

Under real conditions, the system is exposed to external disturbances, such as ambient pressure and temperature variation. These usually vary in the magnitude of hours. The response to a simultaneous temperature increase of 15 K and pressure decrease of 20 mbar over a time of one hour has been studied, corresponding to a decrease of air density of 8%.

In Figure 11 it can be seen that after the change, the mean cell temperature increases about 7 K, as a higher air flow is required under these conditions. As the temperature control considers the measured ambient conditions it is able to reset the cell temperature to the original value, however in a time scale of several days. It is therewith sufficient for compensating annual, but not daily fluctuations.

Figure 11

The effect of ambient air density could be compensated very quickly through a feedforward control which is providing an additional correction of the air flow setpoint. However, it has been shown that the cell temperature oscillations due to load cycling are higher than the ones caused by ambient conditions. Hence, it is not considered as necessary under the given conditions.

5.5 Malfunction and degradation

The system characteristics shown in Figure 2-Figure 4 are subject to changes during the system life due to degradation of the components. Furthermore, malfunction of the measuring may affect system stability. It is hence important to check the stability of the control system under these changed conditions.

In order to simulate fluctuation of load, the system is exposed to a sinusoidal oscillation between 53% and 100% of power with a period of 2000 s. Initially, the ordinarily working system is at steady state. At time of zero, the following incidents occur one at a time:

- Fuel cell degradation: An additional ohmic resistance is implied on the fuel cell, provoking a voltage loss of 50 mV at design current.
- Compressor fouling and degradation: Compressor design efficiency, flow rate and pressure ratio are decreased by 3%.
- Fuel measurement malfunction: Fuel flow is overestimated by 5%. This incident is similar to a change in the heating value of the fuel feed.
- Air measurement malfunction: Air flow is overestimated by 5%.

The resulting mean cell temperature response is shown in Figure 12. It can be seen that the temperature control system tackles all disturbances and the temperature always stays within an acceptable range. Nevertheless, deviations of the temperature remain in some cases. This is because the inferential control scheme is disturbed by a changed relationship between measured and controlled temperature. The effect is strongest for fuel measurement malfunction, as this leads to a changed true fuel utilisation, to which the system characteristics are very sensitive. Precise and possibly redundant measuring of the fuel flow and furthermore certainty of the fuel quality is thus recommended. The fuel cell degradation simulation shows a high peak of the temperature shortly after the incident. However, degradation effects usually occur gradually, and this peak will therewith not occur in practice. On the other hand, an increase in the temperature amplitude is also visible. This is due to mismatching of the true and assumed characteristics and may be eliminated by new adjustment of the controller characteristics after a certain lifetime.

Figure 12

6 Conclusions

A powerful and flexible full dynamic model of a simple hybrid system has been developed that allows the characterisation of part-load performance and testing of control strategies.

From the system configuration and part-load performance, the following conclusions can be drawn for a control strategy:

- The degrees of freedom for the system are fuel flow and air flow. Furthermore fuel utilisation may be varied within certain limits during transients.
- The part-load behaviour of the system shows the presence of unstable regimes (no steady state exists) at high fuel flow and low air flow, and regimes with very low SOFC temperatures at high air flow and low fuel flow.
- Operation with constant mean SOFC temperature is possible within a wide load range, but the temperature is very unstable in the low load regime. A feedback control of temperature is therefore required.

- Measurable respectively calculable inputs to the control system are power, air flow, fuel utilisation and temperature of the fuel leaving the cell.
- Manipulable variables are cell current, fuel flow and generator power.

A multi-loop feedback control scheme is designed. Power is controlled by manipulating the SOFC current; fuel utilisation is controlled by manipulating the fuel flow; air flow is controlled by manipulating generator power; and the mean cell temperature is inferentially controlled by measuring the fuel cell exhaust fuel temperature and correcting the air flow setpoint. The interaction between the control loops does not lead to instability due to the strongly different controller time scales. The setpoints of the air flow and the measured temperature are calculated based on steady state characteristics of the hybrid system at constant fuel cell temperature operation.

The response of the system to load changes, load curve following, ambient air condition change and incidents of malfunction and degradation is tested. The system behaved stable during all the tests. The following conclusions on the system response may be drawn:

- Small load changes in the range of few kW are followed in a time scale of below 1 s.
- Large load changes are followed in a time scale of 10 to 60 s.
- During normal operation, the mean SOFC temperature is stable within a band of 40-65 K around its design value.
- Ambient air conditions have only a small influence on system characteristics, provided their influence on the behaviour between measured and controlled temperature is accounted for.
- Fuel flow measurement errors or variations in fuel quality are severe, as they falsify the calculated control variable of fuel utilisation, which is an important parameter for the system performance. An overestimation of fuel flow by 5% may lead to a permanent cell temperature increase of app. 35 K.
- The temperature variation increases with increasing fuel cell degradation. It may therefore be advisable to readjust the control system characteristics after a certain system degradation.

The depicted quantitative data are only valid for the studied model. However, the qualitative trends are expected to be similar in a genuine system. Hence, the demonstrated methods can be applied on a real system, given that relevant data of its behaviour are available.

Acknowledgement

We thank the Norwegian Research Council, Shell Technology Norway and Statkraft for their financial support.

Nomenclature

Symbols

$\dot{m}$	reduced mass flow
AF	air flow (relative to design value)
c	concentration (mole m^{-3})
c_p	heat capacity at constant pressure (J kg^{-1})
c_s	heat capacity of cell solid (J kg^{-1})

FF fuel flow (relative to design value)

GP generator power (relative to design value)

h heat transfer coefficient (W m^{-2} K^{-1})

I moment of inertia (kg m^2)

k thermal conductivity (W m^{-1} K^{-1})

n reduced shaft speed

P power (relative to design value)

P_b shaft power balance (W)

r_{ij} turnover of species i in reaction j (mole m^{-3} s^{-1})

r_s radius of cell solid wall (m)

SM surge margin

T temperature (K)

t time (s)

TF temperature of fuel leaving the cell (relative to design value)

v gas velocity (m s^{-1})

z axial direction (m)

Greek letters

η_m mechanical efficiency

π pressure ratio

ρ density (kg m^{-3})

ω angular shaft speed (rad s^{-1})

Indexes

∞ ambient

comp compressor

g gas

gen generator

i species

s cell solid

setp setpoint

surge surge condition

turb turbine

References

[1] Stiller, C., Thorud, B., Seljebø, S., Mathisen, Ø., Karoliussen, H., Bolland, O., "Finite-volume modeling and hybrid-cycle performance of planar and tubular solid oxide fuel cells", Journal of Power Sources 141 (2005) 227–240.

[2] Rao, D., Samuelsen, G. S., "A thermodynamic analysis of tubular SOFC based hybrid systems", ASME Paper 2001-GT-0522.

[3] Chan, S. H., Ho, H. K., Tian, Y., "Modeling for part-load operation of solid oxide fuel cell-gas turbine hybrid power plant", Journal of Power Sources 114 (2003) 213-227.

[4] Pålsson, J., Selimovic, A., Sjunnesson, L., "Combined solid oxide fuel cell and gas turbine systems for efficient power and heat generation", Journal of Power Sources 86 (2000) 442-448.

[5] Veyo, S.E., Lundberg, W.L. Vora, S.D., Litzinger, K.P., "Tubular SOFC hybrid power system status", ASME Paper 2003-GT-38943.

[6] Achenbach, E., "Response of a solid oxide fuel cell to load change", Journal of Power Sources 57 (1995) 105-109.

[7] Costamagna, P., Magistri, L., Massardo, A.F., "Design and part-load performance of a hybrid system based on a solid oxide fuel cell reactor and a micro gas turbine", Journal of Power Sources 96 (2001) 352-368.

[8] Campanari, S., "Full load and part load performance prediction for integrated SOFC and microturbine systems", Journal of Engineering for Gas Turbines and Power 122 (2000) 239-246.

[9] Pålsson, J., Selimovic, A., "Design and off-design predictions of a combined SOFC and gas turbine system", ASME Paper 2001-GT-0379.

[10] Kimijima, S., Kasagi, N., "Performance evaluation of gas turbine-fuel cell hybrid micro generation system", ASME Paper 2002-GT-30111.

[11] Stiller, C., Thorud, B., Bolland, O., "Safe dynamic operation of a simple SOFC/GT hybrid system", ASME Paper 2005-GT-68481.

[12] Zhu, Y., Tomsovic, K., "Development of models for analyzing the load-following performance of microturbines and fuel cells", Electric Power Systems Research 62 (2002) 1-11.

[13] Jurado, F., "Study of molten carbonate fuel cell - microturbine hybrid power cycles", Journal of Power Sources 111 (2002) 121–129

[14] Rao, A.D., Samuelsen, G.S., "Analysis strategies for tubular solid oxide fuel cell based hybrid systems", Journal of Engineering for Gas Turbines and Power 124 (2002) 503-509.

[15] Song, T.W., Sohn, J.L., Kim, J.H., Kim, T.S., Ro, S.T., Suzuki, K., "Parametric studies for a performance analysis of a SOFC/MGT hybrid power system based on a quasi-2D model", ASME Paper 2004-GT-53304.

[16] Achenbach, E., Riensche, E., "Methane/steam reforming kinetics for solid oxide fuel cells", Journal of Power Sources 52 (1994) 283-288.

[17] Singhal, S. C., Kendall, K., High Temperature Solid Oxide Fuel Cells - Fundamentals, Design and Applications, Elsevier Ltd, 2003

[18] Marsano, F., Magistri, L., Massardo, A.F., "Ejector performance on a solid oxide fuel cell anodic recirculation system", Journal of Power Sources 129 (2004) 216-228.

[19] Kays, W. M., London, A. L., "Compact Heat Exchangers", McGraw-Hill, 1984

[20] Kurzke, J., "Compressor and turbine maps for gas turbine performance computer programs – Component Map Collection 2", Joachim Kurzke, Dachau, Germany, 2004.

[21] gPROMS (General Process Modelling and Simulation Tool), v.2.3.4, Process Systems Enterprise Ltd., London, http://www.psenterprise.com/

[22] Yi, Y., Smith, T.P., Brouwer, J., Rao, A.D., Samuelsen, G.S., "Simulation of a 220 kW hybrid SOFC gas turbine system and data comparison", Electrochemical Society Proceedings 2003-7 1442-1454.

[23] Johannesen, N. H., Ejector Theory and Experiments, Dissertation, Danish Academy of Technical Sciences, Copenhagen, Denmark, 1951.

[24] Von Spakovsky, M.R., Rancruel, D., Nelson, D., Mazumder, S.K., Burra, R., Acharya, K., Haynes, C., Williams, R., Gemmen, R.S., "Investigation of system and component performance and interaction issues for solid oxide fuel cell based auxiliary power units responding to changes in application load", IECON Proceedings (Industrial Electronics Conference), v 2 (2003) 1574-1579.

[25] Thorud, B., Stiller, C., Weydahl, T., Bolland, O., Karoliussen, H., "Part-load and load-change simulation of tubular SOFC systems", 6th European Solid Oxide Fuel Cell Forum, Lucerne, Switzerland, 2004.

[26] Nakajo, A., Stiller, C., Härkegård, G., Bolland, O., "Modeling of thermal stresses and probability of failure of tubular solid oxide fuel cells", to be submitted to Journal of Power Sources

[27] Stephanopoulos, G., Chemical Process Control – An Introduction to Theory and Practice, Prentice-Hall Inc., New Jersey, 1984.

Figure legend

Figure 1 – Cycle layout and design point values (square marked values remain always constant)

Figure 2 – Steady-state performance: Power, efficiency and shaft speed

Figure 3 – Steady-state performance: TIT, mean SOFC and fuel recycle temperature

Figure 4 – Steady-state performance: Pressure, steam-to-carbon ratio and reforming degree.

Figure 5 – Control system design

Figure 6 – Small load decrease

Figure 7 – Small load increase

Figure 8 – Large load decrease

Figure 9 – Large load increase

Figure 10 – Load following

Figure 11 – Change of ambient conditions

Figure 12 – Malfunction and degradation effects on temperature

Figure 1

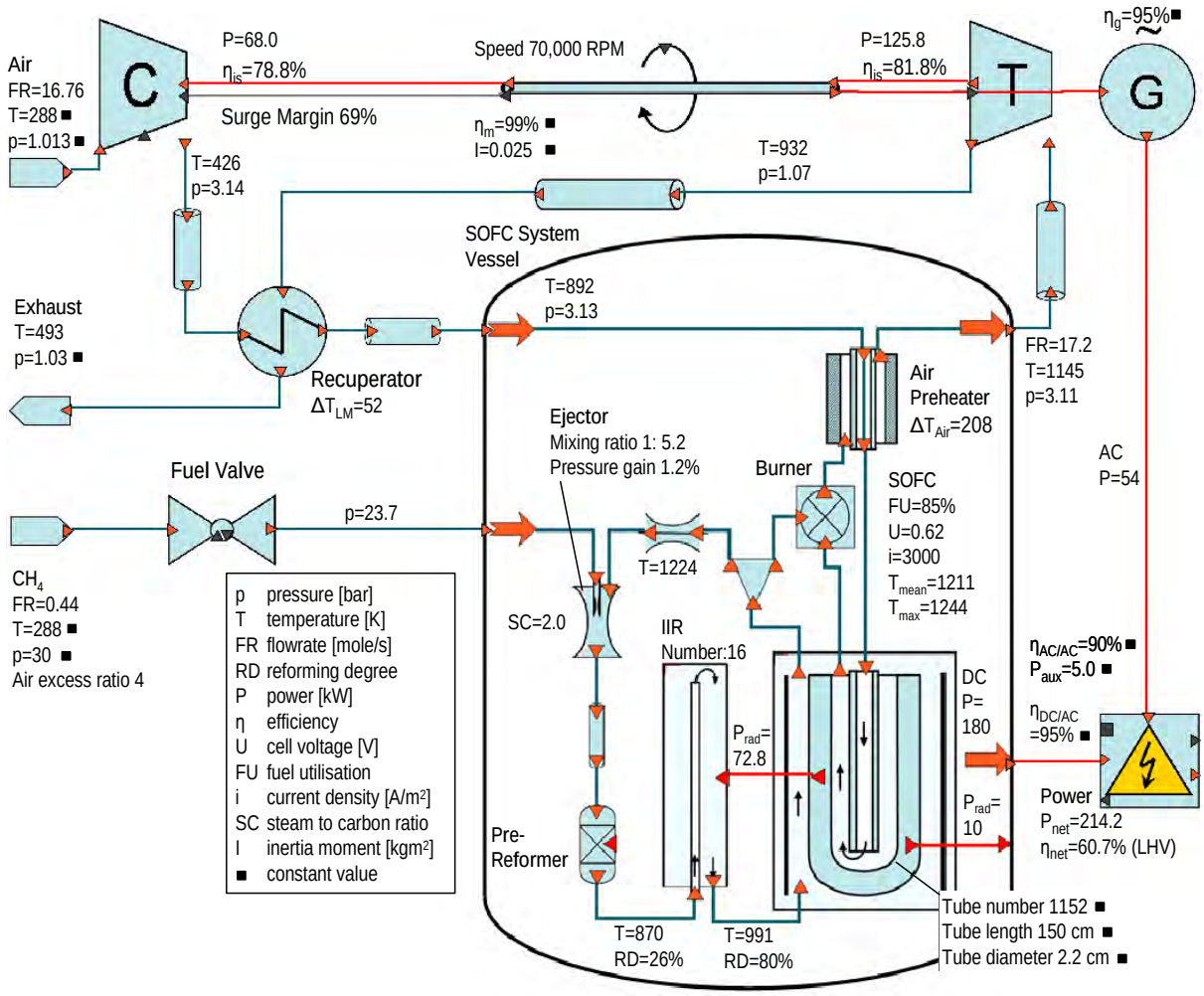
Air
FR=16.76
T=288 ■
p=1.013 ■
C
P=68.0
η_{is}=78.8%
Surge Margin 69%
Speed 70,000 RPM
η_m=99% ■
I=0.025 ■
P=125.8
η_{is}=81.8%
T
G
η_g=95%■
T=426
p=3.14
T=932
p=1.07
SOFC System
Vessel
T=892
p=3.13
Exhaust
T=493
p=1.03 ■
Recuperator
ΔT_{LM}=52
Air
Preheater
ΔT_{Air}=208
FR=17.2
T=1145
p=3.11
AC
P=54
Ejector
Mixing ratio 1: 5.2
Pressure gain 1.2%
Burner
SOFC
FU=85%
U=0.62
i=3000
T_{mean}=1211
T_{max}=1244
Fuel Valve
p=23.7
T=1224
SC=2.0
IIR
Number:16
$\eta_{AC/AC}$=90% ■
P_{aux}=5.0 ■
$\eta_{DC/AC}$
=95% ■
DC
P=
180
P_{rad}=
72.8
P_{rad}=
10
Power
P_{net}=214.2
η_{net}=60.7% (LHV)
CH_4
FR=0.44
T=288 ■
p=30 ■
Air excess ratio 4
Pre-
Reformer
T=870
RD=26%
T=991
RD=80%
Tube number 1152 ■
Tube length 150 cm ■
Tube diameter 2.2 cm ■
p pressure [bar]
T temperature [K]
FR flowrate [mole/s]
RD reforming degree
P power [kW]
η efficiency
U cell voltage [V]
FU fuel utilisation
i current density [A/m²]
SC steam to carbon ratio
I inertia moment [kgm²]
■ constant value

Figure 2

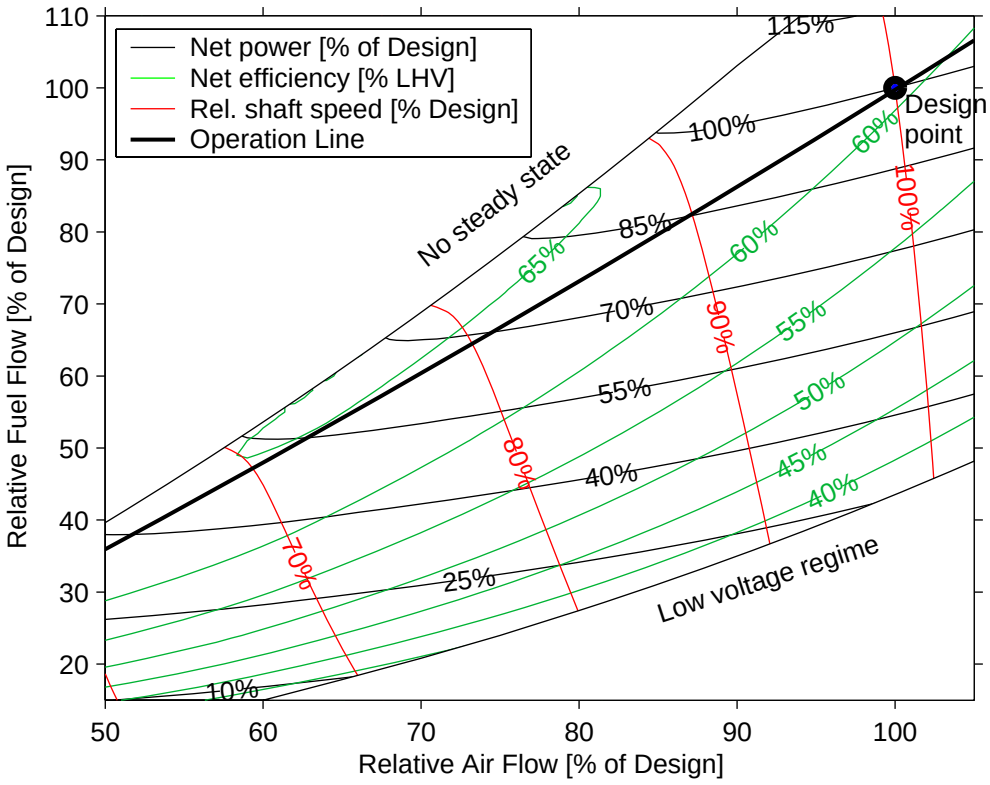
Net power [% of Design]
Net efficiency [% LHV]
Rel. shaft speed [% Design]
Operation Line
No steady state
Design point
Low voltage regime
115%
100%
85%
70%
55%
40%
25%
10%
65%
60%
55%
50%
45%
40%
110%
90%
80%
70%
Relative Fuel Flow [% of Design]
Relative Air Flow [% of Design]
110
100
90
80
70
60
50
40
30
20
50
60
70
80
90
100

Figure 3

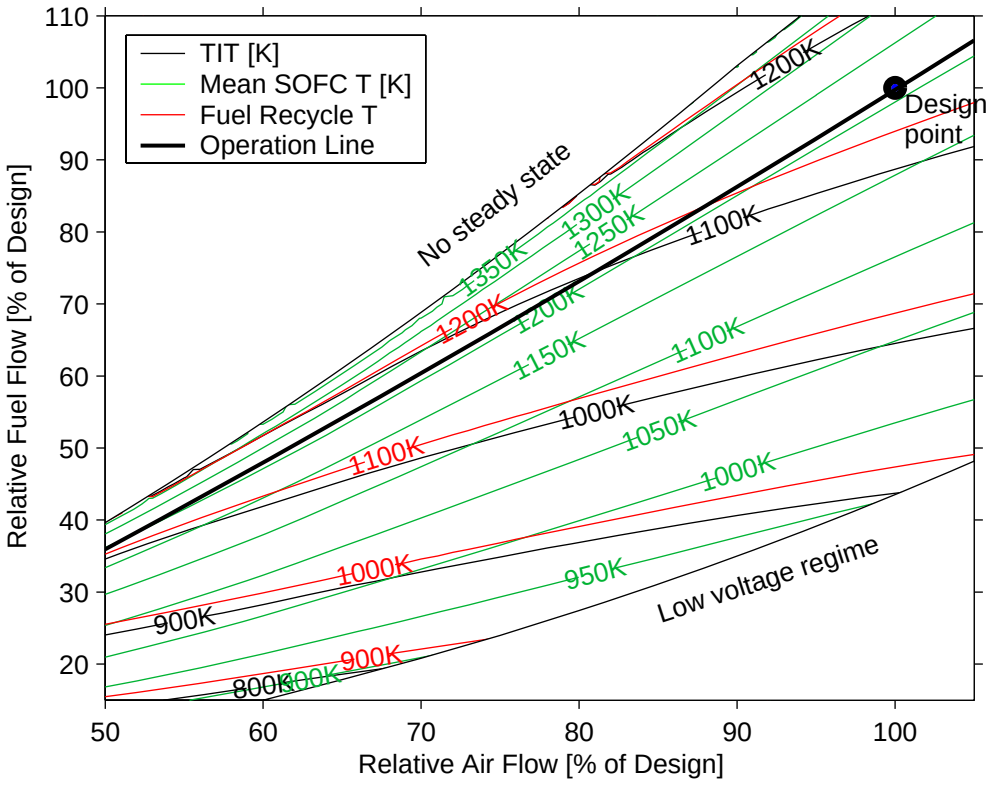
TIT [K]
Mean SOFC T [K]
Fuel Recycle T
Operation Line
No steady state
Design point
Low voltage regime
1200K
1300K
1250K
1350K
1200K
1200K
1150K
1100K
1100K
1000K
1050K
1000K
1100K
1000K
950K
900K
900K
800K
800K
Relative Fuel Flow [% of Design]
Relative Air Flow [% of Design]
110
100
90
80
70
60
50
40
30
20
50
60
70
80
90
100

Figure 4

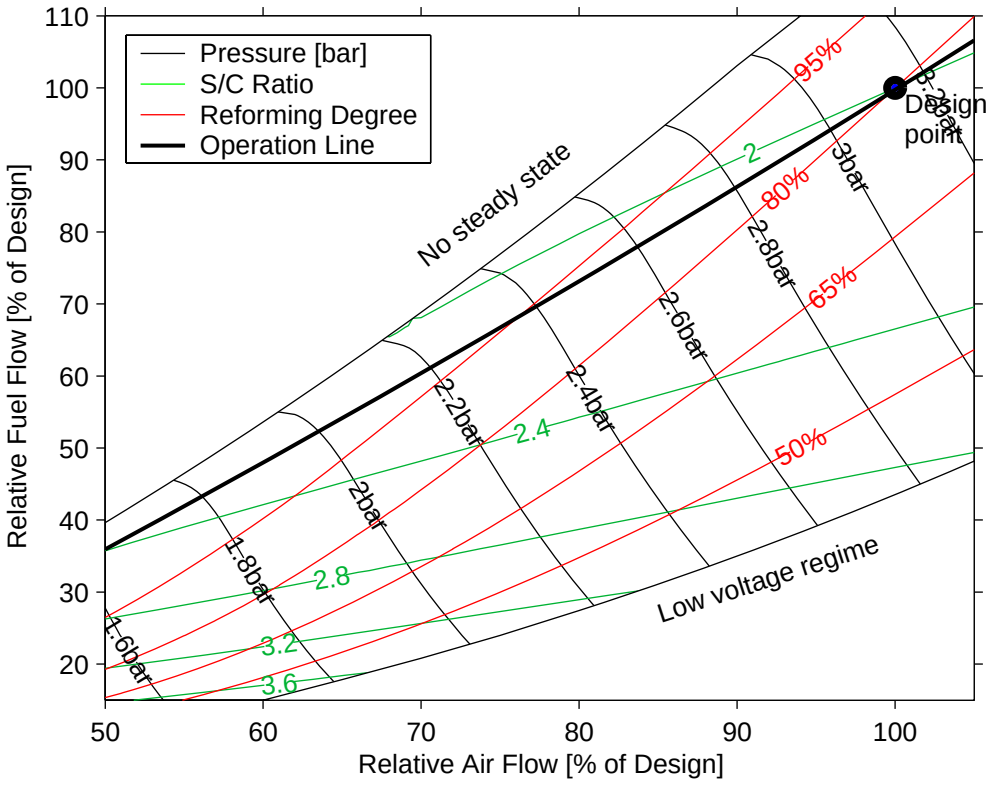
Pressure [bar]
S/C Ratio
Reforming Degree
Operation Line
No steady state
Low voltage regime
Design point
95%
80%
65%
50%
2
2.4
2.8
3.2
3.6
1.6bar
1.8bar
2bar
2.2bar
2.4bar
2.6bar
2.8bar
3bar
Relative Fuel Flow [% of Design]
Relative Air Flow [% of Design]
110
100
90
80
70
60
50
40
30
20
50
60
70
80
90
100

Figure 5

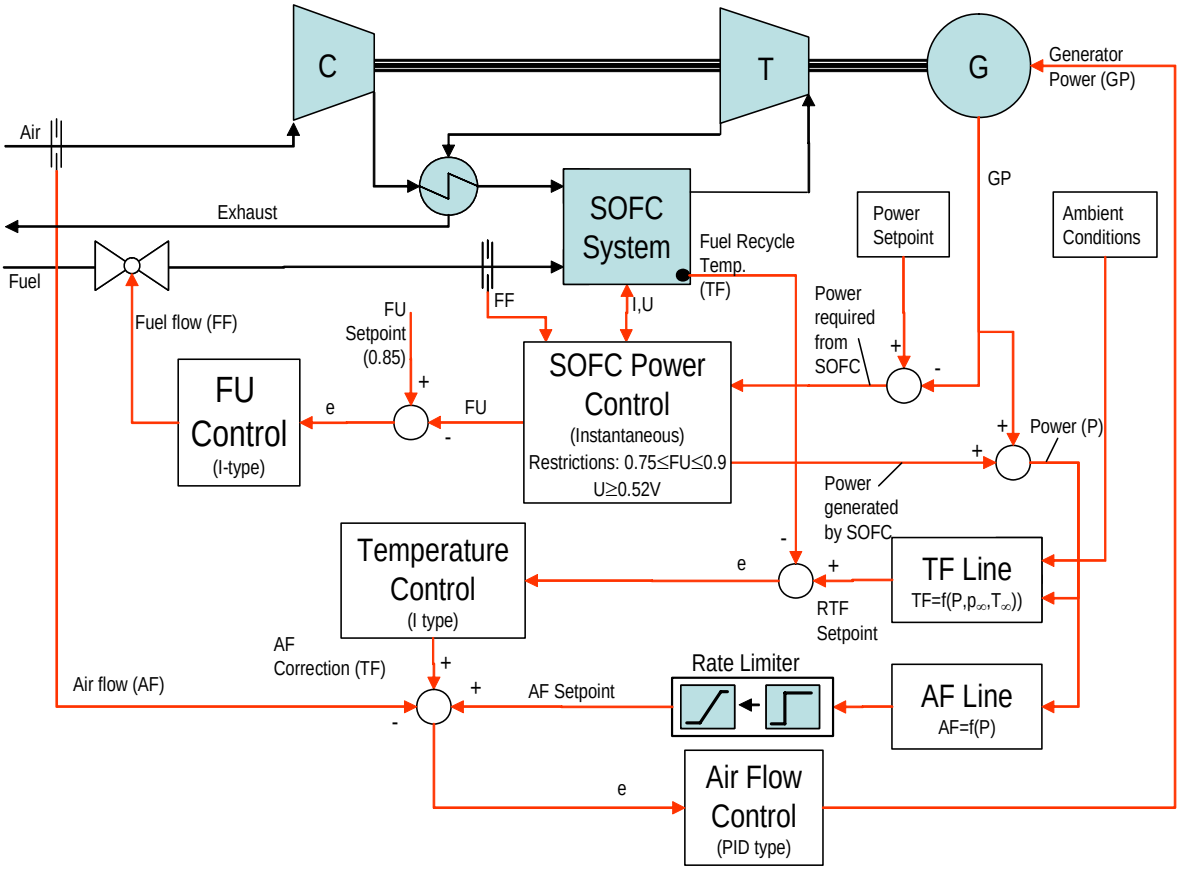
C
T
G
Generator
Power (GP)
Air
Exhaust
Fuel
SOFC
System
Fuel Recycle
Temp.
(TF)
GP
Power
Setpoint
Ambient
Conditions
Power
required
from
SOFC
Fuel flow (FF)
FF
I,U
FU
Setpoint
(0.85)
FU
Control
(I-type)
e
FU
SOFC Power
Control
(Instantaneous)
Restrictions: 0.75≤FU≤0.9
U≥0.52V
Power (P)
Power
generated
by SOFC
Temperature
Control
(I type)
TF Line
TF=f(P,p∞,T∞))
RTF
Setpoint
AF
Correction (TF)
Air flow (AF)
AF Setpoint
Rate Limiter
AF Line
AF=f(P)
Air Flow
Control
(PID type)

Figure 6

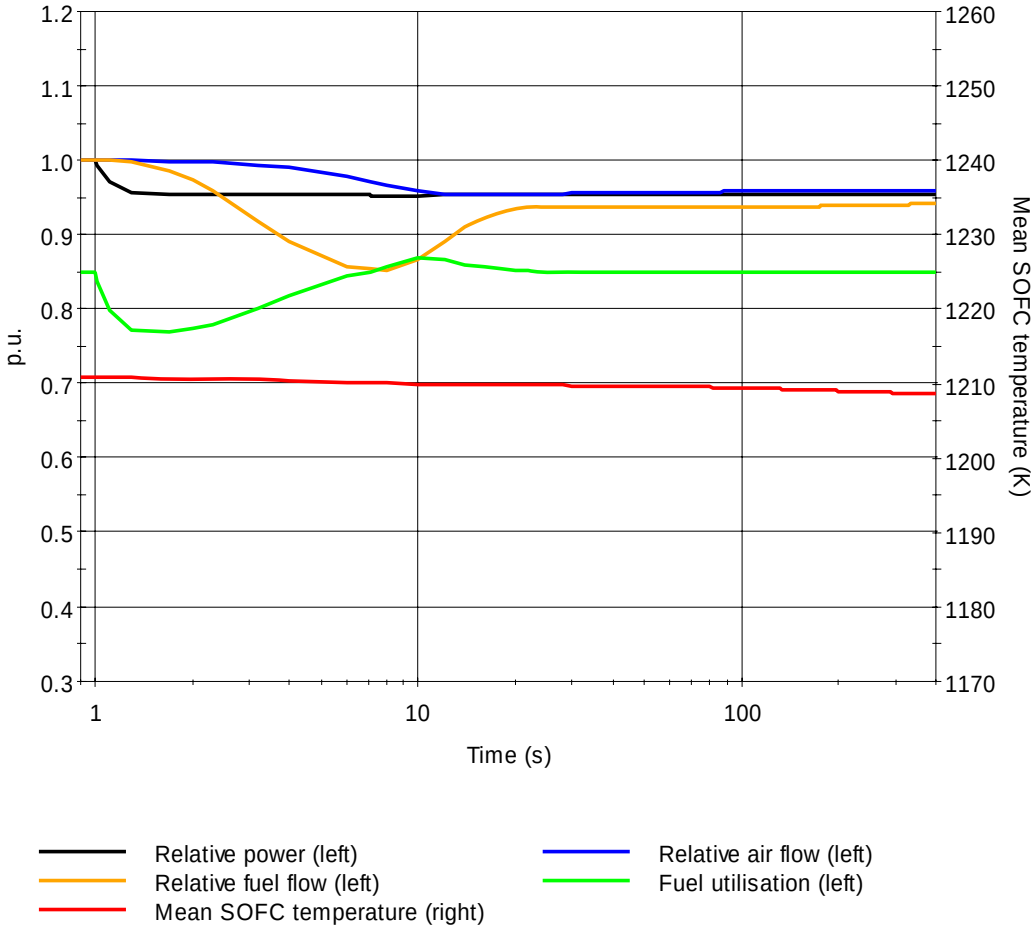
1.2
1.1
1.0
0.9
0.8
0.7
0.6
0.5
0.4
0.3
p.u.
1260
1250
1240
1230
1220
1210
1200
1190
1180
1170
Mean SOFC temperature (K)
1
10
100
Time (s)
Relative power (left)
Relative fuel flow (left)
Mean SOFC temperature (right)
Relative air flow (left)
Fuel utilisation (left)

Figure 7

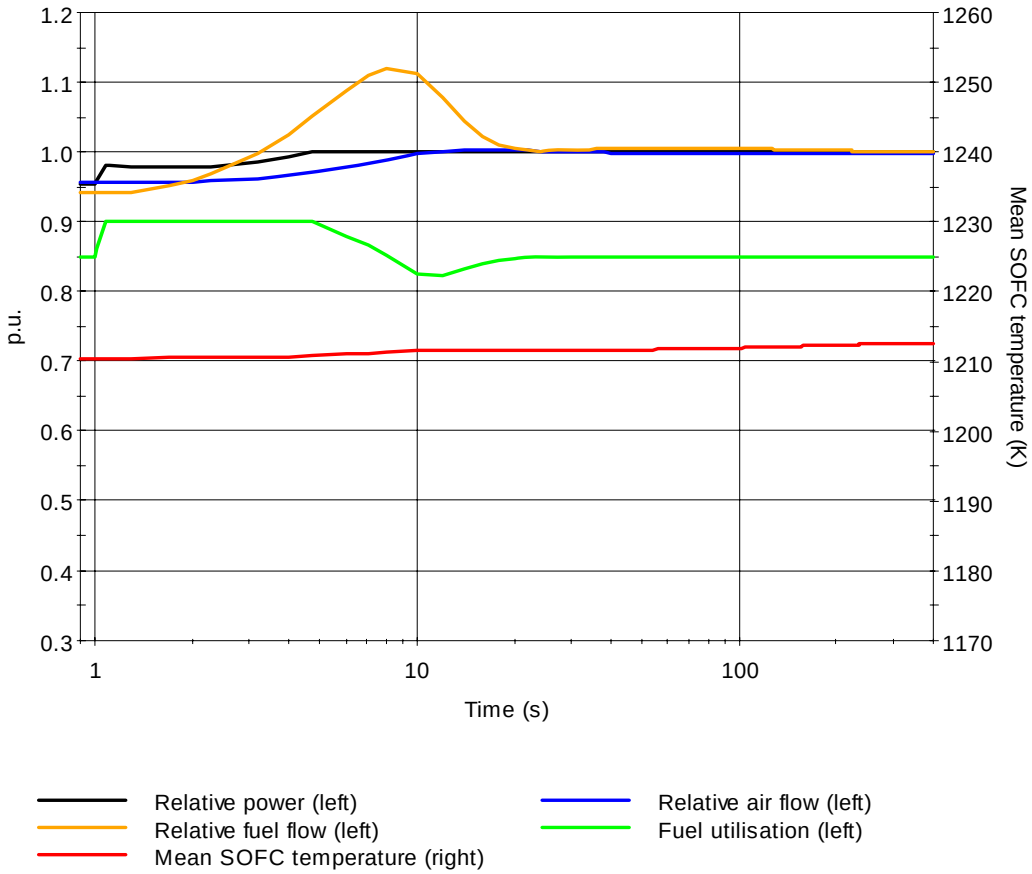
1.2
1.1
1.0
0.9
0.8
0.7
0.6
0.5
0.4
0.3
p.u.
1260
1250
1240
1230
1220
1210
1200
1190
1180
1170
Mean SOFC temperature (K)
1
10
100
Time (s)
Relative power (left)
Relative fuel flow (left)
Mean SOFC temperature (right)
Relative air flow (left)
Fuel utilisation (left)

Figure 8

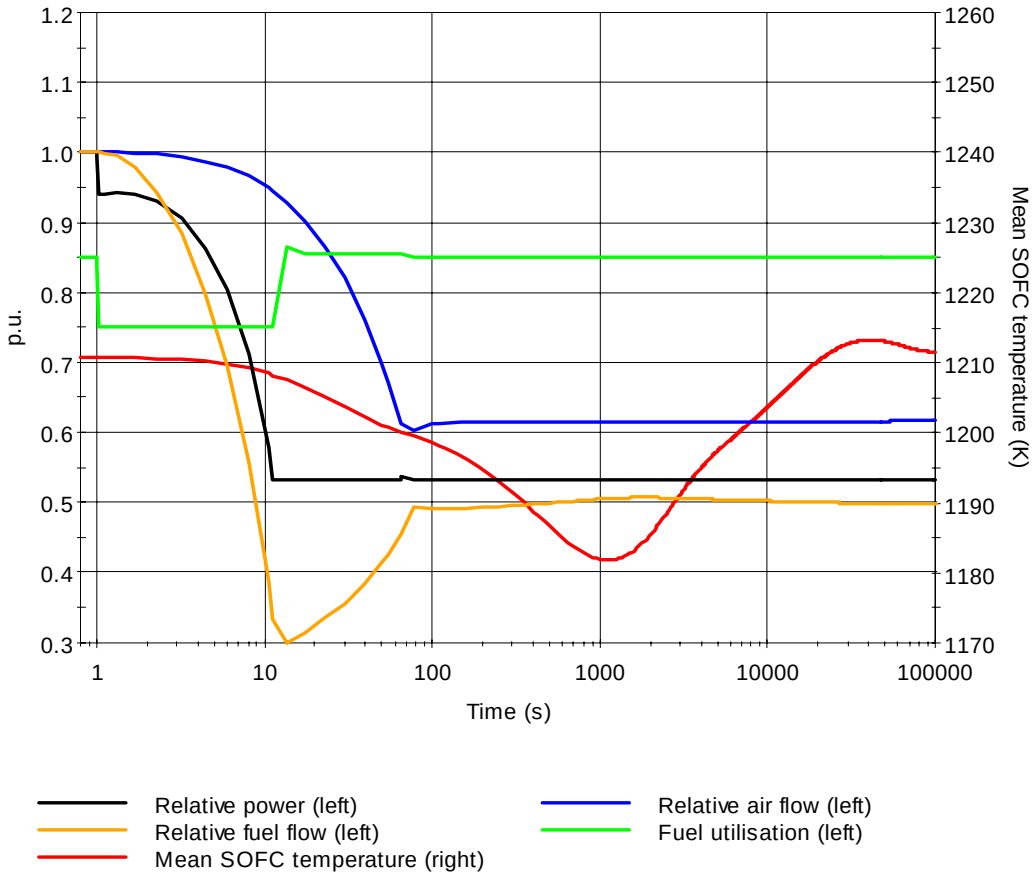
1.2
1.1
1.0
0.9
0.8
0.7
0.6
0.5
0.4
0.3
p.u.
1260
1250
1240
1230
1220
1210
1200
1190
1180
1170
Mean SOFC temperature (K)
1
10
100
1000
10000
100000
Time (s)
Relative power (left)
Relative fuel flow (left)
Mean SOFC temperature (right)
Relative air flow (left)
Fuel utilisation (left)

Figure 9

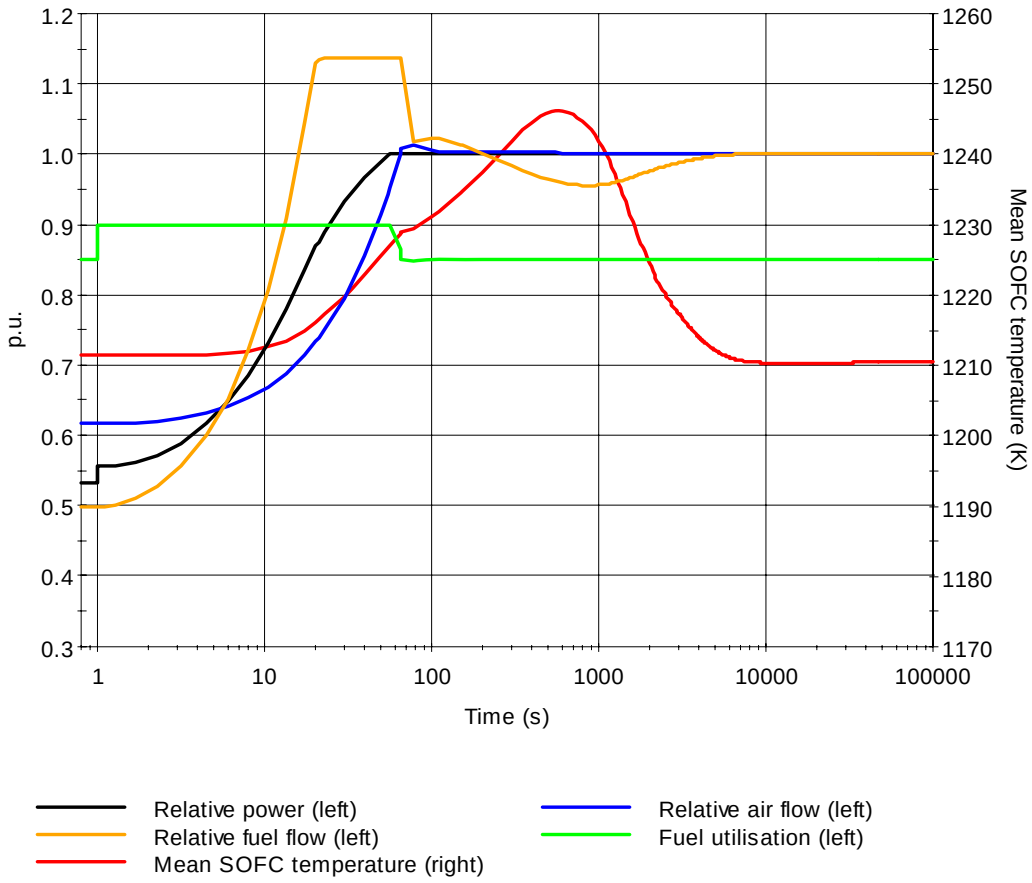
1.2
1.1
1.0
0.9
0.8
0.7
0.6
0.5
0.4
0.3
p.u.
1260
1250
1240
1230
1220
1210
1200
1190
1180
1170
Mean SOFC temperature (K)
1
10
100
1000
10000
100000
Time (s)
Relative power (left)
Relative fuel flow (left)
Mean SOFC temperature (right)
Relative air flow (left)
Fuel utilisation (left)

Figure 10

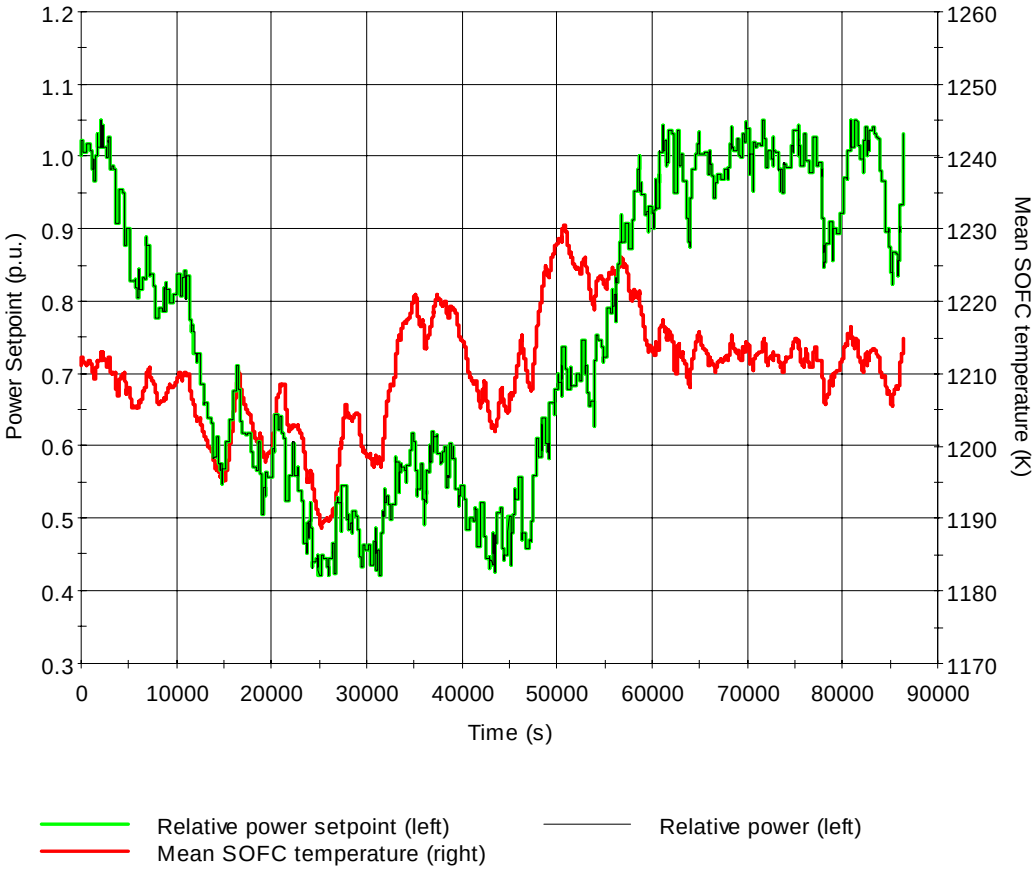
1.2
1.1
1.0
0.9
0.8
0.7
0.6
0.5
0.4
0.3
Power Setpoint (p.u.)
1260
1250
1240
1230
1220
1210
1200
1190
1180
1170
Mean SOFC temperature (K)
0
10000
20000
30000
40000
50000
60000
70000
80000
90000
Time (s)
Relative power setpoint (left)
Mean SOFC temperature (right)
Relative power (left)

Figure 11

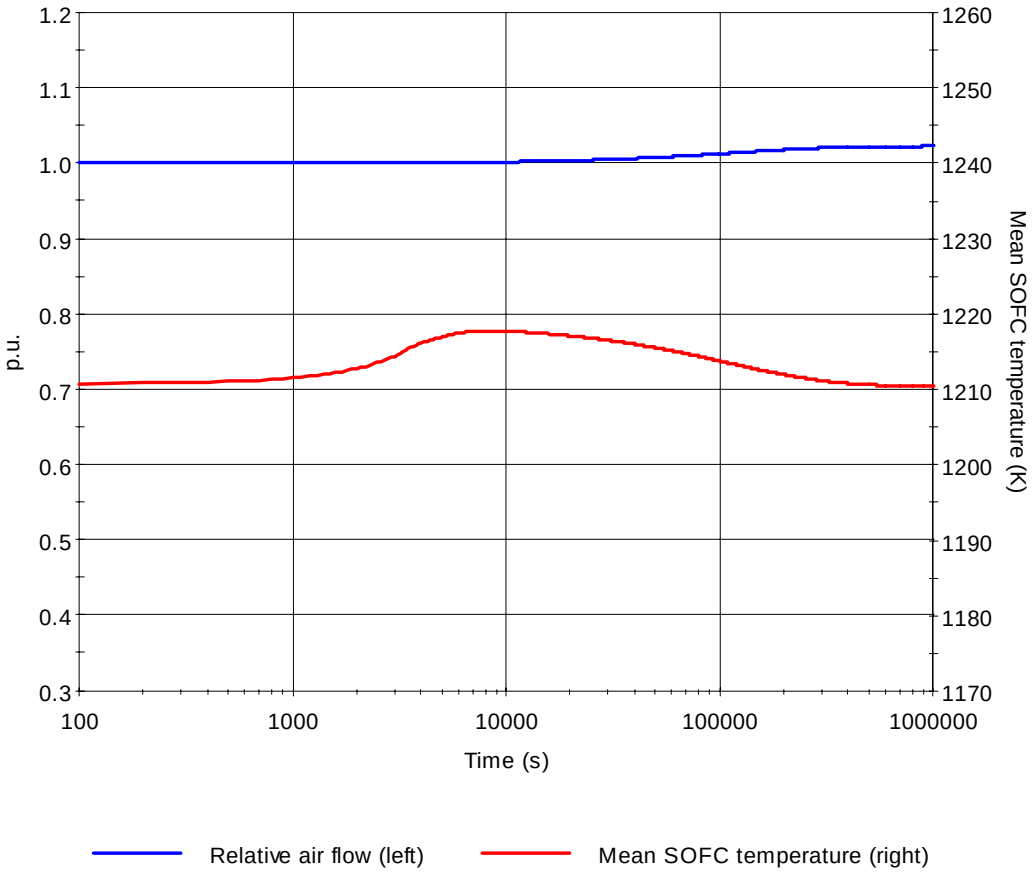
1.2
1.1
1.0
0.9
0.8
0.7
0.6
0.5
0.4
0.3
p.u.
1260
1250
1240
1230
1220
1210
1200
1190
1180
1170
Mean SOFC temperature (K)
100
1000
10000
100000
1000000
Time (s)
Relative air flow (left)
Mean SOFC temperature (right)

Figure 12

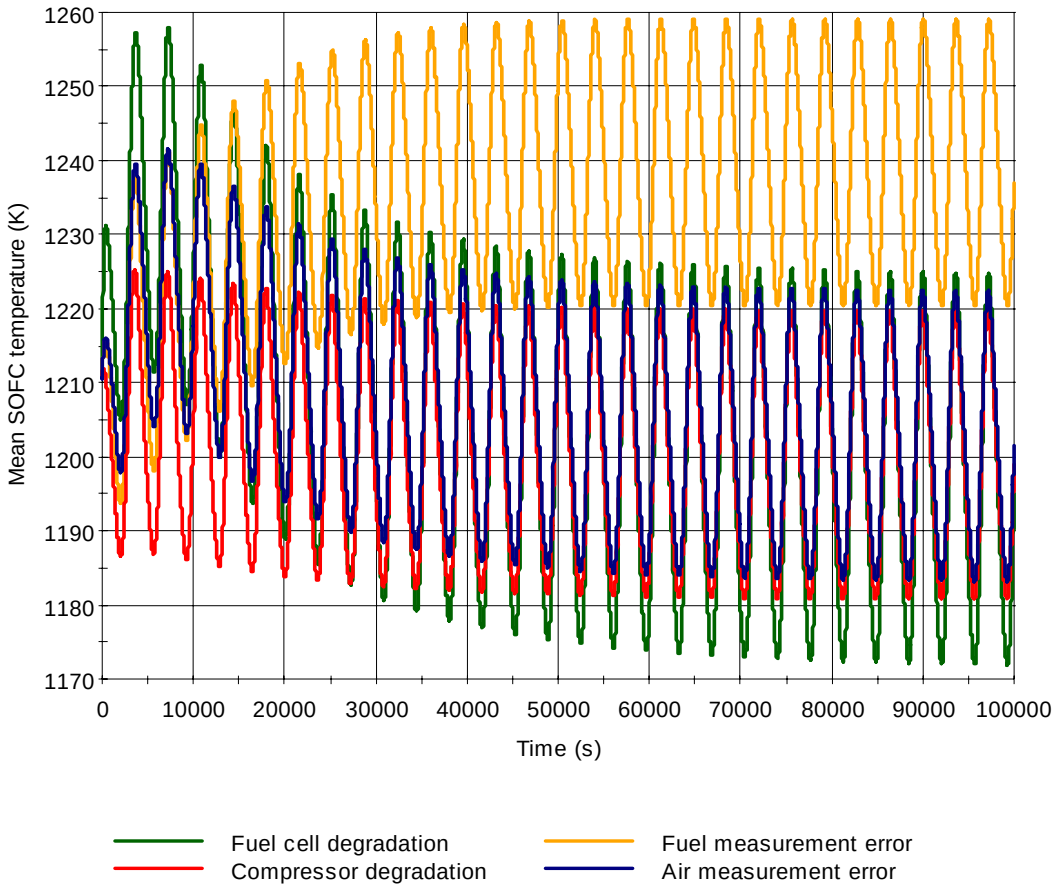
Mean SOFC temperature (K)
1260
1250
1240
1230
1220
1210
1200
1190
1180
1170
0
10000
20000
30000
40000
50000
60000
70000
80000
90000
100000
Time (s)
Fuel cell degradation
Compressor degradation
Fuel measurement error
Air measurement error